ABSTRACT

COALE, JOSEPH MICHAEL. Model Order Reduction for Problems of Nonlinear Radiative Transfer Based on Nonlinear Projective Techniques and Data-Driven Methodologies. (Under the direction of Dmitriy Anistratov).

In this work, a series of reduced order models (ROMs) for problems of thermal radiative transfer (TRT) is developed. These ROMs are formulated using a synthesis of multiple techniques for dimensionality reduction, including nonlinear projection and data-driven methodologies. The nonlinear projective approach is applied to the Boltzmann transport equation (BTE) to derive a hierarchy of low-order moment equations with exact closures that depend weakly on the BTE solution (e.g. the Eddington tensor). A variety of data-based methods for dimensionality reduction and estimation are applied to create a spectrum of approximations for the closures of the low-order moment equations. The considered methods include the proper orthogonal decomposition (POD), the dynamic mode decomposition (DMD), and the POD-Galerkin & POD-Petrov-Galerkin projection approaches. One model is developed that forms approximations for the Eddington tensor that provides closure to the low-order system of moment equations with the POD and DMD. A parameterized ROM is developed using POD approximations of the Eddington tensor and an interpolation scheme in parameter space. Another model finds an approximation for the Eddington tensor in phase space and time simultaneously from TRT solutions obtained with diffusion-based models. An additional model derives a POD-Galerkin projection of the BTE whose solution gives approximate closure to the multilevel system of moment equations. Another model is developed using a POD-Petrov-Galerkin projection of the normalized BTE (NBTE) that solves for a normalized radiation intensity distribution that informs the Eddington tensor, used with the hierarchy of moment equations. Lastly, a numerical method is developed for memory reduction in implicit time integration schemes for the BTE with the low-order system of equations in TRT problems.

Numerical results are presented to demonstrate the performance of these ROMs in the simulation of supersonic radiation shock problems. Each developed model is shown to effectively and robustly reduce the dimensionality of the nonlinear multiphysical class of TRT problems. The accuracy of solutions obtained with these models depends on the rank of approximation. With low-rank every model is shown to produce sufficiently accurate solutions. Most of the presented models are found to have a-priori prediction capability of their accuracy, based on the parameter that determines the rank of approximation.

Model Order Reduction for Problems of Nonlinear Radiative Transfer Based on Nonlinear Projective Techniques and Data-Driven Methodologies

by
Joseph Michael Coale

A dissertation submitted to the Graduate Faculty of
North Carolina State University
in partial fulfillment of the
requirements for the Degree of
Doctor of Philosophy

Nuclear Engineering

Raleigh, North Carolina
2022

APPROVED BY:

Yousry Azmy	Alina Chertock
Steven Shannon	Todd Urbatsch

Dmitriy Anistratov
Chair of Advisory Committee

ACKNOWLEDGEMENTS

This work could not have been completed without the tremendous amount of support and council that I have recieved during my studies from many different parties. I would like to first thank Dmitriy Anistratov for his exceptional advisory and commitment to my own learning, I am truly grateful to have been able to study under such a great scientist. It is my hope to walk a similar path as a future scientist. I must also thank the members of my committee, each of whom has greatly improved upon this work as well as my own knowlege through their council. I am furthermore grateful for the support and patience provided to me from my immediate and extended family members, which I could not have done without. Lastly, I must express my sincere gratitude for the encouragement given to me by my soon-to-be wife Emmy Howell, along with her patience enduring through my somewhat erratic schedule for the past years.

TABLE OF CONTENTS

LIST OF TABLES

LIST OF FIGURES

CHAPTER

1

INTRODUCTION

The ability to accurately model and predict particle transport processes is a necessary component in obtaining detailed understanding and predictive capabilities for a wide class of physics. Depending on the application, one may encounter the need to model the behavior of photons, neutrons, neutrinos, electrons, etc. as they propagate through and interact with a variety of host media. Each of these types of particles can be modelled with different forms of the Boltzmann transport equation (BTE) [1]. Radiative transfer is the primary physics of interest in the following endeavor, where energy is transported through the propagation, emission and absorption of photon radiation [2, 3].

In this work, a series of reduced-order models (ROMs) are developed for the BTE. Each of these models approximates the BTE solution with equations that exist in a lower-dimensional space than the BTE. Such low-dimensional models pose a smaller computational burden to solve than the typically expensive BTE. These ROMs are designed with nonlinear multiphysical problems in mind and posses a wide application space. The fundamental approach used here toward dimensionality reduction of the BTE combines methods of nonlinear projection with data-driven approximation techniques.

1.1 Motivation

Radiative transfer becomes the dominant mode of energy redistribution in materials at extremely high temperatures. The physical phenomena whose behavior is heavily influenced by this mode of energy redistribution can be found in a wide range of fields including plasma physics, astrophysics, atmospheric and ocean sciences, combustion and fire physics, and high-energy-density-physics [4, 5, 6, 7, 8, 9]. Some examples of these phenomena include supernovae explosions, inertial confinement fusion pellet implosions, etc.

These types of phenomena are typically modelled with complex multiphysical systems of differential equations (e.g. radiation hydrodynamics problems) [10, 11, 12, 13]. Inside these systems, the BTE is used to model the involved radiation transport component. Finding the solution to these complex systems is an arduous task, associated with an array of fundamental challenges inherent to the involved equations and necessitating the use of numerical simulation. The systems are often highly nonlinear with the comprising equations being tightly coupled to one another. One common source of such tight coupling is the interaction between the flux of radiation particles and material properties of the host medium. In problems with large radiative transfer effects, the material opacities depend on the particle flux whose behavior in turn is influenced by the opacities themselves. Furthermore the behavior of these systems is characterized by multiple scales in space-time, with distinct characteristics being associated with different energy ranges. This results in stiff systems where the solution must account for non-local effects of radiation which may propagate far beyond the characteristic length of the problem. Lastly, these systems are high-dimensional. This means that a massive number of degrees of freedom (DoF) are required to adequately describe their solution, which imposes large memory requirements and computational load.

The BTE generally drives the overall high-dimensionality exhibited by these systems, residing in a higher dimensional space than the other multiphysical equations it becomes coupled to. In 3D geometry its solution depends on 7 independent variables describing spatial position, particle direction of motion, photon frequency (wave number) and time. For this reason employing a reduced-order model (ROM) for the BTE can be an effective means to decrease computational costs innate to multiphysics problems involving radiative transfer.

ROMs for the BTE seek some approximate low-dimensional representation of the solution to the BTE (the radiation intensity distribution). The most common models find

low-dimensional equation(s) that describe integral quantities of the high-order radiation intensities. These low-order equations can then be used in place of the BTE when modeling phenomena with radiative transfer effects. The resultant system of equations will depend on significantly fewer DoF allowing for solutions to be found at lower computational cost. The development of advanced ROMs for particle transport processes is an active field of research at the current time in an effort to find efficient models for these complex physics with low levels of error.

1.2 Dimensionality Reduction for Particle Transport Problems

Many of the most well-known ROMs for the BTE are derived by leveraging some approximation(s) to remove dependence of the solution on either photon frequency, direction of motion (angle) or both. In other words, these methods attempt to approximate the Boltzmann transport solution in velocity space. The popular P_1 and flux-limited diffusion models solve for integral quantities of the BTE solution using moments of the BTE combined with a linear-in-angle approximation of the radiation intensities [14, 15, 16]. Another group of models are based on the variable Eddington factor (VEF) method that introduces a closure for the radiation pressure term present in the equations that govern the first two moments of the radiation intensity by means of the Eddington tensor. VEF models vary by the way they each approximate the Eddington tensor. The Minerbo model is derived by means of a maximum entropy closure for the Eddington tensor. The M_N method applies the maximum entropy closure for a system of N moment equations [17, 18, 19]. Hence, the Minerbo model is the M_1 method. Other commonly used models apply Kershaw, Wilson, Livermore closures [20, 21, 22, 23]. The capabilities of these ROMs have been extensively studied and remain as useful and computationally cheap methods for many applications. Even so, the accuracy of these models is limited. This has generated a need for investigation into more advanced types of ROMs.

In recent times the majority of research done towards development of more advanced ROMs has been dominated by data-driven type models that have the potential to overcome such limitations on accuracy. These methods find an advantage by making use of the vast amounts of data available from experiments and simulations that have been amassed over the years, with the idea to take advantage of general model-order reduction techniques combined with some given databases to achieve a reduction in dimensionality. Many

such techniques are available to choose from [24, 25, 26, 27, 28], some notable examples including: (i) the proper orthogonal decomposition (POD) (a.k.a. principle component analysis (PCA) or the Karhunen-Loève expansion) [29, 30, 31, 32, 33, 34], (ii) the dynamic mode decomposition (DMD) [35, 36, 37, 38], (iii) deep neural networks (DNNs) [39], (iv) the proper generalized decomposition (PGD) [40], (v) balanced truncation [41] and (vi) reduced basis methods [42]. These techniques have seen extensive use in the fluid dynamics community for the modeling of general nonlinear flows [43, 44], linearized flows [45], compressible flows [46], turbulence [33, 47] and other applications [48, 49]. Naturally the same techniques also have a wide range of applicability in the development of ROMs for particle transport.

Several of these types of models have been developed for linear particle transport problems. A POD-Galerkin projection based methodology has been developed to perform dimensionality reduction in both space and time for linear dynamical systems and applied to problems of linear Boltzmann transport [50]. POD-Petrov-Galerkin projection approaches were used to create ROMs for steady-state, parameterized neutral particle transport problems in 1D geometry [51, 52]. The DMD has been applied as a surrogate model to predict neutron populations in subcritical metal systems [53]. Explorations were done with the PGD for separating (i) spatial and energy variables in multigroup neutron diffusion problems [54], (ii) spatial and angular variables for the BTE in 1D slab geometry [55], and (iii) spatial variables for the BTE in 2D Cartesian geometry [56]. A low-rank manifold projection technique has been used to form a ROM for linear time-dependent radiation transport problems [57, 58, 59, 60]. Neural networks have been used to (i) obtain data-driven estimations of closures for P_N-type systems of moment equations of the linear BTE [61, 62], and (ii) create surrogate models for the 1D linear BTE [63, 64] and the 2D neutron diffusion equation [65]. The POD and reduced-basis methods have been applied to achieve a reduction in the dimensionality along the angular variable for various neutral particle transport problems [66, 67, 68, 69, 70].

Neutron transport in nuclear reactor-physics problems has been the subject of data-driven model reduction research efforts as well. POD-Galerkin and DMD-Galerkin approaches have been used to model the neutronics in various reactor type problems with feedback from delayed neutron precursors [71, 72, 73]. The PGD has been used to model (i) reactor kinetics [74, 75], and (ii) the neutron flux and cross sections for light water reactors [76]. POD-Galerkin projection was applied to modeling steady-state, parameterized molten salt fast reactor problems [77, 78, 79]. A reduced basis method was applied to pin-by-pin reactor calcuations [80]. A POD-Galerkin projection method has been devised

for use with domain-decomposition in reactor simulations [81].

Development of these methods has also been investigated for nonlinear problems of radiative transfer. A moment-based approach has been used with a POD approximation of the Eddington tensor [82, 83]. An effective grey, moment based model for multigroup radiative transfer problems was developed using the POD to approximate frequency-averaged moment closures [84]. Reduction in frequency dimension was found using an optimization problem to derive few-group models of radiative heat transfer in plasma applications [85]. A model has been developed based on a POD-Galerkin projection of the BTE coupled to moment equations [86]. A numerical method to reduce memory requirements in implicit radiative transfer methods based on the POD has been investigated [87]. ROMs for grey nonlinear radiation diffusion problems have been formulated with the PGD [88] and modal identification method (noting that the P_1 model is equivalent to diffusion in steady state) [89]. POD-Galerkin and trajectory piecewise-linear methods have been used to generate ROMs for spacecraft thermal analysis with a nonlinear radiative heat transfer component [90]. POD-based ROMs for radiating fluids have been constructed by applying a linearized estimation of radiative transfer effects based on POD data of non-radiating fluids [91, 92]. The frequency dimension in multigroup SP_1 radiative heat transfer calculations has been reduced using a POD-based methodology [93].

1.3 Thermal Radiative Transfer

All of the ROMs presented in this work are developed on the framework of the fundamental thermal radiative transfer (TRT) problem. The TRT problem models a supersonic flow of photon radiation through matter, neglecting photon scattering, heat conduction and external sources. This problem serves as a valuable platform for the development and testing of new computational methodologies [94, 95, 96]. TRT plays an essential role in the evolution of many phenomena contained in high-energy density physics and plasma physics, and the TRT problem inherets all of the fundamental challenges exhibited by the more general class of radiation hydrodynamics problems. Models that show success on this platform can be extended to this class of radiation hydrodynamics problems.

The TRT problem is formulated by the BTE that models photon radiation

$$\frac{1}{c}\frac{\partial I}{\partial t} + \boldsymbol{\Omega}\cdot\boldsymbol{\nabla} I + \varkappa(\nu,T)I = \varkappa(\nu,T)B(\nu,T), \tag{1.1}$$

$$\boldsymbol{r}\in\Gamma, \quad \boldsymbol{\Omega}\in\mathcal{S}, \quad \nu\in[0,\infty), \quad t\in[0,t^{\text{end}}],$$

$$I|_{t=t_0} = I^0, \quad I|_{\boldsymbol{r}\in\partial\Gamma} = I^{\text{in}} \text{ for } \boldsymbol{n}_\Gamma\cdot\boldsymbol{\Omega} < 0, \tag{1.2}$$

and the material energy balance (MEB) equation that models energy exchange between photons and matter

$$\frac{\partial\varepsilon(T)}{\partial t} = \int_0^\infty\int_{4\pi}\varkappa\big(I-B\big)d\Omega d\nu, \tag{1.3}$$

$$T|_{t=t_0} = T^0. \tag{1.4}$$

Here $I(\boldsymbol{r},\boldsymbol{\Omega},\nu,t)$ is the distribution of photon specific intensities in space ($\boldsymbol{r}$), direction of motion ($\boldsymbol{\Omega}$), frequency (ν) and time (t). Γ and $\partial\Gamma$ are the spatial domain and its surface, respectively, with $\boldsymbol{n}_\Gamma$ as the unit outward normal to $\partial\Gamma$. Directions of photon travel $\boldsymbol{\Omega}$ are contained in the set $\mathcal{S} = \{\boldsymbol{\Omega}\in\mathbb{R}^3 \ : \ |\boldsymbol{\Omega}| = 1\}$. $T(\boldsymbol{r},t)$ is the temperature of matter, $\varkappa(\nu,T)$ is the material opacity, $\varepsilon(T)$ is the material energy density and $B(\nu,T)$ is the Planckian distribution function of black-body radiation, defined as

$$B(\nu,T) = \frac{2}{h^2c^2}\frac{\nu^3}{e^{\frac{\nu}{T}}-1}, \tag{1.5}$$

where ν and T are measured in eV, h is Planck's constant and c is the speed of light. Note that $\varkappa(\nu,T) = \varkappa(\boldsymbol{r},\nu,t,T) = \rho(\boldsymbol{r},t)\kappa(\boldsymbol{r},\nu,t,T)$ where ρ is the material density field and κ is the mass-averaged photon absorption cross section (a.k.a. photon extinction coefficient) defined by the atomic cross sections of the underlying material. We also have that $\varepsilon(T) = \varepsilon(\boldsymbol{r},t,T)$. The functions $\varkappa$, κ, ρ and ε are determined by the specific materials involved in the TRT problem and can accommodate an arbitrary degree of material inhomogeneity (e.g. by taking on a piecewise form).

1.3.1 Multigroup Thermal Radiative Transfer

We consider the TRT problem discretized in photon frequency with the multigroup approximation [97], estimating functions of ν to be piecewise constant on a number of intervals $\nu\in[\nu_{g-1},\nu_g]$ for $g = 1,\ldots,N_g$ such that $0 = \nu_0 < \nu_1 < \cdots < \nu_{N_g} < \infty$. The multigroup BTE is derived by integrating the BTE (Eq. 1.1) over the intervals of photon

frequencies ($\int_{\nu_{g-1}}^{\nu_g} \cdot \, d\nu$) and is written as

$$\frac{1}{c}\frac{\partial I_g}{\partial t} + \boldsymbol{\Omega} \cdot \boldsymbol{\nabla} I_g + \varkappa_{E,g}(T) I_g = \varkappa_{B,g}(T) B_g(T), \tag{1.6}$$

$$\boldsymbol{r} \in \Gamma, \quad \boldsymbol{\Omega} \in \mathcal{S}, \quad g = 1, \ldots, N_g, \quad t \in [0, t^{\text{end}}],$$

$$I_g|_{t=t_0} = I_g^0, \quad I_g|_{\boldsymbol{r} \in \partial\Gamma} = I_g^{\text{in}} \ \text{ for } \ \boldsymbol{n}_\Gamma \cdot \boldsymbol{\Omega} < 0, \tag{1.7}$$

where $I_g = \int_{\nu_{g-1}}^{\nu_g} I_\nu \, d\nu$ is the specific intensity of photons in group g, $B_g = \int_{\nu_{g-1}}^{\nu_g} B_\nu \, d\nu$ is the group g black-body radiation distribution function, and the material opacities in group g are defined as [98, 99, 100]

$$\varkappa_{E,g}(T) = \frac{\int_{\nu_{g-1}}^{\nu_g} \varkappa_\nu(\nu, T) B_\nu(\nu, T_{\text{rad}}) \, d\nu}{\int_{\nu_{g-1}}^{\nu_g} B_\nu(\nu, T_{\text{rad}}) \, d\nu} \tag{1.8}$$

$$\varkappa_{B,g}(T) = \frac{\int_{\nu_{g-1}}^{\nu_g} \varkappa_\nu(\nu, T) B_\nu(\nu, T) \, d\nu}{\int_{\nu_{g-1}}^{\nu_g} B_\nu(\nu, T) \, d\nu}. \tag{1.9}$$

Here T_{rad} is the temperature of radiation. Applying the multigroup approximation to the MEB equation (Eq. 1.3) yields

$$\frac{\partial \varepsilon(T)}{\partial t} = \sum_{g=1}^{N_g} \left(\varkappa_{E,g}(T) \int_{4\pi} I_g \, d\Omega - 4\pi \varkappa_{B,g}(T) B_g(T) \right). \tag{1.10}$$

1.4 Model Reduction Through Nonlinear Projection

The fundmental approach used in this work to develop ROMs for multiphysical particle transport problems is based on a nonlinear projective approach. The BTE is projected onto a series of subspaces to derive a hierarchy of low-order moment equations whose closures take the form of nonlinear functionals with dependence on the Boltzmann transport solution.

The essential nonlinear projection of the BTE is formulated using the multilevel quasidiffusion (QD) method [101], also known as the variable Eddington factor (VEF) method [102]. This method makes use of a multigrid algorithm over the variables describing particle frequency (energy) and direction of motion [103, 104, 12, 105, 98, 99, 100, 106, 107, 108, 109]. This approach has been shown to give advantage in solving multiscale, multiphysical problems when compared to other methods [110]. The multilevel QD (MLQD) method is composed by (i) the high-order BTE and (ii) a hierarchy of low-order

QD (LOQD) equations for moments of the radiation intensity. The LOQD moment equations are exactly closed by means of the Eddington (QD) tensor

$$\mathfrak{f}_g = \frac{\int_{4\pi}(\mathbf{\Omega}\otimes\mathbf{\Omega})I_g\ d\Omega}{\int_{4\pi} I_g\ d\Omega}, \tag{1.11}$$

and other functionals that are weakly dependent on the BTE solution. Each of the LOQD equations represent conservation laws for certain integral quantities of the radiation intensities, and account for different scales of the problems we solve. Multiphysical equations like the MEB equation are coupled to the low-order moment equations on the same dimensional scale as occupied by the multiphysics. This low-dimensional coupling of involved multiphysics provides an initial reduction of dimensionality for particle transport problems, while involving no approximations.

The MLQD methodology provides a powerful and flexible framework for the development of new ROMs. A wide spectrum of ROMs can be derived from the MLQD method by defining approximations for the closures that define the LOQD equations. The features possessed by each of these ROMs can be defined by the types of approximations that are used. However, all such ROMs are able to conserve fundamental particle transport physics and effectively deal with multiscale behaviors by using the LOQD moment equations. Some example ROMs that are derived from this framework include the P_1, diffusion and flux-limited diffusion models. The aforementioned models based on the VEF method are also part of this class of ROMs.

1.5 The Normalized Boltzmann Transport Equation

Some of the ROMs devised in this work make use of the BTE for a normalized radiation intensity function, referred to henceforth as the normalized BTE (NBTE). This equation solves for the normalized radiation intensity distribution

$$\bar{I}_g = \frac{I_g}{\phi_g}, \tag{1.12}$$

where ϕ_g is the zeroth moment of the radiation intensity in group g, defined as

$$\phi_g = \int_{4\pi} I_g\ d\Omega. \tag{1.13}$$

The prospect of using the NBTE in place of the BTE is appealing in certain contexts where

the properties of $\bar{I}_g$ can be leveraged, having shown success in VEF methods [111, 112], flux-limited diffusion theory [113], and Monte-Carlo (MC) applications [114]. In relation to model order reduction and the MLQD methodology [101, 102, 104], there are two properties in particular to $\bar{I}_g$ that are especially valuable. $\bar{I}_g$ acts as the group-wise shape function of intensities, and its fundamental modes can be extracted with less numerical noise since the potentially large fluctuations in magnitude across phase space are contained in ϕ_g. Secondly $\bar{I}_g$ exists in the same space as the Eddington tensor which gives closure to the LOQD system; the Eddington tensor is simply the second angular moment of $\bar{I}_g$, given by

$$\mathfrak{f}_g = \int_{4\pi} (\mathbf{\Omega} \otimes \mathbf{\Omega}) \bar{I}_g \, d\Omega. \tag{1.14}$$

The NBTE can be derived by substituting the definition for $\bar{I}_g$ (Eq. 1.12) into the BTE (Eq. 1.6) to obtain

$$\frac{1}{c}\frac{\partial(\phi_g \bar{I}_g)}{\partial t} + \mathbf{\Omega} \cdot \boldsymbol{\nabla}(\phi_g \bar{I}_g) + \varkappa_{E,g}(\phi_g \bar{I}_g) = \varkappa_{B,g} B_g, \tag{1.15}$$

which after some manipulations can be written in a similar form to the BTE with a modified opacity

$$\frac{1}{c}\frac{\partial \bar{I}_g}{\partial t} + \mathbf{\Omega} \cdot \boldsymbol{\nabla} \bar{I}_g + \hat{\varkappa}_{E,g} \bar{I}_g = \varkappa_{B,g} \bar{B}_g, \tag{1.16}$$

where

$$\bar{B}_g = \frac{B_g}{\phi_g}, \tag{1.17}$$

and

$$\hat{\varkappa}_{E,g} = \varkappa_{E,g} + \frac{1}{c}\frac{\partial \ln(\phi_g)}{\partial t} + \mathbf{\Omega} \cdot \boldsymbol{\nabla} \ln(\phi_g). \tag{1.18}$$

1.6 Main Contributions Presented for Defense

The primary goal of this work is to develop and study a series of advanced ROMs for nonlinear TRT that allows for fast and accurate simulation of high-energy density physical phenomena. These ROMs are based on a synthesis of multiple techniques for dimensionality reduction, including nonlinear projection and data-driven methodologies. Each ROM is founded on the MLQD method, and uses various data-based approaches to find low-dimensional estimations for closures of the involved moment equations. This combined approach for dimensionality reduction allows for the creation of highly-accurate, low-dimensional models with natural handling of multiphysics and nonlinearities. In this

dissertation we present the following main results:

1. A ROM that applies data-based techniques such as the POD and DMD to approximate the Eddington tensor that provides closure to the hierarchy of LOQD moment equations.

2. A ROM that approximates the Eddington tensor for TRT problems by using data from other known solutions obtained by diffusion-based models

3. A ROM that combines a low dimensional, POD based projection of the BTE with the low-order system of QD equations

4. A ROM that combines a low dimensional, POD based projection of the normalized BTE with the low-order system of QD equations

5. A numerical method that uses the POD to reduce memory requirements in implicit time integration schemes for the BTE in the context of the MLQD method

These ROMs are formulated in a way that allows for application to a wide class of multiphysical problems of high-energy density physics. Use of the LOQD moment equations enforces the preservation of fundamental physical properties of the TRT solution. Furthermore the exchange of energy between radiation and matter is handled at the lowest-dimensional scale through the low-order moment equations that exist in the same dimensional space as the MEB equation.

1.6.1 Publications

The results of this research are presented in the following publications:

1. A reduced-order model for thermal radiative transfer problems based on multilevel quasidiffusion method, published in the proceedings of the 2019 International Conference on Mathematics and Computational Methods Applied to Nuclear Science and Engineering (M&C 2019) [82].

2. Data-driven grey reduced-order model for thermal radiative transfer problems based on low-order quasidiffusion equations and proper orthogonal decomposition, published in the transactions of the 2019 annual winter conference of the American Nuclear Society (ANS) [84].

3. Reduced-order models for thermal radiative transfer based on POD-Galerkin method and low-order quasidiffusion equations, published in the proceedings of the 2021 International Conference on Mathematics and Computational Methods Applied to Nuclear Science and Engineering (M&C 2021) [86].

4. Implicit Methods with Reduced Memory for Thermal Radiative Transfer, published in the proceedings of the 2021 International Conference on Mathematics and Computational Methods Applied to Nuclear Science and Engineering (M&C 2021) [87].

5. Reduced order models for nonlinear radiative transfer based on moment equations and POD/DMD of Eddington tensor, preprint on arXiv:2107.09174v1 [math.NA] [83]. The extended version of this preprint will be submitted for journal publication.

These papers that were published as part of the proceedings for international technical conferences were presented as talks at these venues as well, including at the 2019 International Conference on Mathematics and Computational Methods Applied to Nuclear Science and Engineering held in Portland Oregon, the 2019 annual ANS winter conference held in Washington D.C., and the 2021 International Conference on Mathematics and Computational Methods Applied to Nuclear Science and Engineering held in Raleigh North Carolina. A talk entitled *reduced order models for nonlinear radiative transfer problems based on nonlinear projection approach and proper orthogonal decomposition* was given at the 2021 International Conference on Computational Science and Engineering (CSE) of the Society for Industrial and Applied Mathematics (SIAM). Two seminars entitled (i) *model order reduction for nonlinear radiative transfer based on moment equations and data-driven approximations of the Eddington tensor* and (ii) *dimensionality reduction for thermal radiative transfer problems using a moment-based approach combined with the proper orthogonal decomposition* were given in 2021 at the Los Alamos National Laboratory (LANL).

1.7 Acknowledgments

The research presented in this work was funded by

1. The Department of Defense, Defense Threat Reduction Agency, grant number HDTRA1-18-1-0042 (Chapters 4, 6, 7, 8)

2. Sandia National Laboratory, Light Speed Grand Challenge, LDRD, Strong Shock Thrust (Chapter 5)

The content of this information does not necessarily reflect the position or the policy of the federal government, and no official endorsement should be inferred.

1.8 Structure of This Work

The remainder of this work is structured as follows. In Chapter 2, the MLQD method is detailed along with a brief review of the discretization schemes we use. An overview of the data-driven methods used in this work is given in Chapter 3. In Chapter 4, a ROM is presented for 2D TRT problems based on data-driven approximation of the Eddington tensor. A ROM for 2D TRT problems based on estimation of the Eddington tensor from diffusion based solutions is described in Chapter 5. Chapter 6 describes a ROM for 1D TRT problems based on a POD-Galerkin projection of the BTE with low-order moment equations. Chapter 7 presents a ROM for 2D TRT problems based on a POD-Petrov-Galerkin projection of the NBTE with low-order moment equations. Implicit methods with reduced memory for 1D TRT problems are described in Chapter 8. Conclusions and discussions are found in Chapter 9, which is followed by the bibliography and included appendices.

CHAPTER

2

THE MULTILEVEL QUASIDIFFUSION METHOD

In this chapter, the MLQD method is reviewed for multigroup TRT problems. The BTE is projected in two levels onto a series of low-dimensional subspaces to derive the hierarchy of LOQD moment equations. Following this, the schemes used to discretize all involved equations are detailed.

2.1 The Multilevel Quasidiffusion Equations

Two sets of moment equations comprise the MLQD hierarchical system. The first set of moment equations is derived by projecting the BTE onto the space $\mathcal{B}$ spanned by functions of space, frequency and time. This is done with the projection operator $\mathcal{P}_{\Omega,i} : \mathcal{F} \to \mathcal{B}$, where $\mathcal{F}$ is the space of functions of space, direction of motion, frequency and time. The operator is defined such that for some $u \in \mathcal{F}$, $\mathcal{P}_{\Omega,i}u$ is the i^{th} angular moment of u. For instance:

$$\mathcal{P}_{\Omega,0}u = \langle 1, u\rangle_\Omega, \quad \mathcal{P}_{\Omega,1}u = \langle \mathbf{\Omega}, u\rangle_\Omega, \quad \mathcal{P}_{\Omega,2}u = \langle \mathbf{\Omega}\otimes\mathbf{\Omega}, u\rangle_\Omega, \tag{2.1}$$

where the above inner product is defined as $\langle v, u\rangle_\Omega = \int_{4\pi} uv \; d\Omega$. Applying $\mathcal{P}_{\Omega,0}$ and $\mathcal{P}_{\Omega,1}$ to the BTE (Eq. 1.6) yields the zeroth and first angular moment equations of the BTE, respectively

$$\frac{1}{c}\frac{\partial}{\partial t}\langle 1, I_g\rangle_\Omega + \boldsymbol{\nabla}\cdot\langle \boldsymbol{\Omega}, I_g\rangle_\Omega + \varkappa_{E,g}(T)\langle 1, I_g\rangle_\Omega = 4\pi\varkappa_{B,g}(T)B_g(T), \tag{2.2a}$$

$$\frac{1}{c}\frac{\partial}{\partial t}\langle \boldsymbol{\Omega}, I_g\rangle_\Omega + \boldsymbol{\nabla}\cdot\langle \boldsymbol{\Omega}\otimes\boldsymbol{\Omega}, I_g\rangle_\Omega + \varkappa_{E,g}(T)\langle \boldsymbol{\Omega}, I_g\rangle_\Omega = 0. \tag{2.2b}$$

Eq. 2.2a represents the multigroup radiation energy conservation law and Eq. 2.2b represents the multigroup radiation momentum conservation law. This system can be reformulated in terms of the group radiation energy density $E_g = \frac{1}{c}\mathcal{P}_{\Omega,0}I_g$, group radiation flux $\boldsymbol{F}_g = \mathcal{P}_{\Omega,1}I_g$ and group radiation pressure tensor $\mathfrak{h}_g = \mathcal{P}_{\Omega,2}I_g$ to derive the multigroup LOQD equations

$$\frac{\partial E_g}{\partial t} + \boldsymbol{\nabla}\cdot\boldsymbol{F}_g + c\varkappa_{E,g}(T)E_g = 4\pi\varkappa_{B,g}(T)B_g(T), \tag{2.3a}$$

$$\frac{1}{c}\frac{\partial \boldsymbol{F}_g}{\partial t} + c\boldsymbol{\nabla}\cdot(\mathfrak{f}_g E_g) + \tilde{\varkappa}_{R,g}(T)\boldsymbol{F}_g = 0, \tag{2.3b}$$

where exact closure is found by recasting the group radiation pressure tensor $\mathfrak{h}_g$ in terms of the Eddington (QD) tensor defined in Eq. 1.11, which can be expressed as

$$\mathfrak{f}_g = \frac{\langle \boldsymbol{\Omega}\otimes\boldsymbol{\Omega}, I_g\rangle_\Omega}{\langle 1, I_g\rangle_\Omega}. \tag{2.4}$$

In optically thin regions, the opacity $\tilde{\varkappa}_{R,g}$ is set as $\varkappa_{E,g}$. In optically thick regions $\tilde{\varkappa}_{R,g}$ is set to the Rosseland opacity $\varkappa_{R,g}$, defined as

$$\varkappa_{R,g}(T, T_{\text{rad}}) = \left.\frac{\int_{\nu_{g-1}}^{\nu_g}\frac{dB(\nu,T')}{T'}d\nu}{\int_{\nu_{g-1}}^{\nu_g}\frac{1}{\varkappa(\nu,T)}\frac{dB(\nu,T')}{T'}d\nu}\right|_{T'=T_{\text{rad}}}. \tag{2.5}$$

The boundary and initial conditions (BCs and ICs) for Eqs. 2.3 have the following form [101, 103]:

$$\boldsymbol{n}_\Gamma\cdot\boldsymbol{F}_g\big|_{\boldsymbol{r}\in\partial\Gamma} = cC_g\big(E_g\big|_{\boldsymbol{r}\in\partial\Gamma} - E_g^{\text{in}}\big) + F_g^{\text{in}}, \quad E_g\big|_{t=t_0} = E_g^0, \quad \boldsymbol{F}_g\big|_{t=t_0} = \boldsymbol{F}_g^0, \tag{2.6}$$

with the group boundary factors defined as

$$C_g = \left. \frac{\int_{\boldsymbol{\Omega}\cdot\boldsymbol{n}_\Gamma>0} \boldsymbol{n}_\Gamma \cdot \boldsymbol{\Omega} I_g \, d\Omega}{\int_{\boldsymbol{\Omega}\cdot\boldsymbol{n}_\Gamma>0} I_g \, d\Omega} \right|_{r\in\partial\Gamma}, \tag{2.7}$$

where

$$E_g^{\text{in}} = \frac{1}{c}\int_{\boldsymbol{\Omega}\cdot\boldsymbol{n}_\Gamma<0} I_g^{\text{in}} \, d\Omega, \quad F_g^{\text{in}} = \int_{\boldsymbol{\Omega}\cdot\boldsymbol{n}_\Gamma<0} \boldsymbol{n}_\Gamma \cdot \boldsymbol{\Omega} I_g^{\text{in}} \, d\Omega, \tag{2.8}$$

$$E_g^0 = \frac{1}{c}\int_{4\pi} I_g^0 \, d\Omega, \quad \boldsymbol{F}_g^0 = \int_{4\pi} \boldsymbol{\Omega} I_g^0 \, d\Omega. \tag{2.9}$$

Alternative BCs for the LOQD equations can be formulated as [115, 116]

$$\boldsymbol{n}_\Gamma \cdot \boldsymbol{F}_g\big|_{\boldsymbol{r}\in\partial\Gamma} = cG_gE_g\big|_{\boldsymbol{r}\in\partial\Gamma} + 2F_g^{\text{in}}, \tag{2.10}$$

which make use of the so-called 'boundary Eddington tensor'

$$G_g = \left. \frac{\int_{4\pi} |\boldsymbol{n}_\Gamma \cdot \boldsymbol{\Omega}| I_g \, d\Omega}{\int_{4\pi} I_g \, d\Omega} \right|_{r\in\partial\Gamma}. \tag{2.11}$$

Unless otherwise stated, the BCs in Eq. 2.6 are assumed for the LOQD system.

The second set of moment equations is obtained by projecting the multigroup LOQD equations (Eqs. 2.3) onto the space $\mathcal{C}$ spanned by functions of space and time. Here the projection operator $\mathcal{P}_\nu : \mathcal{B} \to \mathcal{C}$ is used, where $\mathcal{P}_\nu u_g = \langle 1, u_g\rangle_\nu$ for $u_g \in \mathcal{B}$. This inner product is defined as $\langle v_g, u_g\rangle_\nu = \sum_{g=1}^{N_g} v_g u_g$ for $u_g, v_g \in \mathcal{B}$. Applying $\mathcal{P}_\nu$ to Eqs. 2.3 gives

$$\frac{\partial}{\partial t}\langle 1, E_g\rangle_\nu + \boldsymbol{\nabla}\cdot\langle 1, \boldsymbol{F}_g\rangle_\nu + c\langle \varkappa_{E,g}(T), E_g\rangle_\nu = 4\pi\langle \varkappa_{B,g}(T), B_g(T)\rangle_\nu, \tag{2.12a}$$

$$\frac{1}{c}\frac{\partial}{\partial t}\langle 1, \boldsymbol{F}_g\rangle_\nu + c\boldsymbol{\nabla}\cdot\langle 1, \mathfrak{f}_g E_g\rangle_\nu + \langle \tilde{\varkappa}_{R,g}(T), \boldsymbol{F}_g\rangle_\nu = 0, \tag{2.12b}$$

which represent conservation laws for the total radiation energy and total radiation momentum, respectively. Eqs. 2.12 can be recast in terms of the total radiation energy density $E = \mathcal{P}_\nu E_g$ and total radiation flux $\boldsymbol{F} = \mathcal{P}_\nu \boldsymbol{F}_g$ to formulate the *effective grey*

LOQD equations [98]

$$\frac{\partial E}{\partial t} + \boldsymbol{\nabla}\cdot\boldsymbol{F} + c\bar{\varkappa}_E(T)E = c\bar{\varkappa}_B a_R T^4, \tag{2.13a}$$

$$\frac{1}{c}\frac{\partial \boldsymbol{F}}{\partial t} + c\boldsymbol{\nabla}\cdot(\bar{\mathfrak{f}}E) + \bar{\mathbf{K}}_R(T)\boldsymbol{F} + \bar{\boldsymbol{\eta}}E = 0, \tag{2.13b}$$

where $a_R = \frac{4\sigma_R}{c}$ is the radiation constant, and σ_R is the Stefan-Boltzmann constant. These equations are exactly closed through the following frequency averaged parameters

$$\bar{\mathfrak{f}} = \frac{1}{\sum_{g=1}^{N_g} E_g}\sum_{g=1}^{N_g}\mathfrak{f}_g E_g, \quad \bar{\varkappa}_E = \frac{\sum_{g=1}^{N_g}\varkappa_{E,g}E_g}{\sum_{g=1}^{N_g}E_g}, \quad \bar{\varkappa}_B = \frac{\sum_{g=1}^{N_g}\varkappa_{B,g}B_g}{\sum_{g=1}^{N_g}B_g}, \tag{2.14a}$$

$$\bar{\mathbf{K}}_R = \operatorname{diag}\big(\bar{\varkappa}_{R,x},\ \bar{\varkappa}_{R,y},\ \bar{\varkappa}_{R,z}\big)\,, \quad \bar{\varkappa}_{R,\alpha} = \frac{\sum_{g=1}^{N_g}\tilde{\varkappa}_{R,g}|F_{\alpha,g}|}{\sum_{g=1}^{N_g}|F_{\alpha,g}|}, \quad \alpha = x,y,z\,, \tag{2.14b}$$

$$\bar{\boldsymbol{\eta}} = \frac{1}{\sum_{g=1}^{N_g}E_g}\sum_{g=1}^{N_g}(\tilde{\varkappa}_{R,g} - \bar{\mathbf{K}}_R)\boldsymbol{F}_g\,. \tag{2.14c}$$

The BCs and ICs for Eqs. 2.13 (with BCs corresponding to those in Eq. 2.6) are defined by

$$\boldsymbol{n}_\Gamma\cdot\boldsymbol{F}\big|_{\boldsymbol{r}\in\partial\Gamma} = c\bar{C}\big(E\big|_{\boldsymbol{r}\in\partial\Gamma} - E^{\text{in}}\big) + F^{\text{in}}, \quad E\big|_{t=t_0} = E^0, \quad \boldsymbol{F}\big|_{t=t_0} = \boldsymbol{F}^0\,, \tag{2.15}$$

where

$$\bar{C} = \left.\frac{\sum_{g=1}^{N_g}C_g\big(E_g - E_g^{\text{in}}\big)}{\sum_{g=1}^{N_g}\big(E_g - E_g^{\text{in}}\big)}\right|_{\boldsymbol{r}\in\partial\Gamma}, \tag{2.16}$$

$$E^{\text{in}} = \sum_{g=1}^{N_g}E_g^{\text{in}}, \quad F^{\text{in}} = \sum_{g=1}^{N_g}F_g^{\text{in}}, \quad E^0 = \sum_{g=1}^{N_g}E_g^0, \quad \boldsymbol{F}^0 = \sum_{g=1}^{N_g}\boldsymbol{F}_g^0. \tag{2.17}$$

BCs for the effective grey LOQD system that correspond to the alternative BCs in Eq. 2.10 are defined as

$$\boldsymbol{n}_\Gamma\cdot\boldsymbol{F}\big|_{\boldsymbol{r}\in\partial\Gamma} = c\bar{G}E\big|_{\boldsymbol{r}\in\partial\Gamma} + 2F^{\text{in}}, \tag{2.18}$$

where

$$\bar{G} = \left. \frac{\sum_{g=1}^{N_g} G_g E_g}{\sum_{g=1}^{N_g} E_g} \right|_{\boldsymbol{r} \in \partial\Gamma}. \tag{2.19}$$

In sum, the MLQD method for TRT problems is formulated by

1. The high-order BTE (Eq. 1.6)
2. The multigroup LOQD system (Eqs. 2.3)
3. The effective grey LOQD system (Eqs. 2.13)
4. The MEB equation (Eq. 1.10) recast in terms of the effective grey unknowns as

$$\frac{\partial \varepsilon(T)}{\partial t} = c\bar{\boldsymbol{\varkappa}}_E E - c\bar{\boldsymbol{\varkappa}}_B a_R T^4. \tag{2.20}$$

The algorithm for solving TRT problems with the MLQD method is shown in Alg. 1. At each time step, the material temperature and Eddington tensor are 'lagged' from the previous time step to create an initial condition (Note T^0 comes from the problem's IC and $\mathfrak{f}_g^0$ is assumed to be $\frac{1}{3}$). A maximum of $s_{\max}$ high-order iterations are performed at each time step, and unless otherwise stated $s_{\max} = \infty$ is assumed. The MLQD method is known to be stable, and as such when $s_{\max} = \infty$ the high-order iterations will converge to the given tolerances at each time step [109]. The QD method with few s iterations can produce solutions close to the converged one [101, 117]. In the same way, a maximum number of low-order multigroup iterations is defined $q_{\max}$ and is presumed to be $q_{\max} = \infty$ unless otherwise stated. At each high-order iteration, the BTE is solved to update the Eddington tensor followed by a set of low-order iterations to converge the LOQD solution with the current $\mathfrak{f}_g$. The zeroth s iteration at each time step skips the BTE solve and uses the lagged information from the previous time step to close the LOQD system.

In practice, the effective grey LOQD moment system is derived in discrete space from the fully discretized multigroup LOQD moment system. As such the Eqs. 2.13 can take different forms than what is shown above depending on the chosen discretization schemes. The discrete form of the effective grey LOQD system used in this work is derived in Sec. 2.4.

Algorithm 1: The MLQD method for solving TRT problems

$n = 0$
while $t^n \leq t^{end}$ **do**
  $n = n + 1$
  $T^{(0)} = T^{n-1}$
  $\mathfrak{f}_g^{(0)} = \mathfrak{f}_g^{n-1}$
  $s = -1$
  while $s < s_{max}$,
    $\|T^{(s)} - T^{(s-1)}\| > \epsilon_1 \|T^{(s)}\| + \epsilon_2$,
    $\|E^{(s)} - E^{(s-1)}\| > \epsilon_1 \|E^{(s)}\| + \epsilon_2$ **do**
    $s = s + 1$
    if $s \geq 1$ **then**
      Update $\varkappa_{E,g}, \varkappa_{B,g}, B_g$ with $T^{(s-1)}$
      Solve the BTE (Eq. 1.6) for I_g
      Compute $\mathfrak{f}_g^{(s)}$ from I_g (Eq. 2.4)
    end
    $q = 0$
    while $q < q_{max}$,
      $\|T^{(s,q)} - T^{(s,q-1)}\| > \epsilon_1 \|T^{(s,q)}\| + \epsilon_2$,
      $\|E^{(s,q)} - E^{(s,q-1)}\| > \epsilon_1 \|E^{(s,q)}\| + \epsilon_2$ **do**
      $q = q + 1$
      Update $\varkappa_{E,g}, \varkappa_{B,g}, \tilde{\varkappa}_{R,g}, B_g$ with $T^{(s-1,q)}$
      Solve multigroup LOQD equations (Eqs. 2.3) with $\mathfrak{f}_g^{(s)}$ for $E_g^{(s,q)}$, $\boldsymbol{F}_g^{(s,q)}$
      Compute spectrum-averaged closures for the effective grey problem with $E_g^{(s,q)}$, $\boldsymbol{F}_g^{(s,q)}$
      Solve effective grey problem (Eqs. 2.13 and 2.20) for $T^{(s,q)}$, $E^{(s,q)}$, $\boldsymbol{F}^{(s,q)}$
    end
    $T^{(s)} \leftarrow T^{(s,q)}$
  end
  $T^n \leftarrow T^{(s)}$
  $\mathfrak{f}_g^n \leftarrow \mathfrak{f}_g^{(s)}$
end

2.2 Discretization of the Boltzmann Transport Equation in 1D Cartesian Geometry

In 1D slab geometry the BTE (Eq. 1.6) is written

$$\frac{1}{c}\frac{\partial I_g}{\partial t} + \mu\frac{\partial I_g}{\partial x} + \varkappa_{E,g}(T)I_g = 2\pi\varkappa_{B,g}(T)B_g(T), \tag{2.21}$$

where μ is the cosine of the angle between the x axis and $\mathbf{\Omega}$ (i.e. the directional cosine of particle motion), $I_g = I_g(x,\mu,t)$ and $T = T(x,t)$.

The discretization scheme for the 1D BTE introduced in this section uses the implicit backward-Euler integration scheme in time, the method of discrete-ordinates in angle [97], and the simple corner balance (SCB) scheme in space [118]. After applying the backward-Euler and discrete-ordinates schemes, the BTE is written

$$\begin{gathered}\frac{1}{c}\frac{I^n_{g,m} - I^{n-1}_{g,m}}{\Delta t^n} + \mu_m\frac{\partial I^n_{g,m}}{\partial x} + \varkappa^n_{E,g}I^n_{g,m} = 2\pi\varkappa^n_{B,g}B^n_g, \\ g = 1,\ldots,N_g, \quad m = 1,\ldots,N_\Omega, \quad n = 1,\ldots\end{gathered} \tag{2.22}$$

where m is the index of directional cosine, n is the time step index, N_Ω is the total number of discrete directions of motion, Δt^n is the n^{th} time step, $\varkappa^n_{E,g} = \varkappa_{E,g}(T^n)$, $\varkappa^n_{B,g} = \varkappa_{B,g}(T^n)$ and $B^n_g = B_g(T^n)$. Spatial discretization is applied to a reformulation of Eq. 2.22 that takes on a pseudo steady-state form

$$\mu_m\frac{\partial I^n_{g,m}}{\partial x} + \tilde{\varkappa}^n_{E,g}I^n_{g,m} = Q^n_{g,m}, \tag{2.23}$$

with a modified opacity $\tilde{\varkappa}^n_{E,g} = \varkappa^n_{E,g} + \frac{1}{c\Delta t^n}$ and source $Q^n_{g,m} = 2\pi\varkappa^n_{B,g}B^n_g + \frac{I^{n-1}_{g,m}}{c\Delta t^n}$. Eq. 2.23 is integrated over the left and right halves of each i^{th} spatial cell to yield two half-cell relations:

$$\mu(I_i - I_{i-\frac{1}{2}}) + \frac{1}{2}\tilde{\varkappa}_{E,i}\Delta x_i I_{L,i} = \frac{1}{2}\Delta x_i Q_{L,i}, \tag{2.24a}$$

$$\mu(I_{i+\frac{1}{2}} - I_i) + \frac{1}{2}\tilde{\varkappa}_{E,i}\Delta x_i I_{R,i} = \frac{1}{2}\Delta x_i Q_{R,i}, \tag{2.24b}$$

where g, m and n subscripts and superscripts have been neglected for brevity. Here I_i is the cell-averaged radiation intensity, $I_{i\pm\frac{1}{2}}$ is the radiation intensity value averaged over the boundary between cells i and $i \pm 1$, and $I_{L/R,i}$ is the radiation intensity on the left/right

sides of the i^{th} cell. Δx_i is the width of the i^{th} cell. Upwinding conditions are introduced such that

$$I_{i+\frac{1}{2}} = I_{R,i}, \quad \mu > 0, \tag{2.25a}$$

$$I_{i-\frac{1}{2}} = I_{L,i}, \quad \mu < 0, \tag{2.25b}$$

and finally the cell-averaged radiation intensity is defined as

$$I_i = \frac{1}{2}(I_{L,i} + I_{R,i}). \tag{2.26}$$

2.3 Discretization of the Boltzmann Transport Equation in 2D Cartesian Geometry

In 2D Cartesian geometry the BTE (Eq. 1.6) is written

$$\frac{1}{c}\frac{\partial I_g}{\partial t} + \Omega_x \frac{\partial I_g}{\partial x} + \Omega_y \frac{\partial I_g}{\partial y} + \varkappa_{E,g}(T) I_g = \varkappa_{B,g}(T) B_g(T), \tag{2.27}$$

with $I_g = I_g(x, y, \mathbf{\Omega}, t)$ and $T = T(x, y, t)$. Two distinct discretizations of the BTE are introduced for 2D Cartesian geometry in this section. Both discretizations use the implicit backward-Euler integration scheme the method of discrete-ordinates, only differing in spatial discretization. The two considered spatial discretizations are the SCB [118] and conservative method of long characteristics [119, 120, 121, 122, 123, 124, 125] schemes.

After applying the backward-Euler and discrete-ordinates schemes, the BTE is written

$$\frac{1}{c}\frac{I^n_{g,m} - I^{n-1}_{g,m}}{\Delta t^n} + \Omega_{x,m}\frac{\partial I^n_{g,m}}{\partial x} + \Omega_{y,m}\frac{\partial I^n_{g,m}}{\partial y} + \varkappa^n_{E,g} I^n_{g,m} = \varkappa^n_{B,g} B^n_g, \tag{2.28}$$
$$g = 1, \ldots, N_g, \quad m = 1, \ldots, N_\Omega, \quad n = 1, \ldots$$

Both spatial discretizations use a reformulation of Eq. 2.28 that takes on a pseudo steady-state form

$$\Omega_{x,m}\frac{\partial I^n_{g,m}}{\partial x} + \Omega_{y,m}\frac{\partial I^n_{g,m}}{\partial y} + \tilde{\varkappa}^n_{E,g} I^n_{g,m} = Q^n_{g,m}, \tag{2.29}$$

with a modified opacity $\tilde{\varkappa}^n_{E,g} = \varkappa^n_{E,g} + \frac{1}{c\Delta t^n}$ and source $Q^n_{g,m} = \varkappa^n_{B,g} B^n_g + \frac{I^{n-1}_{g,m}}{c\Delta t^n}$. Orthogonal spatial grids are considered, with Δx_i and Δy_j defined as the $(i, j)^{\text{th}}$ cell widths in the $\boldsymbol{e}_x$

and $\boldsymbol{e}_y$ directions, respectively. $A_{i,j} = \Delta x_i \Delta y_j$ is the area of the $(i,j)^{\text{th}}$ cell.

2.3.1 Simple Corner Balance

The SCB scheme [118] in 2D geometry subdivides each spatial cell into four subcells as depicted in Fig. 2.1, where intensity values are placed centered on each subcell face and in the outer corners of each subcell.

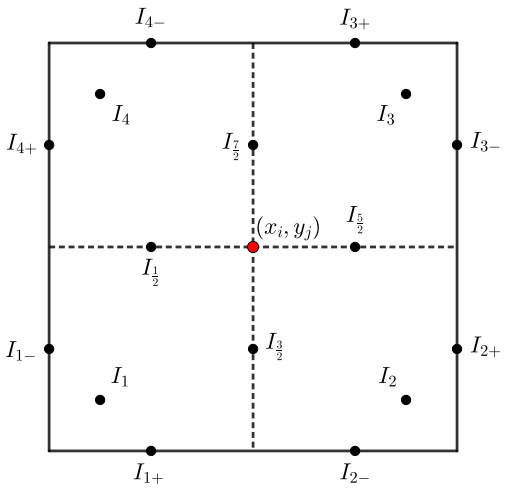

Figure 2.1: Sample cell for the simple corner balance scheme

The BTE is integrated over each subcell to obtain the following relations:

$$\frac{1}{2}\Omega_x \Delta y_j \left(I_{ij,\frac{3}{2}} - I_{ij,1-}\right) + \frac{1}{2}\Omega_y \Delta x_i \left(I_{ij,\frac{1}{2}} - I_{ij,1+}\right) + \frac{1}{4}\tilde{\varkappa}_{E,ij} A_{ij} I_{ij,1} = \frac{1}{4} A_{ij} Q_{ij,1}, \quad (2.30a)$$

$$\frac{1}{2}\Omega_x \Delta y_j \left(I_{ij,2+} - I_{ij,\frac{3}{2}}\right) + \frac{1}{2}\Omega_y \Delta x_i \left(I_{ij,\frac{5}{2}} - I_{ij,2-}\right) + \frac{1}{4}\tilde{\varkappa}_{E,ij} A_{ij} I_{ij,2} = \frac{1}{4} A_{ij} Q_{ij,2}, \quad (2.30b)$$

$$\frac{1}{2}\Omega_x \Delta y_j \left(I_{ij,3-} - I_{ij,\frac{7}{2}}\right) + \frac{1}{2}\Omega_y \Delta x_i \left(I_{ij,3+} - I_{ij,\frac{5}{2}}\right) + \frac{1}{4}\tilde{\varkappa}_{E,ij} A_{ij} I_{ij,3} = \frac{1}{4} A_{ij} Q_{ij,3}, \quad (2.30c)$$

$$\frac{1}{2}\Omega_x \Delta y_j \left(I_{ij,\frac{7}{2}} - I_{ij,4+}\right) + \frac{1}{2}\Omega_y \Delta x_i \left(I_{ij,4-} - I_{ij,\frac{1}{2}}\right) + \frac{1}{4}\tilde{\varkappa}_{E,ij} A_{ij} I_{ij,4} = \frac{1}{4} A_{ij} Q_{ij,4}, \quad (2.30d)$$

where g, m and n subscripts and superscripts have been neglected for brevity. Eqs. 2.30 are combined with the following relations between the intensities in the cell corners and

on the inner-most subcell faces

$$I_{ij,\frac{1}{2}} = \frac{1}{2}\big(I_{ij,1} + I_{ij,4}\big), \tag{2.31a}$$

$$I_{ij,\frac{3}{2}} = \frac{1}{2}\big(I_{ij,1} + I_{ij,2}\big), \tag{2.31b}$$

$$I_{ij,\frac{5}{2}} = \frac{1}{2}\big(I_{ij,2} + I_{ij,3}\big), \tag{2.31c}$$

$$I_{ij,\frac{7}{2}} = \frac{1}{2}\big(I_{ij,3} + I_{ij,4}\big). \tag{2.31d}$$

Upwinding conditions are introduced such that the intensities on each cell-edge forward of the particle direction $\mathbf{\Omega}$ are determined from their respective cell-corner intensities, as depicted in Fig. 2.2:

$$I_{ij,2+} = I_{ij,2}, \quad I_{ij,3+} = I_{ij,3}, \quad I_{ij,3-} = I_{ij,3}, \quad I_{ij,4-} = I_{ij,4}, \qquad \Omega_x > 0,\ \Omega_y > 0 \tag{2.32a}$$

$$I_{ij,3+} = I_{ij,3}, \quad I_{ij,4+} = I_{ij,4}, \quad I_{ij,4-} = I_{ij,4}, \quad I_{ij,1-} = I_{ij,1}, \qquad \Omega_x < 0,\ \Omega_y > 0 \tag{2.32b}$$

$$I_{ij,4+} = I_{ij,4}, \quad I_{ij,1+} = I_{ij,1}, \quad I_{ij,1-} = I_{ij,1}, \quad I_{ij,2-} = I_{ij,2}, \qquad \Omega_x < 0,\ \Omega_y < 0 \tag{2.32c}$$

$$I_{ij,1+} = I_{ij,1}, \quad I_{ij,2+} = I_{ij,2}, \quad I_{ij,2-} = I_{ij,2}, \quad I_{ij,3-} = I_{ij,3}, \qquad \Omega_x > 0,\ \Omega_y < 0 \tag{2.32d}$$

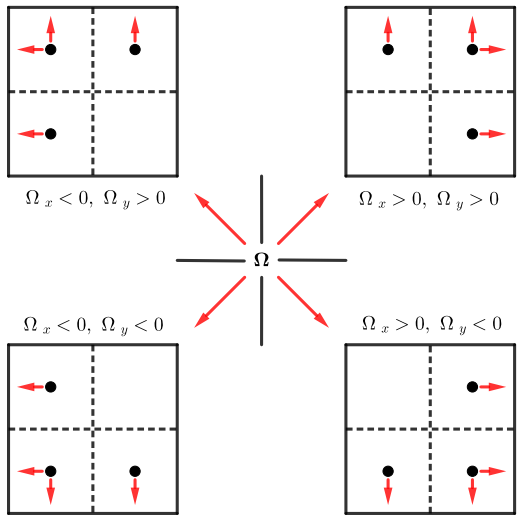

Figure 2.2: Upwinding of the solution intensities for a sample cell

Finally, relations are defined for the cell-edge and cell-averaged intensities based on subcell intensities:

$$I_{i,j} = \frac{1}{4}\big(I_{ij,1} + I_{ij,2} + I_{ij,3} + I_{ij,4}\big), \tag{2.33a}$$

$$I_{i-\frac{1}{2},j} = \frac{1}{2}\big(I_{ij,1-} + I_{ij,4+}\big), \tag{2.33b}$$

$$I_{i,j-\frac{1}{2}} = \frac{1}{2}\big(I_{ij,1+} + I_{ij,2-}\big), \tag{2.33c}$$

$$I_{i+\frac{1}{2},j} = \frac{1}{2}\big(I_{ij,2+} + I_{ij,3-}\big), \tag{2.33d}$$

$$I_{i,j+\frac{1}{2}} = \frac{1}{2}\big(I_{ij,3+} + I_{ij,4-}\big), \tag{2.33e}$$

where $I_{i,j}$ is the cell-averaged radiation intensity for cell (i,j), $I_{i+\frac{1}{2},j}$ is the radiation intensity averaged over the cell face between cells (i,j) and $(i+1,j)$, and $I_{i,j+\frac{1}{2}}$ is the radiation intensity averaged over the cell face between cells (i,j) and $(i,j+1)$. This completes the SCB discretization.

2.3.2 Conservative Long Characteristics

The method of conservative long characteristics [119, 120, 121, 122, 123, 124, 125] is derived by first performing a change of coordinates from (x,y) to (u,v) where $\boldsymbol{e}_u = \boldsymbol{\Omega}$ and $\boldsymbol{e}_u \cdot \boldsymbol{e}_v = 0$ as shown in Fig. 2.3. The directional derivative of I then becomes

$$\frac{\partial I}{\partial u} = \frac{\partial I}{\partial x}\frac{\partial x}{\partial u} + \frac{\partial I}{\partial y}\frac{\partial y}{\partial u} = \Omega_x \frac{\partial I}{\partial x} + \Omega_y \frac{\partial I}{\partial y} = \boldsymbol{\Omega} \cdot \boldsymbol{\nabla} I. \tag{2.34}$$

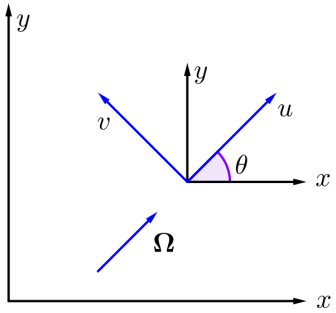

Figure 2.3: Local coordinates in the x-y plane

The transport equation along characteristics is given

$$\frac{\partial I(u)}{\partial u} + \tilde{\varkappa}_E(u) I(u) = Q(u), \tag{2.35}$$

where once again g, m and n subscripts and superscripts have been eschewed for brevity. Now Eq. 2.35 can be integrated along a characteristic segment, where $u \in [u^-, u^+]$, to find

$$I(u^+) = I(u^-) \exp\left(- \int_{u^-}^{u^+} \tilde{\varkappa}_E(u') du' \right) + \int_{u^-}^{u^+} Q(u) \exp\left(- \int_{u}^{u^+} \tilde{\varkappa}_E(u') du' \right) du. \tag{2.36}$$

It is assumed that Q and $\tilde{\varkappa}_E$ are constant inside the characteristic segment, simplifying this equation to

$$I(u^+) = I(u^-) e^{-\tilde{\varkappa}_E (u^+ - u^-)} + \frac{Q}{\tilde{\varkappa}_E} \big(1 - e^{\tilde{\varkappa}_E (u^+ - u^-)}\big). \tag{2.37}$$

When defining the points u^+ and u^-, an underlying spatial grid is assumed to be present with individual cells where the quantities Q and $\tilde{\varkappa}_E$ are uniform. u^+ and u^- are defined as the intersection (entry and exit) points of a given characteristic with the cell boundaries in the underlying grid (see Fig. C.2). We assume that for each direction m there are K_m discrete characteristic rays traced across the underlying spatial grid with widths $w_{m,k}$, and each k^{th} characteristic ray will be comprised of $S_{m,k}$ interlinked segments. The ray tracing algorithm to generate these characteristic rays is detailed in Appendix C.

When projected onto the $x - y$ plane, each $(m, k, s)^{\text{th}}$ segment has length $\ell_{m,k,s}$. If ζ_m is the angle between $\mathbf{\Omega}_m$ and the z axis, then $\ell_{m,k,s} = (u^+ - u^-) \sin(\zeta_m)$. Therefore Eq. 2.37 can be written as

$$I_{m,k,s+1} = I_{m,k,s} e^{-\frac{\tilde{\varkappa}_{E,i,j} \ell_{m,k,s}}{\sin(\zeta_m)}} + \frac{Q_{m,i,j}}{\tilde{\varkappa}_{E,i,j}} \big(1 - e^{-\frac{\tilde{\varkappa}_{E,i,j} \ell_{m,k,s}}{\sin(\zeta_m)}}\big), \tag{2.38}$$
$$k = 1, \ldots, K_m, \quad s = 1, \ldots, S_{m,k},$$

where $I_{m,k,s+1}$ is the radiation intensity at the outgoing face of the $(m, k, s)^{\text{th}}$ segment, $\tilde{\varkappa}_{E,i,j}$ and $Q_{m,i,j}$ is the modified opacity and source in the $(i, j)^{\text{th}}$ cell that is traced over by the $(m, k, s)^{\text{th}}$ segment. To conserve the discrete particle balance, the length of each segment is modified to be

$$\ell^*_{m,k,s} = \gamma_{i,j} \ell_{m,k,s}, \quad \gamma_{i,j} = \frac{A_{i,j}}{\frac{1}{4\pi} \sum_m \omega_m \sum_{k,s \in C_{m,i,j}} \ell_{m,k,s} w_{m,k}}, \tag{2.39}$$

where $C_{m,i,j}$ is the set of characteristic segments contained in cell (i,j) for direction m, and $\{\omega_m\}_{m=1}^{N_\Omega}$ is the set of angular quadrature weights. The optical thickness of each tube segment is then

$$\tau_{m,k,s} = \frac{\tilde{\varkappa}^n_{E,i,j}\ell^*_{m,k,s}}{\sin(\zeta_m)}, \tag{2.40}$$

and Eq. 2.38 becomes

$$I_{m,k,s+1} = I_{m,k,s}e^{-\tau_{m,k,s}} + \frac{Q_{m,i,j}}{\tilde{\varkappa}_{E,i,j}}\big(1 - e^{-\tau_{m,k,s}}\big). \tag{2.41}$$

The segment-average radiation intensity is defined as

$$\bar{\bar{I}}_{m,k,s} = \alpha_{m,k,s}I_{m,k,s} + (1-\alpha_{m,k,s})I_{m,k,s+1}, \quad \alpha_{m,k,s} = \frac{1}{\tau_{m,k,s}} - \frac{e^{-\tau_{m,k,s}}}{1-e^{-\tau_{m,k,s}}}. \tag{2.42}$$

The cell-average radiation intensities are

$$I_{m,i,j} = \frac{\sum_{k,s\in C_{m,i,j}} \ell^*_{m,k,s}w_{m,k}\bar{\bar{I}}_{m,k,s}}{\sum_{k,s\in C_{m,i,j}} \ell^*_{m,k,s}w_{m,k}} \tag{2.43}$$

The face-average radiation intensities are

$$I_{m,i+\frac{1}{2},j} = \frac{\sum_{k,s\in F_{m,i+\frac{1}{2},j}} w_{m,k}I_{m,k,s}}{\sum_{k,s\in F_{m,i+\frac{1}{2},j}} w_{m,k}}, \quad I_{m,i,j+\frac{1}{2}} = \frac{\sum_{k,s\in F_{m,i,j+\frac{1}{2}}} w_{m,k}I_{m,k,s}}{\sum_{k,s\in F_{m,i,j+\frac{1}{2}}} w_{m,k}} \tag{2.44}$$

where $F_{m,i+\frac{1}{2},j}$ and $F_{m,i,j+\frac{1}{2}}$ are the sets of characteristic segments whose upwind faces intersect the $(i+\frac{1}{2},j)$ and $(i,j+\frac{1}{2})$ cell edges, respectively, for direction m.

2.4 Discretization of the Multilevel Quasidiffusion Equations

To discretize the multigroup LOQD equations (Eqs. 2.3) we apply fully implicit temporal approximation based on the backward Euler scheme and a second-order finite volume scheme in space on orthogonal spatial grids [126, 127]. Fig. 2.4 shows a sample spatial cell i and notations. The multigroup radiation energy balance equation (Eq. 2.3a) is integrated over the cell i. The multigroup radiation momentum balance equations (Eq. 2.3b) are integrated over each half of the spatial cell. The resultant discretized multigroup LOQD

equations are given by

$$\frac{A_i}{\Delta t^n}\left(E_{g,i}^n - E_{g,i}^{n-1}\right) + \sum_{f\in\omega_i} F_{g,f}^n \ell_f + c\varkappa_{E,g,i}^n E_{g,i}^n A_i = 4\pi\varkappa_{B,g,i}^n B_{g,i}^n A_i \,, \tag{2.45a}$$

$$\begin{aligned}\frac{A_f}{c\Delta t^n}\left(F_{g,f}^n - F_{g,f}^{n-1}\right) &+ \boldsymbol{e}_\alpha\cdot\boldsymbol{n}_f c\left(\mathfrak{f}_{\alpha\alpha,g,f}^n E_{g,f}^n - \mathfrak{f}_{\alpha\alpha,g,i}^n E_{g,i}^n\right)\ell_f \\ &+ \boldsymbol{e}_\beta\cdot\boldsymbol{n}_{f+1} c\left(\mathfrak{f}_{\alpha\beta,g,f+1}^n E_{g,f+1}^n - \mathfrak{f}_{\alpha\beta,g,f-1}^n E_{g,f-1}^n\right)\frac{\ell_{f+1}}{2} + \tilde{\varkappa}_{R,g,i}^n F_{g,f}^n A_f = 0\,, \\ &\qquad\qquad \alpha,\beta = x,y\,, \quad \beta\neq\alpha\,, \end{aligned} \tag{2.45b}$$

where

$$\mathfrak{f}_g = \begin{pmatrix} \mathfrak{f}_{xx,g} & \mathfrak{f}_{xy,g} \\ \mathfrak{f}_{xy,g} & \mathfrak{f}_{yy,g} \end{pmatrix}, \tag{2.46}$$

i is the cell index; f is the index of faces of the i^{th} cell; ℓ_f is the length of the face f; ω_i is the set of faces of the i^{th} cell, $\boldsymbol{n}_f$ is the unit outward normal of the cell face f and $\boldsymbol{n}_f = \boldsymbol{e}_\alpha$ for the orthogonal grids; $E_{g,i}$ and $E_{g,f}$ are cell-average and face-average radiation energy densities, respectively; $F_{g,f} = \boldsymbol{n}_f\cdot\boldsymbol{F}_g$ is the normal component of the radiation flux; A_i is the area of the i^{th} cell; A_f is the area of the half-cell associated with the edge f; n is the index of the instant of time; $\Delta t^n = t^n - t^{n-1}$ is the n^{th} time step.

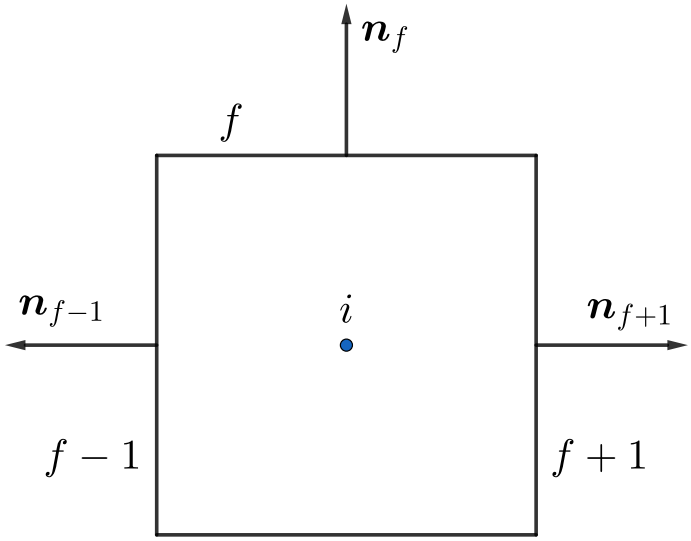

Figure 2.4: Notations in the cell i.

The discretization of the effective grey LOQD equations (Eqs. 2.13) is algebraically consistent with the above scheme (Eqs. 2.45). The discrete total radiation energy balance equation is derived by applying the projection operator $\mathcal{P}_\nu$ to Eq. 2.45a and takes the following form

$$\frac{A_i}{\Delta t^n}\Big(E_i^n - E_i^{n-1}\Big) + \sum_{f\in\omega_i} F_f^n \ell_f + c\bar{\varkappa}_{E,i}^n E_i^n A_i = c\bar{\varkappa}_{B,i}^n a_R (T_i^n)^4\,, \tag{2.47}$$

where

$$\bar{\varkappa}_{E,i}^n = \frac{\sum_{g=1}^{N_g} \varkappa_{g,i}^n E_{g,i}^n}{\sum_{g=1}^{N_g} E_{g,i}^n}\,, \quad \bar{\varkappa}_{B,i}^n = \frac{\sum_{g=1}^{N_g} \varkappa_{g,i}^n B_{g,i}^n}{\sum_{g=1}^{N_g} B_{g,i}^n}\,. \tag{2.48}$$

Next the discretized multigroup radiation momentum balance equation (Eq. 2.45b) is cast in terms of $F_{g,f}^n$. Applying $\mathcal{P}_\nu$ to the resulting equation for $F_{g,f}^n$ yields an equation for the total radiation flux at each cell face

$$F_f^n = -c\bigg(\boldsymbol{e}_\alpha\cdot\boldsymbol{n}_f\Big(\bar{\mathcal{D}}_{\alpha\alpha,f}^n E_f^n - \bar{\mathcal{D}}_{\alpha\alpha,i}^n E_i^n\Big)\ell_f + \frac{1}{2}\boldsymbol{e}_\beta\cdot\boldsymbol{n}_{f+1}\Big(\bar{\mathcal{D}}_{\alpha\beta,f+1}^n E_{g,f+1}^n - \bar{\mathcal{D}}_{\alpha\beta,f-1}^n E_{f-1}^n\Big)\ell_{f+1}\bigg) + p_f^n\,, \tag{2.49}$$

where

$$\bar{\mathcal{D}}_{\alpha\beta,f'}^n = \frac{\sum_{g=1}^{N_g} (\tilde{\varkappa}_{g,i}^n)^{-1} \varkappa_{\alpha\beta,i}^n E_{g,f'}^n}{\sum_{g=1}^{N_g} E_{g,f'}^n} \qquad f' = f-1, f, f+1\,, \tag{2.50}$$

$$\tilde{\varkappa}_{g,i}^n = \varkappa_{g,i}^n + \frac{1}{c\Delta t^n}\,, \quad p_f^n = \sum_{g=1}^{N_g} \frac{F_{g,f}^{n-1}}{1 + c\Delta t^n \varkappa_{g,i}^n}\,. \tag{2.51}$$

CHAPTER

3

DATA-DRIVEN METHODS

Several data-driven methodologies are considered in this work for the creation of ROMs. This chapter provides a review of each of these methods. The POD is outlined in Sec. 3.1, followed by the DMD in Sec. 3.2. Sec. 3.3 provides an overview of POD-Galerkin & POD-Petrov-Galerkin projection methods.

3.1 The Proper Orthogonal Decomposition

The POD originated in the field of probability theory, used in analyzing stochastic signals. The POD theorem [128] states that stochastic functions can be expanded in terms of deterministic functions with random coefficients, allowing for a separation of deterministic and stochastic parts of the original function. Later the POD was repurposed as a method to extract underlying fundamental structures in functions of space-time [29, 129, 130]. By treating evaluations of a spatial-temporal function at different instance of time as separate *realizations* of the function, the POD yields an expansion in terms of spatial modes with temporally dependent coefficients. These spatial modes are commonly referred to as the POD modes of a function. One of the most prominent advantages of the POD compared

to other expansion methods is that it converges optimally fast in the quadratic mean.

3.1.1 The Biorthogonal Decomposition

Although many applications are only concerned with the POD modes describing some function(s), the POD fundamentally yields a spatial-temporal decomposition, called the biorthogonal decomposition [32]. Traditionally the biorthogonal decomposition applies to complex-valued functions $a(x,t) \in \mathbb{C}$ of space x and time t. This can be generalized to functions of any dimension however, by considering x to represent some arbitrary phase space occupied by a. For instance, the phase space occupied by the radiation intensity function I consists of spatial dimension $\boldsymbol{r}$, frequency of photons ν and direction of motion $\boldsymbol{\Omega}$. In this sense the biorthogonal decomposition yields a decomposition in *phase-space* and time.

Without loss of generality, let $\mathfrak{X}$ and $\mathfrak{T}$ represent the phase-space and temporal domains (which may be either continuous or discrete) upon which the function $a(x,t)$ is defined. A linear operator $\mathcal{G} : L^2(\mathfrak{X}) \to L^2(\mathfrak{T})$ and its adjoint $\mathcal{G}^* : L^2(\mathfrak{T}) \to L^2(\mathfrak{X})$ are defined by the function $a(x,t)$ as follows

$$(\mathcal{G}u) = \int_{\mathfrak{X}} au \; dx, \quad \forall u \in L^2(\mathfrak{X}), \tag{3.1}$$

$$(\mathcal{G}^*v) = \int_{\mathfrak{T}} a^*v \; dt, \quad \forall v \in L^2(\mathfrak{T}), \tag{3.2}$$

where a^* is the complex conjugate of a. If $a \in L^2(\mathfrak{X} \times \mathfrak{T})$ and $\mathcal{G}$ is compact, then there exists the following decomposition [32]

$$a(x,t) = \sum_{\ell=1}^{\infty} \alpha_\ell u_\ell^*(x) v_\ell(t), \tag{3.3}$$

$$\alpha_1 \geq \alpha_2 \geq \cdots \geq 0, \quad \lim_{N\to\infty} \alpha_N = 0, \quad \langle u_\ell, u_{\ell'} \rangle_x = \langle v_\ell, v_{\ell'} \rangle_t = \delta_{\ell,\ell'},$$

where $\langle u_\ell, u_{\ell'} \rangle_x = \int_{\mathfrak{X}} u_\ell u_{\ell'}^* \; dx$ and $\langle v_\ell, v_{\ell'} \rangle_t = \int_{\mathfrak{T}} v_\ell v_{\ell'}^* \; dt$. The functions $\{u_\ell\}$ and $\{v_\ell\}$ are eigenfunctions of the operators $\mathcal{G}^*\mathcal{G}$ and $\mathcal{G}\mathcal{G}^*$, respectively, and each are associated with the eigenvalues $\{\alpha_\ell^2\}$.

3.1.2 Expansion and Projection of Discrete Data

Let us now consider the POD in the fully-discrete case restricted to real-valued functions, where we have some vector function $\boldsymbol{a}(t) : \mathbb{R} \to \mathbb{R}^d$, evaluated at some set of instances $\{t^n\}_{n=0}^m$. The evaluated function values are collected in the set $\{\boldsymbol{a}^n\}_{n=0}^m$ where $\boldsymbol{a}^n = \boldsymbol{a}(t^n)$. This dataset is transformed to have zero-mean as the set $\{\hat{\boldsymbol{a}}^n\}_{n=0}^m$, defined as

$$\hat{\boldsymbol{a}}^n = \boldsymbol{a}^n - \bar{\boldsymbol{a}}, \quad \bar{\boldsymbol{a}} = \frac{1}{m+1}\sum_{n=0}^{m} \boldsymbol{a}^n. \tag{3.4}$$

The POD finds an orthonormal basis $\{\boldsymbol{u}_\ell\}_{\ell=1}^k$ onto which the data vectors $\{\hat{\boldsymbol{a}}^n\}_{n=0}^m$ can be projected in an optimal sense. The POD basis functions are formulated in such a way that the projection of $\{\boldsymbol{a}^n\}_{n=0}^m$ onto $\text{span}\{\bar{\boldsymbol{a}}, \boldsymbol{u}_1, \boldsymbol{u}_2, \ldots, \boldsymbol{u}_k\}$ has minimal error in the Frobenius norm [131], satisfying the following minimization problem

$$\{\boldsymbol{u}_\ell\}_{\ell=1}^k = \arg\min_{\boldsymbol{u}_1,\ldots,\boldsymbol{u}_k} \sum_{n=0}^{m} \left\| \hat{\boldsymbol{a}}^n - \sum_{\ell=1}^{k} \langle \hat{\boldsymbol{a}}^n, \boldsymbol{u}_\ell \rangle \boldsymbol{u}_\ell \right\|_2^2. \tag{3.5}$$

An interpretation of this minimization is that the POD modes optimally capture the energy associated with the given data set [32]. The rank-k POD representation of the data $\{\boldsymbol{a}^n\}_{n=0}^m$ is constructed from the data mean $\bar{\boldsymbol{a}}$, POD basis functions $\{\boldsymbol{u}_\ell\}_{\ell=1}^k$ and coefficients

$$\alpha_\ell^n = \langle \hat{\boldsymbol{a}}^n, \boldsymbol{u}_\ell \rangle, \quad n = 0, \ldots, m, \quad \ell = 1, \ldots, k. \tag{3.6}$$

The original data points can be approximated by the summation

$$\boldsymbol{a}^n \approx \bar{\boldsymbol{a}} + \sum_{\ell=1}^{k} \alpha_\ell^n \boldsymbol{u}_\ell. \tag{3.7}$$

The POD basis functions representing a given dataset are equivalent to the left singular vectors of the matrix $\mathbf{A} = [\hat{\boldsymbol{a}}^0, \ldots, \hat{\boldsymbol{a}}^m] \in \mathbb{R}^{d\times(m+1)}$. The thin (reduced) singular value decomposition (SVD) of $\mathbf{A}$ is

$$\mathbf{A} = \mathbf{U}\mathbf{S}\mathbf{V}^\top, \tag{3.8}$$

where $\mathbf{U} \in \mathbb{R}^{d\times r}$ and $\mathbf{V} \in \mathbb{R}^{(m+1)\times r}$ hold the first r left and right singular vectors of $\mathbf{A}$ in their columns, respectively, and $\mathbf{S} \in \mathbb{R}^{r\times r}$ holds the r nonzero singular values of $\mathbf{A}$ along its diagonal in descending order, where $r = \text{rank}(\mathbf{A})$. The POD basis vectors are therefore the first k columns of $\mathbf{U}$ and the POD projection coefficients are $\alpha_\ell^n = v_{n,\ell}\sigma_\ell$, where

σ_ℓ is the ℓ^{th} singular value of $\mathbf{A}$ and $v_{n,\ell}$ is the $(n,\ell)^{\text{th}}$ element of $\mathbf{V}$. The rank-k POD representation of the entire dataset $\{\hat{\boldsymbol{a}}^n\}_{n=0}^m$ is thus equivalent to the rank-k truncated SVD (TSVD) of $\mathbf{A}$

$$\mathbf{A} \approx \mathbf{A}_k = \mathbf{U}_k \mathbf{S}_k \mathbf{V}_k^\top, \quad k \leq r \tag{3.9}$$

where $\mathbf{U}_k \in \mathbb{R}^{d\times k}$ and $\mathbf{V}_k \in \mathbb{R}^{(m+1)\times k}$ hold the first k left and right singular vectors of $\mathbf{A}$ in their columns, respectively, and $\mathbf{S}_k \in \mathbb{R}^{k\times k}$ holds the first k singular values of $\mathbf{A}$ along its diagonal in descending order.

$\mathbf{A}_k$ is actually the orthogonal projection of $\mathbf{A}$ onto $\{\boldsymbol{u}_\ell\}_{\ell=1}^k$, written as $\mathbf{A}_k = \mathbf{U}_k\mathbf{U}_k^\top\mathbf{A}$. The error introduced by this orthogonal projection is given by [132]

$$\|\mathbf{A} - \mathbf{U}_k\mathbf{U}_k^\top\mathbf{A}\|_F^2 = \sum_{\ell=k+1}^{r} \sigma_\ell^2. \tag{3.10}$$

The relative error of the POD approximation in the Frobenius norm is therefore

$$\xi^2 = \frac{\|\mathbf{A} - \mathbf{A}_k\|_F^2}{\|\mathbf{A}\|_F^2} = \frac{\sum_{\ell=k+1}^r \sigma_\ell^2}{\sum_{\ell=1}^r \sigma_\ell^2}. \tag{3.11}$$

$(1-\xi^2)$ can be interpreted as the ratio of energy encompassed by the first k POD modes to the total energy comprised by all POD modes of the given data [47]. Thus the interpretation of ξ^2 is the relative amount of energy that has been truncated from the full POD basis by using only the first k POD modes. When the POD is performed, we choose some desired value for ξ and find the rank k that satisfies the following expression

$$k = \min\left\{ j \ : \ \frac{\sum_{\ell=j+1}^r \sigma_\ell^2}{\sum_{\ell=1}^r \sigma_\ell^2} \leq \xi^2 \right\} \tag{3.12}$$

3.2 The Dynamic Mode Decomposition

The DMD was initially introduced in the literature as a method to extract important dynamical modes from data of fluid flows [36]. Soon after, research was done to improve the underlying DMD theory which yielded several advances in the methodology [133, 37]. One of the most interesting aspects of the method lies in its ties to Koopman theory [134, 135, 136, 38]. The Koopman operator is an infinite dimensional, linear operator that defines the temporal evolution of observables defined for dynamical systems [38].

The DMD generates the best-fit linear operator $\mathbf{B}$ (in the 2-norm sense) to the data

$\{\boldsymbol{a}^n\}_{n=0}^m$, generating the following dynamic system:

$$\frac{d\tilde{\boldsymbol{a}}(t)}{dt} = \mathbf{B}\tilde{\boldsymbol{a}}(t), \tag{3.13}$$

under the assumption that the time instances $\{t^n\}_{n=0}^m$ are uniformly spaced, i.e.

$$t^{n+1} = t^n + \Delta t, \quad n = 0, \ldots, m-1\,. \tag{3.14}$$

The solution to Eq. 3.13 approximates the original functional $\boldsymbol{a}(t)$, defined in terms of the eigenpairs $(\boldsymbol{\varphi}_\ell, \omega_\ell)$ of $\mathbf{B}$

$$\tilde{\boldsymbol{a}}(t) = \sum_{\ell=1}^{k} \beta_\ell \boldsymbol{\varphi}_\ell e^{\omega_\ell t}, \tag{3.15}$$

where $\{\beta_\ell\}_{\ell=1}^k$ are some scalar coefficients. The rank-k DMD representation of the dataset $\{\boldsymbol{a}^n\}_{n=0}^m$ is comprised by the set of eigenpairs and coefficients $\{(\boldsymbol{\varphi}_\ell, \omega_\ell, \beta_\ell)\}_{\ell=1}^k$.

To find the eigenpairs $(\boldsymbol{\varphi}_\ell, \omega_\ell)$, the following orbital data matrices are defined

$$\mathbf{X} = [\boldsymbol{a}^0\ \boldsymbol{a}^1\ \ldots\ \boldsymbol{a}^{m-1}] \in \mathbb{R}^{n\times m}, \quad \hat{\mathbf{X}} = [\boldsymbol{a}^1\ \boldsymbol{a}^2\ \ldots\ \boldsymbol{a}^{m}] \in \mathbb{R}^{n\times m}, \tag{3.16}$$

then $\tilde{\mathbf{B}} = \hat{\mathbf{X}}\mathbf{X}^+$ is the closest approximation to $\mathbf{B}$ that can be found given $\{\boldsymbol{a}^n\}_{n=0}^m$ in the Frobenius norm where $+$ signifies the Moore-Penrose pseudo inverse [132]. The eigenpairs of $\tilde{\mathbf{B}}$, written as $(\tilde{\boldsymbol{\varphi}}_\ell, \chi_\ell)$, are closely related to the eigenpairs of $\mathbf{B}$ [37]. $\tilde{\boldsymbol{\varphi}}_\ell$ are called reduced eigenvectors, and can be used to calculate each corresponding eigenvector $\boldsymbol{\varphi}_\ell$. $\tilde{\boldsymbol{a}}(t)$ can be found with the pairs $(\boldsymbol{\varphi}_\ell, \chi_\ell)$ at each point $\{t^n\}_{n=0}^m$ using the expansion

$$\tilde{\boldsymbol{a}}(t^n) = \sum_{\ell=1}^{k} \beta_\ell \boldsymbol{\varphi}_\ell (\chi_\ell)^n, \quad n = 0, \ldots, m. \tag{3.17}$$

This expression yields the DMD expansion (Eq. 3.15) with the transformation $\omega_\ell = \frac{\ln(\chi_\ell)}{\Delta t}$. The pairs $(\boldsymbol{\varphi}_\ell, \chi_\ell)$ are called DMD modes and eigenvalues and are in practice calculated via the projected linear operator $\tilde{\mathbf{B}}_k = \mathbf{U}_k^\top \tilde{\mathbf{B}} \mathbf{U}_k$, whose eigenpairs are written as $(\tilde{\boldsymbol{\varphi}}_\ell^{(k)}, \chi_\ell)$. Here $\mathbf{U}_k$ holds the left singular vectors of $\mathbf{X}$ in its columns. Note that the eigenvalues of $\tilde{\mathbf{B}}_k$ are the DMD eigenvalues. The process of calculating the eigenpairs $(\boldsymbol{\varphi}_\ell, \chi_\ell)$ is outlined in Alg. 2 [37].

In Alg. 2 there are two types of DMD modes that can be calculated: (i) *exact* DMD modes and (ii) *projected* DMD modes. In practice the *exact* DMD modes are preferred, as

they can be shown to be the eigenvalues of the linear operator $\mathbf{B}$ that lie in the image of $\hat{\mathbf{X}}$. The *projected* DMD modes have been shown to be simply the projection of the exact modes onto the image of $\mathbf{X}$ [37]. Because the *exact* DMD modes are generally regarded as the default in literature we find it important to note that for the ROMs developed in this paper, when the DMD is invoked we actually use the *projected* modes.

Algorithm 2: Algorithm for computing DMD modes and eigenvalues [37]

Input: solution data $\{\boldsymbol{a}^n\}_{n=0}^m$ and ξ

1. Construct data matrices $\mathbf{X}, \hat{\mathbf{X}} \leftarrow \{\boldsymbol{a}^n\}_{n=0}^m$ (Eq. 3.16)
2. Compute TSVD $\mathbf{X} \approx \mathbf{U}_k \mathbf{S}_k \mathbf{V}_k^\top$ with $k \leq \text{rank}(\mathbf{X})$ satisfying Eq. 3.12 with ξ
3. Compute reduced DMD matrix $\tilde{\mathbf{B}}_k = \mathbf{U}_k^\top \hat{\mathbf{X}} \mathbf{V}_k \mathbf{S}_k^{-1}$
4. Find eigenpairs $\{(\tilde{\boldsymbol{\varphi}}_\ell^{(k)}, \chi_\ell)\}_{\ell=1}^k$ of $\tilde{\mathbf{B}}_k$
5. Compute DMD modes:
   - (Exact DMD) $\boldsymbol{\varphi}_\ell \leftarrow \frac{1}{\chi_\ell} \hat{\mathbf{X}} \mathbf{V}_k \mathbf{S}_k^{-1} \tilde{\boldsymbol{\varphi}}_\ell^{(k)}, \quad \chi_\ell \neq 0, \quad \ell = 1, \ldots, k$
   - (Projected DMD) $\hat{\boldsymbol{\varphi}}_\ell \leftarrow \mathbf{U}_k \tilde{\boldsymbol{\varphi}}_\ell^{(k)}, \quad \ell = 1, \ldots, k$

Output: DMD modes $\{\boldsymbol{\varphi}_\ell\}_{\ell=1}^k$ or $\{\hat{\boldsymbol{\varphi}}_\ell\}_{\ell=1}^k$ and DMD eigenvalues $\{\chi_\ell\}_{\ell=1}^k$

The projected DMD modes were used in the original formulation of the DMD [36], which can be interpreted as a method that approximates the last data-vector as a linear combination of all former vectors [133], i.e.

$$\boldsymbol{a}^m = \sum_{n=0}^{m-1} c_n \boldsymbol{a}^n + \varsigma, \tag{3.18}$$

where c_n are some scalar coefficients and ς is the residual incurred by the DMD approximation. It comes naturally then, that when the exact DMD modes are used instead of the projected DMD modes, the DMD can be interpreted as approximating the *first* data-vector as a linear combination of all latter vectors,

$$\boldsymbol{a}^0 = \sum_{n=1}^{m} \hat{c}_n \boldsymbol{a}^n + \hat{\varsigma}, \tag{3.19}$$

since the exact DMD modes lie in the image of $\hat{\mathbf{X}}$. This effective 'shift' of the DMD residual to the first data-vector can come at a large cost to the time-dependent problems considered here, where the initial transients tend to be more difficult to capture compared to later times. It is with this in mind that we choose to utilize the projected DMD modes in this work when applying the expansion in Eq. 3.15.

After calculating the DMD modes and eigenvalues via Alg. 2, the vector of expansion coefficients $\boldsymbol{\beta} = (\beta_1, \ldots, \beta_k)^\top$ must still be found. Let $\boldsymbol{\Phi} = [\hat{\boldsymbol{\varphi}}_1 \ \ldots \ \hat{\boldsymbol{\varphi}}_k]$ be the matrix of (projected) DMD modes and $\boldsymbol{\Xi} = \text{diag}(\chi_1, \ldots, \chi_k)$ be the diagonal matrix that holds the DMD eigenvalues in descending order. Then the DMD expansion of vector $\boldsymbol{a}^n$ (Eq. 3.17) can be written in matrix form as follows

$$\boldsymbol{\Phi}(\boldsymbol{\Xi})^n \boldsymbol{\beta} = \boldsymbol{a}^n, \quad n = 0, \ldots, m. \tag{3.20}$$

The vector $\boldsymbol{\beta}$ can be found as the solution to this equation for any chosen $n \in [0, \ldots, m]$. This requires inverting a $d \times k$ dense linear system however, and for large d can become expensive. Applying $\mathbf{U}_k^\top$ (see Alg. 2) to the left on both sides of Eq. 3.20 and selecting $n = 0$ yields the following $k \times k$ linear system

$$\tilde{\boldsymbol{\Phi}}\boldsymbol{\beta} = \mathbf{U}_k^\top \boldsymbol{a}^0, \tag{3.21}$$

where $\tilde{\boldsymbol{\Phi}} = [\tilde{\boldsymbol{\varphi}}_1 \ \ldots \ \tilde{\boldsymbol{\varphi}}_k]$ is the matrix of reduced DMD modes. The same reduced system can be derived if $\boldsymbol{\Phi}$ was defined with the exact DMD modes [27].

3.2.1 Equilibrium-Subtracted DMD

A variant of the DMD is also considered for model-order reduction purposes which we will refer to as the equilibrium-subtracted DMD, or DMD-E. The DMD-E differs from the DMD by constructing the linear operator $\mathbf{B}$ to fit the equilibrium-subtracted data $\{\breve{\boldsymbol{a}}^n\}_{n=0}^{m'}$, where $\breve{\boldsymbol{a}}^n = \boldsymbol{a}^n - \boldsymbol{a}_e$ and $\boldsymbol{a}_e$ is an equilibrium solution vector [133, 137] for the given problem. Note that the DMD-E in the case when $\boldsymbol{a}_e = \bar{\boldsymbol{a}}$ (ref. Eq. 3.4) is equivalent to the Fourier expansion of the data [133]. The same algorithm used for the DMD (ref. Alg. 2) is used to calculate the DMD-E eigenvectors and modes, only replacing $\{\boldsymbol{a}^n\}_{n=0}^{m}$ with $\{\breve{\boldsymbol{a}}^n\}_{n=0}^{m'}$. The DMD-E representation of a dataset is therefore characterized by the set of eigenpairs and coefficients $\{(\hat{\boldsymbol{\varphi}}_\ell, \omega_\ell, \beta_\ell)\}_{\ell=1}^{k}$, along with the vector $\boldsymbol{a}_e$. The original

function $\boldsymbol{a}(t)$ is reconstructed through the following expansion, similar to Eq. 3.15, as

$$\boldsymbol{a}(t) \approx \boldsymbol{a}_e + \sum_{\ell=1}^{k} \beta_\ell \hat{\boldsymbol{\varphi}}_\ell e^{\omega_\ell t}. \tag{3.22}$$

The vector $\boldsymbol{a}_e$ is chosen from any equilibrium solution of the underlying system that determines $\boldsymbol{a}(t)$ [137]. The time-dependent TRT problems under consideration here possess a steady-state solution that is approached as $t \to \infty$. The most natural choice for this application is then to let $\boldsymbol{a}_e = \lim_{t\to\infty} \boldsymbol{a}(t)$. In this study $\boldsymbol{a}_e = \boldsymbol{a}(t^m)$ is used to approximate the steady-state solution, so that $m' = m - 1$ and the equilibrium subtracted data is

$$\check{\boldsymbol{a}}^n = \boldsymbol{a}^n - \boldsymbol{a}^m, \quad n = 0, \ldots, m-1. \tag{3.23}$$

3.3 POD-Galerkin Projection

The POD-Galerkin approach to model reduction allows one to derive low-dimensional representations of differential equations [30, 33, 138, 131]. In essence, an equation can be projected onto a subset of the proper orthogonal modes that describe a known set of solutions to that equation. This can be viewed as a discretization scheme that makes use of problem-specific global basis functions. Let us again consider the function $a(x,t) \in \mathbb{C}$, where x is the set of variables comprising the phase-space occupied by a. Let a be described by the following residual equation

$$\mathcal{R}(x,t;a)a = 0, \tag{3.24}$$

where the operator $\mathcal{R} : \mathfrak{X} \times \mathfrak{T} \to \mathbb{C}$ has some nonlinear dependence on a. An approximation of a can be found by truncating the expansion in Eq. 3.3 to k terms

$$a(x,t) \approx \sum_{\ell=1}^{k} \lambda_\ell(t) u_\ell^*(x), \tag{3.25}$$

where $\lambda_\ell = \alpha_\ell v_\ell(t)$. This can be viewed as an expansion of a in some set of basis functions $\{u_\ell^*\}_{\ell=1}^k$ that span all phase space, with temporally-dependent coefficients $\{\lambda_\ell\}_{\ell=1}^k$. This

expansion is substituted in Eq. 3.24 to yield

$$\mathcal{R}(x,t;a)\sum_{\ell=1}^{k}\lambda_\ell(t)u_\ell^*(x)=0. \tag{3.26}$$

followed by a projection onto the basis $\{u_\ell^*\}_{\ell=1}^k$ by applying the inner product $\langle u_{\ell'}^*,\cdot\rangle_x$ for all $\ell'=1,\ldots,k$

$$\sum_{\ell=1}^{k}\langle u_{\ell'}^*,\mathcal{R}\lambda_\ell u_\ell^*\rangle_x=0, \tag{3.27}$$
$$\ell'=1,\ldots,k.$$

Let us assume that $\mathcal{R}$ is separable into two components $\mathcal{R}(x,t;a)=\partial_t+\mathcal{L}(x;a)$ such that Eq. 3.27 can be written as a system of first-order ordinary differential equations (ODEs) for the functions $\{\lambda_\ell\}_{\ell=1}^k$

$$\sum_{\ell=1}^{k}\langle u_{\ell'}^*,u_\ell^*\rangle_x\partial_t\lambda_\ell(t)+\langle u_{\ell'}^*,\mathcal{L}u_\ell^*\rangle_x\lambda_\ell(t)=0, \tag{3.28a}$$

$$\lambda_\ell|_{t=0}=\langle u_\ell^*,a|_{t=0}\rangle_x,\ \ell=1,\ldots,k, \tag{3.28b}$$
$$\ell'=1,\ldots,k.$$

With the presumption that each u_ℓ^* is an a-priori known function, Eq. 3.28a is a $k\times k$ dense linear system whose solution is for the generalized coordinates of a in the basis $\{u_\ell\}_{\ell=1}^k$ (i.e. for $\{\lambda_\ell\}_{\ell=1}^k$).

3.3.1 POD-Galerkin Projection in Discrete Space

In the fully discrete case, considering only real functions, the function $a(x,t)\in\mathbb{R}$ is described by a vector of elements in phase space $\boldsymbol{a}^n\in\mathbb{R}^d$ at each time step $n\in[0,\ldots,m]$. The discrete analogue of Eq. 3.24, where we restrict ourselves to single-step implicit time integration schemes (e.g. backward-Euler), is

$$\mathcal{R}^n(\boldsymbol{a}^n,\boldsymbol{a}^{n-1})\boldsymbol{a}^n=0, \tag{3.29}$$

where $\mathcal{R}^n:\mathbb{R}^d\to\mathbb{R}^d$ is the discrete residual operator. The POD basis that describes $\{\boldsymbol{a}^n\}_{n=0}^m$ optimally in the Frobenius norm comprises the left singular vectors of the matrix

$\mathbf{A} = [\boldsymbol{a}^0, \ldots, \boldsymbol{a}^m]$, as described in Sec. 3.1. Here, a POD basis is instead sought to represent $\{\boldsymbol{a}^n\}_{n=0}^m$ optimally in the W norm, satisfying the following optimization problem [131]:

$$\{\boldsymbol{u}_\ell\}_{\ell=1}^k = \arg\min_{\boldsymbol{u}_1,\ldots,\boldsymbol{u}_k} \sum_{n=1}^{N_t} \Delta t^n \left\| \boldsymbol{a}^n - \sum_{\ell=1}^k \langle \boldsymbol{a}^n, \boldsymbol{u}_\ell \rangle_W \boldsymbol{u}_\ell \right\|_W^2, \tag{3.30}$$

where the norm $||\cdot||_W^2$ is a discrete analogue to the norm $||\cdot||_x^2$ and is defined by the specific discretization schemes used to form $\mathcal{R}^n$. More specifically

$$\langle \boldsymbol{u}_{\ell'}, \boldsymbol{u}_\ell \rangle_W = \boldsymbol{u}_{\ell'}^\top \mathbf{W} \boldsymbol{u}_\ell, \tag{3.31}$$

where the elements of $\mathbf{W} \in \mathbb{R}^{d\times d}$ are the quadrature weights corresponding to the given discretizations in phase space. In order for the POD basis $\{\boldsymbol{u}_\ell\}_{\ell=1}^k$ to satisfy the minimization condition in Eq. 3.30, calculations must be done using the weighted snapshot matrix

$$\hat{\mathbf{A}} = \mathbf{W}^{1/2} \mathbf{A} \mathbf{H}^{1/2}, \tag{3.32}$$

where $\mathbf{H}$ is the temporal counterpart to $\mathbf{W}$ containing the weights introduced by the chosen scheme for time integration. The POD basis functions for this expansion are found as the first k columns of the matrix $\mathbf{U} = [\boldsymbol{u}_1 \ \ldots \ \boldsymbol{u}_r] \in \mathbb{R}^{d\times r}$, defined by

$$\mathbf{U} = \mathbf{W}^{-1/2} \hat{\mathbf{U}}, \tag{3.33}$$

where $r = \text{rank}(\hat{\mathbf{A}})$ and $\hat{\mathbf{U}}$ is the matrix whose columns hold the left singular vectors of $\hat{\mathbf{A}}$.

The vector $\boldsymbol{a}^n$ can now be expanded in the first k POD basis functions

$$\boldsymbol{a}^n \approx \sum_{\ell=1}^k \lambda_\ell^n \boldsymbol{u}_\ell, \tag{3.34}$$

where $\{\lambda_\ell^n\}_{\ell=1}^k$ are scalar coefficients that depend on the time step n. Substituting this expansion into Eq. 3.29 gives

$$\sum_{\ell=1}^k \lambda_\ell^n \mathcal{R}^n \boldsymbol{u}_\ell = 0. \tag{3.35}$$

This equation is overdetermined granted that $k < d$. Applying the inner product $\langle \boldsymbol{u}_{\ell'}, \cdot \rangle_W$

to this equation for $\ell' = 1, \ldots, k$ yields

$$\sum_{\ell=1}^{k} \lambda_\ell^n \langle \boldsymbol{u}_{\ell'}, \mathcal{R}^n \boldsymbol{u}_\ell \rangle_W = 0, \tag{3.36a}$$

$$\lambda_\ell^0 = \langle \boldsymbol{u}_\ell, a^0 \rangle_W, \ \ell = 1, \ldots, k, \tag{3.36b}$$

$$\ell' = 1, \ldots, k,$$

which as before is a $k \times k$ dense linear system with solution $\{\lambda_\ell^n\}_{\ell=1}^k$. Note that Eq. 3.36a enforces the condition that the residual $\mathcal{R}^n \sum_{\ell=1}^k \lambda_\ell^n \boldsymbol{u}_\ell \approx \mathcal{R}^n \boldsymbol{a}^n$ be $W-$orthogonal to the POD basis functions $\{\boldsymbol{u}_\ell\}_{\ell=1}^k$.

The computational benefits of finding $\{\boldsymbol{a}^n\}_{n=0}^m$ using Eqs. 3.34 & 3.36 should be apparent compared to the use of Eq. 3.29. In practice $k \ll d$ so that the vector of unknowns in the projected equations $\boldsymbol{\lambda} \in \mathbb{R}^k$ has many fewer DoF than the original unknown vector $\boldsymbol{a}^n$. Finding $\boldsymbol{\lambda}$ via Eqs. 3.36 therefore poses a significantly smaller computational burden than would be required to solve Eq. 3.29.

3.3.2 Petrov-Galerkin Projection in Discrete Space

As noted in the previous section, the solution of a Galerkin projected reduced-order system satisfies an orthogonality condition on the full-order residual $\mathcal{R}^n \tilde{\boldsymbol{a}}^n$ with $\tilde{\boldsymbol{a}}^n = \sum_{\ell=1}^k \lambda_\ell^n \boldsymbol{u}_i$. This condition does not guarantee stability, since it enforces no bound on the magnitude of the residual. *Petrov-Galerkin* projection techniques [139, 140, 141] rectify this problem by finding a test basis $\boldsymbol{\Psi} = [\boldsymbol{\psi}_1 \ \ldots \ \boldsymbol{\psi}_k] \in \mathbb{R}^{d \times k}$ which imposes some optimality (minimization) condition on the residual. Projecting Eq. 3.35 onto this test basis yields the following $k \times k$ system

$$\sum_{\ell=1}^{k} \lambda_\ell^n \langle \boldsymbol{\psi}_{\ell'}, \mathcal{R}^n \boldsymbol{u}_\ell \rangle_W = 0, \tag{3.37}$$

$$\sum_{\ell=1}^{k} \langle \boldsymbol{\psi}_{\ell'}, \boldsymbol{u}_\ell \rangle_W \lambda_\ell^0 = \langle \boldsymbol{\psi}_{\ell'}, \boldsymbol{a}^0 \rangle_W, \tag{3.38}$$

$$\ell' = 1, \ldots, k.$$

When using Petrov-Galerkin projection schemes, we elect to define our test basis functions as $\boldsymbol{\psi}_\ell = \frac{d\mathcal{R}^n(\lambda_\ell \boldsymbol{u}_\ell)}{d\lambda_\ell}$. This choice emanates from Thm. 3.3.1. This same choice of test basis is used in the least-squares Petrov-Galerkin (LSPG) projection schemes and can

be shown to minimize the residual $\mathcal{R}^n(\mathbf{U}\boldsymbol{\lambda})$ in the 2-norm [139, 140]. Thm. 3.3.1 extends these results for the W norm.

Lemma 3.3.1. *The norm $\|\cdot\|_W$ is strictly convex if $\mathbf{W}$ is symmetric positive definite*

Proof. By the definition of the W norm,

$$\|\boldsymbol{x}\|_W^2 = \boldsymbol{x}^\top \mathbf{W} \boldsymbol{x}. \tag{3.39}$$

Let $f(\boldsymbol{x}) = \|\boldsymbol{x}\|_W^2$, then

$$\frac{df(\boldsymbol{x})}{d\boldsymbol{x}} = 2\boldsymbol{x}^\top \mathbf{W}, \quad \frac{d^2 f(\boldsymbol{x})}{d\boldsymbol{x}^2} = 2\mathbf{W}, \tag{3.40}$$

since $\mathbf{W}$ is symmetric. The Hessian of $f(\boldsymbol{x})$ is therefore positive definite, since $\mathbf{W}$ is positive definite. This implies $f(\boldsymbol{x})$ strictly convex. □

Theorem 3.3.1. *The solution to Eq. 3.37 with test basis functions $\boldsymbol{\psi}_\ell = \frac{d\mathcal{R}^n(\lambda_\ell \boldsymbol{u}_\ell)}{d\lambda_\ell}$ satisfies the following minimization problem*

$$\boldsymbol{\lambda} = \arg\min_{\boldsymbol{\xi} \in \mathbb{R}^k} \|\mathcal{R}^n(\mathbf{U}\boldsymbol{\xi})\|_W^2, \tag{3.41}$$

where $\boldsymbol{\lambda} = (\lambda_1 \dots \lambda_k)^\top$.

Proof. Let $f(\boldsymbol{x}(\boldsymbol{\lambda})) = \|\boldsymbol{x}(\boldsymbol{\lambda})\|_W^2$ with $\boldsymbol{x}(\boldsymbol{\lambda}) = \mathcal{R}^n(\mathbf{U}\boldsymbol{\lambda})$. Assuming $\mathbf{W}$ symmetric positive definite, f must have a unique minimizer $\hat{\boldsymbol{x}} = \boldsymbol{x}(\hat{\boldsymbol{\lambda}})$ by Lemma 3.3.1. This point occurs at $\frac{df}{d\boldsymbol{x}} = 0$, or equivalently at $\frac{df}{d\boldsymbol{\lambda}} = 0$ since $\frac{df}{d\boldsymbol{\lambda}} = \frac{df}{d\boldsymbol{x}} \frac{d\boldsymbol{x}}{d\boldsymbol{\lambda}}$. These latter two derivatives are

$$\frac{df}{d\boldsymbol{x}} = 2\boldsymbol{x}^\top \mathbf{W}, \quad \frac{d\boldsymbol{x}}{d\boldsymbol{\lambda}} = \frac{d\mathcal{R}^n(\mathbf{U}\boldsymbol{\lambda})}{d\boldsymbol{\lambda}}. \tag{3.42}$$

Setting $\frac{df}{d\boldsymbol{\lambda}} = 0$ therefore leads to the following

$$\frac{df}{d\boldsymbol{x}} \frac{d\boldsymbol{x}}{d\boldsymbol{\lambda}} = 2\boldsymbol{x}^\top \mathbf{W} \frac{d\mathcal{R}^n(\mathbf{U}\boldsymbol{\lambda})}{d\boldsymbol{\lambda}} = \mathbf{0}^\top, \tag{3.43}$$

or equivalently

$$\left(\frac{d\mathcal{R}^n(\mathbf{U}\boldsymbol{\lambda})}{d\boldsymbol{\lambda}}\right)^\top \mathbf{W}\boldsymbol{x} = \mathbf{0}, \tag{3.44}$$

where $\mathbf{0} \in \mathbb{R}^k$ is the vector of all 0's. Using the definitions for $\boldsymbol{x}$ and $\boldsymbol{\Psi}$ in Eq. 3.44 gives us the relation $\boldsymbol{\Psi}^T \mathbf{W} \mathcal{R}^n(\mathbf{U}\boldsymbol{\lambda}) = 0$, which is equivalent to the system in Eq. 3.37. Therefore

the solution $\boldsymbol{\lambda}$ to Eqs. 3.37 with $\boldsymbol{\Psi} = \frac{d\mathcal{R}^n(\mathbf{U}\boldsymbol{\lambda})}{d\boldsymbol{\lambda}}$ satisfies the minimization problem in Eq. 3.41. □

Remark 3.3.1. *In this work when Petrov-Galerkin projection schemes are used, the matrix* $\mathbf{W}$ *is constructed in such a way that all of the involved quadrature weights are positive.* $\mathbf{W}$ *is also formulated as a diagonal matrix. As such* $\mathbf{W}$ *is symmetric positive definite in all applications considered here.*

CHAPTER

4

A ROM BASED ON DATA-DRIVEN APPROXIMATION OF THE EDDINGTON TENSOR

In this chapter a ROM is derived that uses data-driven techniques to estimate the Eddington tensor which gives closure to the multigroup LOQD system (Eqs. 2.3). The resulting models consist of the hierarchy of LOQD moment equations (Eqs. 2.3 & 2.13), the MEB equation (Eq. 2.20) and some data-driven functional that approximates the Eddington tensor. The POD, DMD and DMD-E are considered (see Ch. 3). A parameterization of the ROM is developed for the temperature of incoming radiation at the problem boundary (the radiation drive). Results from a dimensionless study of the TRT problem inform the specific parameterization. Numerical results are shown to demonstrate the ROM's performance. These models are shown to be accurate even with low-rank representations of the Eddington tensor. A subset of the results presented in this chapter have been published in [82, 83] and presented at the 2019 International Conference on Mathematics and Computational Methods Applied to Nuclear Science and Engineering.

4.1 Approximation of Discrete Data

At an abstract level, the considered class of ROMs for TRT is constructed with some data-driven functional that approximates closures for the LOQD moment equations. In practice the chosen data-driven functional must approximate discrete grid functions of the Eddington tensor and LOQD boundary factors. These grid functions will vary based on the scheme used to discretize the multigroup LOQD system in space. The finite-volumes scheme described in Sec. 2.4 is used here and confined to orthogonal spatial grids, denoting the number of cells in the $\boldsymbol{e}_x$- and $\boldsymbol{e}_y$- directions as N_x and N_y respectively.

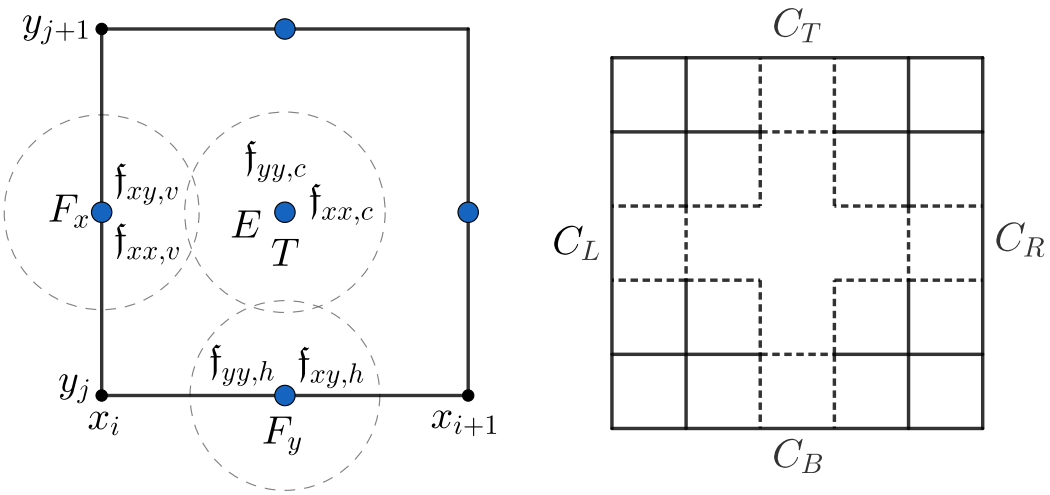

(a) Cell-wise grid functions

(b) Boundary factors

Figure 4.1: Discrete grid functions of the Eddington tensor and boundary factors shown on a sample 2D spatial mesh

Fig. 4.1 displays the discrete grid functions of the Eddington tensor and boundary factors defined by considered discretization. Functions of cell centers, vertically aligned cell faces and horizontally aligned cell faces are denoted by subscripts of c, v and h respectively. Four distinct boundary factor grid functions are defined that each reside on a section of the domain boundary.

Each grid function of the Eddington tensor and boundary factors is collected over the entire spatial grid as vectors

$$\mathfrak{f}^n_{\alpha\beta,g,\gamma} \in \mathbb{R}^{\mathfrak{N}_\gamma}, \quad \gamma = v, h, c, \quad \alpha, \beta = x, y, \tag{4.1a}$$

$$\boldsymbol{C}^n_{\theta,g} \in \mathbb{R}^{\mathfrak{N}_\theta}, \quad \theta = L, B, R, T, \tag{4.1b}$$

with dimensions

$$\mathfrak{N}_L = \mathfrak{N}_R = N_y, \quad \mathfrak{N}_B = \mathfrak{N}_T = N_x, \tag{4.2a}$$

$$\mathfrak{N}_v = (N_x + 1)N_y, \quad \mathfrak{N}_h = N_x(N_y + 1), \quad \mathfrak{N}_c = N_x N_y. \tag{4.2b}$$

The vectors in Eq. 4.1 can be subsequently 'stacked' by frequency group to construct complete data vectors for each quantity at the n^{th} time step

$$\boldsymbol{f}^n_{\alpha\beta,\gamma} = \begin{pmatrix} \mathfrak{f}^n_{\alpha\beta,1,\gamma} \\ \mathfrak{f}^n_{\alpha\beta,2,\gamma} \\ \vdots \\ \mathfrak{f}^n_{\alpha\beta,N_g,\gamma} \end{pmatrix} \in \mathbb{R}^{N_g \mathfrak{N}_\gamma}, \quad \boldsymbol{C}^n = \begin{pmatrix} \boldsymbol{C}^n_1 \\ \boldsymbol{C}^n_2 \\ \vdots \\ \boldsymbol{C}^n_{N_g} \end{pmatrix} \in \mathbb{R}^{2N_g(N_x+N_y)}, \tag{4.3}$$

where

$$\boldsymbol{C}^n_g = \begin{pmatrix} \boldsymbol{C}^n_{L,g} \\ \boldsymbol{C}^n_{B,g} \\ \boldsymbol{C}^n_{R,g} \\ \boldsymbol{C}^n_{T,g} \end{pmatrix} \in \mathbb{R}^{2(N_x+N_y)}. \tag{4.4}$$

It is exactly those vectors (Eq. 4.3) whose data-driven approximation is sought. Although this formulation is specific to our chosen discretization, it can be easily altered for use with any other scheme by changing the selected grid functions. The only difference will then be in the structure of the vectors in Eq. 4.1. When using projection-based methods like the POD (ref. Sec. 3.1) or the DMD (ref. Sec. 3.2), this approximation is found through some low-rank representation(s) of a-prioiri known Eddington tensor data. A mapping operator is also created to form the correct discrete grid functions of the Eddington tensor and boundary factors from this low-rank data.

4.2 Low-Rank Projection of the Eddington Tensor with the POD and DMD

Both the POD and DMD find a low-rank representation of some matrix $\mathbf{A}$, written as $\mathcal{A}_k$ with $k \leq \text{rank}(\mathbf{A})$. Using the notations defined in Ch. 3, $\mathcal{A}_k$ is defined as the following set corresponding to the data-driven projection method of choice

$$\mathcal{A}_k = \begin{cases} \bar{\boldsymbol{a}} \cup \{\boldsymbol{u}_\ell,\ \boldsymbol{v}_\ell,\ \sigma_\ell\}_{\ell=1}^{k}, & \text{POD} \\ \{\hat{\boldsymbol{\varphi}}_\ell,\ \omega_\ell,\ \beta_\ell\}_{\ell=1}^{k}, & \text{DMD} \\ \boldsymbol{a}_e \cup \{\hat{\boldsymbol{\varphi}}_\ell,\ \omega_\ell,\ \beta_\ell\}_{\ell=1}^{k}, & \text{DMD-E} \end{cases} \tag{4.5}$$

Given a solution to the TRT problem (Eqs. 1.6 & 1.10) for N_t time steps, the vectors in Eq. 4.3 are collected in chronological order as columns of the following snapshot matrices

$$\mathbf{A}^{\mathfrak{f}_{\alpha\beta,\gamma}} = [\boldsymbol{f}^1_{\alpha\beta,\gamma}\ \boldsymbol{f}^2_{\alpha\beta,\gamma}\ \cdots\ \boldsymbol{f}^{N_t}_{\alpha\beta,\gamma}] \in \mathbb{R}^{N_g\mathfrak{N}_\gamma \times N_t}, \tag{4.6}$$

$$\mathbf{A}^{c} = [\boldsymbol{C}^1\ \boldsymbol{C}^2\ \cdots\ \boldsymbol{C}^{N_t}] \in \mathbb{R}^{2N_g(N_x+N_y)\times N_t}. \tag{4.7}$$

Let $\mathbf{A}^{\mathfrak{f}_{\alpha\beta,\gamma}}(\vartheta)$, $\mathbf{A}^{c}(\vartheta)$ be the snapshot matrices that contain the solution to the TRT problem defined with a set of parameters $\vartheta \in \boldsymbol{\Theta}$, where $\boldsymbol{\Theta}$ is the space of all possible (feasible) parameter values. The solutions to multiple realizations of the TRT problem, each defined with one of the parameter sets contained in $\{\vartheta_i\}_{i=1}^{N_\vartheta} \subset \boldsymbol{\Theta}$, are then held in the matrices $\mathbf{A}^{\mathfrak{f}_{\alpha\beta,\gamma}}(\vartheta_i)$, $\mathbf{A}^{c}(\vartheta_i)$. The rank-$k$ projection of the data enclosed by each of these matrices is $\mathcal{A}_k^{\mathfrak{f}_{\alpha\beta,\gamma}}(\vartheta_i)$ and $\mathcal{A}_k^{c}(\vartheta_i)$.

When grid functions of the Eddington tensor and boundary factors need to be calculated from $\{\mathcal{A}_k^{\mathfrak{f}_{\alpha\beta,\gamma}}(\vartheta_i)\}_{i=1}^{N_\vartheta}$ and $\{\mathcal{A}_k^{c}(\vartheta_i)\}_{i=1}^{N_\vartheta}$, the mapping operator $\mathcal{M}(t,\vartheta)$ is applied such that

$$\mathcal{M}(t,\vartheta)\{\mathcal{A}_k^{\mathfrak{f}_{\alpha\beta,\gamma}}(\vartheta_i)\}_{i=1}^{N_\vartheta} = \tilde{\boldsymbol{f}}_{\alpha\beta,\gamma}(t) \in \mathbb{R}^{N_g\mathfrak{N}_\gamma}. \tag{4.8}$$

Here $\tilde{\boldsymbol{f}}_{\alpha\beta,\gamma}(t)$ approximates the γ grid function of the α,β component of the Eddington tensor for the TRT problem with parameters ϑ at time t. The application of $\mathcal{M}(t,\vartheta)$ to $\{\mathcal{A}_k^{c}(\vartheta_i)\}_{i=1}^{N_\vartheta}$ similarly approximates the boundary factors for this TRT problem. $\mathcal{M}(t,\vartheta)$ can be broken up into the application of two seperate operators $\mathcal{I}(\vartheta)$ and $\mathcal{H}(t)$

$$\mathcal{M}(t,\vartheta)\{\mathcal{A}_k(\vartheta_i)\}_{i=1}^{N_\vartheta} \equiv \mathcal{I}(\vartheta)\{\mathcal{H}(t)\mathcal{A}_k(\vartheta_i)\}_{i=1}^{N_\vartheta}, \tag{4.9}$$

where the superscript of $\mathcal{A}_k$ has been dropped for convenience. $\mathcal{H}(t)$ constructs a grid

function at time t from its low-rank representation and $\mathcal{I}(\vartheta)$ is an interpolation function of grid functions in $\boldsymbol{\Theta}$. If t is one of the time instances used to generate the original snapshot matrices $\{\mathbf{A}(\vartheta_i)\}_{i=1}^{N_\vartheta}$, then $\mathcal{H}(t)\mathcal{A}_k$ is equivalent to either Eq. 3.7, 3.15 or 3.22 depending on the method used to create $\mathcal{A}_k$. Otherwise $\mathcal{H}(t)$ constructs the grid functions nearest in time to t and interpolates to t.

In essence, the obtained projections hold fundamental information on the Boltzmann transport solution (i.e. the radiation intensities). The Eddington tensor itself is a projection of the radiation intensities onto a low-dimensional subspace. That information is projected again onto a subspace of even lower dimensionality using the POD and DMD. This holds several benefits. The computational burden of computing the LOQD closures is lessened as we can store the needed high-order data efficiently in memory, and fewer computations are required to interpolate between this data. The rank k of approximation is easily modified to accommodate different simulations, allowing one to adjust the approximation errors and computational load (via the parameter ξ, see Eq. 3.12).

4.3 Formulation of the Reduced Order Model

The class of ROMs derived in this chapter model TRT physics with the multilevel system of LOQD equations coupled with the MEB equation, using approximate low-rank closures. This model is henceforth referred to as the data-driven Eddington tensor (DET) ROM and is formulated by

- A low-rank representation of known data for the Eddington tensor and low-order boundary factors, found using either the POD, DMD or DMD-E
- The multigroup LOQD equations (Eqs. 2.3), closed by the Eddington tensor that is defined via a rank-k POD- or DMD- expansion
- The effective grey problem formed by the effective grey LOQD equations and the MEB equation (Eqs. 2.13)

This class of ROMs is formulated as having an *offline* and *online* stage. Each of these two stages are executed separately from one another. The offline stage must only be computed once per used dataset, and performs all necessary actions to obtain the low-rank sets of data $\{\mathcal{A}_k^{\mathbf{f}}(\vartheta_i)\}_{i=1}^{N_\vartheta}$ and $\{\mathcal{A}_k^{c}(\vartheta_i)\}_{i=1}^{N_\vartheta}$. The online stage is the one executed when the DET ROM is employed to solve a given TRT problem, and assumes the availability of its required low-rank data.

When preparing a DET model to solve a TRT problem (the offline stage), several realizations of the TRT problem (Eqs. 1.6 & 1.10) are solved with the MLQD method, which will be referred to as our full-order model (FOM) henceforth. These realizations correspond to different parameters $\vartheta_i \in \boldsymbol{\Theta}$. Some of these parameters can include (i) the distribution of incoming radiation on the problem boundaries (I_g^{in}) in frequency and angle, (ii) the initial state of the problem ($T^0,\ I_g^0$), (iii) the opacity function $\varkappa_\nu$. The solutions to these realizations are projected onto low-rank subspaces as described in Sec. 4.2.

Algorithm 3: Obtaining the solution to TRT problems with the DET class of ROMs

Input: $\{\mathcal{A}_k^{\mathfrak{f}}(\vartheta_i)\}_{i=1}^{N_\vartheta},\ \{\mathcal{A}_k^{c}(\vartheta_i)\}_{i=1}^{N_\vartheta},\ \mathcal{M}$
$n = 0$
while $t_n \leq t^{end}$ **do**
  $n = n + 1$
  Compute $\tilde{\mathfrak{f}}_g = \mathcal{M}(t^n, \vartheta)\{\mathcal{A}_k^{\mathfrak{f}}(\vartheta_i)\}_{i=1}^{N_\vartheta}$
  Compute $\tilde{C}_g = \mathcal{M}(t^n, \vartheta)\{\mathcal{A}_k^{c}(\vartheta_i)\}_{i=1}^{N_\vartheta}$
  $T^{(0)} = T^{n-1}$
  $q = 0$
  while $\|T^{(q)} - T^{(q-1)}\| > \epsilon_1\|T^{(q)}\| + \epsilon_2,\quad \|E^{(q)} - E^{(q-1)}\| > \epsilon_1\|E^{(q)}\| + \epsilon_2$ **do**
    Update $B_g, \varkappa_{E,g}, \varkappa_{B,g}, \tilde{\varkappa}_{R,g}$ with $T^{(q)}$
    Solve multigroup LOQD equations (Eqs. 2.3) with $\tilde{\mathfrak{f}}_g$ & $\tilde{C}_g$ for $E_g^{(q)},\ \boldsymbol{F}_g^{(q)}$
    Compute spectrum-averaged coefficients $\bar{\varkappa}_E,\ \bar{\varkappa}_B,\ \bar{\boldsymbol{C}},\ \bar{\mathfrak{f}},\ \bar{\mathcal{D}}$
    Solve effective grey problem (Eqs. 2.13 and 2.20) for $T^{(q+1)},\ E^{(q+1)},\ \boldsymbol{F}^{(q+1)}$
    $q = q + 1$
  end
  $T^n \leftarrow T^{(q)}$
end

Once the ROM has been prepared via the offline stage, it can be deployed to solve TRT problems using the online stage. The algorithm to solve TRT problems with these ROMs is outlined in Alg. 3. At each time step n, an approximation for the multigroup Eddington tensor and boundary factors on the discrete grid in phase space is calculated by applying the operator $\mathcal{M}$ to the input low-rank representations of $\mathfrak{f}_g$ and C_g. Iterations are performed to find the solution to the multilevel system of LOQD moment equations coupled

with the MEB equation, using the approximate Eddington tensor and boundary factors to close the system. In parametric applications, the quality of an obtained solution will depend not only on the rank k of data approximation, but also on the chosen interpolation scheme $\mathcal{I}$, and the scheme used to sample TRT solutions about the considered parameter space.

4.4 Numerical Results

The true objective of any ROM is to find solutions of problems that have yet to be solved (i.e. for $\vartheta \notin \{\vartheta_i\}_{i=1}^{N_\vartheta}$). Before such an application can be considered however, certain qualities of the ROM must first be identified. It is imperative to first demonstrate how well the ROM can reconstruct an already known solution ($\vartheta \in \{\vartheta_i\}_{i=1}^{N_\vartheta}$). If the ROM fails to achieve a desired level of accuracy here, or introduces nonphysical effects that cannot be tolerated, then parameterization is hopeless.

The nonlinear characteristics of our target class of problems prevents the derivation of any formal theory that can predict this behavior. Such theoretical results are restricted only to the Eddington tensor. For instance, when using the POD with any value of $\xi \in [0, 1]$ used to define the ROM's rank k (see Eq. 3.12) it is guaranteed that [132]

$$\frac{\|\mathcal{H}(\cdot)\mathcal{A}_k^{\mathsf{f}}(\vartheta) - \mathbf{A}^{\mathsf{f}}(\vartheta)\|_F}{\|\mathbf{A}^{\mathsf{f}}(\vartheta)\|_F} \leq \xi, \tag{4.10}$$

where $\mathcal{H}(\cdot)\mathcal{A}_k^{\mathsf{f}}(\vartheta) = \mathbf{A}_k^{\mathsf{f}}(\vartheta)$ is the rank k POD representation of $\mathbf{A}^{\mathsf{f}}(\vartheta)$. There exist no rigorous theoretical reasons to expect similar behavior in the solution for the radiation energy densities E and material temperature T. Although one can show that the full-rank ROM ($\xi = 0$) will reproduce the full-order solution for E and T, the essential question is how these values will converge with ξ. Analysis of how well the ROM can approximate TRT solutions in time (and phase space) with different values of ξ is another research item.

At the moment there is no theory addressing these items and therefore numerical tests must be performed on the method to investigate its properties and performance. A 'base-case' or reference FOM solution is found for some test problem to form the ROM database, and then the same test problem is solved again with the ROM. Comparisons of the ROM solution to the known FOM solution can be carried out on the considered discrete grids in phase space and time. It is important to note that the only errors incurred

by our FOM are due to discretization and as such the FOM will converge to the continuous TRT solution in the limit $N_x, N_y, N_\Omega, N_g, N_t \to \infty$ while the spatial and temporal domains remain constant. Therefore we formulate a conjecture that if the solution of the DET model converges to the discrete FOM solution then it will too converge to the continuous solution given a database generated on a fine-enough grid.

4.4.1 F-C Test A

Numerical tests of the DET class of ROMs are performed on a 2-dimensional extension of the well-known Fleck-Cummings (F-C) problem [142], which is described in detail in Appendix D. This section describes the specific form of the F-C test used in this analysis, referred to as the **F-C Test A**.

This test takes the form of a square homogeneous domain in the $x - y$ plane, 6 cm in length on both sides. The domain is initially at a temperature of T^0, the left boundary of the domain is subject to incoming radiation with blackbody spectrum at a temperature of T^{in}, and there is no incoming radiation at the other boundaries. The material is characterized by an analytic opacity function and material energy density, given in Eqs. D.1 & D.2. The BTE is discretized with the SCB scheme (ref. Sec. 2.3.1) and all low order equations are discretized with a finite volumes scheme (ref. Sec. 2.4). When generating ROM solutions to the F-C problem, the following convergence criteria are used (ref. Alg. 3): $\epsilon_1 = 10^{-14}$ and $\epsilon_2 = 10^{-15}$.

A uniform grid of 20×20 cells (i.e. $N_x = N_y = 20$) with side lengths of $\Delta x = \Delta y = 0.3$ cm is used to discretize the domain. $N_g = 17$ frequency groups are defined as shown in Table D.1. The Abu-Shumays angular quadrature set q461214 with 36 discrete directions per quadrant is used [143]. The total number of angular directions is $N_\Omega = 144$. The F-C problem is solved for the time interval $0 \leq t \leq 6$ ns with $N_t = 300$ uniform time steps $\Delta t = 2 \times 10^{-2}$ ns.

For this considered discretization, the Eddington tensor $\mathbf{f}_g$ occupies $\mathfrak{N}_\mathbf{f} = 2(\mathfrak{N}_v + \mathfrak{N}_h + \mathfrak{N}_c)N_g = 4.216 \times 10^4$ DoF at a single instance of time. In comparison, the DoF occupied by the radiation intensities from the simple corner balance scheme equals $\mathfrak{N}_I = 4N_xN_yN_gN_\Omega = 3.9168 \times 10^6$. This means that even before compressing the Eddington tensor with the POD or DMD, the required memory occupation is $\frac{\mathfrak{N}_I}{\mathfrak{N}_\mathbf{f}} = 93$ times smaller than for the radiation intensities.

4.4.2 Analysis of POD Data & Singular Values

The snapshot data used to construct the matrices $\mathbf{A}^{\mathfrak{f}_{\alpha\beta,\gamma}}$ and $\mathbf{A}^{c}$ (see Eqs. 4.6 & 4.7) is obtained by solving the TRT problem on the given grid in phase-space and time by means of the MLQD method (the FOM). Convergence criteria for this FOM simulation is set to $\epsilon_1 = 10^{-14}$ and $\epsilon_2 = 10^{-15}$ (see Alg. 1). Here the parameters $T^0 = 1$ eV and $T^{\text{in}} = 1$ KeV are considered as the 'base-case' to perform analysis on.

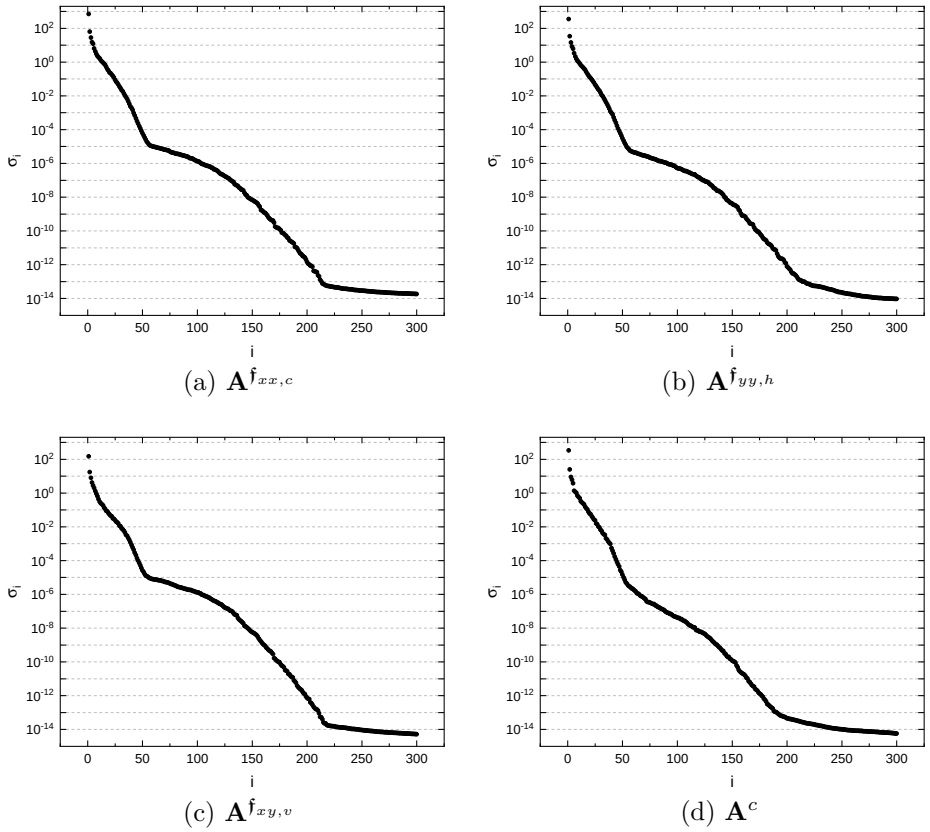

(a) $\mathbf{A}^{\mathfrak{f}_{xx,c}}$ (b) $\mathbf{A}^{\mathfrak{f}_{yy,h}}$

(c) $\mathbf{A}^{\mathfrak{f}_{xy,v}}$ (d) $\mathbf{A}^{c}$

Figure 4.2: Singular value distributions of select snapshot matrices of grid functions of the Eddington tensor and boundary factor for the F-C test (included matrices are: (a) $\mathbf{A}^{\mathfrak{f}_{xx,c}}$, (b) $\mathbf{A}^{\mathfrak{f}_{yy,h}}$, (c) $\mathbf{A}^{\mathfrak{f}_{xy,v}}$, (d) $\mathbf{A}^{c}$)

The singular values of a select few of those snapshot matrices found for this base case are depicted in Fig. 4.2. The singular values of those databases not shown here do not deviate significantly from the chosen plots. The singular values for each of the databases decay in a similar manner with 3 distinct sharp drops in magnitudes before reaching a value of approximately 10^{-14} where decay halts. The singular values that have a value

at or below 10^{-14} have reached the limit of machine precision and can be considered numerically zero.

Although the POD, DMD and DMD-E make use of slight variations on these snapshot matrices, the singular value distributions of those variant matrices are very similar to those pictured. For the databases without their final column, used for the DMD, their SVD is almost exactly the same as for the full matrices since the final column holds near steady-state data and does not add much new information to the span of the columns. For the POD when the databases are centered about their column-mean, the only significant difference from the shown plots is in the first singular value which decreases by roughly an order of magnitude. The second singular value is also seen to decrease by roughly half. The equilibrium-subtracted databases used for the DMD-E acquire singular value spectra very similar to those obtained through the POD.

When the POD, DMD and DMD-E are applied to the databases $\mathbf{A}^{\mathfrak{f}_{\alpha\beta,\gamma}}$ and $\mathbf{A}^{c}$, the rank k of projection is determined to satisfy Eq. 3.12 for some value ξ. Tabs. 4.1, 4.2 and 4.3 display the ranks that satisfy this relation for a spectrum of values for ξ. This same data is graphically depicted in Fig. 4.3.

ξ	$\mathcal{A}^{\mathfrak{f}_{xx,c}}$	$\mathcal{A}^{\mathfrak{f}_{xx,v}}$	$\mathcal{A}^{\mathfrak{f}_{yy,c}}$	$\mathcal{A}^{\mathfrak{f}_{yy,h}}$	$\mathcal{A}^{\mathfrak{f}_{xy,v}}$	$\mathcal{A}^{\mathfrak{f}_{xy,h}}$	$\mathcal{A}^{c}$
10^{-2}	15	17	15	15	14	17	14
10^{-4}	34	36	34	34	37	36	35
10^{-6}	49	49	52	49	65	68	48
10^{-8}	115	110	120	115	129	127	87
10^{-10}	152	148	154	153	159	158	132
10^{-12}	179	178	180	180	185	184	160
10^{-14}	203	203	205	205	207	207	188
10^{-16}	300	300	300	300	300	300	300

Table 4.1: Ranks k for each approximate database corresponding to different values of ξ for the POD

The ranks used for the POD, DMD and DMD-E behave similarly with changes in ξ for each snapshot matrix, gradually increasing with decreases in ξ until $\xi = 10^{-16}$ where each database's rank increases by roughly 100. This is due to the singular value decay structures shown in Fig. 4.2 where decay stops after about 200 singular values. The only significant difference in the used ranks between each of these methods given the same

ξ is that the DMD always uses a lower rank than the POD and DMD-E. This is an artifact of the centering and equilibrium-subtraction operations done on the databases prior to the calculation of each SVD for the POD and DMD-E. Here these operations only significantly decreased the first and second singular values of each matrix. This has the effect of reducing only the denominator of Eq. 3.12 for all $k > 1$ and therefore inflating the rank required to satisfy a given ξ.

ξ	$\mathcal{A}^{\mathbf{f}_{xx,c}}$	$\mathcal{A}^{\mathbf{f}_{xx,v}}$	$\mathcal{A}^{\mathbf{f}_{yy,c}}$	$\mathcal{A}^{\mathbf{f}_{yy,h}}$	$\mathcal{A}^{\mathbf{f}_{xy,v}}$	$\mathcal{A}^{\mathbf{f}_{xy,h}}$	$\mathcal{A}^{c}$
10^{-2}	6	7	6	6	7	9	5
10^{-4}	28	30	28	28	30	30	25
10^{-6}	43	44	44	43	46	46	42
10^{-8}	90	79	100	87	111	111	61
10^{-10}	138	136	142	139	148	147	112
10^{-12}	168	165	170	169	175	175	147
10^{-14}	195	194	196	196	199	199	173
10^{-16}	286	286	287	287	292	291	274
10^{-18}	299	299	299	299	299	299	299

Table 4.2: Ranks k for each approximate database corresponding to different values of ξ for the DMD

ξ	$\mathcal{A}^{\mathbf{f}_{xx,c}}$	$\mathcal{A}^{\mathbf{f}_{xx,v}}$	$\mathcal{A}^{\mathbf{f}_{yy,c}}$	$\mathcal{A}^{\mathbf{f}_{yy,h}}$	$\mathcal{A}^{\mathbf{f}_{xy,v}}$	$\mathcal{A}^{\mathbf{f}_{xy,h}}$	$\mathcal{A}^{c}$
10^{-2}	14	16	15	15	14	16	14
10^{-4}	34	36	34	34	36	35	34
10^{-6}	48	49	51	48	62	64	48
10^{-8}	114	109	119	114	125	127	85
10^{-10}	151	148	154	152	158	157	131
10^{-12}	179	177	180	179	184	183	160
10^{-14}	203	202	204	204	207	206	186
10^{-16}	298	298	298	298	298	298	298

Table 4.3: Ranks k for each approximate database corresponding to different values of ξ for the DMD-E

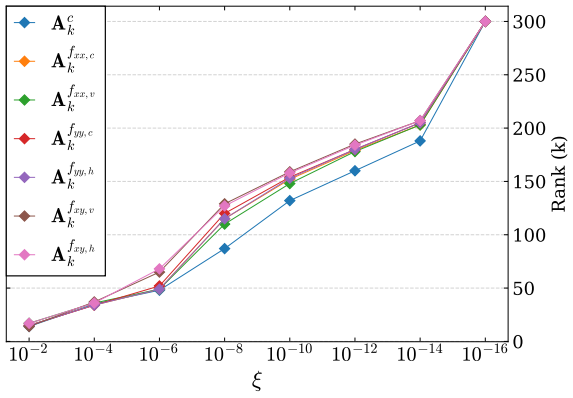

(a) POD

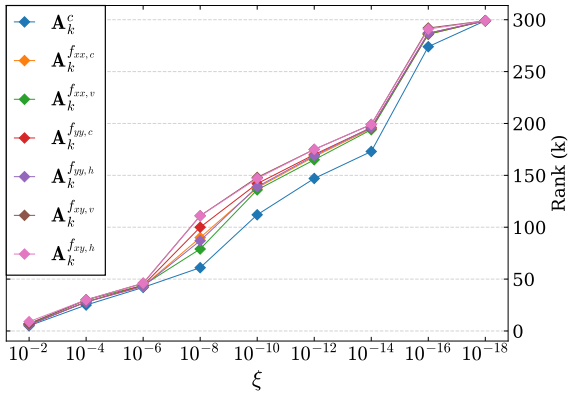

(b) DMD

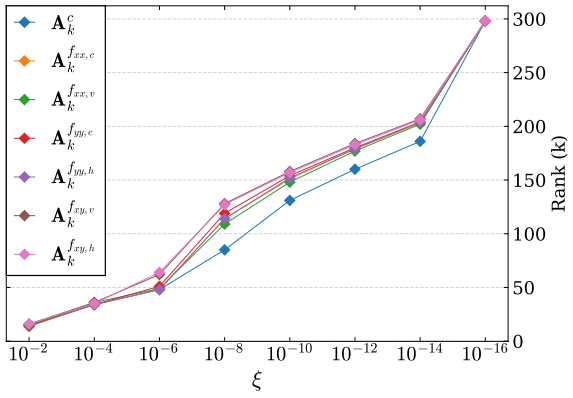

(c) DMD-E

Figure 4.3: Plotted ranks k for each approximate database corresponding to different values of ξ using the POD, DMD & DMD-E (see Tabs. 4.1 - 4.3)

4.4.3 Convergence of ROM Solutions

How (and if) the DET solution of the F-C test converges to the reference FOM solution is now analyzed. Figs. 4.4, 4.5 and 4.6 show the relative error (w.r.t. the FOM solution) for the material temperature (T) and total radiation energy density (E) calculated in the 2-norm over space at each instant of time in $t \in [0, 6\text{ns}]$ where each unique curve corresponds to the ROM solution generated for a given value of ξ.

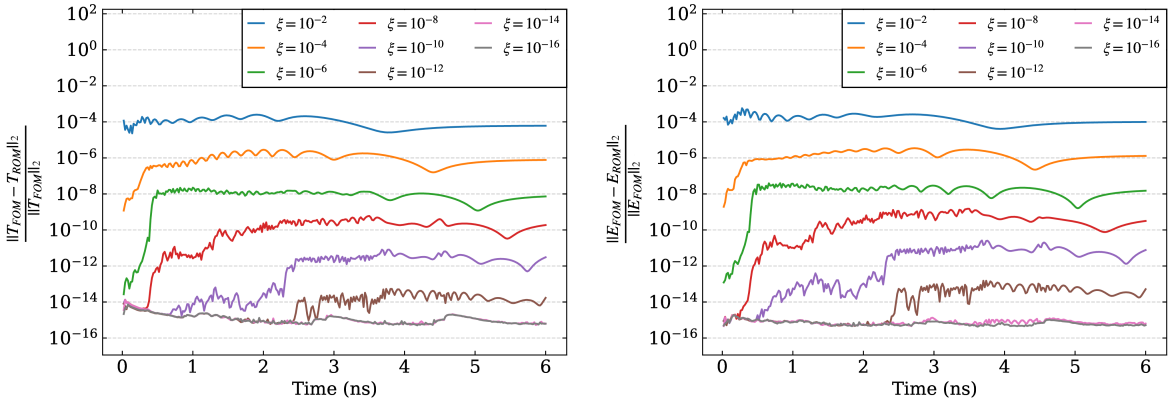

(a) Material Temperature (b) Radiation Energy Density

Figure 4.4: Relative errors in the 2-norm of the DET ROM using the POD for several ξ, plotted vs time

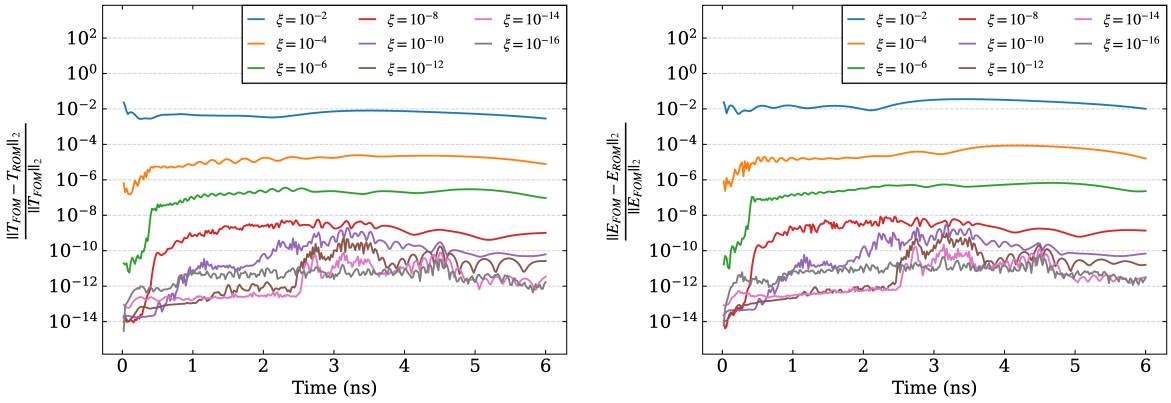

(a) Material Temperature (b) Radiation Energy Density

Figure 4.5: Relative errors in the 2-norm of the DET ROM using the DMD for several ξ, plotted vs time

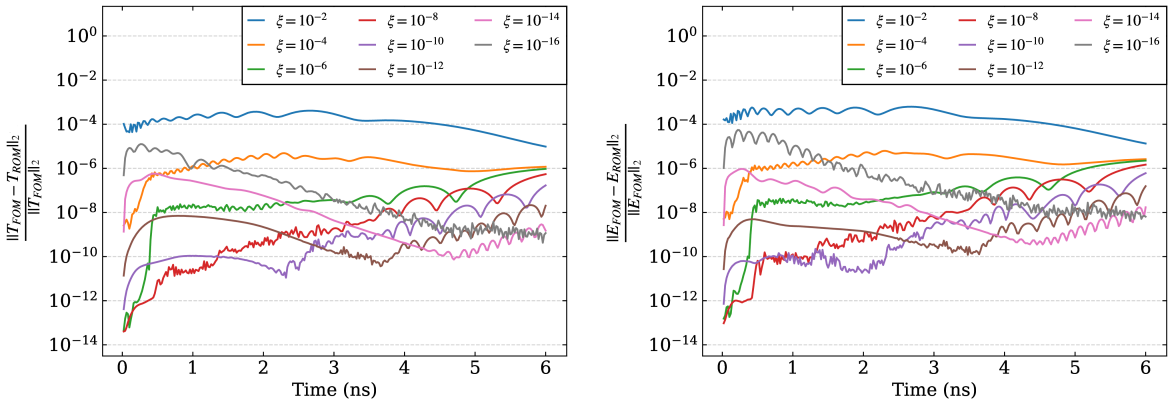

(a) Material Temperature

(b) Radiation Energy Density

Figure 4.6: Relative errors in the 2-norm of the DET ROM using the DMD-E for several ξ, plotted vs time

Considering first the ROM using the POD, Fig. 4.4 demonstrates a uniform convergence of errors in time as ξ is decreased. The error curves all behave similarly in time as well, first increasing in the rapidly evolving physical regime of wave evolution followed by stabilization to the neighborhood of some value for times after roughly 0.5ns. The highest observed errors are on the order of 10^{-4}, corresponding to the ROM with $\xi = 10^{-2}$. When $\xi = 10^{-16}$, the POD ROM invokes a full-rank representation of the Eddington tensor data and finds errors on the order of 10^{-15}, successfully obtaining the FOM solution to numerical precision. Next looking at the ROM using the DMD, Fig. 4.5 shows uniform convergence of the ROM errors in time for ξ decreasing until $\xi = 10^{-12}$. Further decreases in ξ have the effect of decreasing errors while $t > 2.5$ns and increasing errors for $t < 2.5$ns. The lowest errors for a single value of ξ exist on the order of $10^{-12} - 10^{-10}$. These effects are attributed to numerical noise, of which the DMD has known susceptibility to [37, 133]. Results for $\xi = 10^{-18}$ are not shown here as there is no significant change from those seen for $\xi = 10^{-16}$. The highest errors observed with the DMD are on the order of 10^{-2} for $\xi = 10^{-2}$, 2 orders of magnitude higher than observed for the POD with the same ξ. Lastly, the ROM using the DMD-E suffers from an amplified sensitivity to high-rank approximations compared to the ROM with the DMD. Errors shown in Fig. 4.6 are seen to converge up until $\xi = 10^{-10}$, after which further decreases in ξ lead to increases in the ROM errors. This effect is primarily observed for the early time instances of the problem. In contrast, the later times tend to stagnate at the same level of error as ξ decreases.

A different view of the data presented in Figs. 4.4 - 4.6 is given in Figs. 4.7, 4.8 and 4.9. These plots graph the ROM errors (w.r.t. the FOM solution) in the relative 2-norm against ξ, with each curve corresponding to a specific instant in time. This view is provided to enhance the clarity in which convergence behavior is assessed. Let the errors of each ROM be written as the function $\epsilon(x) = \frac{\|x_{\text{FOM}} - x_{\text{ROM}}\|_2}{\|x_{\text{FOM}}\|_2}$. From Fig. 4.7, it is immediately evident that the errors associated with the POD ROM have the relationship $\epsilon(E) \approx \epsilon(T) \approx \xi \cdot 10^{-2}$ up to the point where stagnation occurs from limitations of the finite precision of calculations. Fig. 4.8 shows a similar relationship for the DMD ROM, with $\epsilon(E) \approx \epsilon(T) \approx \xi$ for $\xi \geq 10^{-8}$. A decrease in the rate of convergence is observed for $\xi < 10^{-8}$ with this ROM before stagnation occurs around an order of $10^{-12} - 10^{-10}$. This slow in convergence rate is attributed again to an increase in numerical noise as rank is increased.

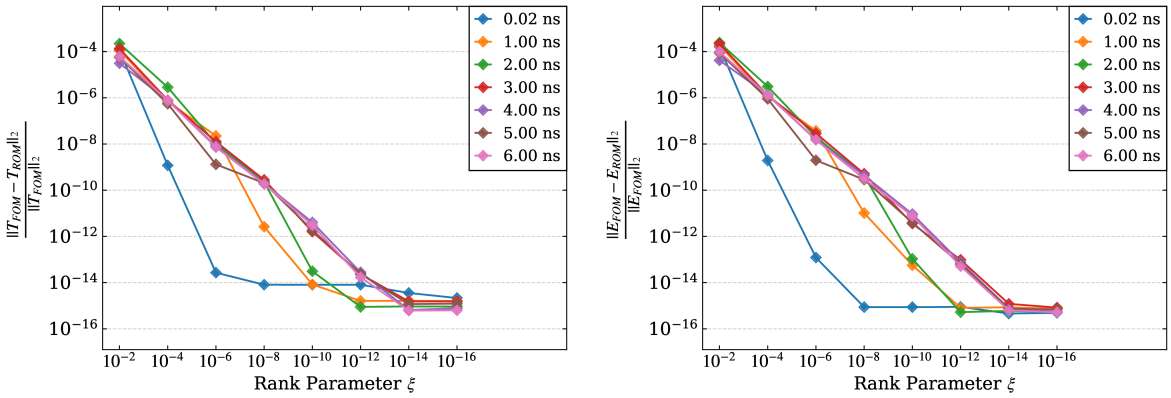

(a) Material Temperature

(b) Radiation Energy Density

Figure 4.7: Relative errors in the 2-norm of the DET ROM using the POD at several times, plotted vs ξ

Lastly considering the DMD-E ROM, Fig. 4.9 demonstrates more clearly the observed numerical sensitivity for small ξ. An initial increase in error level is seen at times $t = .02, 1$ ns for $\xi = 10^{-10}$, and the errors at $t = 2$ ns increase at $\xi = 10^{-12}$. This behavior is accredited to a large magnification of numerical errors as seen with the DMD. The DMD-E can be interpreted as the DMD on a set of residual vectors representing the distance of the expanded data to the near steady-state solution. The residual vectors for near steady-state data are then expected to have elements of very small magnitude which can contribute

to numerical issues in the decomposition. This combined with the inherent sensitivity of the DMD to numerics can lead to large amplifications of error. This interpretation also gives justification to the behaviors seen in Fig. 4.6. The exponentials in Eq. 3.22 are expected to decrease toward zero as time moves onward so that the 'steady-state' solution is only represented by the constant term. Any amount of noise introduced into the DMD-E expansion will become less prevalent as t grows and the exponentials shrink.

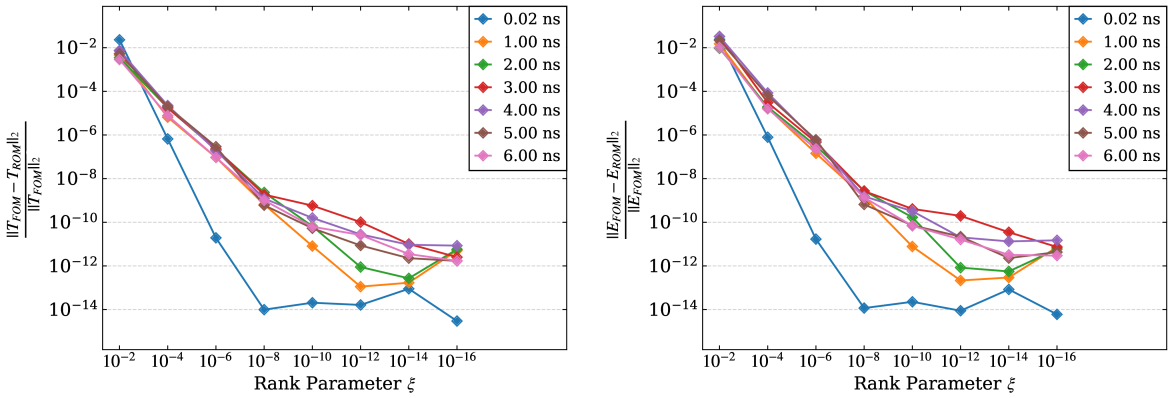

(a) Material Temperature (b) Radiation Energy Density

Figure 4.8: Relative errors in the 2-norm of the DET ROM using the DMD at several times, plotted vs ξ

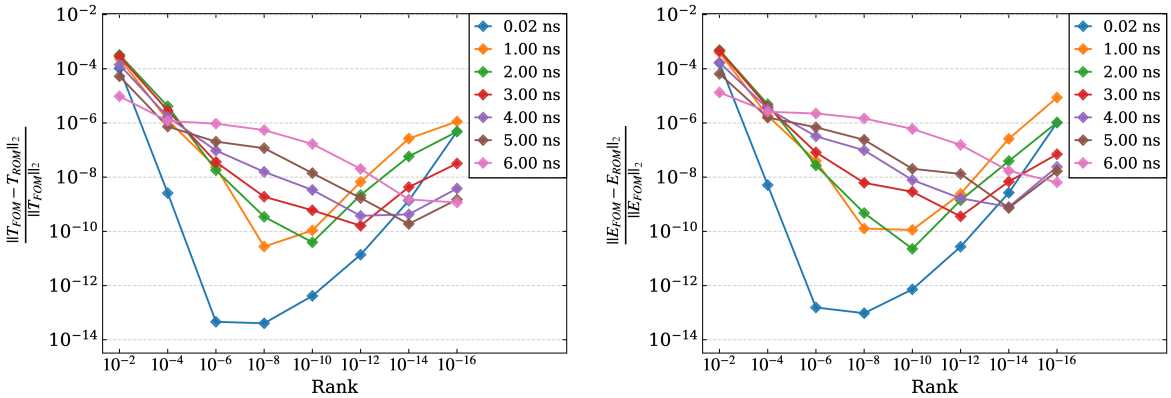

(a) Material Temperature (b) Radiation Energy Density

Figure 4.9: Relative errors in the 2-norm of the DET ROM using the DMD-E at several times, plotted vs ξ

The results presented up this point indicate that when equipped with methods like the POD and DMD, the DET class of ROMs can successfully and predictably converge to the FOM solutions they were trained on. This property is not exhibited with use of the DMD-E. Even so, in every case the DET ROMs are shown to perform well with low-rank. So far this analysis has restricted itself to the 2-norm of errors in space. What remains now is to analyze the characteristics of the ROM errors from the FOM solution locally in space. Here consideration is only done for $\xi = 10^{-2}, 10^{-4}$, as these lowest-rank ROMs are the most practical for applied use and are subject to the highest errors. Figs. 4.10, 4.11 and 4.12 show the spatially local relative errors in T and E at select instances of time. Each of these figures takes the form of two tables that display the relative pointwise error in the DET ROM across the spatial domain of the F-C test. The first (top) table shows errors in the material temperature (T) and the second (bottom) shows errors in the total radiation energy density (E). Each row corresponds to a different value of ξ and each column to the specific instant of time. The selected time instances are $t = 1, 2, 3$ ns, respectively. None of the other instances in $t \in [0, 6\text{ns}]$ differ greatly from those shown, in fact the color scale shown to the right of each row depicts the entire range of values for all time instances. Each plot makes it apparent that the spatial distribution of errors in those low-rank ROMs is relatively uniform. The values of all spatial errors reside in a close neighborhood to the relative 2-norm collective errors associated with the given ROM and instant of time (ref. Figs. 4.4 - 4.6).

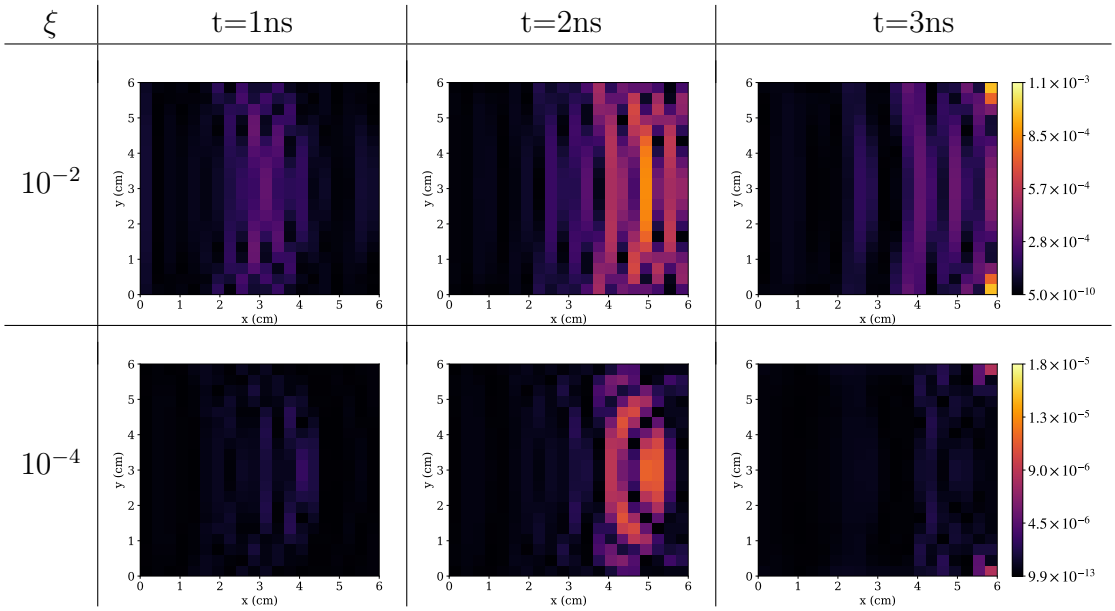

(a) Material Temperature

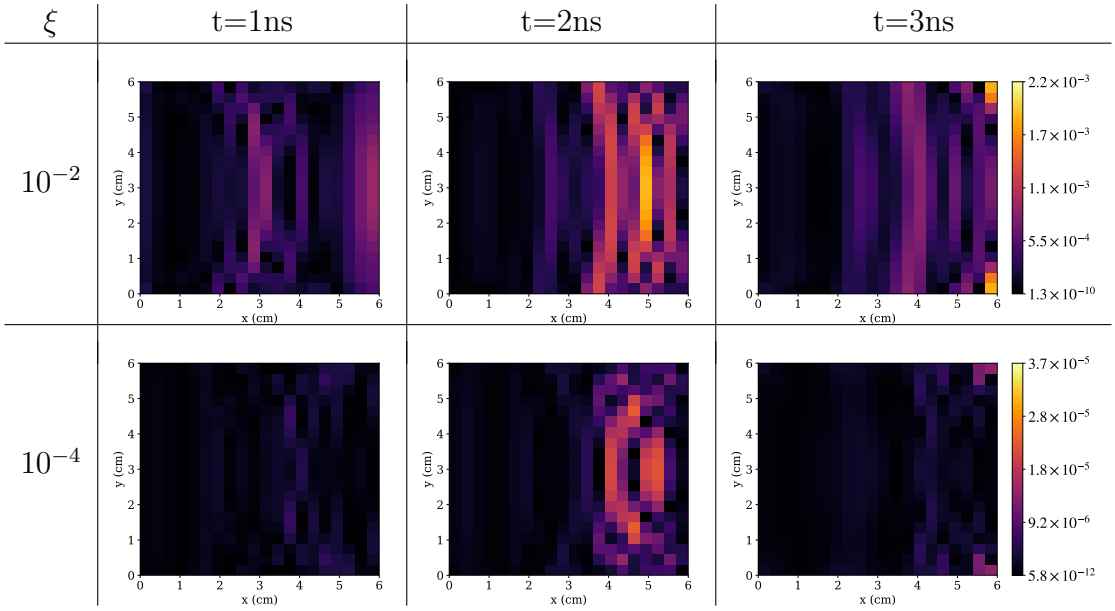

(b) Radiation Energy Density

Figure 4.10: Cell-wise relative error in material temperature (T) and total radiation energy density (E) over the spatial domain at times t=1, 2, 3 ns for the DET ROM equipped with the POD for $\xi = 10^{-2}, 10^{-4}$.

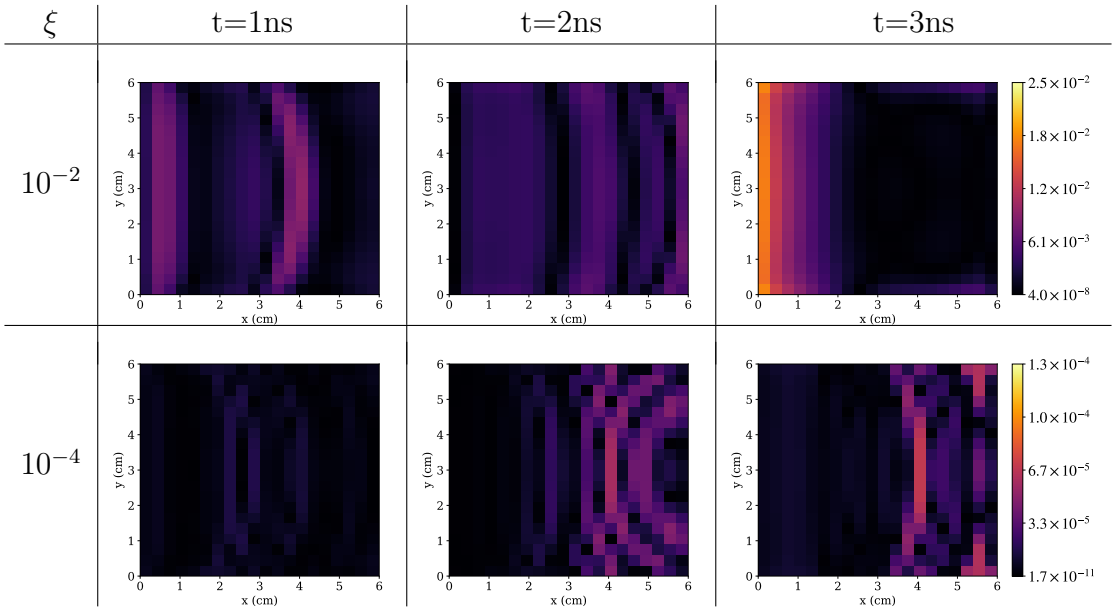

(a) Material Temperature

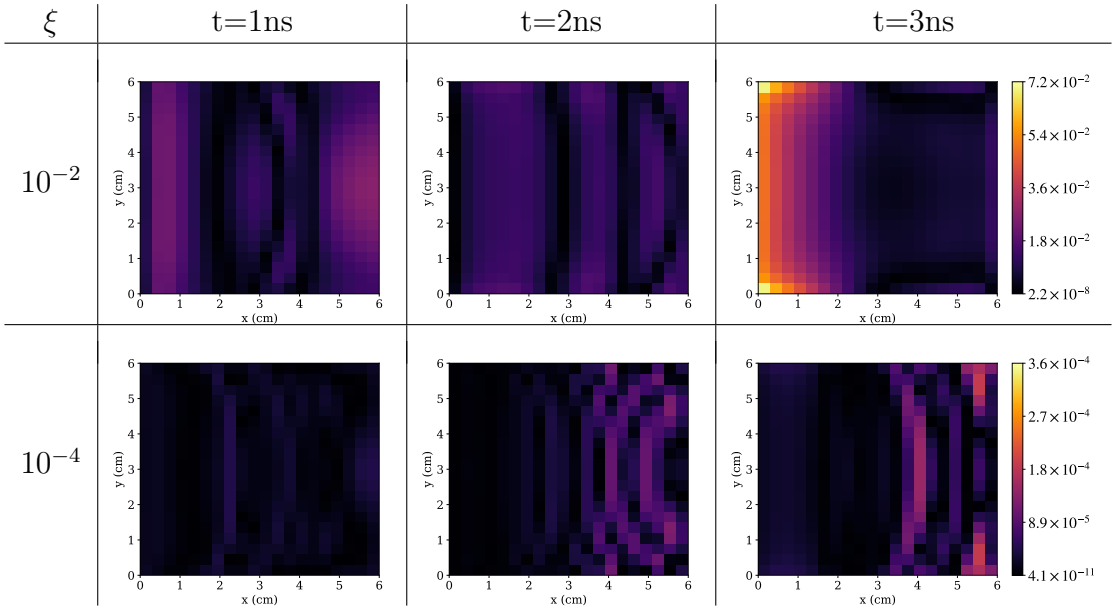

(b) Radiation Energy Density

Figure 4.11: Cell-wise relative error in material temperature (T) and total radiation energy density (E) over the spatial domain at times t=1, 2, 3 ns for the DET ROM equipped with the DMD for $\xi = 10^{-2}, 10^{-4}$.

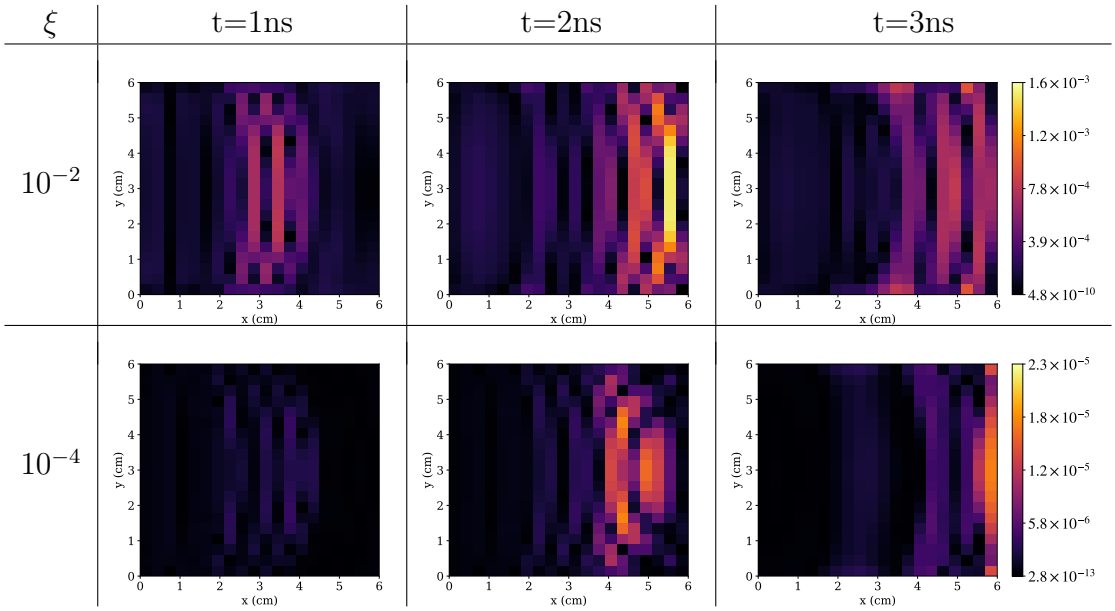

(a) Material Temperature

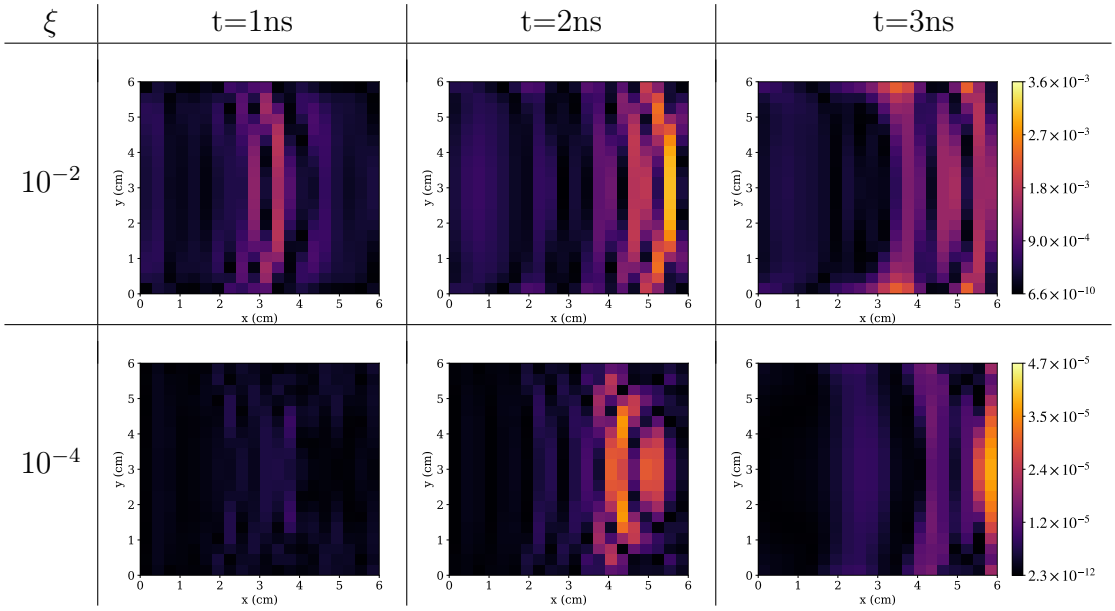

(b) Radiation Energy Density

Figure 4.12: Cell-wise relative error in material temperature (T) and total radiation energy density (E) over the spatial domain at times t=1, 2, 3 ns for the DET ROM equipped with the DMD-E for $\xi = 10^{-2}, 10^{-4}$.

4.5 Reproduction of Physical Quantities

Now that the error analysis of the DET ROMs is complete, what remains is to investigate how well these ROMs capture the physics of their target class of problems. The F-C test mimics the class of supersonic radiation shock problems and experiments [144, 145, 146, 147], with radiation flowing from the high-temperature 'drive' at the left boundary to the 'cold' right boundary. In these applications, the *breakout time* of radiation is a particularly important physical quantity or measurement. Typically in the literature, breakout time is measured as the elapsed time until a certain level of radiative flux is detected coming from the material through which radiation is driven [144, 146, 147]. This is an integral measurement of many physical effects and as such if the DET ROMs can successfully reproduce the FOM breakout time(s) for the F-C test, combined with the results from Sec. 4.4.3, the ROMs can be said to correctly reproduce (i) the radiation wavefront, (ii) the speed at which the wavefront propagates. This does not, however, give indication of how well the DET ROMs can recreate the correct *spectrum* of radiation. A separate analysis must be done to investigate this element of the physics, presented in Sec. 4.5.2.

4.5.1 Modeling of Radiation Wave Breakout

To give a more complete picture not only will the radiation flux ($\boldsymbol{F}$) be analyzed, but also the radiation energy density (E) and material temperature (T) present at the right boundary of the F-C test. Let the boundary-averages of these quantities be

$$\bar{F}_R = \frac{1}{L_R}\int_0^{L_R} \boldsymbol{e}_x \cdot \boldsymbol{F}(x_R, y)\ dy, \tag{4.11}$$

$$\bar{E}_R = \frac{1}{L_R}\int_0^{L_R} E(x_R, y)\ dy, \tag{4.12}$$

$$\bar{T}_R = \frac{1}{L_R}\int_0^{L_R} T(x_R, y)\ dy, \tag{4.13}$$

where $L_R = x_R = 6$cm. Fig. 4.13 plots the FOM solution of these quantities vs time. $\bar{T}_R$ smoothly increases in value between approximately $t \in [0, 3\text{ns}]$, after which it plateaus at around 0.45 KeV. $\bar{F}_R$ and $\bar{E}_R$ on the other hand evolve with two sharp increases in value followed by plateaus. The initial increase of these values for $t \in [0, 0.5\text{ns}]$ is indicative of when the high energy radiation has penetrated across the domain. The second increase in value between roughly $t \in [2, 2.5\text{ns}]$ corresponds to when the radiation

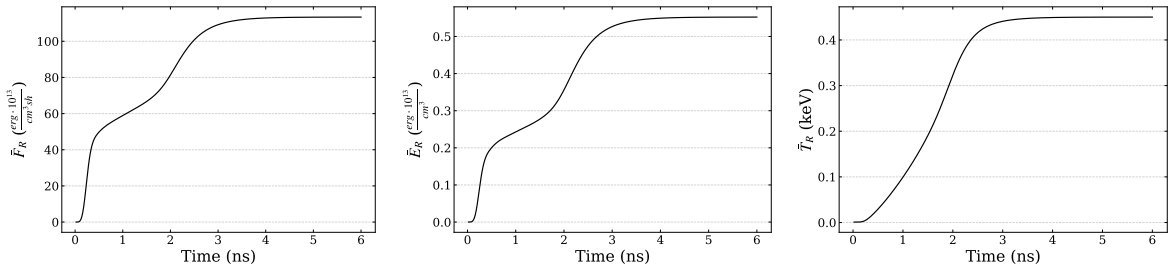

(a) $\bar{F}_R$ (b) $\bar{E}_R$ (c) $\bar{T}_R$

Figure 4.13: Total radiation flux ($\bar{F}_R$), total radiation energy density ($\bar{E}_R$) and material temperature ($\bar{T}_R$) averaged over the right boundary of the spatial domain plotted vs time. Shown solutions are generated by the FOM.

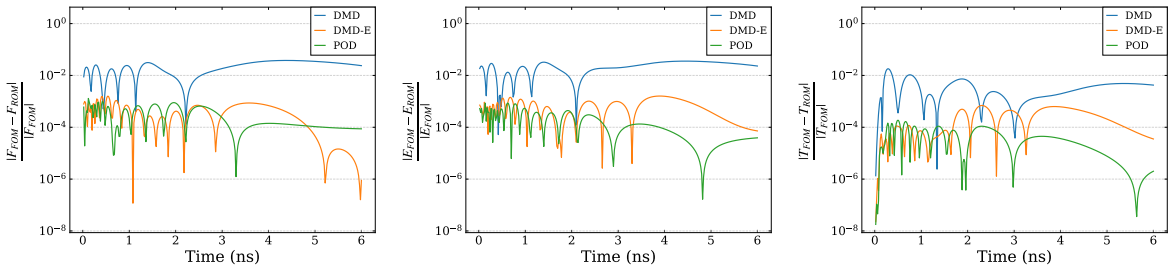

(a) $\bar{F}_R$ (b) $\bar{E}_R$ (c) $\bar{T}_R$

Figure 4.14: Relative error for the DET ROMs with $\xi = 10^{-2}$ for data located at and integrated over the right boundary of the domain.

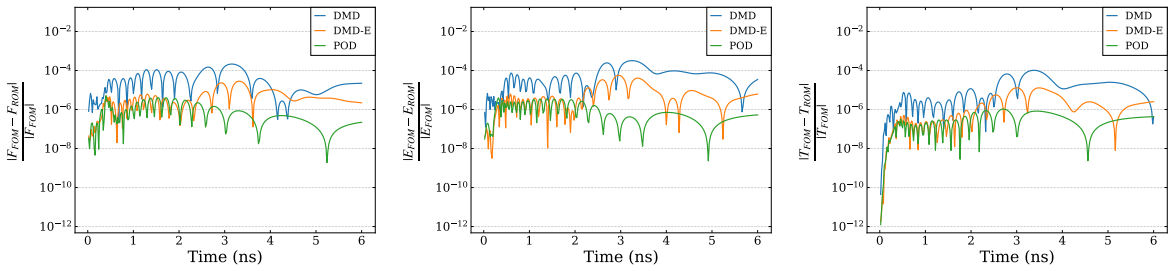

(a) $\bar{F}_R$ (b) $\bar{E}_R$ (c) $\bar{T}_R$

Figure 4.15: Relative error for the DET ROMs with $\xi = 10^{-4}$ for data located at and integrated over the right boundary of the domain.

in more optically-thick frequency groups has penetrated the domain.

Figs. 4.14 and 4.15 plot the relative error in $\bar{F}_R$, $\bar{E}_R$, and $\bar{T}_R$ produced by the DET ROMs (w.r.t. the FOM solution) using the POD, DMD and DMD-E with low rank corresponding to $\xi = 10^{-2}, 10^{-4}$. Each quantity is reproduced to a similar order of accuracy as was seen in Figs. 4.4 - 4.6. The DMD ROM has the highest errors for all quantities while the POD and DMD-E show similar levels of accuracy to one another. The error levels tend to oscillate about some value for the entire temporal range, with the exception of $\bar{T}_R$ in the case $\xi = 10^{-4}$. These errors begin at a level roughly an order of magnitude lower than observed for $\bar{E}_R$ and $\bar{F}_R$, and increase to a similar level of $\bar{E}_R$ and $\bar{F}_R$ at around $t = 2.5$ ns. This is the point where optically-thick radiation is demonstrated to penetrate the test domain (ref. Figs. 4.13). Radiation at these frequencies has the most impact on energy redistribution and therefore the material temperature, and these effects could contribute to the increase in error. Although not shown, this same effect is seen for $\xi < 10^{-4}$ as well.

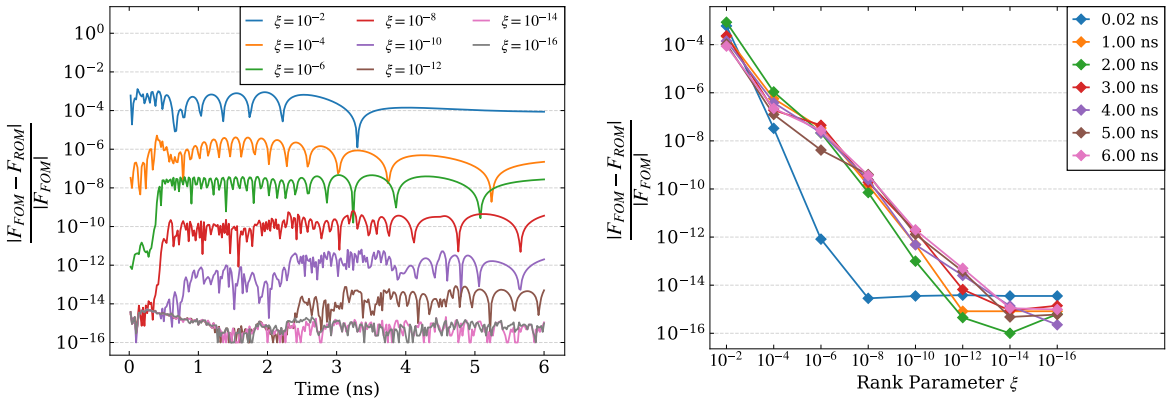

(a) Relative error vs. time

(b) Relative error vs ξ

Figure 4.16: Relative errors of the DET ROM solution for $\bar{F}_R$ using the POD plotted vs time and ξ

If the DET ROMs (with $\xi = 10^{-2}, 10^{-4}$) were to predict the breakout time of radiation based on when any of $\bar{F}_R$, $\bar{E}_R$, or $\bar{T}_R$ reach a certain arbitrary value in their ranges, the predicted time should be accurate to the levels shown in Figs. 4.14 and 4.15. If the convergence behaviors of these quantities to the FOM solution are comparable to those shown in Figs. 4.7 - 4.9 then the order of accuracy can be predicted based on ξ if using

the POD or DMD. Fig. 4.16 confirms this predictive capability. This figure shows the relative error in the DET solution (using the POD) for $\bar{F}_R$ plotted vs. both time and ξ. The results are akin to those shown for the relative 2-norm errors in E and T over the spatial domain. Similar results are found for the DMD ROM.

4.5.2 Radiation Spectrum

The final component of TRT physics to consider in this analysis is the spectrum of radiation. Thus far investigations have been restricted to integral quantities, shielding the group structure of obtained DET solutions from exposure. The goal here is to demonstrate that these ROMs can well preserve not just integral quantities but also the frequency-dependent structure of the problems they solve.

Fig. 4.17 plots the frequency spectrum of radiation energy densities (E_g) for the F-C test obtained by the FOM. Each plot graphs the radiation energy densities vs photon energy for a select point in the spatial domain and several instants of time (each curve represents a different temporal point). Plots on the left hand side show the entire frequency spectrum, and plots on the right are zoomed in to show the radiation peak with higher resolution. Note that these zoomed-in plots only disregard the final point in the spectrum. Each point is located at the center of a discrete energy group (see Tab. D.1) on the frequency-axis, and the value it takes on is the group-averaged radiation energy density $\bar{E}_g = \frac{E_g}{\nu_g - \nu_{g-1}}$. The chosen spatial points include (i) the midpoint of the domain, (ii) the midpoint of the right boundary, (iii) the bottom corner of the right boundary (since the F-C test is y-symmetric, the top and bottom corners are equivalent). These points were chosen as an illustration of different levels of transport effects, with large variations in anisotropy of radiation. The instants of time were chosen based off of Fig. 4.13 to sufficiently sample temporal regions of interest.

Figs. 4.18, 4.19 and 4.20 plot the relative errors of the average multigroup radiation energy densities produced by the DET ROMs using the POD, DMD and DMD-E, respectively, all with $\xi = 10^{-2}$. The 'zoomed' view of the frequency spectrum is used here to make the plots more readable, noting that the relative errors for the last frequency group do not significantly deviate from the errors of the final few groups. Figs. 4.21, 4.22 and 4.23 show this same data for solutions found with $\xi = 10^{-4}$. In all cases, the corner point has the highest levels of deviation from the FOM solution. The domain midpoint also displays the lowest levels of error. The degradation in accuracy for the DET ROMs as anisotropy increases is predominantly found in low-energy groups, whereas the groups that

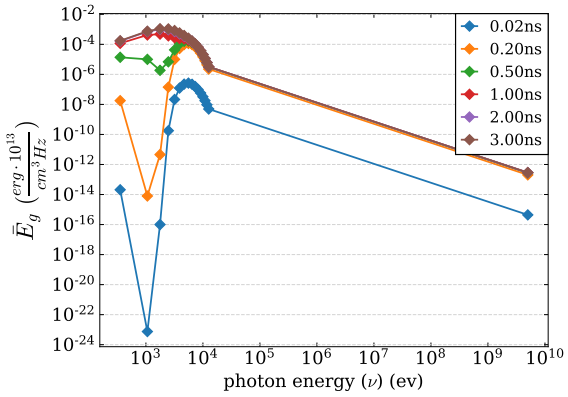

(a) $y = 3\text{cm}$, $x = 3\text{cm}$

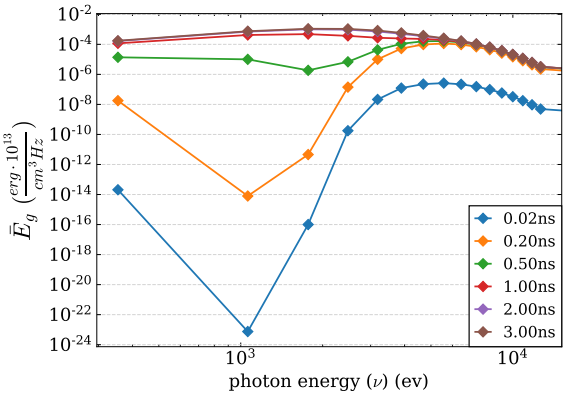

(b) $y = 3\text{cm}$, $x = 3\text{cm}$

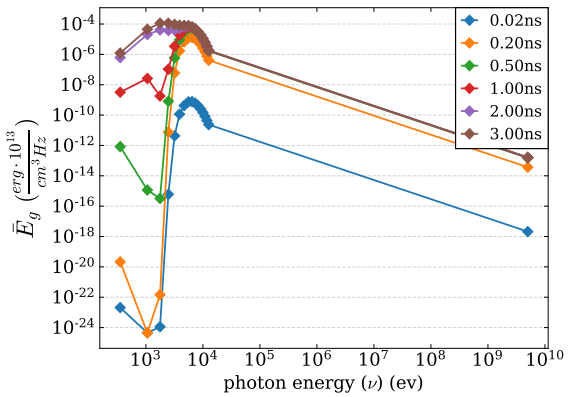

(c) $y = 3\text{cm}$, $x = 6\text{cm}$

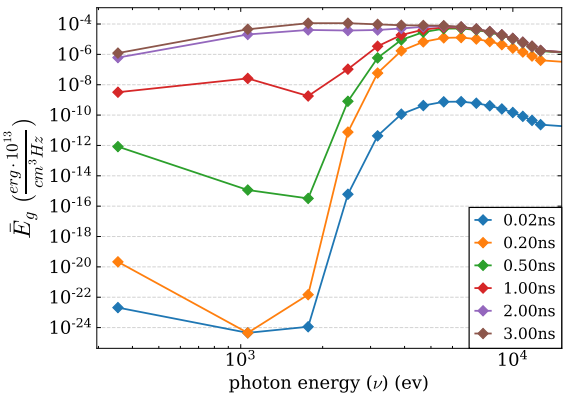

(d) $y = 3\text{cm}$, $x = 6\text{cm}$

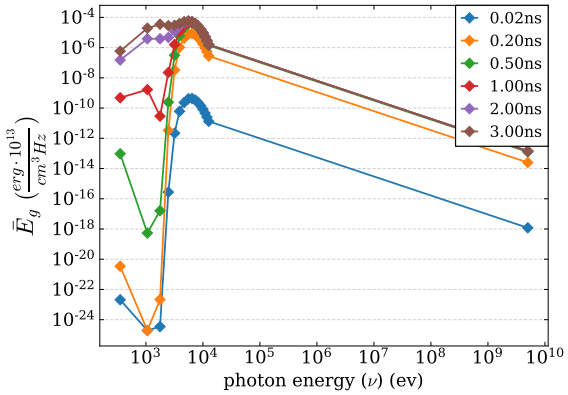

(e) $y = 0\text{cm}$, $x = 6\text{cm}$

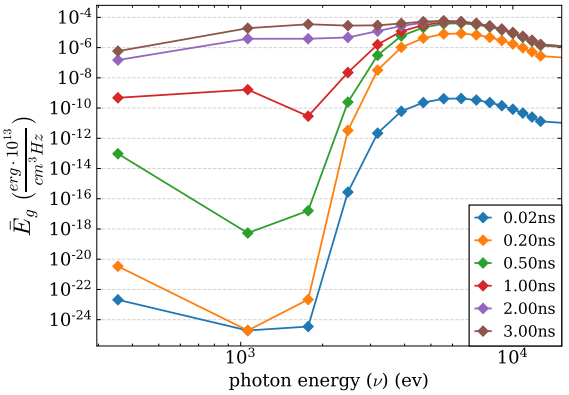

(f) $y = 0\text{cm}$, $x = 6\text{cm}$

Figure 4.17: Radiation energy density spectrum located at (i) the domain midpoint, (ii) the midpoint of the right boundary, (iii) the corner of the right boundary, taken at several time instances. The plots on the right show a zoomed in view of the spectrum peak.

make up the majority of radiation in the problem are generally found with an accuracy similar to what is seen for the total radiation energy density (E) in the 2-norm over space. Furthermore, the error associated with low-energy groups is worst in the early times of the problem where very little radiation in those energy ranges has been able to propagate across the domain (see Fig. 4.17).

The accuracy of the multigroup radiation energy densities can be related to ξ just as was done for the total radiation energy densities. Figs. 4.18 - 4.23 demonstrate that these errors decrease by roughly an order of 10^2 across all photon energies when ξ is decreased from $10^{-2} \rightarrow 10^{-4}$ for all considered time instances. A more complete picture of how these errors behave with ξ is given in Figs. 4.24, 4.25 and 4.26. These plots provide an integral view of the spectral errors in the DET ROM solutions; each depicts the relative spectral error in the 2-norm and infinity-norm across the interval $t \in [0, 6\text{ns}]$ for the three chosen points in space. Results are shown only for the DET ROM equipped with the POD and for the entire considered range of ξ. In the 2-norm sense and before the limits of finite precision become dominant, the errors at each spatial point do not exceed ξ. In the infinity norm these errors are only slightly elevated, with the largest increase being seen in the first frequency group. When the DMD is used instead of the POD, similar results are found with expected elevation of error levels for each ξ.

This concludes the primary evaluation of the DET class of ROMs without parameterization. The results shown here provide compelling evidence of the ROMs' abilities to capture full-order solutions with high accuracy. These results demonstrate that the DET ROMs converge sufficiently uniformly with ξ, such that in practice the choice of ROM can be informed with a prediction of accuracy that directly corresponds to the specified value for ξ. Parameterization of these ROMs is well justified and is provided in the following section.

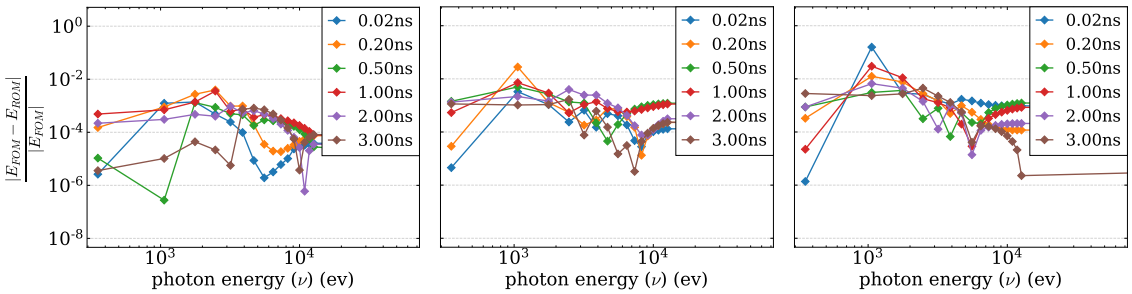

(a) $y = 3$cm, $x = 3$cm (b) $y = 3$cm, $x = 6$cm (c) $y = 0$cm, $x = 6$cm

Figure 4.18: Relative errors of the radiation spectrum produced by the DET ROM with the POD for $\xi = 10^{-2}$ located at (i) the domain midpoint, (ii) the midpoint of the right boundary, (iii) the corner of the right boundary, taken at several time instances.

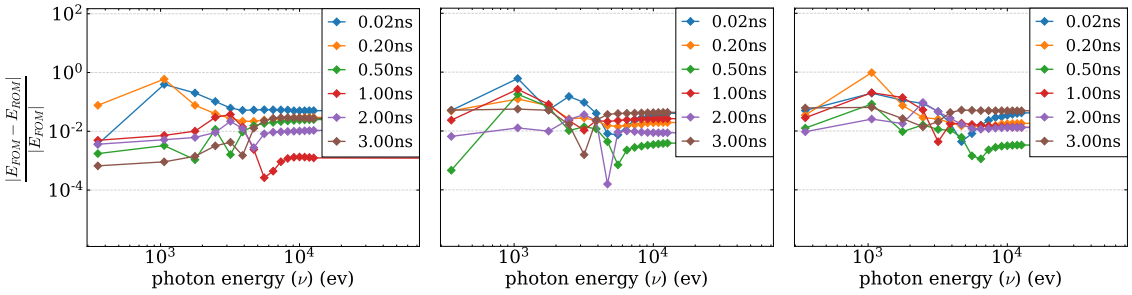

(a) $y = 3$cm, $x = 3$cm (b) $y = 3$cm, $x = 6$cm (c) $y = 0$cm, $x = 6$cm

Figure 4.19: Relative errors of the radiation spectrum produced by the DET ROM with the DMD for $\xi = 10^{-2}$ located at (i) the domain midpoint, (ii) the midpoint of the right boundary, (iii) the corner of the right boundary, taken at several time instances.

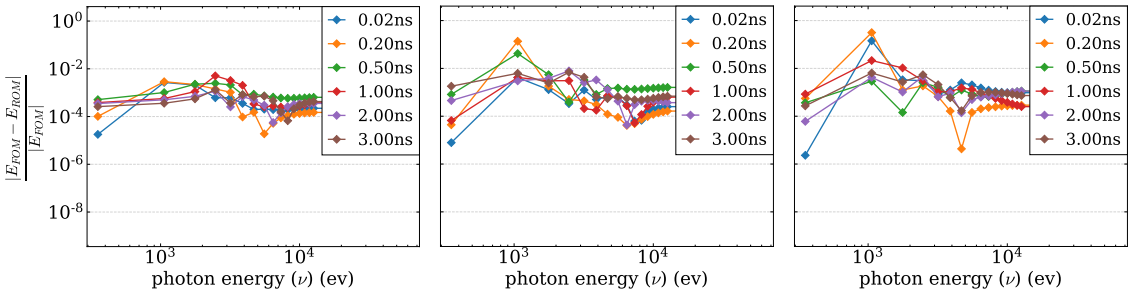

(a) $y = 3$cm, $x = 3$cm (b) $y = 3$cm, $x = 6$cm (c) $y = 0$cm, $x = 6$cm

Figure 4.20: Relative errors of the radiation spectrum produced by the DET ROM with the DMD-E for $\xi = 10^{-2}$ located at (i) the domain midpoint, (ii) the midpoint of the right boundary, (iii) the corner of the right boundary, taken at several time instances.

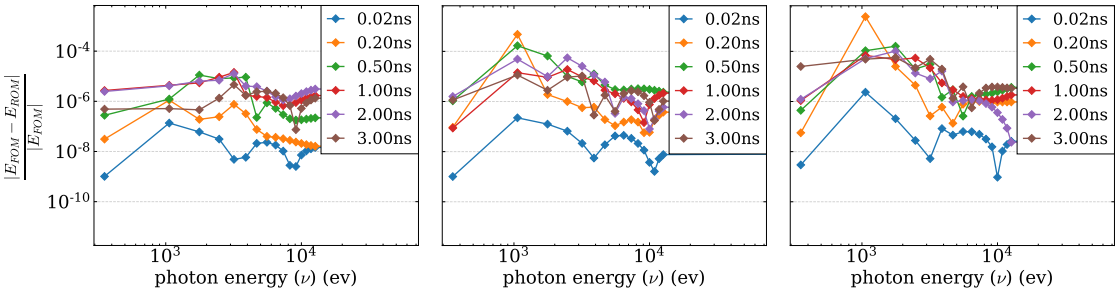

(a) $y = 3$cm, $x = 3$cm (b) $y = 3$cm, $x = 6$cm (c) $y = 0$cm, $x = 6$cm

Figure 4.21: Relative errors of the radiation spectrum produced by the DET ROM with the POD for $\xi = 10^{-4}$ located at (i) the domain midpoint, (ii) the midpoint of the right boundary, (iii) the corner of the right boundary, taken at several time instances.

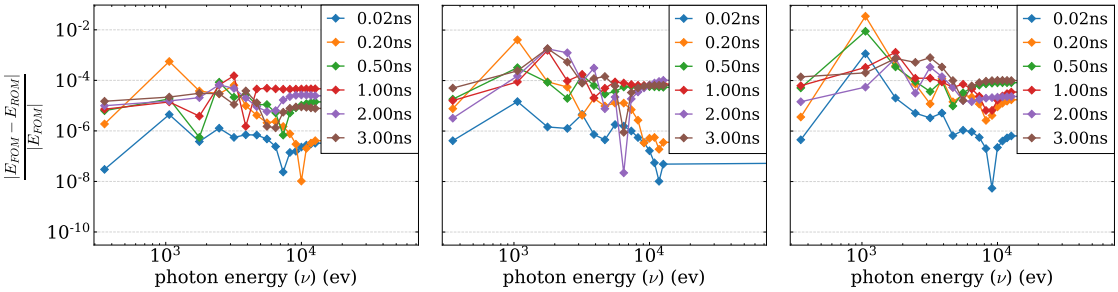

(a) $y = 3$cm, $x = 3$cm (b) $y = 3$cm, $x = 6$cm (c) $y = 0$cm, $x = 6$cm

Figure 4.22: Relative errors of the radiation spectrum produced by the DET ROM with the DMD for $\xi = 10^{-4}$ located at (i) the domain midpoint, (ii) the midpoint of the right boundary, (iii) the corner of the right boundary, taken at several time instances.

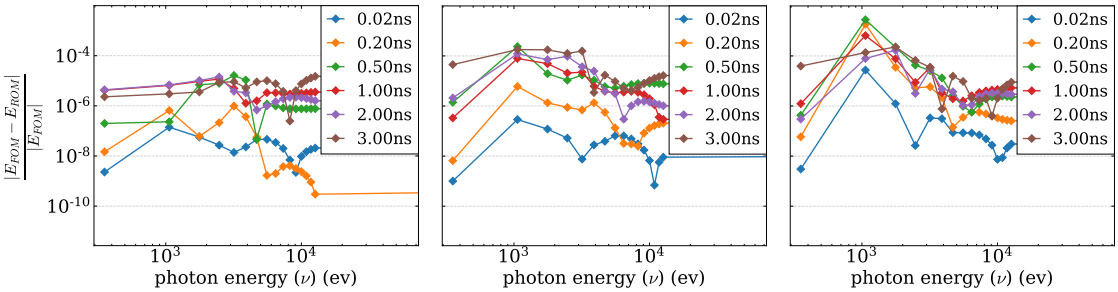

(a) $y = 3$cm, $x = 3$cm (b) $y = 3$cm, $x = 6$cm (c) $y = 0$cm, $x = 6$cm

Figure 4.23: Relative errors of the radiation spectrum produced by the DET ROM with the DMD-E for $\xi = 10^{-4}$ located at (i) the domain midpoint, (ii) the midpoint of the right boundary, (iii) the corner of the right boundary, taken at several time instances.

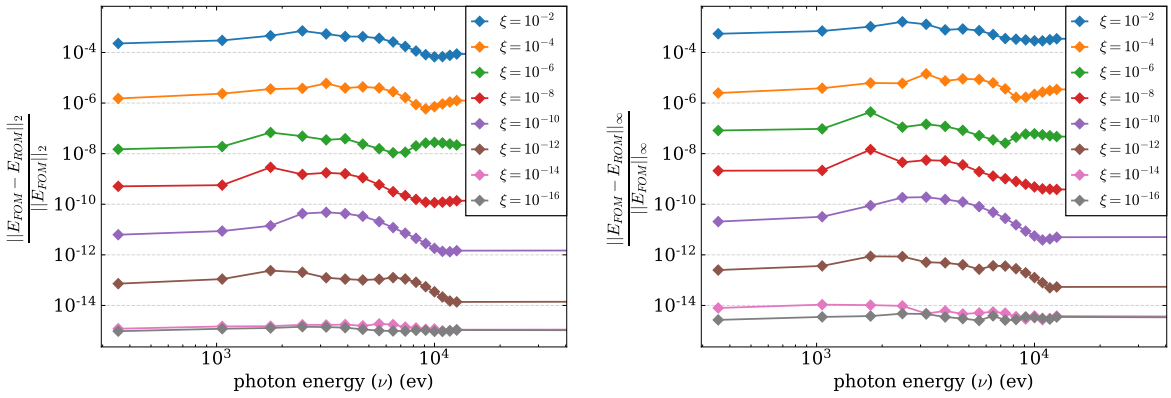

(a) 2 norm

(b) infinity norm

Figure 4.24: Relative errors of the radiation spectrum produced by the DET ROM with the POD located at the domain midpoint in the 2-norm and ∞-norm along the temporal interval $t \in [0, 6\text{ns}]$

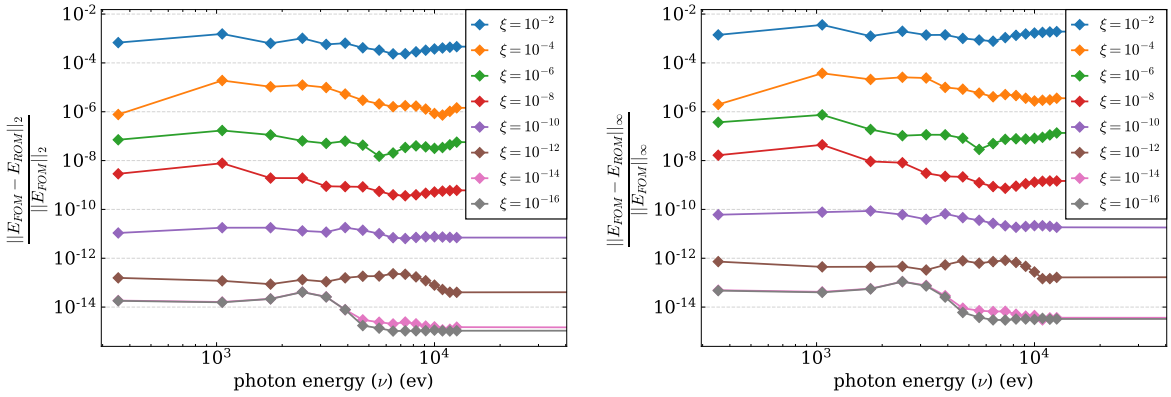

(a) 2 norm

(b) infinity norm

Figure 4.25: Relative errors of the radiation spectrum produced by the DET ROM with the POD located at the midpoint of the right boundary in the 2-norm and ∞-norm along the temporal interval $t \in [0, 6\text{ns}]$

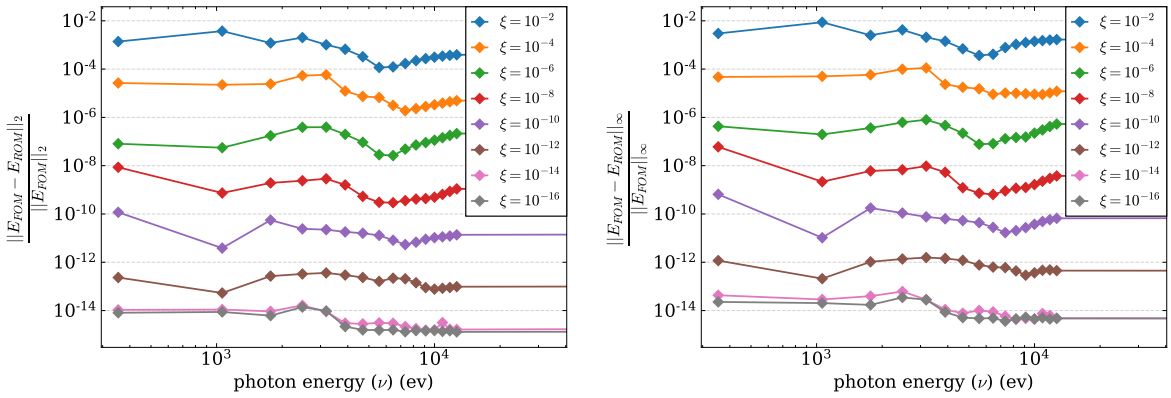

(a) 2 norm

(b) infinity norm

Figure 4.26: Relative errors of the radiation spectrum produced by the DET ROM with the POD located at the corner of the right boundary in the 2-norm and ∞-norm along the temporal interval $t \in [0, 6\text{ns}]$

4.6 Parameterization of the DET ROMs

In this section a parameterization of the DET ROMs is analyzed using the single parameter $\vartheta = T^{\text{in}}$. The space of considered parameter values is set to the interval $\mathbf{\Theta} \equiv [0.5, 1.5\text{KeV}]$. The interpolation function $\mathcal{I}(\vartheta)$ (see Eq. 4.9) is set to a natural cubic spline. Two uniformly sampled grids in $\mathbf{\Theta}$ are used to determine the points $\{T_i^{\text{in}}\}_{i=1}^{N_\vartheta}$ where the FOM is invoked to generate the necessary high-order data for the ROM offline stage. The chosen grids are displayed in Tab. 4.4, using $N_\vartheta = 5, 9$. In this way $\{T_i^{\text{in}}\}_{i=1}^{N_\vartheta=5} \subset \{T_i^{\text{in}}\}_{i=1}^{N_\vartheta=9}$ and the 9-point grid halves the distance between each T_i^{in} compared to the 5-point grid.

The interval of $T^{\text{in}} \in [0.5, 1.5\text{KeV}]$ is chosen as a difficult stress-test for the DET ROMs. This interval is a large one, covering 1 KeV of change between the possible values of the boundary temperature (or radiation drive). The F-C test's physics change considerably over this range. For instance, the spectrum of radiation formed by the left-boundary condition has its peak at $\nu = 2.82T^{\text{in}}$. Therefore the bulk of radiation that forms the wavefront propagating through the test domain varies over a 1 KeV range as well. Different portions of this range will result in distinct, separate physical characterizations of the F-C test in space-time. When $T^{\text{in}} = 1.5\text{KeV}$, the problem will be dominated by high-energy radiation in the streaming regime. In contrast, when $T^{\text{in}} = 0.5\text{KeV}$ the F-C test will be dominated by low-frequency radiation close to the diffusive regime.

i	T_i^{in} (KeV)
1	0.5
2	0.75
3	1.0
4	1.25
5	1.5

(a) 5 pts

i	T_i^{in} (KeV)
1	0.5
2	0.625
3	0.75
4	0.875
5	1.0
6	1.125
7	1.25
8	1.375
9	1.5

(b) 9 pts

Table 4.4: Uniformly sampled points for T^{in} in the range $T^{\text{in}} \in [0.5, 1.5 \text{ KeV}]$ with 5 and 9 points

It is worth noting that in the parameterized case, the only additional source of error to the DET ROM solution compared to the non-parameterized case comes from $\mathcal{I}(\vartheta)$. As such for any well-chosen interpolation function and a fine enough grid in ϑ, the DET ROM's behavior will be the same as shown in Sec. 4.4. In practice coarse parameter grids are desirable, and it is most important to identify $\mathcal{I}(\vartheta)$ that can introduce errors on the level less than observed for the non-parameterized DET ROMs with low rank ($\xi = 10^{-2}, 10^{-4}$). In this way the parameterized DET ROM can produce solutions for unsampled parameter values with similar levels of error as for the non-parameterized case with low rank. Two different natural cubic spline interpolation functions are investigated here: $\mathcal{I}(T^{\text{in}})$ and $\mathcal{I}((T^{\text{in}})^{-3})$. The first interpolation function is considered as a simple baseline one. The latter is selected based on a dimensionless analysis of the grey TRT problem using the F-C opacity function, which is detailed in Appendix E. The results of this analysis demonstrate proportionality of the grey F-C opacity to the inverse cube of temperature. These results also show that the grey F-C TRT solution scales with the inverse cube of the characteristic temperature for a given problem, which we define as T^{in}

The parameterized DET ROMs using the grids shown in Tab. 4.4 to create the full-order databases (in the offline stage) are evaluated (with the online stage) at the points shown in Tab. 4.5. Each test point is chosen to be equidistant from its closest two points on the respective sampling grid. This will effectively evaluate the DET ROMs along the entire considered range of T^{in} at the parameter values that should be the hardest to simulate given the uniformly sampled grids. In the following analysis, only the POD is

i	T_i^{in} (KeV)
1	0.625
2	0.875
3	1.125
4	1.375

(a) 5 pt grid

i	T_i^{in} (KeV)
1	0.5625
2	0.6875
3	0.8125
4	0.9375
5	1.0625
6	1.1875
7	1.3125
8	1.4375

(b) 9 pt grid

Table 4.5: Test points for T^{in} to evaluate the paramterized DET ROMs using FOM sample points on the grids in Tab. 4.4 in the range $T^{\text{in}} \in [0.5, 1.5 \text{ KeV}]$ with 5 and 9 points

considered to project the full-order databases and only with values $\xi = 10^{-2}, 10^{-4}$. The POD has proven to be the best performing method of data compression to be used with the DET ROMs, and low-rank ROMs are the most important in parametric applications.

Figs. 4.27 and 4.28 plot the relative errors in the material temperature and total radiation energy density in the 2-norm over space produced by the parameterized DET ROM using the 5-point grid in T^{in} and $\xi = 10^{-2}$. Errors are plotted vs. time. Fig. 4.27 shows results for the model using $\mathcal{I}(T^{\text{in}})$ and Fig. 4.27 shows results for the model using $\mathcal{I}((T^{\text{in}})^{-3})$. Each curve corresponds to the ROM solution at one of the test points defined in Tab. 4.5 for the 5-point grid. All errors are calculated with respect to the FOM solution evaluated at the same value for T^{in} as the ROM (i.e. at each test point). Here the ROM using $\mathcal{I}((T^{\text{in}})^{-3})$ has higher accuracy than the ROM using $\mathcal{I}(T^{\text{in}})$ for each considered boundary temperature over the entire time range. With $\mathcal{I}(T^{\text{in}})$, the ROM errors increase as T^{in} decreases. A similar effect is seen for the ROM using $\mathcal{I}((T^{\text{in}})^{-3})$, although all test values for T^{in} are captured with errors less than 10^{-3} except for when $T^{\text{in}} = 0.625$ KeV, where the errors are bounded by 10^{-2}. Figs. 4.29 and 4.30 plot the same data as the previous figures, but for the ROMs using $\xi = 10^{-4}$. The results are largely the same for this case as was seen for $\xi = 10^{-2}$, only with less oscillatory behavior.

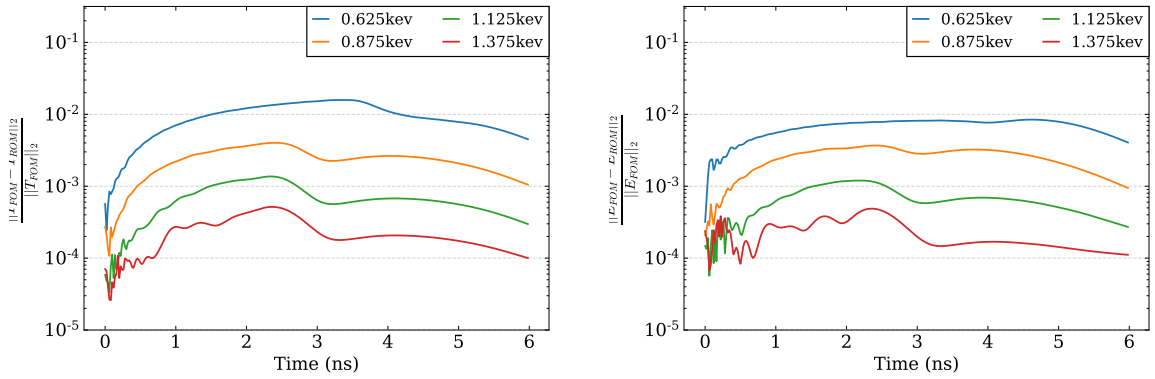

(a) Material Temperature (b) Radiation Energy Density

Figure 4.27: Relative errors in the 2-norm of the DET ROM with the POD and $\xi = 10^{-2}$, evaluated at the T^{in} values in Tab. 4.5 with the interpolation function $\mathcal{I}(T^{\text{in}})$ defined for the values shown in Tab. 4.4 for $N_\vartheta = 5$. Errors are plotted vs. time

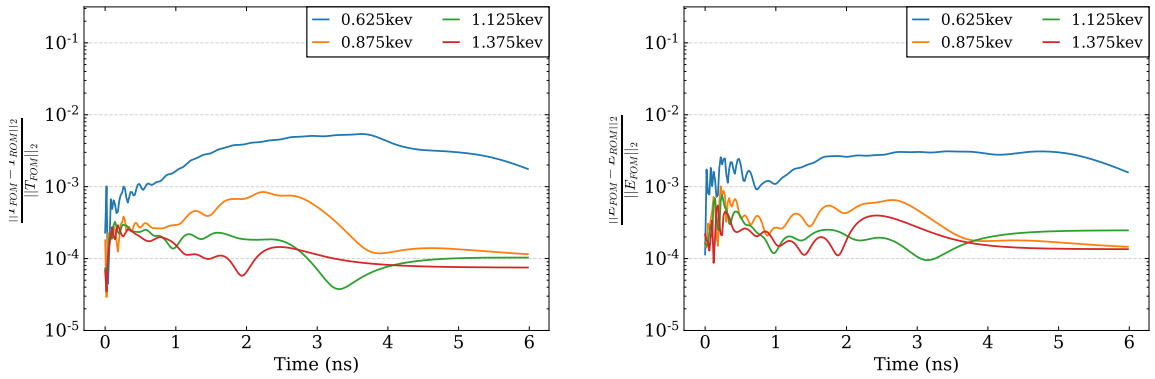

(a) Material Temperature (b) Radiation Energy Density

Figure 4.28: Relative errors in the 2-norm of the DET ROM with the POD and $\xi = 10^{-2}$, evaluated at the T^{in} values in Tab. 4.5 with the interpolation function $\mathcal{I}((T^{\text{in}})^{-3})$ defined for the values shown in Tab. 4.4 for $N_\vartheta = 5$. Errors are plotted vs. time

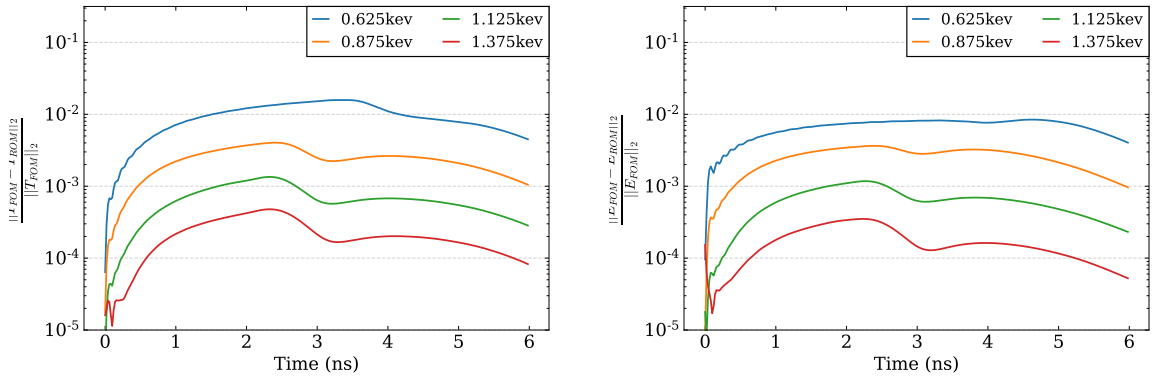

(a) Material Temperature (b) Radiation Energy Density

Figure 4.29: Relative errors in the 2-norm of the DET ROM with the POD and $\xi = 10^{-4}$, evaluated at the T^{in} values in Tab. 4.5 with the interpolation function $\mathcal{I}(T^{\text{in}})$ defined for the values shown in Tab. 4.4 for $N_\vartheta = 5$. Errors are plotted vs. time

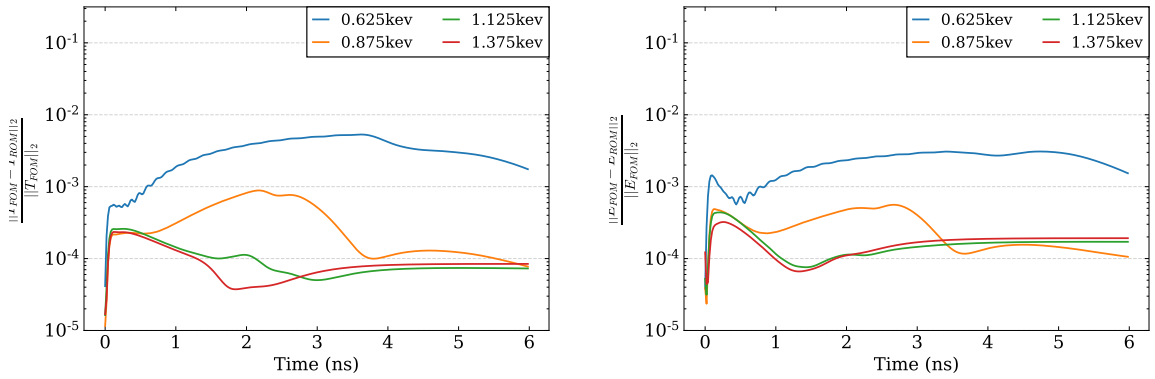

(a) Material Temperature (b) Radiation Energy Density

Figure 4.30: Relative errors in the 2-norm of the DET ROM with the POD and $\xi = 10^{-4}$, evaluated at the T^{in} values in Tab. 4.5 with the interpolation function $\mathcal{I}((T^{\text{in}})^{-3})$ defined for the values shown in Tab. 4.4 for $N_\vartheta = 5$. Errors are plotted vs. time

Figs. 4.31 and 4.32 plot the relative errors in the material temperature and total radiation energy density in the 2-norm over space produced by the parameterized DET ROM using the 9-point grid in T^{in} and $\xi = 10^{-2}$. Fig. 4.31 shows results for the model using $\mathcal{I}(T^{\text{in}})$ and Fig. 4.32 shows results for the model using $\mathcal{I}((T^{\text{in}})^{-3})$. Each curve corresponds to the ROM solution at one of the test points defined in Tab. 4.5 for the 9-point grid. All errors are calculated with respect to the FOM solution evaluated at the same value for T^{in} as the ROM (i.e. at each test point). For values of $T^{\text{in}} > 1$ KeV, all errors can be considered the same as for the non-parameterized case using $\xi = 10^{-2}$ with the POD (see Fig. 4.4). The values of $T^{\text{in}} < 1$ KeV are more difficult to capture, and as seen for the 5-point grid the ROM errors increase as T^{in} decreases. However, using $\mathcal{I}((T^{\text{in}})^{-3})$ yields lower error levels than $\mathcal{I}(T^{\text{in}})$ for all tested $T^{\text{in}} < 1$ KeV except for $T^{\text{in}} = 0.5625$ KeV where both models find similar accuracy.

Next Figs. 4.33 and 4.34 plot the same error data as shown in the previous two plots for the 9-point grid, but using $\xi = 10^{-4}$ instead of $\xi = 10^{-2}$. Once again the former plot uses $\mathcal{I}(T^{\text{in}})$ while the latter uses $\mathcal{I}((T^{\text{in}})^{-3})$. Here the lowest errors are on the order of 10^{-5}, found for large T^{in}. Smaller values of T^{in} are still only accurate to order $10^{-3} - 10^{-2}$. With the exception of the smallest tested T^{in} ($T^{\text{in}} = 0.5625$ KeV), the model using $\mathcal{I}((T^{\text{in}})^{-3})$ performs better than the model with $\mathcal{I}(T^{\text{in}})$ in every other case. The ROM with $\mathcal{I}((T^{\text{in}})^{-3})$ is able to reproduce the FOM solution for the F-C test for all considered $T^{\text{in}} > 1$ KeV with errors levels less than 10^{-4}.

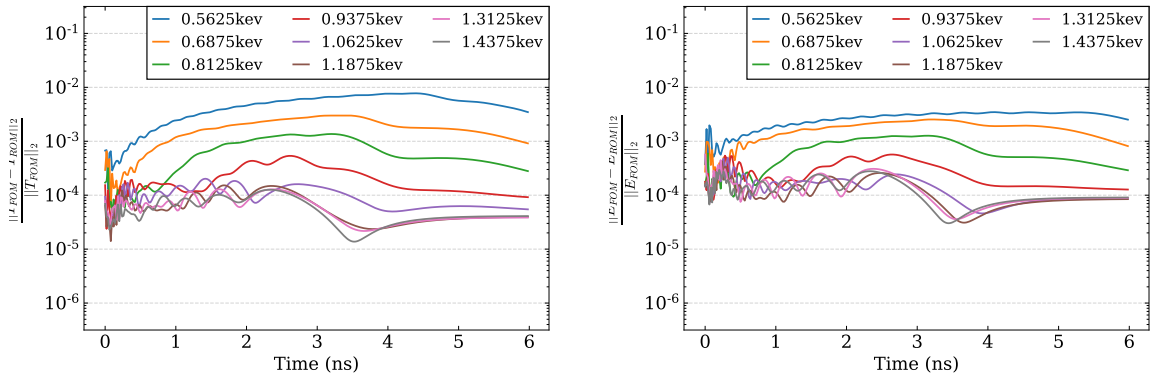

(a) Material Temperature (b) Radiation Energy Density

Figure 4.31: Relative errors in the 2-norm of the DET ROM with the POD and $\xi = 10^{-2}$, evaluated at the T^{in} values in Tab. 4.5 with the interpolation function $\mathcal{I}(T^{\text{in}})$ defined for the values shown in Tab. 4.4 for $N_\vartheta = 9$. Errors are plotted vs. time

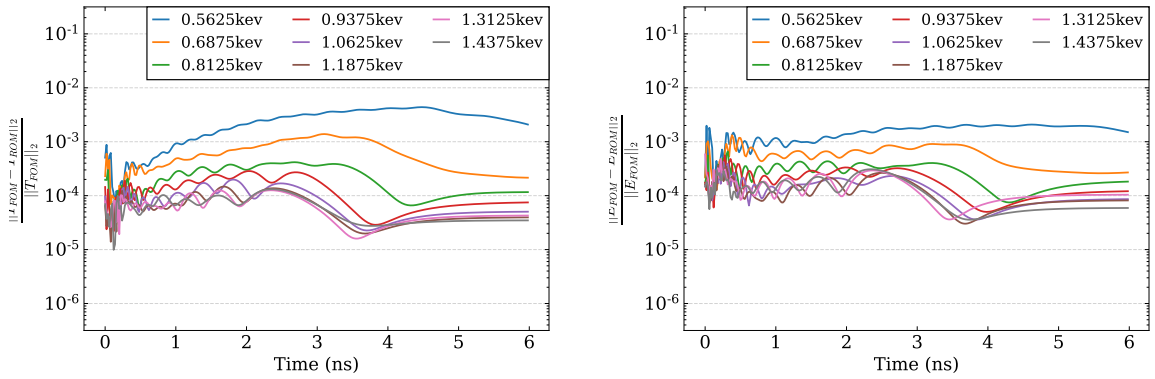

(a) Material Temperature (b) Radiation Energy Density

Figure 4.32: Relative errors in the 2-norm of the DET ROM with the POD and $\xi = 10^{-2}$, evaluated at the T^{in} values in Tab. 4.5 with the interpolation function $\mathcal{I}((T^{\text{in}})^{-3})$ defined for the values shown in Tab. 4.4 for $N_\vartheta = 9$. Errors are plotted vs. time

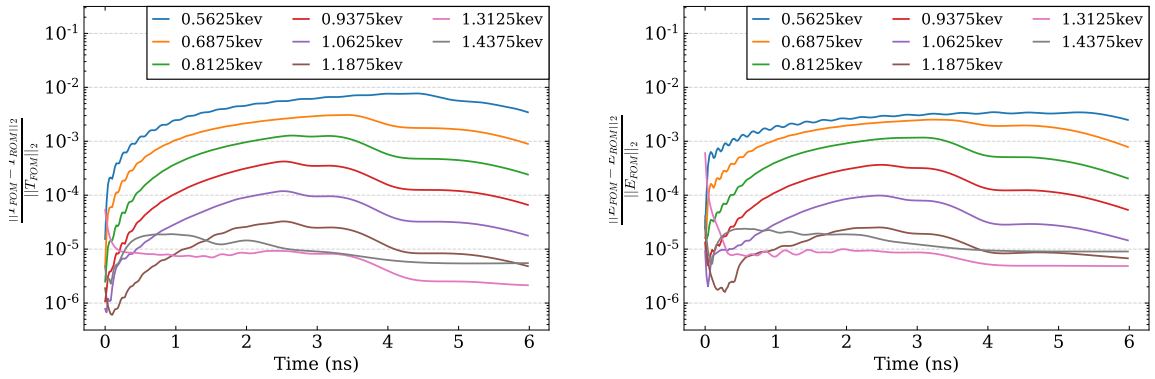

(a) Material Temperature (b) Radiation Energy Density

Figure 4.33: Relative errors in the 2-norm of the DET ROM with the POD and $\xi = 10^{-4}$, evaluated at the T^{in} values in Tab. 4.5 with the interpolation function $\mathcal{I}(T^{\text{in}})$ defined for the values shown in Tab. 4.4 for $N_\vartheta = 9$. Errors are plotted vs. time

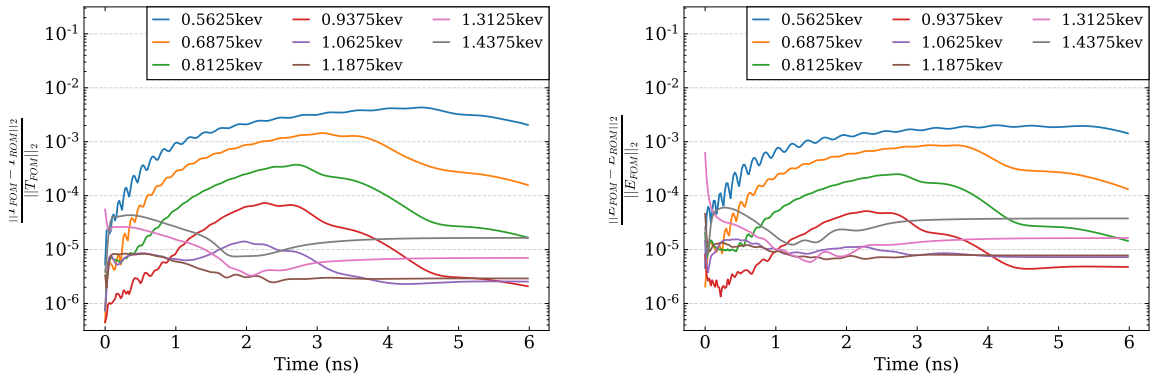

(a) Material Temperature (b) Radiation Energy Density

Figure 4.34: Relative errors in the 2-norm of the DET ROM with the POD and $\xi = 10^{-4}$, evaluated at the T^{in} values in Tab. 4.5 with the interpolation function $\mathcal{I}((T^{\text{in}})^{-3})$ defined for the values shown in Tab. 4.4 for $N_\vartheta = 9$. Errors are plotted vs. time

4.6.1 Sampling Data in the Inverse Cube of Temperature

The results so far demonstrate that interpolating over the parameter T^{in} using a function of $(T^{\text{in}})^{-3}$ performs well for parameterization, and better than using a function of T^{in}. However, the parameterized ROM's accuracy is seen to decrease by 2-3 orders of magnitude when T^{in} decreases from 1.5 KeV towards 0.5 KeV. This effect could be attributed to the use of a uniformly sampled grid in T^{in} to define the interpolation function $\mathcal{I}$, instead of one uniformly sampled in $(T^{\text{in}})^{-3}$. Tab. 4.6 provides the grid points for $\{T_i^{\text{in}}\}_{i=1}^{N_\vartheta}$ using $N_\vartheta = 5, 9$ found by uniformly sampling $(T^{\text{in}})^{-3}$ in the interval $T^{\text{in}} \in [0.5, 1.5 \text{ KeV}]$. Note that these grid points are much more clustered in the low-temperature range of the interval than those shown in Tab. 4.4.

i	T_i^{in} (KeV)
1	0.5
2	0.54807497
3	0.6223699
4	0.76630943
5	1.5

(a) 5 pts

i	T_i^{in} (KeV)
1	0.5
2	0.52183923
3	0.54807497
4	0.58053476
5	0.6223699
6	0.67965488
7	0.76630943
8	0.92303688
9	1.5

(b) 9 pts

Table 4.6: Uniformly sampled points along $(T^{\text{in}})^{-3}$ in the range $T^{\text{in}} \in [0.5, 1.5 \text{ KeV}]$ with 5 and 9 points

The offline phase of the DET ROM can now consist of finding FOM solutions to the F-C test at T^{in} values shown in Tab. 4.6. Then the DET ROMs can be evaluated at test points in the considered interval. Tab. 4.7 gives the set of T^{in} values that are equidistant (in the inverse cubic sense) from each point in the 5- and 9-point grids in Tab. 4.6. One possible issue with this set of test points is that with a single exception, only the first half of the considered parameter space is tested. In the following analysis, the parameterized DET ROM interpolating with $\mathcal{I}((T^{\text{in}})^{-3})$ defined on the grids in Tab. 4.6 will be tested on the values for T^{in} defined both in Tabs. 4.7 and 4.5. In this way, the entire interval can be more sufficiently investigated and models with grids sampled over both T^{in} and

$(T^{\text{in}})^{-3}$ can be compared at the same test points.

i	T_i^{in} (KeV)
1	0.52183923
2	0.58053476
3	0.67965488
4	0.92303688

(a) 5 pt grid

i	T_i^{in} (KeV)
1	0.51045317
2	0.53431434
3	0.56337245
4	0.6
5	0.64849932
6	0.71781683
7	0.83129526
8	1.08738037

(b) 9 pt grid

Table 4.7: Test points for T^{in} to evaluate the parameterized DET ROMs using FOM sample points on the grids in Tab. 4.6 in the range $T^{\text{in}} \in [0.5, 1.5 \text{ KeV}]$ with 5 and 9 points

Figs. 4.35 and 4.36 plot the relative errors in the material temperature and total radiation energy density in the 2-norm over space produced by the parameterized DET ROM using the 5-point grid in $(T^{\text{in}})^{-3}$ and $\xi = 10^{-2}$. Errors are plotted vs. time. Both figures display results using the interpolation function $\mathcal{I}((T^{\text{in}})^{-3})$ defined by the points in Tab. 4.6. Fig. 4.35 shows results for the model evaluated at the test points in Tab. 4.5 and Fig. 4.36 shows results for the model evaluated at the test points in Tab. 4.7. Each curve corresponds to the ROM solution at one of the respective test points, and errors are calculated with respect to the FOM solution evaluated at the same value for T^{in} as the ROM (i.e. at each test point). This same set of error plots for these models using $\xi = 10^{-4}$ instead of $\xi = 10^{-2}$ is depicted in Figs. 4.37 and 4.38. For both values of ξ the error plots are mostly the same, save for some extra small oscillations when $\xi = 10^{-2}$. The only significant difference is the error at the point $T^{\text{in}} = 0.625$ KeV decreases when $\xi = 10^{-4}$ compared to $\xi = 10^{-2}$. $T^{\text{in}} = 0.625$ KeV also has the best accuracy while $\xi = 10^{-2}$ for all test values. This is in part due to how close $T^{\text{in}} = 0.625$ KeV is to one of the grid points used to define $\mathcal{I}((T^{\text{in}})^{-3})$ when $N_\vartheta = 5$ (ref. Tab. 4.6). At the other test points defined in Tab. 4.5, this model shows lower accuracy than for the one whose interpolation function is defined by uniform points in T^{in} (ref. Figs. 4.28 & 4.30). Considering the test points found for the $(T^{\text{in}})^{-3}$ grid, the errors in time are similar for all test T^{in}. Importantly,

errors are not seen to increase as T^{in} decreases.

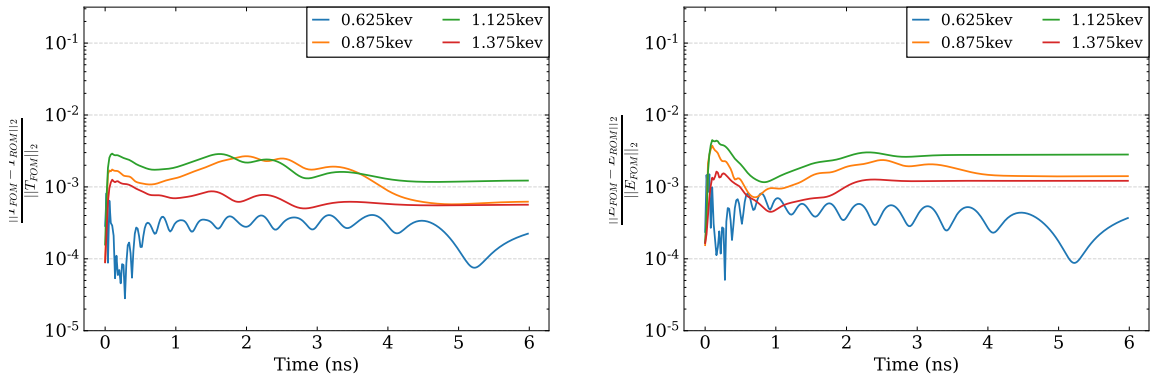

(a) Material Temperature (b) Radiation Energy Density

Figure 4.35: Relative errors in the 2-norm of the DET ROM with the POD and $\xi = 10^{-2}$, evaluated at the T^{in} values in Tab. 4.5 with the interpolation function $\mathcal{I}((T^{\text{in}})^{-3})$ defined for the values shown in Tab. 4.6 for $N_\vartheta = 5$. Errors are plotted vs. time

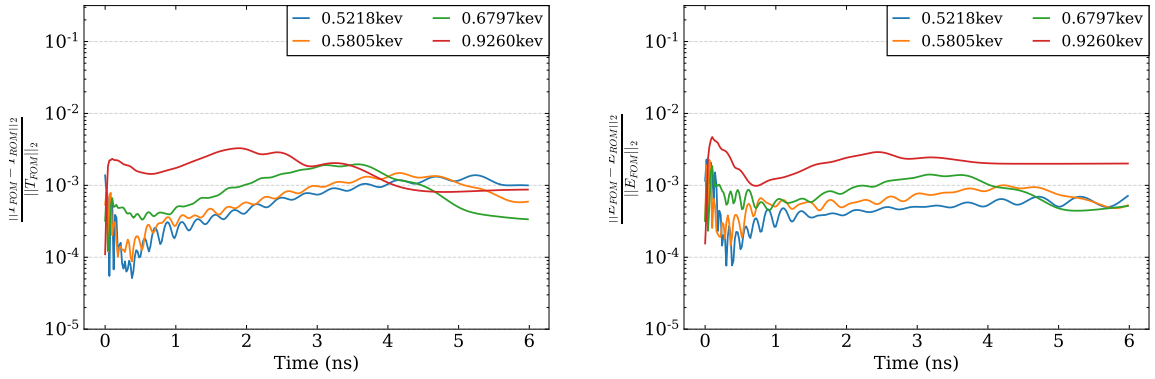

(a) Material Temperature (b) Radiation Energy Density

Figure 4.36: Relative errors in the 2-norm of the DET ROM with the POD and $\xi = 10^{-2}$, evaluated at the T^{in} values in Tab. 4.7 with the interpolation function $\mathcal{I}((T^{\text{in}})^{-3})$ defined for the values shown in Tab. 4.6 for $N_\vartheta = 5$. Errors are plotted vs. time

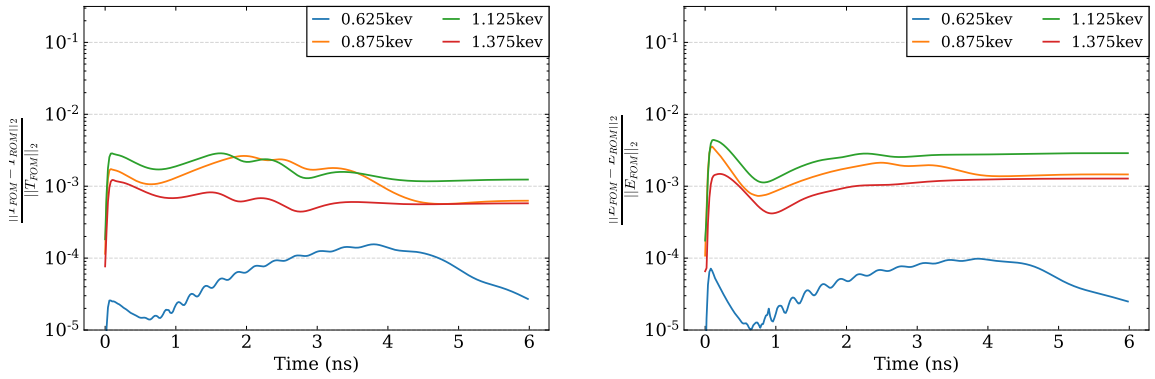

(a) Material Temperature (b) Radiation Energy Density

Figure 4.37: Relative errors in the 2-norm of the DET ROM with the POD and $\xi = 10^{-4}$, evaluated at the T^{in} values in Tab. 4.5 with the interpolation function $\mathcal{I}((T^{\text{in}})^{-3})$ defined for the values shown in Tab. 4.6 for $N_\vartheta = 5$. Errors are plotted vs. time

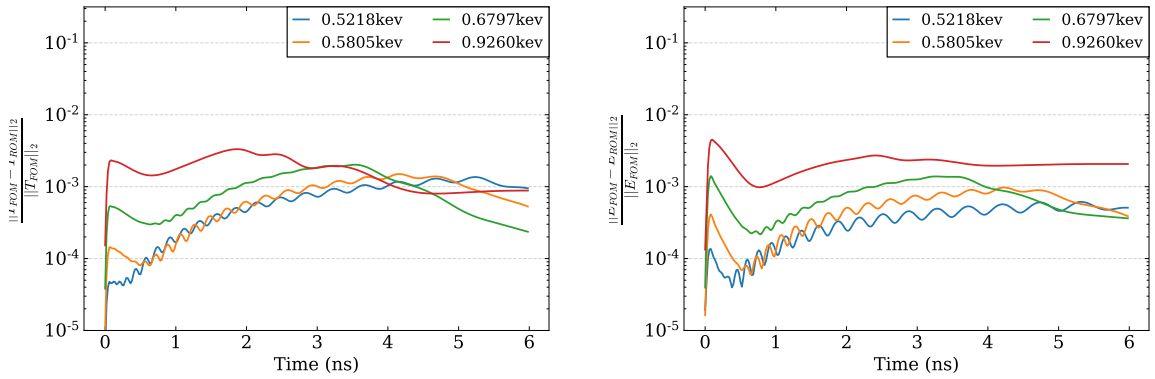

(a) Material Temperature (b) Radiation Energy Density

Figure 4.38: Relative errors in the 2-norm of the DET ROM with the POD and $\xi = 10^{-4}$, evaluated at the T^{in} values in Tab. 4.7 with the interpolation function $\mathcal{I}((T^{\text{in}})^{-3})$ defined for the values shown in Tab. 4.6 for $N_\vartheta = 5$. Errors are plotted vs. time

Figs. 4.39 and 4.40 plot the relative errors in the material temperature and total radiation energy density in the 2-norm over space produced by the parameterized DET ROM using the 9-point grid in $(T^{\text{in}})^{-3}$ and $\xi = 10^{-2}$. Both figures display results using the interpolation function $\mathcal{I}((T^{\text{in}})^{-3})$ defined by the points in Tab. 4.6. Figure 4.39 shows results for the model evaluated at the test points in Tab. 4.5 and Fig. 4.40 shows results for the model evaluated at the test points in Tab. 4.7. Each curve corresponds to the ROM solution at one of the respective test points, and errors are calculated with respect to the FOM solution evaluated at the same value for T^{in} as the ROM. This same set of error plots for these models using $\xi = 10^{-4}$ instead of $\xi = 10^{-2}$ is depicted in Figs. 4.41 and 4.42.

When $\xi = 10^{-2}$, the errors for all tested $T^{\text{in}} < 1$ Kev are on the order of 10^{-4}. As T^{in} progress beyond 1 KeV, there is some slight elevation in the error levels. Notably, the errors for $T^{\text{in}} < 1$ Kev are on the expected level for the non-parameterized DET ROMs with the POD using $\xi = 10^{-2}$ (see Fig. 4.4). This is an improvement from the models that sampled FOM solutions uniformly in T^{in} (ref. Fig. 4.32). When ξ is decreased to $\xi = 10^{-4}$, error levels decrease for $T^{\text{in}} < 1$ Kev while staying essentially the same for $T^{\text{in}} > 1$ Kev. This is the opposite behavior as observed for the models defined in the previous section. While test points for $T^{\text{in}} < 1$ Kev are found with accuracy on the order of 10^{-4} at most, those for higher temperatures remain elevated on order 10^{-3}.

Clearly the accurate reproduction of the F-C test solution for $T^{\text{in}} < 1$ Kev benefits from sampling along the inverse cube of T^{in}. This makes sense given that interpolating over $(T^{\text{in}})^{-3}$ yields better accuracy than for interpolation over T^{in}. This is not the case however, for $T^{\text{in}} > 1$ Kev when the problem becomes more heavily driven by high-frequency radiation with very low optical thickness. One possible reason could be that the sampled points in Tab. 4.7 do not sufficiently cover this area in the parameter space. One appealing idea would be to sample $T^{\text{in}} < 1$ Kev by a inverse cubic relationship, and sample $T^{\text{in}} > 1$ Kev linearly with T^{in}.

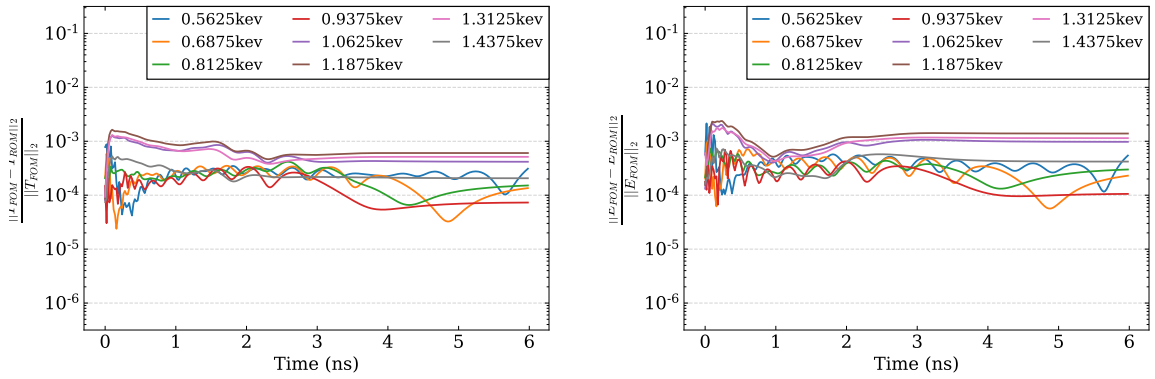

(a) Material Temperature (b) Radiation Energy Density

Figure 4.39: Relative errors in the 2-norm of the DET ROM with the POD and $\xi = 10^{-2}$, evaluated at the T^{in} values in Tab. 4.5 with the interpolation function $\mathcal{I}((T^{\text{in}})^{-3})$ defined for the values shown in Tab. 4.6 for $N_\vartheta = 9$. Errors are plotted vs. time

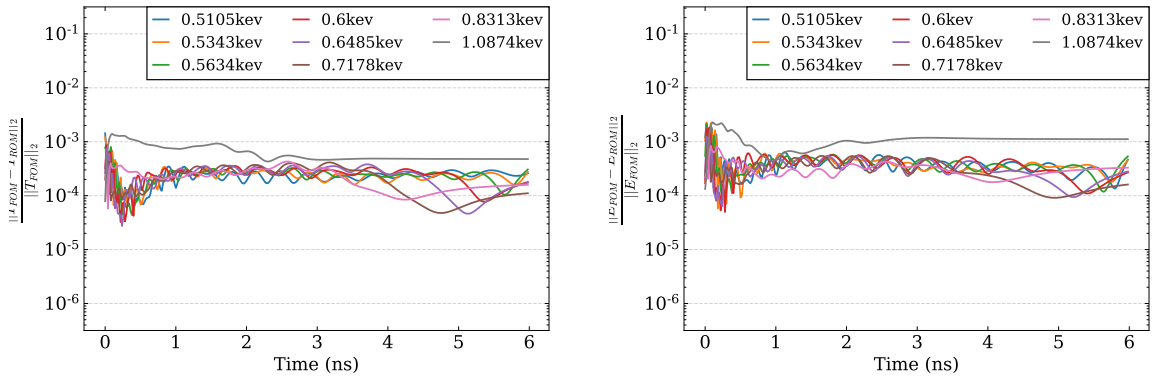

(a) Material Temperature (b) Radiation Energy Density

Figure 4.40: Relative errors in the 2-norm of the DET ROM with the POD and $\xi = 10^{-2}$, evaluated at the T^{in} values in Tab. 4.7 with the interpolation function $\mathcal{I}((T^{\text{in}})^{-3})$ defined for the values shown in Tab. 4.6 for $N_\vartheta = 9$. Errors are plotted vs. time

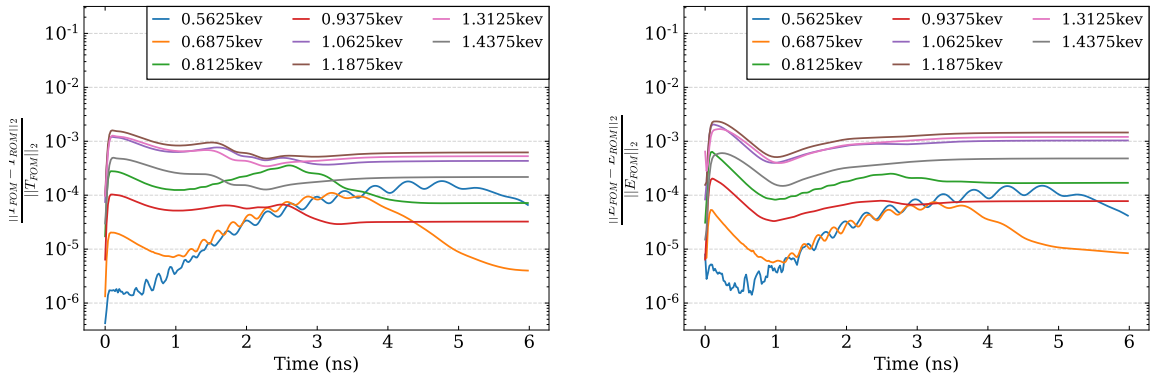

(a) Material Temperature (b) Radiation Energy Density

Figure 4.41: Relative errors in the 2-norm of the DET ROM with the POD and $\xi = 10^{-4}$, evaluated at the T^{in} values in Tab. 4.5 with the interpolation function $\mathcal{I}((T^{\text{in}})^{-3})$ defined for the values shown in Tab. 4.6 for $N_\vartheta = 9$. Errors are plotted vs. time

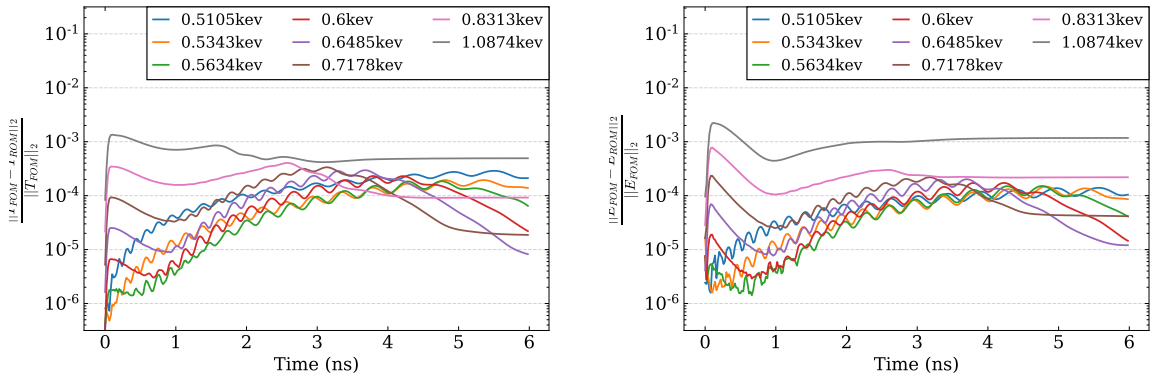

(a) Material Temperature (b) Radiation Energy Density

Figure 4.42: Relative errors in the 2-norm of the DET ROM with the POD and $\xi = 10^{-4}$, evaluated at the T^{in} values in Tab. 4.7 with the interpolation function $\mathcal{I}((T^{\text{in}})^{-3})$ defined for the values shown in Tab. 4.6 for $N_\vartheta = 9$. Errors are plotted vs. time

4.6.2 Separated Low & High Energy Sampling

In this section a sampling scheme is presented for use with the interpolation function $\mathcal{I}((T^{\text{in}})^{-3})$ that selects points independently for the two subintervals $T^{\text{in}} \in [0.5, 1.0 \text{ KeV}]$ and $T^{\text{in}} \in [1.0, 1.5 \text{ KeV}]$. The results shown previously demonstrate that sampling along the inverse cube of T^{in} gives good results for the low-energy portion of the interval, and sampling along T^{in} linearly gives better results for the high-energy portion. Furthermore, the points below $T^{\text{in}} = 1$ KeV tend to require a finer sampling grid than the points above $T^{\text{in}} = 1$ KeV to achieve similar levels of accuracy (with their respective well-performing sampling schemes).

A sampling scheme that can provide uniform accuracy for the parameterized DET ROMs across the whole interval $T^{\text{in}} \in [0.5, 1.5 \text{ KeV}]$ should then handle both half-intervals differently. The scheme presented here utilizes uniform sampling over $T^{\text{in}} \in [0.5, 1.0 \text{ KeV}]$ in the inverse cubic sense, and uniform sampling over $T^{\text{in}} \in [1.0, 1.5 \text{ KeV}]$ in the linear sense. Furthermore, since the high-energy subinterval can have a coarser sampled grid, for N sampled points between $T^{\text{in}} \in [1.0, 1.5 \text{ KeV}]$ there are defined $2N - 1$ sampled points between $T^{\text{in}} \in [0.5, 1.0 \text{ KeV}]$. Every grid will share the three points $T^{\text{in}} = 0.5,\ 1,\ 1.5$ KeV.

Tab. 4.8 presents the sampled points in T^{in} for this scheme with 2 levels of refinement. A grid with $N_\vartheta = 7$ is presented, where 3 points are used to sample the high-energy subinterval and 5 points are used in the low-energy subinterval. The second grid with $N_\vartheta = 13$ uses 5 and 9 points in the high and low energy subintervals, respectively. The test points where the parameterized DET ROMs will be evaluated for error analysis are shown in Tab. 4.9. These test points are defined to be equidistant between each adjacent sampling point in the inverse cubic and linear senses for the low and high energy subintervals, respectively.

Figs. 4.43 and 4.44 plot the relative errors in the material temperature and total radiation energy density in the 2-norm over space produced by the parameterized DET ROM using $\xi = 10^{-2}$ and $\xi = 10^{-4}$ respectively at the 7-point grid test points shown in Tab. 4.9. In both cases the interpolation function $\mathcal{I}((T^{\text{in}})^{-3})$ is used, defined for the sampled points in the 7-point grid shown in Tab. 4.8. The error levels for both T and E at every tested value for T^{in} are bounded by roughly 2×10^{-3} and reside in a close interval to one another at each instant of time. The tested values for $T^{\text{in}} > 1$ KeV have greater accuracy than those values for $T^{\text{in}} < 1$ KeV in general during the interval $t \geq 1$ ns with the exception of $T^{\text{in}} = 0.811$ KeV. For $\xi = 10^{-2}$ the errors vs. time are close to

i	T_i^{in} (KeV)
1	0.5
2	0.54288352
3	0.60570686
4	0.71376586
5	1.0
6	1.25
7	1.5

(a) 7 pts

i	T_i^{in} (KeV)
1	0.5
2	0.51968284
3	0.54288352
4	0.57087432
5	0.60570686
6	0.65097453
7	0.71376586
8	0.81096027
9	1.0
10	1.125
11	1.25
12	1.375
13	1.5

(b) 13 pts

Table 4.8: Sampling grids for $T^{\text{in}} \in [0.5, 1.5 \text{ KeV}]$ with uniform sampling along $(T^{\text{in}})^{-3}$ while $T^{\text{in}} \in [0.5, 1.0 \text{ KeV}]$ and uniform sampling along T^{in} while $T^{\text{in}} \in [1.0, 1.5 \text{ KeV}]$. Sampling is done such that if N points are sampled above 1 KeV, $2N - 1$ points are sampled below 1 KeV. A 7- and 13- point grid is shown

i	T_i^{in} (KeV)
1	0.51968284
2	0.57087432
3	0.65097453
4	0.81096027
5	1.125
6	1.375

(a) 7 pt grid

i	T_i^{in} (KeV)
1	0.5094617
2	0.53077697
3	0.55617613
4	0.58726073
5	0.62671325
6	0.67949031
7	0.75620478
8	0.88606187
9	1.0625
10	1.1875
11	1.3125
12	1.4375

(b) 13 pt grid

Table 4.9: Test points for T^{in} to evaluate the parameterized DET ROMs using FOM sample points on the grids in Tab. 4.8 in the range $T^{\text{in}} \in [0.5, 1.5 \text{ KeV}]$ with 7 and 13 points. These are the 'midpoints' between each sampled T^{in} in Tab. 4.8, in the $(T^{\text{in}})^{-3}$ sense for $T^{\text{in}} \leq 1$ KeV and in the T^{in} sense for $T^{\text{in}} > 1$ KeV

those seen for the non-parameterized case (see Fig. 4.4), and when $\xi = 10^{-4}$ these error values decrease in the range $t \leq 2$ ns.

Figs. 4.45 and 4.46 plot the relative errors in the material temperature and total radiation energy density in the 2-norm over space produced by the parameterized DET ROM using $\xi = 10^{-2}$ and $\xi = 10^{-4}$ respectively at the 13-point grid test points shown in Tab. 4.9. In both cases the interpolation function $\mathcal{I}((T^{\text{in}})^{-3})$ is used, defined for the sampled points in the 13-point grid shown in Tab. 4.8. Here the error levels across time are the same as seen for the non-parameterized case for all tested T^{in} when $\xi = 10^{-2}$. All error levels decrease when $\xi = 10^{-4}$. The points when $T^{\text{in}} > 1$ KeV are observed to decrease somewhat uniformly in time with ξ, and the points for $T^{\text{in}} < 1$ KeV decrease more significantly at early times, increasing with time until roughly $t = 3$ ns where a plateau around 10^{-4} is reached.

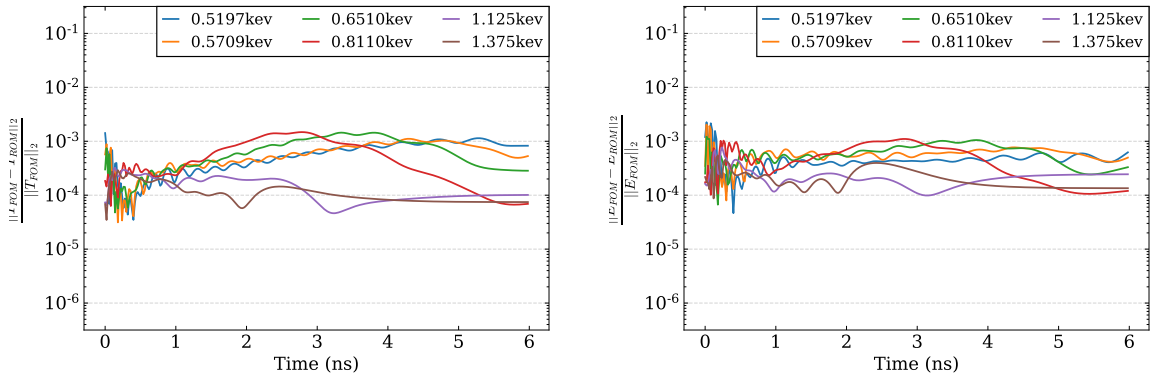

(a) Material Temperature (b) Radiation Energy Density

Figure 4.43: Relative errors in the 2-norm of the DET ROM with the POD and $\xi = 10^{-2}$, evaluated at the T^{in} values in Tab. 4.9 with the interpolation function $\mathcal{I}((T^{\text{in}})^{-3})$ defined for the values shown in Tab. 4.8 for $N_\vartheta = 7$. Errors are plotted vs. time

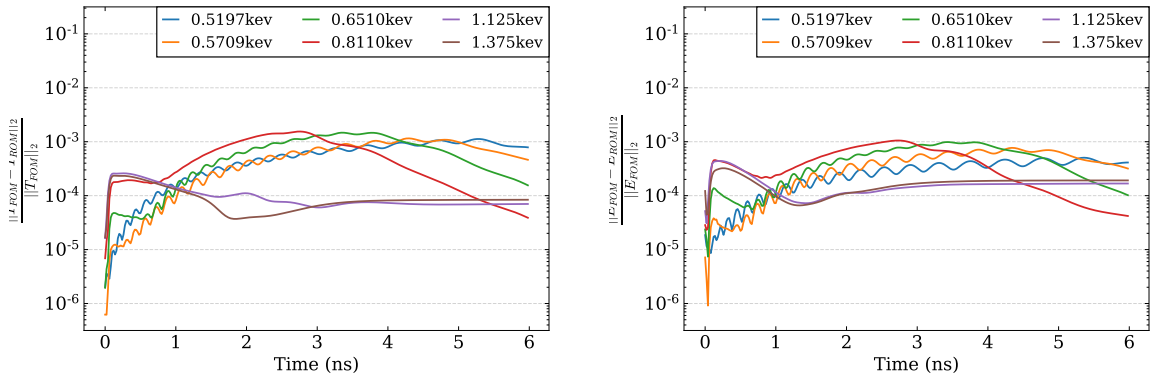

(a) Material Temperature (b) Radiation Energy Density

Figure 4.44: Relative errors in the 2-norm of the DET ROM with the POD and $\xi = 10^{-4}$, evaluated at the T^{in} values in Tab. 4.9 with the interpolation function $\mathcal{I}((T^{\text{in}})^{-3})$ defined for the values shown in Tab. 4.8 for $N_\vartheta = 7$. Errors are plotted vs. time

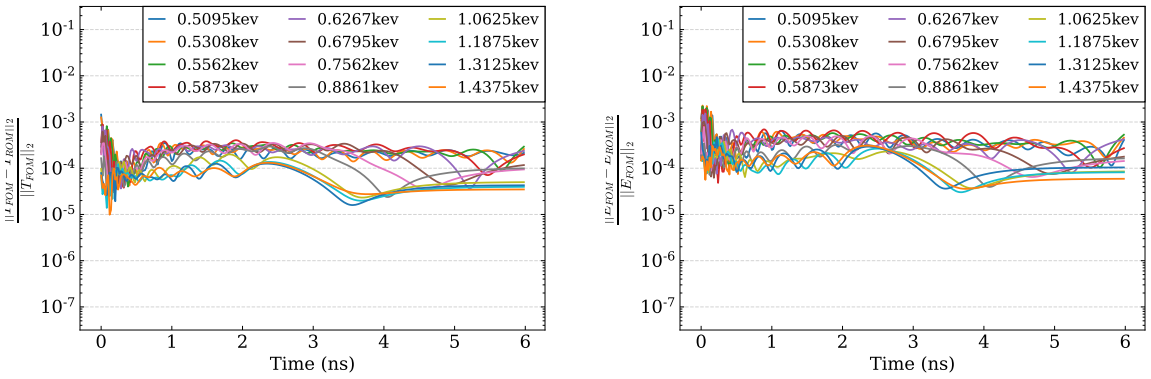

(a) Material Temperature (b) Radiation Energy Density

Figure 4.45: Relative errors in the 2-norm of the DET ROM with the POD and $\xi = 10^{-2}$, evaluated at the T^{in} values in Tab. 4.9 with the interpolation function $\mathcal{I}((T^{\text{in}})^{-3})$ defined for the values shown in Tab. 4.8 for $N_\vartheta = 13$. Errors are plotted vs. time

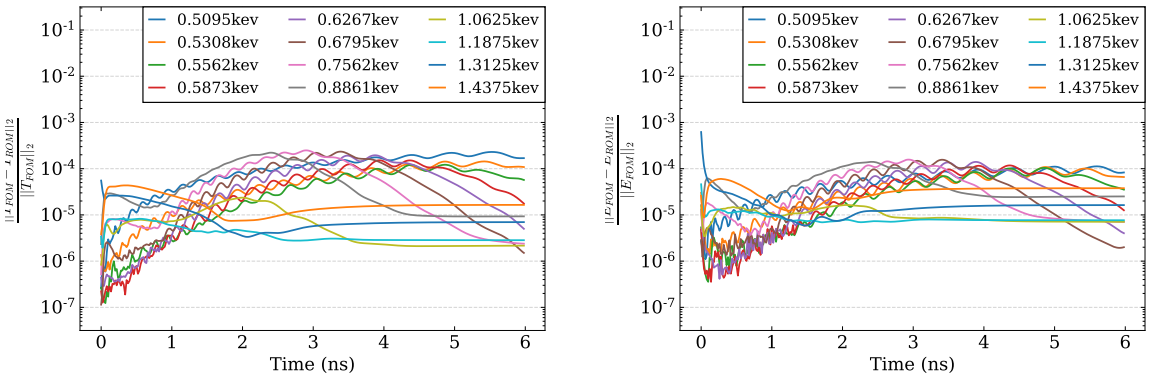

(a) Material Temperature (b) Radiation Energy Density

Figure 4.46: Relative errors in the 2-norm of the DET ROM with the POD and $\xi = 10^{-4}$, evaluated at the T^{in} values in Tab. 4.9 with the interpolation function $\mathcal{I}((T^{\text{in}})^{-3})$ defined for the values shown in Tab. 4.8 for $N_\vartheta = 13$. Errors are plotted vs. time

4.7 Discussion

In this chapter a new class of ROMs for TRT is presented derived with the nonlinear-projective methodology (see Sec. 2.1) that employs data-driven approximations for the Eddington tensor to find closures. Analysis of these ROMs was performed in the non-parameterized and parameterized cases. The ROMs were proven effective in efficiently reducing dimensionality of TRT problems and shown capable of producing solutions with a spectrum of accuracy depending on the used rank of approximation. A linear relationship was found between the ROM solution accuracy and the rank of approximation while using the POD and DMD, allowing for a-priori predictions of the ROM solution error levels based on the rank parameter ξ. ROMs at low rank were shown to produce errors that are relatively uniform across space, frequency and time. The ROMs were furthermore able to reproduce certain important qualities with high accuracy such as the radiation present at and traveling through the drive-opposite (right) boundary. Parameterization was investigated for temperature of radiation at the boundary source of the numerical tests that drives a Marshak wave. An inverse cubic parameterization in this temperature was shown to produce solutions with relatively uniform accuracy across the entire considered interval of temperatures.

The results and analysis of the DET ROMs encourage continued development, and several pathways for future research can be identified. The ROM parameterization can be extended to be multivariate, considering other parameters such as material opacities. Other data-based methods of approximating the Eddington tensor can also be explored, such as using methods of symmetry-reduction [148, 149] to improve basis generation or neural networks to provide a different type of closure approximation [61, 62].

CHAPTER

5

A ROM BASED ON ESTIMATION OF THE EDDINGTON TENSOR FROM DIFFUSION BASED SOLUTIONS

In this chapter a ROM is formulated with the ability to make use of data from diffusion-type approximate models of radiative transfer such as flux-limited diffusion (FLD). An estimation of the Eddington tensor that closes the hierarchy of LOQD moment equations is generated using a known approximate temperature distribution in space and time obtained by means of a diffusion-based TRT model. A linear multigroup Boltzmann transport equation is constructed whose opacity and emission source are evaluated at the known temperature for the whole phase space and considered interval of time. The linear BTE can be solved with a single transport sweep at each instant of time, and the following high-order solution well approximates the intensity shape function required to calculate the Eddington tensor. Numerical results are shown to demonstrate the ROM's performance, using temperature distributions from three diffusion-type models: FLD, P_1 and $P_{1/3}$.

5.1 Fundamental Approach

ROMs for TRT such as the FLD, P_1 and VEF models [14, 15, 16, 102] are well understood and widely used for many applications. They can be used as radiative transfer models in large-scale multiphysics simulations robustly and efficiently, although the accuracy of their obtained solutions is limited. Over time large databases of solutions to a wide range of problems in high-energy density physics have been amassed through these simulations. This presents an opportunity for a new ROM to leverage this available data and generate solutions with increased accuracy.

The formulation of this ROM is based on the idea to calculate an approximate radiation distribution shape function in phase space and time for a given physical system using a known temperature distribution in the domain and time interval of the problem. This shape function is defined by the normalized radiation intensities computed with a linear radiative transfer problem (performing just one transport sweep) where the opacities and emission source are specified with the known temperature distribution in space-time. This provides the shape function required in calculating the Eddington tensor which formulates closures to the low-order moment (LOQD) equations. This model is motivated by demonstrations that the high-order transport solution computed with a scattering source term evaluated by a diffusion solution yields a sufficiently accurate shape function for estimation of the Eddington tensor [150, 151].

If $\hat{T}(\boldsymbol{r},t) \approx T(\boldsymbol{r},t)$ for a TRT problem (Eqs. 1.6 & 1.10) is known for $\boldsymbol{r} \in \Gamma$ and $t \in [0, t^{\text{end}}]$, the following linear Boltzmann problem can be formulated

$$\frac{1}{c}\frac{\partial \hat{I}_g}{\partial t} + \boldsymbol{\Omega}\cdot\boldsymbol{\nabla}\hat{I}_g + \varkappa_{E,g}(\hat{T})\hat{I}_g = \varkappa_{B,g}(\hat{T})B_g(\hat{T}), \tag{5.1}$$

$$\boldsymbol{r}\in\Gamma, \quad \boldsymbol{\Omega}\in\mathcal{S}, \quad g=1,\ldots,N_g, \quad t\in[0,t^{\text{end}}],$$

$$\hat{I}_g|_{t=t_0} = I_g^0, \quad \hat{I}_g|_{\boldsymbol{r}\in\partial\Gamma} = I_g^{\text{in}} \ \text{ for } \ \boldsymbol{n}_\Gamma\cdot\boldsymbol{\Omega} < 0. \tag{5.2}$$

Eq. 5.1 can be efficiently solved with a single transport sweep per time step to find the approximate distribution of radiation intensities $\hat{I}_g$, which will give a good estimation for the transport effects of the original TRT problem assuming $\|\hat{T} - T\|$ is not too large. To obtain an ideal distribution of radiation intensities, ray tracing techniques can be used along with the method of conservative long characteristics (see Sec. 2.3.2). Once $\hat{I}_g$ has been calculated, an approximate Eddington tensor $\hat{\mathbf{f}}_g$ for the TRT problem can be found via Eq. 2.4. The MLQD system closed with $\hat{\mathbf{f}}_g$ and coupled to the MEB equation

can then be used to solve the TRT problem to find an improved update for the material temperatures ($\hat{\hat{T}}$) and radiation field ($\hat{\hat{E}}$ & $\hat{\hat{\boldsymbol{F}}}$).

Alg. 4 outlines the process of using this proposed ROM to solve TRT problems. The required input is an already known approximate material temperature distribution $\hat{T}$ for the entire spatial and temporal interval of interest. $\hat{T}$ is used to construct the linear high-order radiative transfer problem by fixing the opacity function and emission source in phase space and time. The approximate radiation intensities $\hat{I}_g$ are found for some set of frequency groups and directions of motion on the spatial-temporal domain where $\hat{T}$ is defined. The Eddington tensor $\hat{\mathbf{f}}_g$ in all defined frequency groups and the domain in space-time is calculated using $\hat{I}_g$ in Eq. 2.4. $\hat{\mathbf{f}}_g$ is used to close the multilevel system of LOQD equations coupled to the MEB equation in space-time and frequency, which is solved for an updated material temperature distribution $\hat{\hat{T}}$ and radiation field $\hat{\hat{E}}_g,\ \hat{\hat{\boldsymbol{F}}}_g$ on the spatial and temporal intervals and frequency groups where $\hat{\mathbf{f}}_g$ is defined.

Algorithm 4: Construction of an improved TRT solution using a diffusion solution to estimate the Eddington tensor that closes the LOQD moment system over the entire considered phase space and time simultaneously.

Input: $\hat{T}(\boldsymbol{r}, t)$ for $\boldsymbol{r} \in \Gamma,\ t \in [0, t^{\text{end}}]$

1. Solve the BTE with fixed opacity and source evaluated at $\hat{T}(\boldsymbol{r}, t)$ for all $\boldsymbol{r} \in \Gamma$, $t \in [0, t^{\text{end}}]$ (Eq. 5.1) to find $\hat{I}_g(\boldsymbol{r}, \boldsymbol{\Omega}, t)$ for $\boldsymbol{r} \in \Gamma,\ t \in [0, t^{\text{end}}],\ \boldsymbol{\Omega} \in \mathcal{S},\ g = 1, \ldots, N_g$
2. Project $\hat{I}_g(\boldsymbol{r}, \boldsymbol{\Omega}, t)$ to generate $\hat{\mathbf{f}}_g(\boldsymbol{r}, t)$ (via Eq. 2.4) defined for $\boldsymbol{r} \in \Gamma,\ t \in [0, t^{\text{end}}]$, $g = 1, \ldots, N_g$
3. Solve MLQD system closed with $\hat{\mathbf{f}}_g(\boldsymbol{r}, t)$ and coupled with MEB (Eqs. 2.3, 2.13, & 2.20) over all $\boldsymbol{r} \in \Gamma,\ t \in [0, t^{\text{end}}],\ g = 1, \ldots, N_g$
4. Extract $\hat{\hat{T}}(\boldsymbol{r}, t),\ \hat{\hat{E}}_g(\boldsymbol{r}, t),\ \hat{\hat{\boldsymbol{F}}}_g(\boldsymbol{r}, t)$ from MLQD solution for $\boldsymbol{r} \in \Gamma,\ t \in [0, t^{\text{end}}]$, $g = 1, \ldots, N_g$

Output: $\hat{\hat{T}},\ \hat{\hat{E}}_g,\ \hat{\hat{\boldsymbol{F}}}_g$

There are several interpretations to this methodology, henceforth referred to as the transport-corrected approximation (TCA) ROM, depending on the chosen source of $\hat{T}$. At its most fundamental level, the TCA ROM is a method to 'correct' approximate

solutions by estimating the transport effects in the given system. If $\hat{T}$ is found from a set of experimentally obtained data, or sparse/gappy data, then this method can instead be seen as a sophisticated interpolation/extrapolation procedure to generate solutions based on select known points. Else if $\hat{T}$ is found from some other ROM solution to the given TRT problem, the proposed model is one that can enhance other ROM solutions by adding high-order information. Another interpretation for when $\hat{T}$ comes from a reduced-order solution is as a variant of the DET ROMs (see Ch. 4) with a cheap offline phase.

In this study only the case where $\hat{T}$ comes from the solution of a radiative transfer ROM. Specifically, the ROMs considered for this purpose are the multigroup P_1 and $P_{1/3}$ models [14], and a select FLD model.

5.1.1 The Flux Limited Diffusion Model

With a multigroup FLD model, the TRT problem (Eqs. 1.6 & 1.10) is approximated by the following system

$$\frac{\partial E_g}{\partial t} + \boldsymbol{\nabla} \cdot (D_g(T, E_g)\boldsymbol{\nabla} E_g) + c\varkappa_{E,g}(T)E_g = 4\pi\varkappa_{B,g}(T)B_g(T), \tag{5.3}$$

$$\frac{\partial \varepsilon(T)}{\partial t} = \sum_{g=1}^{N_g} \Big(c\varkappa_{E,g}(T)E_g - 4\pi\varkappa_{B,g}(T)B_g(T) \Big). \tag{5.4}$$

Eq. 5.3 is the FLD equation, and $D_g(T, E_g)$ is the flux-limited diffusion coefficient which takes on different formulations depending on the specific FLD model. We use the form proposed by E. Larsen [14]

$$D_g(T, E_g) = \left[\big(3\varkappa_{E,g}(T)\big)^2 + \left(\frac{1}{E_g}\boldsymbol{\nabla} E_g\right)^2 \right]^{\frac{1}{2}}. \tag{5.5}$$

5.1.2 The P_1 and $P_{1/3}$ Models

The P_1 model for radiative transfer [14] approximates the TRT problem (Eqs. 1.6 & 1.10) with the following system

$$\frac{\partial E_g}{\partial t} + \boldsymbol{\nabla} \cdot \boldsymbol{F}_g + c\varkappa_{E,g}(T)E_g = 4\pi\varkappa_{B,g}(T)B_g(T), \tag{5.6a}$$

$$\frac{1}{c}\frac{\partial \boldsymbol{F}_g}{\partial t} + \frac{c}{3}\boldsymbol{\nabla} E_g + \tilde{\varkappa}_{R,g}(T)\boldsymbol{F}_g = 0, \tag{5.6b}$$

coupled with the MEB equation (Eq. 5.4). The P_1 equations are simply the first two moments of the BTE that are closed with a linear-in-angle approximation for the radiation intensities, taking the same formulation as the LOQD system (Eqs. 2.3) with $\mathfrak{f}_g = \frac{1}{3}\mathbb{I}$. Here $\mathbb{I}$ is the identity matrix.

The $P_{1/3}$ model for radiative transfer [14, 15] was originally derived to find solutions which have the correct propagation speed of radiation in a vacuum (i.e. c). The P_1 equations are known to propagate radiation in the optically thin limit at a speed of $\frac{c}{\sqrt{3}}$, and diffusion propagates radiation with infinite speed in this limit. The $P_{1/3}$ equations are a modification of the P_1 equations (Eqs. 5.6) with a weight of $\frac{1}{3}$ applied to the time derivative of the radiation flux

$$\frac{\partial E_g}{\partial t} + \boldsymbol{\nabla} \cdot \boldsymbol{F}_g + c\varkappa_{E,g}(T)E_g = 4\pi\varkappa_{B,g}(T)B_g(T), \tag{5.7a}$$

$$\frac{1}{3c}\frac{\partial \boldsymbol{F}_g}{\partial t} + \frac{c}{3}\boldsymbol{\nabla} E_g + \tilde{\varkappa}_{R,g}(T)\boldsymbol{F}_g = 0. \tag{5.7b}$$

5.2 Numerical Results

The TCA ROM is analyzed through numerical testing using the F-C problem [142]. This test problem is described in Appendix D and Sec. 4.4. The primary goal of this analysis is to demonstrate how accurately the proposed ROM can reproduce the solution to a TRT problem from an array of different approximate solutions. The physics embedded in $\hat{T}$ will vary depending on which diffusion type model is used in its computation. For instance the FLD, P_1 and $P_{1/3}$ models may all produce different propagation speeds (and spectral distributions) of the radiation wavefront. These effects change how energy is redistributed in the F-C test and alters the distribution of material temperatures in space-time. It is important to understand how these effects are manifested in the TCA ROM's solutions.

This numerical test problem used to analyze the TCA ROM is the **F-C Test A** (see Sec. 4.4.1) using the conservative method of long characteristics to discretize the BTE (ref. Sec. 2.3.2). The maximum width enforced by the ray tracing algorithm is $w_{\max} = 0.01$cm. $T^{\text{in}} = 1$ KeV and $T^0 = 1$ eV are considered. All measures of accuracy are calculated against the FOM solution to this F-C test obtained by the MLQD method (Sec. 2.1) on the same discrete grid in space and time. Each ROM possesses the same level of discretization error as the FOM. In the limit of fine grids these comparisons will give the

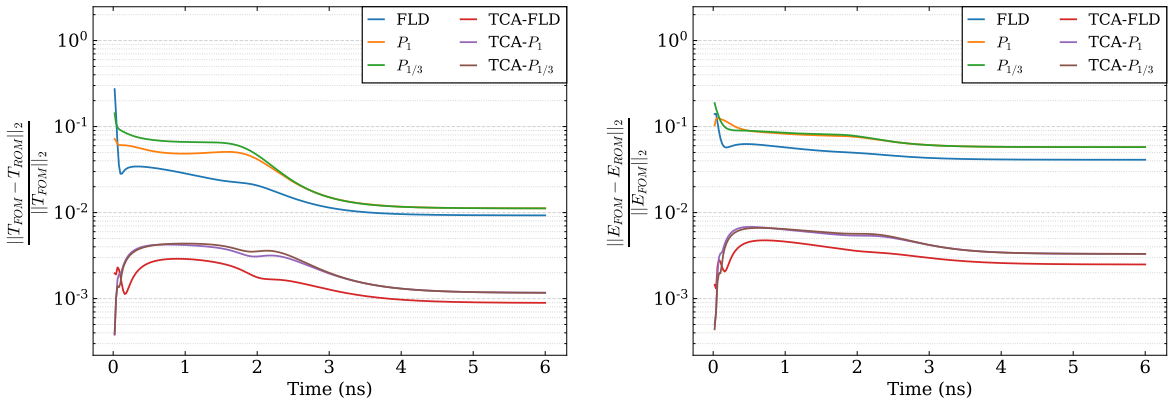

(a) Material Temperature

(b) Radiation Energy Density

Figure 5.1: Relative errors in the 2-norm for solutions of the FLD, P_1 and $P_{1/3}$ models, and for the TCA ROM applied to those models, plotted vs time.

'true' error introduced by each model's inherent approximations.

Fig. 5.1 plots relative errors (w.r.t. the FOM solution) for the material temperature and total radiation energy density calculated in the 2-norm over space at each instant of time in $t \in [0, 6\text{ns}]$. Separate curves are shown for each considered diffusive ROM and for the TCA ROM applied to those diffusive ROMs. In each case the proposed ROM's solution finds an increase in accuracy for both quantities compared to each diffusive ROM's solution. The errors in T and E from the TCA ROM solution are on the order of 10^{-3} for the whole interval of time, whereas the diffusive model solution errors exist on order 10^{-2} for the majority of time instances. The TCA ROM is seen to increase the accuracy of the model it is applied to by roughly an order of magnitude. The FLD model possesses the highest accuracy of all tested diffusive ROMs, and the TCA ROM with highest accuracy is the one applied to the FLD solution.

Next the TCA ROM is studied in its ability to capture TRT physics. The radiation breakout time is first investigated (see Sec. 4.5), followed by the frequency spectrum of radiation. We explore here how the TCA ROM is able to improve upon the physics capture of each diffusive ROM, each of which is known to produce nonphysical effects [14, 15, 16]. Fig. 5.2 displays the absolute relative error of the total radiation flux and energy densities and the material temperature integrated along the right boundary of the F-C test, defined in Eqs. 4.11 to be $\bar{F}_R$, $\bar{E}_R$ and $\bar{T}_R$ respectively. These quantities are graphed vs time. The FOM solution for $\bar{F}_R$, $\bar{E}_R$ and $\bar{T}_R$ is shown in Fig. 4.13. The

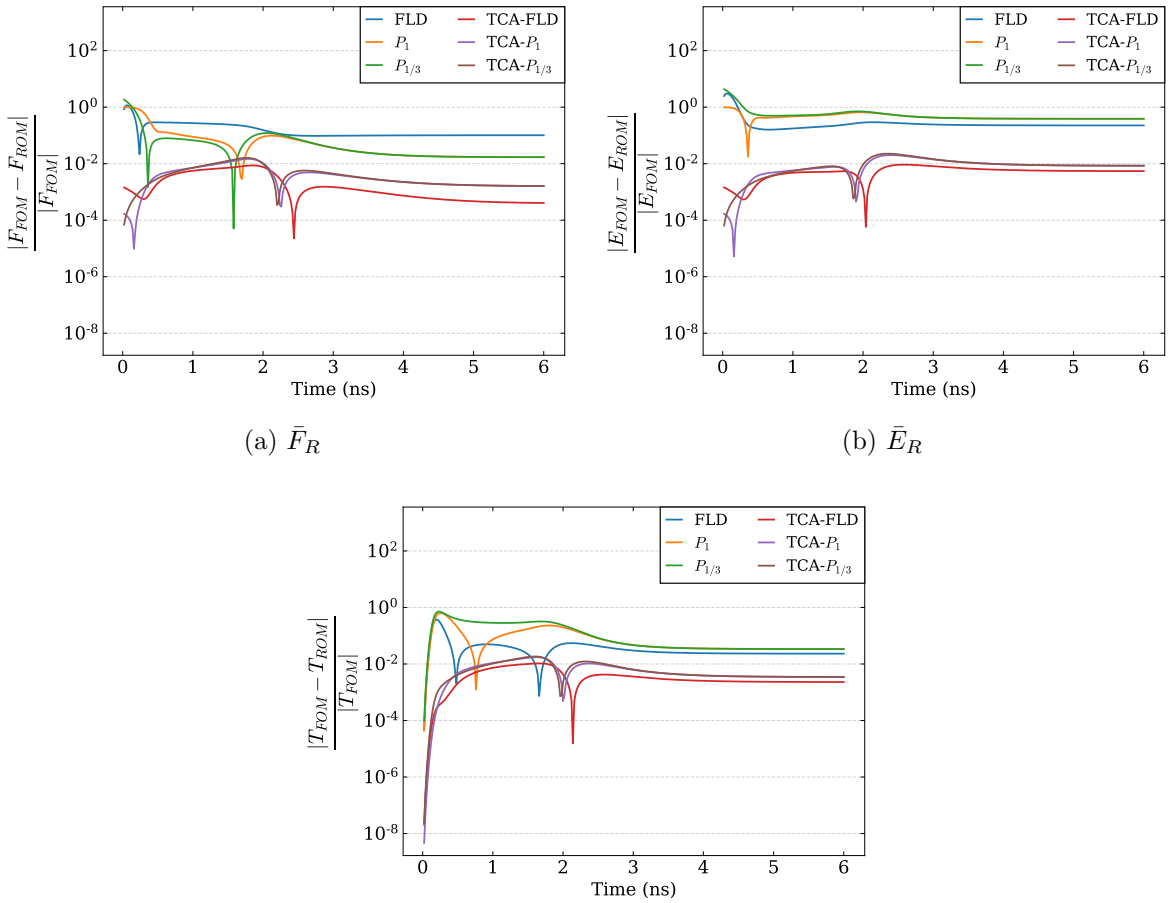

(a) $\bar{F}_R$

(b) $\bar{E}_R$

(c) $\bar{T}_R$

Figure 5.2: Relative error for the FLD, P_1 and $P_{1/3}$ models, and the TCA ROM applied to those models, for data located at and integrated over the right boundary of the domain.

relative errors for each quantity are decreased using the TCA ROM by 1-2 orders of magnitude for most instances of time. The most dramatic increase in accuracy is for the FLD $\bar{F}_R$ by about 3 orders of magnitude. In fact, the FLD $\bar{F}_R$ is the least accurate and the TCA ROM $\bar{F}_R$ using the FLD solution is the most accurate of the models shown. The explanation for this effect comes from the fact that the TCA ROM only acts on the approximate material temperature it is given, and the FLD solution for $\bar{T}_R$ (and T in general from Fig. 5.1) is the most accurate of the diffusive ROMs.

The final portion of analysis examines the frequency spectrum of radiation energy densities for each ROM. The FOM solution for these spectral quantities is given in

Fig. 4.17 (see Sec. 4.5.2 for description). Figures will only be shown for a 'zoomed in' portion of the entire interval of photon energies, noting that only a single point is left out whose errors are not significantly different than those shown. Figs. 5.3, 5.4 and 5.5 depict the relative errors of the spectral radiation energy densities found by the FLD, P_1 and $P_{1/3}$ models respectively. Each subfigure shows errors at a specific point in the F-C test domain: (i) the domain midpoint, (ii) the midpoint of the right boundary, (iii) the bottom corner of the right boundary. Each curve is taken at a specific instant of time chosen to represent significant behaviors in $\bar{E}_R$. Each of the diffusive ROMs best approximates the low-frequency spectrum of radiation in the optically thick regime. Higher-frequency groups have the largest levels of error. Furthermore the entire spectrum is found to significantly higher accuracy at the domain midpoint that at the right boundary where the solution is more anisotropic.

Figs. 5.6, 5.7 and 5.8 depict the relative errors of the spectral radiation energy densities found by the TCA ROM applied to the FLD, P_1 and $P_{1/3}$ solutions respectively. The errors in every frequency group are decreased and there are fewer peaks in the spectrum when the error becomes very large. The low- and mid-frequency portions of the spectrum find an increase in accuracy of roughly an order of magnitude across all models for each considered spatial point and time instance. The high-frequency portion of the spectrum's errors are much more drastically decreased by between 1 and 4 orders of magnitude, with the largest decreases in the highest frequency groups.

An integral view (in time) of the information presented by the previous spectral plots is provided in Figs. 5.9, 5.10 and 5.11. These plots show the spectral errors of each model for one of the considered spatial points, where the errors have been collected in norms over time. Specifically each figure displays the relative spectral error in the 2-norm and infinity-norm across the interval $t \in [0, 6\text{ns}]$. This integral view is used to give a more clear sense of how the TCA ROMs improve upon the radiation spectrum of the diffusive ROMs, having seen the dynamics represented in the previous plots. The infinity norm measurements are only slightly elevated from those in the 2-norm, and the TCA ROM is demonstrated to improve upon low-frequency group errors by roughly an order of magnitude at each considered point in space. The increase in accuracy from the diffusion solutions significantly improves as frequency increases starting from roughly $\nu = 3$ KeV. This is where the peak of (non-local) radiation emanating from the boundary drive should be located in frequency, as the Planckian spectrum $B(\nu, T)$ peaks at $\nu = 2.82T$.

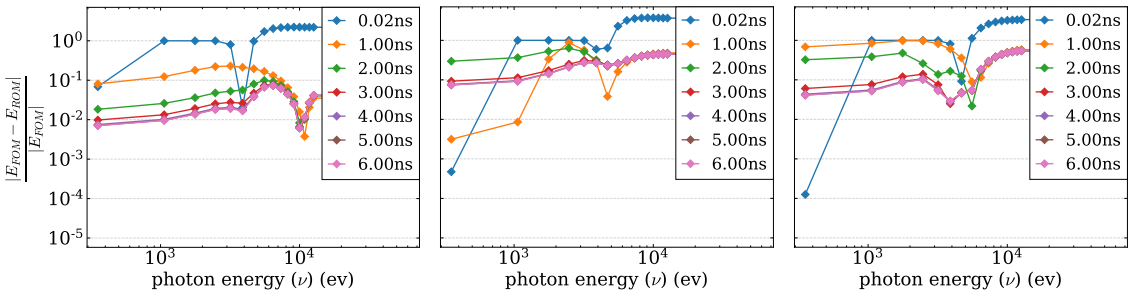

(a) $y = 3$cm, $x = 3$cm (b) $y = 3$cm, $x = 6$cm (c) $y = 0$cm, $x = 6$cm

Figure 5.3: Relative errors of the radiation spectrum produced by the FLD model located at (i) the domain midpoint, (ii) the midpoint of the right boundary, (iii) the corner of the right boundary, taken at several time instances.

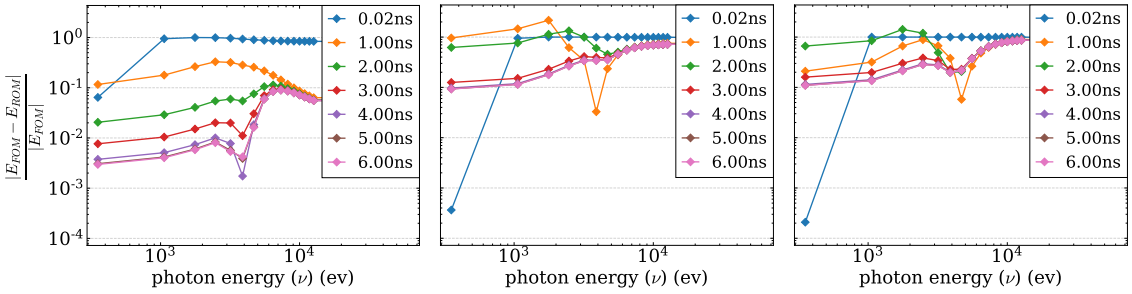

(a) $y = 3$cm, $x = 3$cm (b) $y = 3$cm, $x = 6$cm (c) $y = 0$cm, $x = 6$cm

Figure 5.4: Relative errors of the radiation spectrum produced by the P_1 model located at (i) the domain midpoint, (ii) the midpoint of the right boundary, (iii) the corner of the right boundary, taken at several time instances.

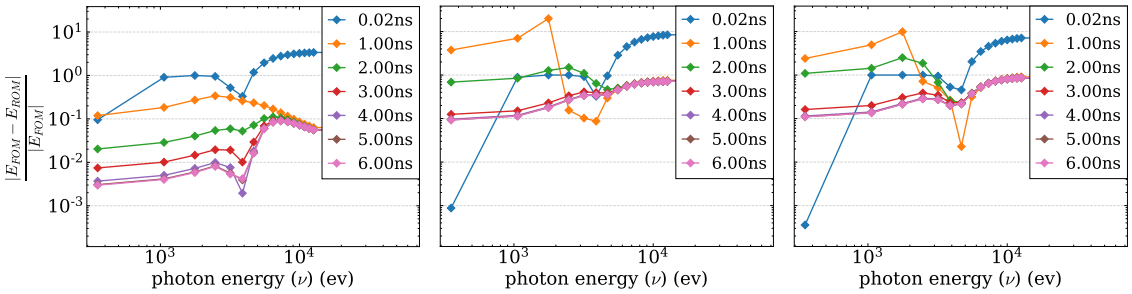

(a) $y = 3$cm, $x = 3$cm (b) $y = 3$cm, $x = 6$cm (c) $y = 0$cm, $x = 6$cm

Figure 5.5: Relative errors of the radiation spectrum produced by the $P_{1/3}$ model located at (i) the domain midpoint, (ii) the midpoint of the right boundary, (iii) the corner of the right boundary, taken at several time instances.

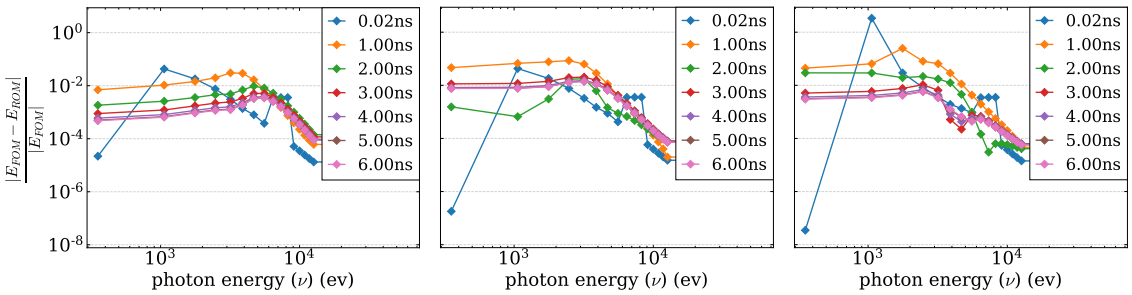

(a) $y = 3$cm, $x = 3$cm (b) $y = 3$cm, $x = 6$cm (c) $y = 0$cm, $x = 6$cm

Figure 5.6: Relative errors of the radiation spectrum produced by the TCA ROM using temperatures produced by the FLD model located at (i) the domain midpoint, (ii) the midpoint of the right boundary, (iii) the corner of the right boundary, taken at several time instances.

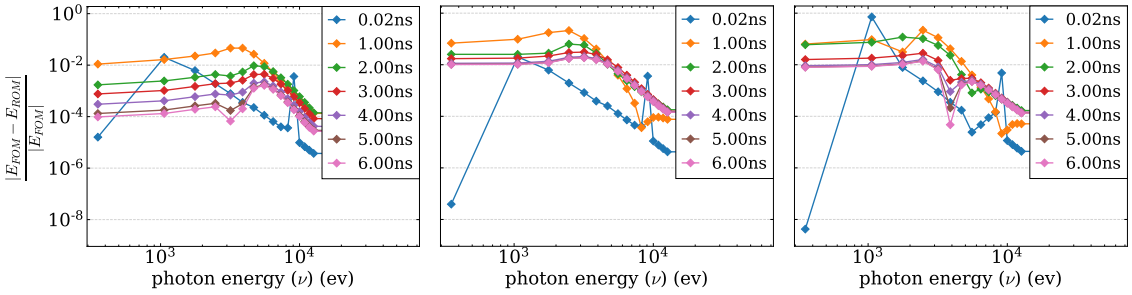

(a) $y = 3$cm, $x = 3$cm (b) $y = 3$cm, $x = 6$cm (c) $y = 0$cm, $x = 6$cm

Figure 5.7: Relative errors of the radiation spectrum produced by the TCA ROM using temperatures produced by the P_1 model located at (i) the domain midpoint, (ii) the midpoint of the right boundary, (iii) the corner of the right boundary, taken at several time instances.

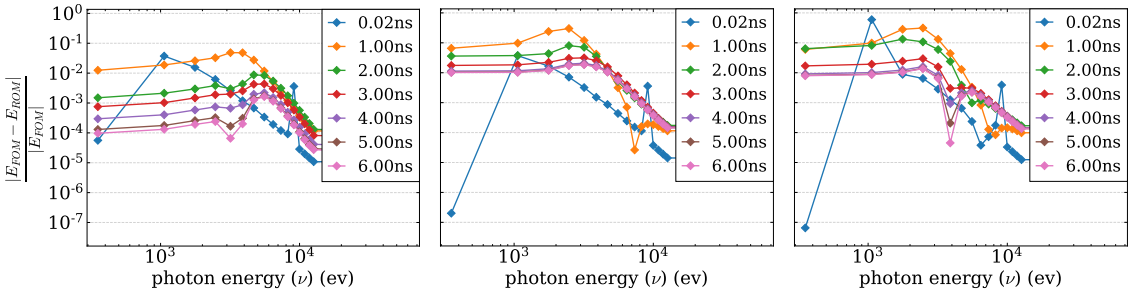

(a) $y = 3$cm, $x = 3$cm (b) $y = 3$cm, $x = 6$cm (c) $y = 0$cm, $x = 6$cm

Figure 5.8: Relative errors of the radiation spectrum produced by the TCA ROM using temperatures produced by the $P_{1/3}$ model located at (i) the domain midpoint, (ii) the midpoint of the right boundary, (iii) the corner of the right boundary, taken at several time instances.

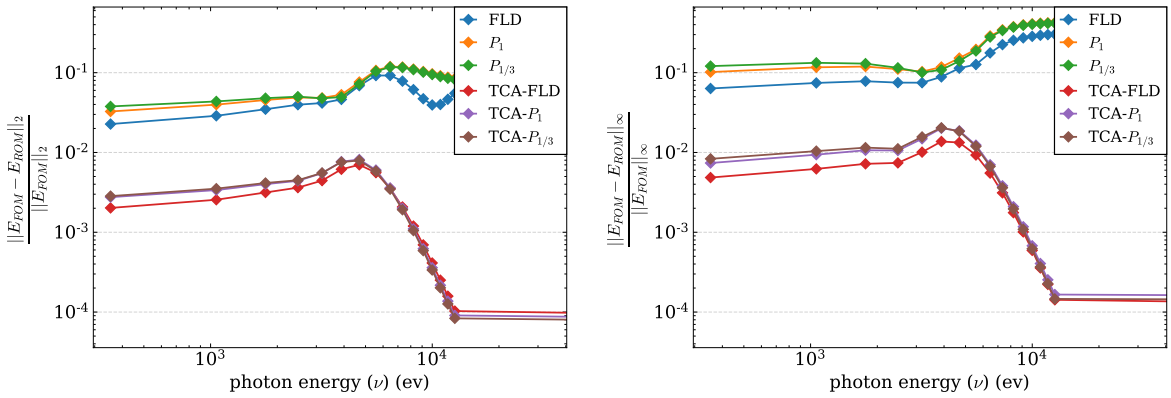

(a) 2 norm

(b) infinity norm

Figure 5.9: Relative errors of the radiation spectrum produced located at the domain midpoint in the 2-norm and ∞-norm along the temporal interval $t \in [0, 6\text{ns}]$

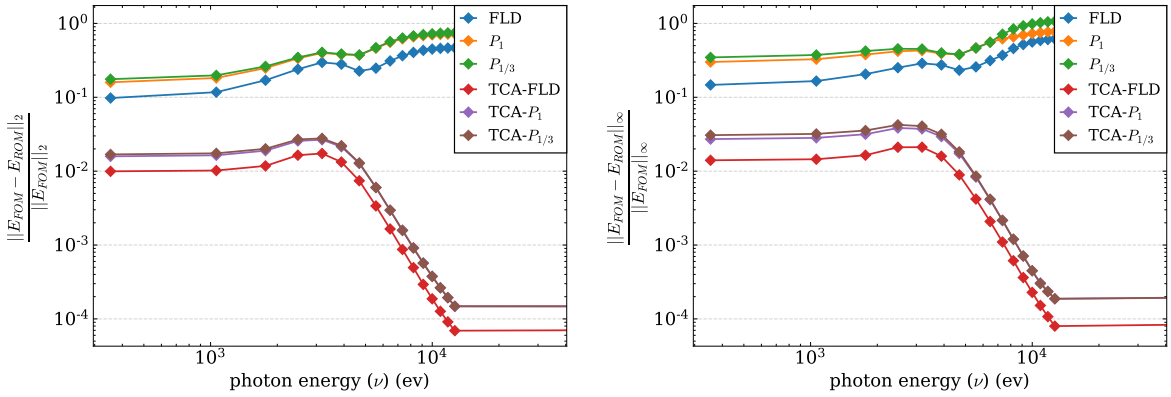

(a) 2 norm

(b) infinity norm

Figure 5.10: Relative errors of the radiation spectrum produced located at the midpoint of the right boundary in the 2-norm and ∞-norm along the temporal interval $t \in [0, 6\text{ns}]$

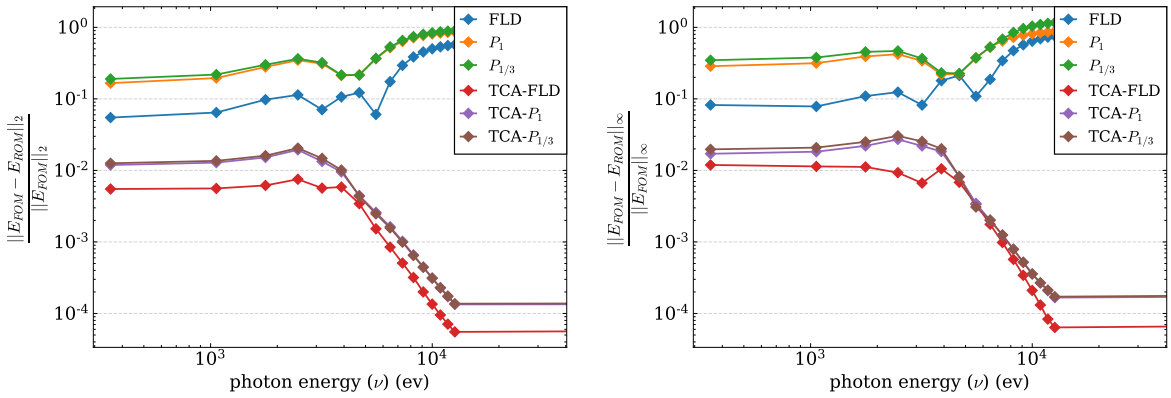

(a) 2 norm

(b) infinity norm

Figure 5.11: Relative errors of the radiation spectrum produced located at the corner of the right boundary in the 2-norm and ∞-norm along the temporal interval $t \in [0, 6\text{ns}]$

5.3 Discussion

In this chapter a ROM is introduced for TRT problems that approximates the Eddington tensor over all phase space and time simultaneously from a known diffusion-based solution of a problem on the same phase space and time. Three diffusion models were considered to be used with the TCA ROM on this problem: a FLD model, and the P_1, $P_{1/3}$ models. Each of the diffusion ROMs was shown to recreate the FOM solution with errors on the order of 10^{-2} and 10^{-1}, with the FLD model being the most accurate. The TCA ROM provided an increase in accuracy of 1-2 orders of magnitude in the total radiation energy density and material temperature when applied to each diffusion-based solution. The entire spectrum of radiation present at different points in the test domain was improved upon as well compared to the diffusion solutions. The most significant reduction in error from the diffusion solutions in the frequency spectrum was in the high-frequency range with strong transport effects.

In sum, the TCA ROM has been demonstrated to produce accurate solutions to the TRT problem given a known approximate temperature distribution in space-time obtained with a variety of diffusion models, all of which produce different physical effects. Possible future extensions of this ROM include parameterization of the model with interpolation between diffusion solutions for a series of TRT problems, or the use of other approximate

models for TRT such as VEF models in place of diffusion.

An especially compelling item for the continued development of this model is an extension to a global iteration process for solving TRT problems. When the TCA ROM is applied to a diffusion solution in a phase-space and time simultaneously, a solution with improved accuracy in this phase space and time is produced. The TCA ROM could then be applied once again to this improved solution, repeatedly until the radiation field and material temperature converge to some level in the phase-space and time. This process can be cast into the form of an iteration process whose iterations are each performed over all time instances, using a 'global' diffusion solve as the initial guess or zeroth iteration. Preliminary results for this methodology have demonstrated that each cycle improves the solution accuracy and that this process will converge after a sufficient number of iterations.

CHAPTER

6

A ROM USING A POD-BASED PROJECTION OF THE BTE WITH LOW-ORDER EQUATIONS

In this chapter a ROM is formulated based on a matrix-free (transport sweep compatible) POD-Galerkin projection of the BTE that can determine the Eddington tensor which yields closure for the nonlinear system of LOQD moment equations and the MEB equation. The proper orthogonal modes that describe a known set of photon intensity distributions in phase space and time are used as a global basis onto which the BTE can be projected (see Sec. 3.3). Numerical results are presented to demonstrate the ROM performance and accuracy using low-rank approximations of the radiation intensities. The results presented in this chapter have been published in [86] and presented at the 2021 International Conference on Mathematics and Computational Methods Applied to Nuclear Science and Engineering.

6.1 Fundamental Approach

The DET class of ROMs for TRT (see Ch. 4) models radiative transfer with the multilevel set of LOQD moment equations that are closed with an approximate Eddington tensor obtained directly through methods like the POD and DMD. At a high level this closure allows for accounting of high-order information and transport effects in some projected space. In this chapter, the BTE which provides the high-order information required to compute the Eddington tensor is projected with a POD-Galerkin approach (ref. Sec. 3.3). The BTE is projected onto some low-dimensional space where an approximation of the intensity shape function can be calculated at low computational cost, which is expressed as an expansion in some global basis that can describe the Eddington tensor.

The multigroup BTE (Eq. 1.6) is written in operator form as

$$\frac{1}{c}\partial_t \boldsymbol{I} + \mathcal{L}\boldsymbol{I} + \mathcal{K}(T)\boldsymbol{I} = \mathcal{Q}(T), \tag{6.1}$$

where $\boldsymbol{I} = (I_1, \ldots, I_{N_g})^\top$ and

$$\mathcal{L} \equiv \boldsymbol{\Omega}\cdot\boldsymbol{\nabla}, \quad \mathcal{K} \equiv \operatorname{diag}(\varkappa_{E,1}, \ldots, \varkappa_{E,N_g}), \quad \mathcal{Q} \equiv (\varkappa_{B,1}B_1, \ldots, \varkappa_{B,N_g}B_{N_g})^\top. \tag{6.2}$$

The radiation intensities are expanded in some set of basis functions $\{\boldsymbol{u}_\ell\}_{\ell=1}^k$ that span all phase space

$$\boldsymbol{I}_k(\boldsymbol{r}, \boldsymbol{\Omega}, t) = \sum_{\ell=1}^{k} \lambda_\ell(t)\boldsymbol{u}_\ell(\boldsymbol{r}, \boldsymbol{\Omega}), \tag{6.3}$$

with $\boldsymbol{u}_\ell = (u_{\ell,1} \ldots, u_{\ell,N_g})^\top$. This expansion is substituted in Eq. 6.1 to yield

$$\sum_{\ell=1}^{k}\left[\frac{1}{c}\boldsymbol{u}_\ell\partial_t\lambda_\ell + \lambda_\ell\mathcal{L}\boldsymbol{u}_\ell + \lambda_\ell\mathcal{K}(T)\boldsymbol{u}_\ell\right] = \mathcal{Q}(T), \tag{6.4}$$

followed by a projection onto the basis $\{\boldsymbol{u}_\ell\}_{\ell=1}^k$ by applying the inner product $\langle \boldsymbol{u}_{\ell'}, \cdot\rangle$ for all $\ell' = 1, \ldots, k$ which gives the following ODE for $\lambda_\ell(t)$:

$$\sum_{\ell=1}^{k}\left[\frac{1}{c}\langle \boldsymbol{u}_{\ell'}, \boldsymbol{u}_\ell\rangle\partial_t\lambda_\ell + \lambda_\ell\langle \boldsymbol{u}_{\ell'}, \mathcal{L}\boldsymbol{u}_\ell\rangle + \lambda_\ell\langle \boldsymbol{u}_{\ell'}, \mathcal{K}(T)\boldsymbol{u}_\ell\rangle\right] = \langle \boldsymbol{u}_{\ell'}, \mathcal{Q}(T)\rangle, \tag{6.5a}$$

$$\lambda|_{t=0} = \langle \boldsymbol{u}_\ell, \boldsymbol{I}|_{t=0}\rangle, \quad \ell = 1, \ldots, k, \tag{6.5b}$$

$$\ell' = 1, \ldots, k.$$

This inner product is defined as

$$\langle \boldsymbol{u}_{\ell'}, \boldsymbol{u}_{\ell} \rangle = \sum_{g=1}^{N_g} \int_{4\pi} d\Omega \int_{\Gamma} d^3\boldsymbol{r} \; u_{\ell,g} u_{\ell',g}. \tag{6.6}$$

Eq. 6.5a is a dense $k \times k$ system of equations with solution $\{\lambda_\ell\}_{\ell=1}^{k}$. The high-order solution to the BTE is found by solving Eq. 6.5a and using the coefficients λ_ℓ for the expansion in Eq. 6.3.

6.2 Projection of the Boltzmann Equation in Discrete Space

Let the BTE be discretized in time with the backward Euler time integration scheme, in angle with the method of discrete ordinates and in space with the simple corner balance discretization, restricted to 1D slab geometry (see Sec. 2.2). In this case the elements of $\boldsymbol{I}^n \in \mathbb{R}^{\mathfrak{N}_I}$ are $I^n_{g,m,i,l}$ with $g = 1, \ldots, N_g$, $m = 1, \ldots, N_\Omega$, $i = 1, \ldots, N_x$ being indices of the frequency group, direction of motion, and $x-$position on the spatial grid, respectively. $l = L, R$ denotes the left or right side of a spatial cell and thus $\mathfrak{N}_I = 2N_g N_\Omega N_x$. In discrete form, Eq. 6.1 becomes

$$\frac{1}{c\Delta t^n}(\boldsymbol{I}^n - \boldsymbol{I}^{n-1}) + \mathcal{L}_h \boldsymbol{I}^n + \mathcal{K}^n_h(T)\boldsymbol{I}^n = \mathcal{Q}^n_h(T). \tag{6.7}$$

The source vector $\mathcal{Q}^n_h \in \mathbb{R}^{\mathfrak{N}_I}$ absorbs the boundary conditions, with elements defined as

$$\left(\mathcal{Q}^n_h(T)\right)_{g,m,i,l} = 2\pi \varkappa^n_{B,g,i}(T) B^n_{g,i}(T) + \mathcal{Q}^{\text{in}}_{g,m,i,l} \tag{6.8}$$

where

$$\mathcal{Q}^{\text{in}}_{g,m,i,l} = \begin{cases} \delta_{i,1}\delta_{l,L} I^{\text{in}+}_{g,m} & m \in \{m \; : \; \mu_m > 0\} \\ \delta_{i,N_x}\delta_{l,R} I^{\text{in}-}_{g,m} & m \in \{m \; : \; \mu_m < 0\} \end{cases} \tag{6.9}$$

and $I^{\text{in}\pm}$ is the incoming radiation on the left/right boundaries of the problem, with $\delta_{i,j}$

denoting the Kronecker delta. The operator $\mathcal{L}_h : \mathbb{R}^{\mathfrak{N}_I} \to \mathbb{R}^{\mathfrak{N}_I}$ is defined as follows:

$$(\mathcal{L}_h \boldsymbol{I}^n)_{g,m,i,L} = \begin{cases} \frac{\mu_m}{\Delta x_i}(I_{g,m,i,R} + I_{g,m,i,L} - 2\alpha_{i,1} I_{g,m,i-1,R}) & m \in \{m \ : \ \mu_m > 0\} \\ \frac{\mu_m}{\Delta x_i}(I_{g,m,i,R} - I_{g,m,i,L}) & m \in \{m \ : \ \mu_m < 0\} \end{cases} \tag{6.10a}$$

$$(\mathcal{L}_h \boldsymbol{I}^n)_{g,m,i,R} = \begin{cases} \frac{\mu_m}{\Delta x_i}(I_{g,m,i,R} - I_{g,m,i,L}) & m \in \{m \ : \ \mu_m > 0\} \\ \frac{\mu_m}{\Delta x_i}(2\alpha_{i,N_x} I_{g,m,i+1,L} - I_{g,m,i,R} - I_{g,m,i,L}) & m \in \{m \ : \ \mu_m < 0\} \end{cases} \tag{6.10b}$$

Here $\alpha_{i,j} = 1 - \delta_{i,j}$. Finally, the operator $\mathcal{K}_h^n(T) : \mathbb{R}^{\mathfrak{N}_I} \to \mathbb{R}^{\mathfrak{N}_I}$ is given by

$$(\mathcal{K}_h^n(T)\boldsymbol{I}^n)_{g,m,i,l} = \varkappa_{E,g,i}^n(T) I_{g,m,i,l}^n. \tag{6.11}$$

6.2.1 Formulation of the POD Basis

The numerical solution to the BTE over N_t time steps can be collected into a snapshot matrix with chronologically ordered columns

$$\mathbf{A}^I = [\boldsymbol{I}^1 \ \boldsymbol{I}^2 \ \ldots \ \boldsymbol{I}^{N_t}] \in \mathbb{R}^{\mathfrak{N}_I \times N_t}. \tag{6.12}$$

The matrix $\mathbf{A}^I$ informs a POD basis $\{\boldsymbol{u}_\ell\}_{\ell=1}^k$ which is formulated to give an optimal approximation of the snapshots $\boldsymbol{I}^n$ in the W norm, defined by our specific discretization schemes in phase space (ref. Sec. 3.3.1). Here the discrete weighted inner product $\langle \cdot, \cdot \rangle_W$ must correspond to the continuous inner product defined earlier (Eq. 6.6) which represents an integration over phase space. Let the right face of the i^{th} cell in the discrete spatial grid be $x_{i+\frac{1}{2}}$, where $x_{i+\frac{1}{2}} = x_{i-\frac{1}{2}} + \Delta x_i$. Then for two functions $\boldsymbol{u}(x), \boldsymbol{v}(x) \in \mathbb{R}^{N_g N_\Omega}$ with elements $u_{g,m}(x)$ and $v_{g,m}(x)$, the inner product in discrete space is

$$\langle \boldsymbol{u}, \boldsymbol{v} \rangle_W = \sum_{g=1}^{N_g} \sum_{m=1}^{N_\Omega} w_m \sum_{i=1}^{N_x} \int_{x_{i-\frac{1}{2}}}^{x_{i+\frac{1}{2}}} u_{g,m}(x) v_{g,m}(x) \, dx. \tag{6.13}$$

where $\{w_m\}$ is the set of angular quadrature weights. The SCB scheme defines the integration over each i^{th} spatial cell by

$$\int_{x_{i-\frac{1}{2}}}^{x_{i+\frac{1}{2}}} u_{g,m}(x) \, dx = \frac{\Delta x_i}{2}(u_{g,m,i,R} + u_{g,m,i,L}), \tag{6.14}$$

where $u_{g,m,i,R}$ and $u_{g,m,i,L}$ are the values of $u_{g,m}(x)$ at the right and left sides of the i^{th} cell respectively. With this, the weighted inner product is defined for any vectors $\boldsymbol{u}_\ell, \boldsymbol{u}_{\ell'} \in \mathbb{R}^{\mathfrak{N}_I}$

as

$$\langle \boldsymbol{u}_{\ell'}, \boldsymbol{u}_{\ell} \rangle_W = \sum_{g=1}^{N_g} \sum_{m=1}^{N_\Omega} \sum_{i=1}^{N_x} \frac{w_m \Delta x_i}{2} (u_{\ell',g,m,i,L} u_{\ell,g,m,i,L} + u_{\ell',g,m,i,R} u_{\ell,g,m,i,R}), \tag{6.15}$$

which can also be written in the form $\langle \boldsymbol{u}_{\ell'}, \boldsymbol{u}_{\ell} \rangle_W = \boldsymbol{u}_{\ell'}^\top \mathbf{W} \boldsymbol{u}_{\ell}$ where the matrix of weights is defined by

$$\mathbf{W} = \bigoplus_{g=1}^{N_g} \bigoplus_{m=1}^{N_\Omega} \bigoplus_{i=1}^{N_x} \frac{w_m \Delta x_i}{2} \mathbb{I}_2, \quad \mathbb{I}_2 = \mathrm{diag}(1,1). \tag{6.16}$$

In order for the POD basis $\{\boldsymbol{u}_\ell\}_{\ell=1}^k$ to satisfy the minimization condition in Eq. 3.30, calculations must be done using the weighted snapshot matrix [131]

$$\hat{\mathbf{A}}^I = \mathbf{W}^{1/2} \mathbf{A}^I \mathbf{H}^{1/2}, \tag{6.17}$$

where $\mathbf{H} = \mathrm{diag}(\Delta t^1, \ \ldots, \ \Delta t^{N_t})$ is an analogue to $\mathbf{W}$ corresponding to the temporal weights introduced by the chosen scheme for time integration. The POD basis functions for our expansion are calculated as the first k columns of the matrix $\mathbf{U} = [\boldsymbol{u}_1 \ \ldots \ \boldsymbol{u}_r] \in \mathbb{R}^{\mathfrak{N}_I \times r}$, defined by

$$\mathbf{U} = \mathbf{W}^{-1/2} \hat{\mathbf{U}}, \tag{6.18}$$

where $r = \mathrm{rank}(\hat{\mathbf{A}}^I)$ and $\hat{\mathbf{U}}$ is the matrix whose columns hold the left singular vectors of $\hat{\mathbf{A}}^I$ (see Sec. 3.3.1).

6.2.2 Projection onto the POD Basis

The discrete vectors of radiation intensities are expanded about the POD basis functions

$$\boldsymbol{I}_k^n = \sum_{\ell=1}^{k} \lambda_\ell^n \boldsymbol{u}_\ell, \quad k \leq r. \tag{6.19}$$

Substituting this expansion into Eq. 6.7 yields

$$\sum_{\ell=1}^{k} \left[\frac{\boldsymbol{u}_\ell}{c \Delta t^n} (\lambda_\ell^n - \lambda_\ell^{n-1}) + \lambda_\ell^n \mathcal{L}_h \boldsymbol{u}_\ell + \lambda_i^n \mathcal{K}_h^n(T) \boldsymbol{u}_\ell \right] = \mathcal{Q}_h^n(T). \tag{6.20}$$

Eq. 6.20 is then projected onto the POD basis by applying the inner product $\langle \boldsymbol{u}_{\ell'}, \cdot \rangle_W$ for

all $\ell' = 1, \ldots, k$ to find the following system of (time dependent) equations:

$$\frac{1}{c\Delta t^n}(\lambda_{\ell'}^n - \lambda_{\ell'}^{n-1}) + \sum_{\ell=1}^{k} \lambda_\ell^n \langle \boldsymbol{u}_{\ell'}, \mathcal{L}_h \boldsymbol{u}_\ell \rangle_W + \sum_{\ell=1}^{k} \lambda_\ell^n \langle \boldsymbol{u}_{\ell'}, \mathcal{K}_h^n(T) \boldsymbol{u}_\ell \rangle_W = \langle \boldsymbol{u}_{\ell'}, \mathcal{Q}_h^n(T) \rangle_W, \quad (6.21a)$$

$$\lambda_\ell^0 = \langle \boldsymbol{u}_\ell, \boldsymbol{I}^0 \rangle_W, \quad \ell = 1, \ldots, k, \quad (6.21b)$$

$$\ell' = 1, \ldots, k$$

where the orthonormality of the POD basis functions in the W norm has been leveraged.

6.3 Formulation of the Reduced Order Model

The class of ROMs derived in this chapter model TRT physics with the POD-Galerkin (POD-G) projected BTE combined with the multilevel system of LOQD equations coupled with the MEB equation. This model is henceforth referred to as the POD-G BTE-QD ROM and is formulated by

- The POD-Galerkin projected BTE (Eq. 6.21a) which solves for radiation intensities that lie in the space spanned by the chosen basis $\{\boldsymbol{u}_\ell\}_{\ell=1}^k$
- The multigroup LOQD equations (Eqs. 2.3), closed by the Eddington tensor that is defined via the rank k POD-Galerkin expansion of intensities
- The effective grey problem formed by the effective grey LOQD equations and the MEB equation (Eqs. 2.13)

Calculation of the POD basis functions used in these ROMs can be done before solving any TRT problems and comprises the method's offline stage. The online stage of the ROMs when used to solve TRT problems is outlined in Alg. 5. Of the inner products used to define the POD-G BTE (Eq. 6.21a), those that only depend on the basis functions (e.g. $\langle \boldsymbol{u}_{\ell'}, \mathcal{L}_h \boldsymbol{u}_\ell \rangle_W$) can be pre-computed before solving a problem. The inner products that contain nonlinear terms with respect to the material temperature must, conversely, be continuously updated during the iteration process.

Algorithm 5: Obtaining the solution to TRT problems with the POD-G BTE-QD ROM

Input: k, $\{\boldsymbol{u}_\ell\}_{i=1}^k$

Calculate $\langle \boldsymbol{u}_{\ell'}, \mathcal{L}_h \boldsymbol{u}_\ell \rangle_W$ for $\ell, \ell' = 1, \ldots, k$

$n = 0$

while $t^n \leq t^{end}$ **do**

  $n = n + 1$

  $T^{(0)} = T^{n-1}$

  $\mathfrak{f}_g^{(0)} = \mathfrak{f}_g^{n-1}$

  $s = -1$

  while $\|T^{(s)} - T^{(s-1)}\| > \epsilon_1 \|T^{(s)}\| + \epsilon_2$, $\|E^{(s)} - E^{(s-1)}\| > \epsilon_1 \|E^{(s)}\| + \epsilon_2$ **do**

    $s = s + 1$

    if $s \geq 1$ **then**

      Update $\langle \boldsymbol{u}_{\ell'}, \mathcal{K}_h^n(T) \boldsymbol{u}_\ell \rangle_W$, $\langle \boldsymbol{u}_{\ell'}, \mathcal{Q}_h^n(T) \rangle_W$ with $T^{(s-1)}$ for $\ell, \ell' = 1, \ldots, k$

      Solve the POD-G BTE (Eq. 6.21a) for $\{\lambda_\ell\}_{\ell=1}^k$

      Compute $\boldsymbol{I}_k^n = \sum_{\ell=1}^k \lambda_\ell^n \boldsymbol{u}_\ell$

      Compute $\mathfrak{f}_g^{(s)}$ from $\boldsymbol{I}_k^n$ (Eq. 2.4)

    end

    $q = 0$

    while $\|T^{(s,q)} - T^{(s,q-1)}\| > \epsilon_1 \|T^{(s,q)}\| + \epsilon_2$, $\|E^{(s,q)} - E^{(s,q-1)}\| > \epsilon_1 \|E^{(s,q)}\| + \epsilon_2$ **do**

      $q = q + 1$

      Update $\varkappa_{E,g}, \varkappa_{B,g}, \tilde{\varkappa}_{R,g}, B_g$ with $T^{(s-1,q)}$

      Solve multigroup LOQD equations (Eqs. 2.3) with $\mathfrak{f}_g^{(s)}$ for $E_g^{(s,q)}$, $\boldsymbol{F}_g^{(s,q)}$

      Compute spectrum-averaged closures for the effective grey problem with $E_g^{(s,q)}$, $\boldsymbol{F}_g^{(s,q)}$

      Solve effective grey problem (Eqs. 2.13 and 2.20) for $T^{(s,q)}$, $E^{(s,q)}$, $\boldsymbol{F}^{(s,q)}$

    end

    $T^{(s)} \leftarrow T^{(s,q)}$

  end

  $T^n \leftarrow T^{(s)}$

  $\mathfrak{f}_g^n \leftarrow \mathfrak{f}_g^{(s)}$

end

6.4 Numerical Results

Numerical results for this ROM are presented here as a demonstration of performance in the absence of theory that can be used to predict the ROM's behavior (see Sec. 4.4 for further motivation). This is an important step in the development of a ROM such as this one before further considerations can be righteously attended to, such as parameterization of the model or the use of hyper-reduction techniques to further reduce the ROM's complexity. The ROM must be first proven robust to the nonlinear class of TRT problems.

6.4.1 F-C Test B

To test and analyze the POD-G BTE-QD ROM, the F-C test problem in 1D slab geometry is used (see Sec. 4.4.1 & Appendix D). This section describes the specific form of the F-C test used in this analysis, referred to as the **F-C Test B**. The slab is 6 cm thick, and initially at a temperature of T^0. The left boundary of the domain is subject to incoming radiation with blackbody spectrum at a temperature of T^{in}, and the right boundary is subject to a vacuum condition (no incoming radiation). Values of $T^0 = 1$ eV and $T^{\text{in}} = 1$ KeV are used here. The parameters of convergence criteria for iterations are $\epsilon_1 = 10^{-14}$, $\epsilon_2 = 10^{-15}$ (ref. Alg. 5). The BTE is discretized with the simple corner balance scheme in space (see Sec. 2.2) and low-order QD equations are discretized with a finite volumes scheme (ref. Sec. 2.4).

The time interval for the problem is $t \in [0, 6\text{ns}]$ which is discretized into $N_t = 300$ uniform time steps $\Delta t = 2 \times 10^{-2}$ ns. The spatial mesh consists of a uniform $N_x = 60$ cells with width $\Delta x = 0.1$ cm. The angular mesh has 8 discrete directions ($N_\Omega = 8$) using the double S_4 Gauss-Legendre quadrature set. $N_g = 17$ energy groups are defined as shown in Table D.1. The number of DoF describing $\boldsymbol{I}^n$ at each instant of time t^n is $\mathfrak{N}_I = 1.632 \times 10^4$. The number of DoF in phase space and time is equal to $\mathfrak{N}_I N_t = 4.896 \times 10^6$.

6.4.2 Analysis of POD Databases & Singular Values

Using a single POD basis to describe the entire temporal interval $t \in [0, 6\text{ns}]$ has been found to be problematic for this methodology. The F-C test evolves with several distinct physical regimes, which can be difficult to capture with a single basis. A high rank of expansion can be required to capture the structure of all regimes, and the iterative process can become sensitive to the basis quality. If the chosen set of basis functions does not

sufficiently represent any one regime, the ROM can produce nonphysical effects in the corresponding temporal interval in the F-C test.

For these reasons several POD bases were formed to describe select subintervals of the overall time window as done with the principal interval decomposition [152]. These subintervals were chosen to describe the different physical regimes encountered in the F-C test, which evolves in three distinct stages: (i) rapid wave formation, (ii) wave propagation, and (iii) slow continual heating of the domain to steady state. A separate database is constructed by the FOM for each of these stages, whose temporal ranges are the following: $t \in [0, 0.3\,\text{ns}]$, $t \in (0.3, 1.2\,\text{ns}]$, and $t \in (1.2, 6\,\text{ns}]$. These intervals were chosen based on qualitative evaluation of the TRT physics in the solution snapshots (see Fig. D.3).

The resulting database matrices that hold the set of discrete intensities for each of the three stages of the F-C test are denoted by $\mathbf{A}_i^I \in \mathbb{R}^{\mathfrak{N}_I \times N_{t,i}}$, $i = 1, 2, 3$. The columns of each database are snapshots of the solution at $N_{t,1}, N_{t,2}, N_{t,3}$ instants of time, respectively, ordered chronologically. The full ranks r_i of $\mathbf{A}_i^I$ are equal to $r_1 = N_{t,1} = 15,\ r_2 = N_{t,2} = 45,\ r_3 = N_{t,3} = 240$ respectively. The singular values (σ_ℓ) of each of the three databases are depicted in Fig. 6.1. The first database shows a slow rate of decrease in magnitude of its singular values over the entire range, whereas the singular values of the other two databases first experience rapid decrease followed by a plateau where the change in their magnitudes slows significantly. From the matrices $\mathbf{A}_i^I$, POD bases $\{\boldsymbol{u}_{i,\ell}\}_{\ell=1}^{k_i}$, $i = 1, 2, 3$ are calculated for each of these time intervals.

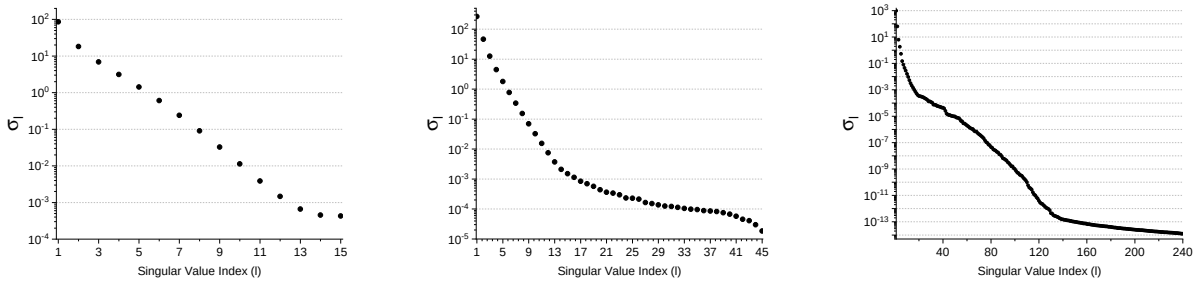

(a) $\mathbf{A}_1$ $(0 \leq t \leq 0.3\,\text{ns})$ (b) $\mathbf{A}_2$ $(0.3 < t \leq 1.2\,\text{ns})$ (c) $\mathbf{A}_3$ $(1.2 < t \leq 6\,\text{ns})$

Figure 6.1: Singular values of the database matrices of intensities over three time subintervals of the problem

The F-C test is solved with the POD-G BTE-QD model by expanding I with each of

the three POD bases based on the time frames they were generated for (e.g. I is expanded with $\{\boldsymbol{u}_{1,\ell}\}_{\ell=1}^{k_1}$ while $0 \leq t \leq 0.3$ ns). The ranks (k_1, k_2, k_3) of the expansion in Eq. 6.19 are determined as the values that satisfy Eq. 3.12 given some desired ξ. The ranks found for $\xi \in [10^{-5}, 10^{-16}]$ are shown in Fig. 6.2. Values of $\xi > 10^{-5}$ are not shown in this analysis, as the ROM using these ξ produces unsuitable solutions. The POD bases for $\mathbf{A}_1^I$ and $\mathbf{A}_2^I$ reach full rank ($k_1 = 15,\ k_2 = 45$) at $\xi = 10^{-6}$ and $\xi = 10^{-8}$, respectively. Full-rank is not found for the basis of $\mathbf{A}_3^I$ ($k_3 = 240$) until $\xi = 10^{-16}$. This behavior is expected since compared to $\mathbf{A}_3^I$, the full ranks of $\mathbf{A}_1^I$ and $\mathbf{A}_2^I$ are relatively small. The singular values of both $\mathbf{A}_1^I$ and $\mathbf{A}_2^I$ also occupy a smaller range than for $\mathbf{A}_3$. Another notable behavior is that $k_3 < k_2$ for $\xi < 10^{-8}$, indicating that the solution contained in the time range over which $\mathbf{A}_2^I$ was generated is the most difficult to represent with few POD modes. This is reasonable given that $\mathbf{A}_2^I$ accounts for the solution during propagation of the radiation wavefront from the left boundary to the right, which is known to be a difficult phenomena for the POD to represent with low rank [148, 149].

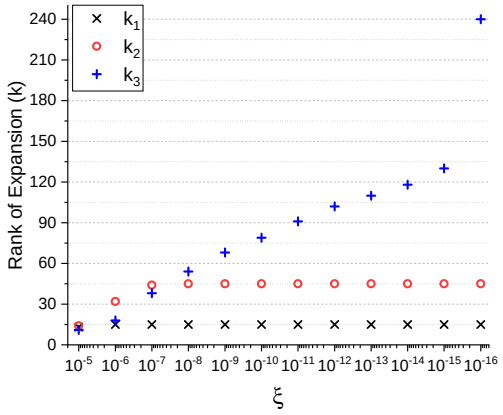

Figure 6.2: Rank of expansion for each database corresponding to different ξ

6.4.3 Analysis of ROM Errors

Numerical results for the errors of the POD-G BTE-QD model relative to the FOM solution on the F-C test in the 2-norm are displayed in Fig. 6.3 for the material temperature and radiation energy density vs. time. Each unique curve shows the relative error of the

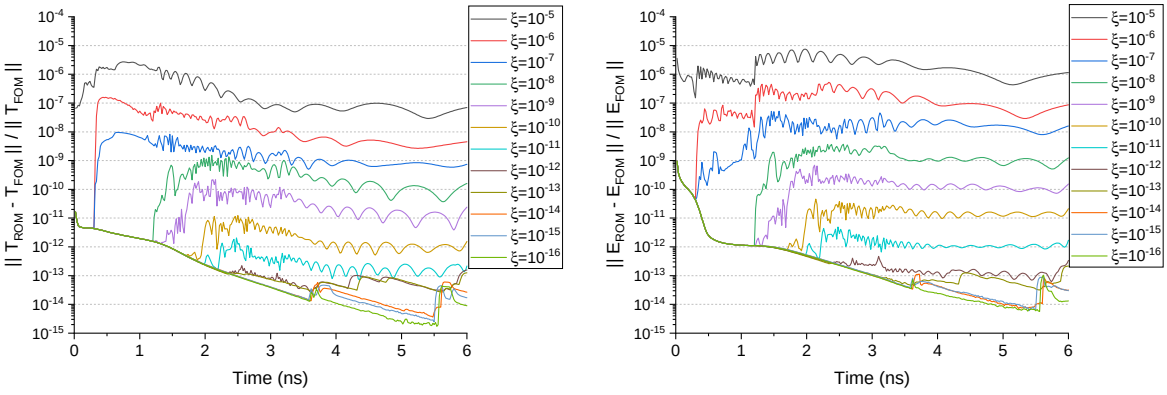

(a) Temperature

(b) Radiation Energy Density

Figure 6.3: Relative errors of the POD-G BTE-QD ROM compared to the FOM solution in the 2-norm vs. time

ROM solution for a specific value of ξ. Fig. 6.3 shows that as ξ decreases, the relative error of the ROM converges towards zero uniformly in time until the errors are close to 10^{-15} and some numerical noise becomes prevalent. Upon inspection, the ROM with $\xi = 10^{-6}, 10^{-7}$ is exceptionally accurate for $t \leq 0.3$ ns. This comes from the full-rank basis representation of $\mathbf{A}_1^I$ that occurs for all $\xi < 10^{-5}$, as was shown in Fig. 6.2. Similarly, the high accuracy for $t \leq 1.2$ ns while using $\xi < 10^{-7}$ follows from the fact that the full-rank basis representation of $\mathbf{A}_2^I$ is used for $\xi < 10^{-7}$. Considering overall accuracy, even with low-rank ($\xi = 10^{-5}$) the POD-G BTE-QD model maintains a relative error in both material temperature and radiation energy density below 10^{-5}. When using all POD modes ($\xi = 10^{-16}$) the POD-G BTE-QD model converges to the FOM solution within bounds of 10^{-11} with the exception of the radiation energy density while $t < 0.5$ ns. This comes from higher errors found at the radiation wavefront during formation, which is a difficult process to capture given how rapidly it progresses and can be prone to larger numerical errors than other parts of the solution.

Similarly to Fig. 6.3, Fig. 6.4 also displays the relative error in the solution of the F-C test obtained by the POD-G BTE ROM compared to the FOM solution in the 2-norm, but plotted vs. ξ. In Fig. 6.4 each curve corresponds to a specific instant of time, showing how the error of the ROM changes with respect to ξ when time is held static. This plot clearly demonstrates the convergence behavior of the ROM solution as ξ decreases to zero for most time steps. The errors in both quantities can be expressed as roughly $\xi \cdot 10^{-1}$.

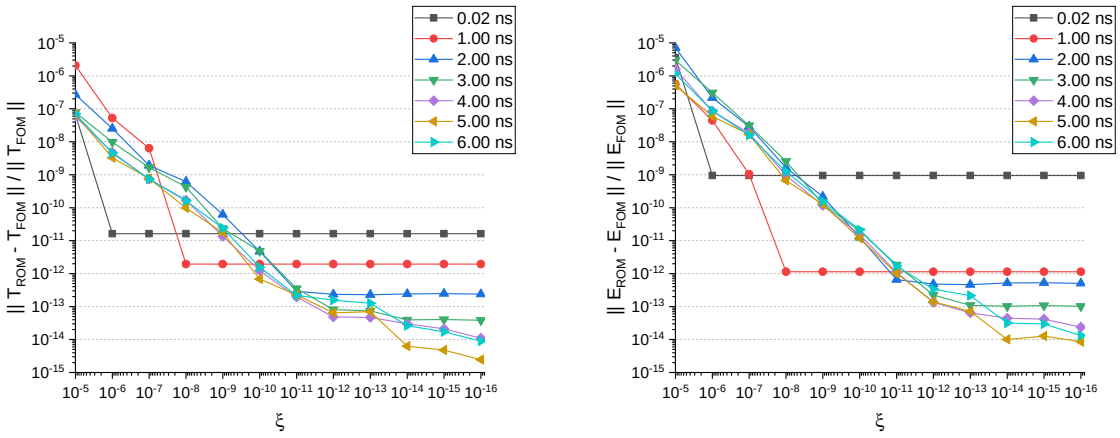

(a) Temperature

(b) Radiation Energy Density

Figure 6.4: Relative errors of the POD-G BTE-QD model compared to the FOM solution in the 2-norm vs. ξ

6.5 Discussion

In this chapter a new ROM for TRT problems is derived based on the nonlinear projection approach and Galerkin projection combined with the POD. The model is able to efficiently reduce the dimensionality of TRT problems and was demonstrated to produce solutions with high accuracy using low-rank expansions of the radiation intensities. The ROM errors w.r.t the FOM solution on the same grid in phase space and time are shown to converge linearly with the rank parameter ξ as well. The results demonstrate this ROM is able to effectively solve the nonlinear TRT problem using a low dimensional representation of the high-order solution, and therefore justify extensions of the model to 2D geometry or to parametric applications. Furthermore, the use of hyper-reduction techniques like the discrete empirical interpolation method (DEIM) or the DMD [153, 137] could be used to reduce the complexity of the ROM.

Preliminary investigations of this model in 2D Cartesian geometry have been explored. Here the numerical issues observed in 1D geometry are increased, and further development is required before this extension can be viable. One desirable feature is to enforce positivity of the expanded intensities. Work may also be done to improve the generation of POD bases, such as with the use of symmetry-reduction methods [148, 149] which are known to improve basis generation for traveling waves.

CHAPTER

7

A ROM USING A POD-BASED PROJECTION OF THE NBTE AND LOW-ORDER EQUATIONS

In this chapter a POD-Petrov-Galerkin projection of the normalized BTE is derived that can be coupled to the system of LOQD and MEB equations to solve TRT problems. The NBTE is first discretized with a novel scheme developed in this chapter. A Petrov-Galerkin projection is constructed for this discretized NBTE using full-order solutions of the radiation intensities that are retroactively normalized during the method's offline phase. This projection scheme is formulated in a matrix free way that is compatible with transport sweeps. The Eddington tensor that closes the system of low-order QD (VEF) equations is found as a linear superposition of the photon intensity shape function provided by the POD projected NBTE. In practice, the POD-Petrov-Galerkin projected NBTE is significantly lower in dimensionality than the moment equations it becomes coupled to. Furthermore this ROM is naturally parametric, since the projected NBTE includes nonlinear terms that depend on the material temperatures T.

7.1 The Normalized Boltzmann Transport Equation

In Ch. 4, a class of ROMs was developed to solve TRT problems with the multilevel set of LOQD and MEB equations by finding some data-based approximation of the Eddington tensor [82, 83]. In Ch. 6 a model was developed to approximate the Eddington tensor using a POD based projection of the BTE whose solution provides information on the high-order photon intensities in phase space [86]. In this Chapter, a ROM is derived by finding a POD based projection of the NBTE which can be coupled to the multilevel set of LOQD and MEB equations via the Eddington tensor. The viability and robustness of this proposed ROM is explored in detail here in the absence of consideration for parameterization and hyper-reduction. Such considerations are generally valuable only when they can be applied to a model whose fundamental behavior is well understood.

The NBTE is attractive because of its close relation to the Eddington tensor. The shape function of radiation intensities required to find the Eddington tensor is provided by the NBTE solution as the normalized radiation intensity distribution. The normalized intensities $\bar{I}$ lie in the same space as and are related to the Eddington tensor with a linear relationship. Therefore any global basis that describes $\bar{I}$ also directly describes the Eddington tensor by way of some linear superposition. In other words, the Eddington tensor will lie in the span of basis functions that describes the normalized intensities.

The normalized photon intensity function also has properties that make it more suitable than I for compression and description via few fundamental modes. For instance, $\bar{I}$ is naturally bounded by $\int_{4\pi} \bar{I}\, d\Omega = 1$, whereas I itself can span hundreds of orders of magnitude across phase space. In finite arithmetic this can limit the precision to which even a full rank POD basis can represent the radiation intensities. For the same calculations $\bar{I}$ will experience drastically less precision loss, and should even beget lower-rank representations with the same accuracy compared to I.

The NBTE (Eq. 1.16) can be used in place of the BTE in the MLQD system. In this case the Eddington tensor can be calculated with Eq. 1.14. Gol'din's boundary factors (Eq. 2.7) still take on a linear-fractional form when written in terms of $\bar{I}$ however. To make better use of $\bar{I}$ the low-order boundary conditions derived by Miften & Larsen [115, 116] (Eqs. 2.10 & 2.18) can be used instead, which are closed via the so-called 'boundary Eddington tensor' (Eq. 2.11) that exists in the same space as $\mathbf{f}_g$ and $\bar{I}$

$$G_g = \langle |\boldsymbol{n}_\Gamma \cdot \boldsymbol{\Omega}|, \bar{I}_g \rangle_\Omega. \tag{7.1}$$

Thus, the MLQD system for TRT problems can be reformulated using the NBTE as

1. The high-order NBTE
2. The multigroup LOQD system (Eqs. 2.3) with BCs in Eq. 2.10
3. The effective grey LOQD system (Eqs. 2.13) with BCs in Eq. 2.18
4. The MEB equation (Eq. 2.20)

7.1.1 Discretization of the Normalized Boltzmann Transport Equation

Here discretizations of the NBTE are derived in a consistent manner to those schemes shown in Sec. 2.3 for the BTE. In 2D Cartesian geometry, the NBTE (Eq. 1.15) is written as

$$\frac{1}{c}\frac{\partial(\phi_g\bar{I}_g)}{\partial t}+\Omega_x\frac{\partial(\phi_g\bar{I}_g)}{\partial x}+\Omega_y\frac{\partial(\phi_g\bar{I}_g)}{\partial y}+\varkappa_{E,g}(T)\phi_g\bar{I}_g=\varkappa_{B,g}(T)B_g(T), \tag{7.2}$$

with $\bar{I}_g=\bar{I}_g(x,y,\mathbf{\Omega},t)$ and $\phi_g=\phi_g(x,y,t)$. The NBTE is discretized in time using the implicit backward-Euler integration scheme and in angle using the method of discrete-ordinates, yielding

$$\frac{1}{c}\frac{\phi_g^n\bar{I}_{g,m}^n-\phi_g^{n-1}\bar{I}_{g,m}^{n-1}}{\Delta t^n}+\Omega_{x,m}\frac{\partial(\phi_g^n\bar{I}_{g,m}^n)}{\partial x}+\Omega_{y,m}\frac{\partial(\phi_g^n\bar{I}_{g,m}^n)}{\partial y}+\varkappa_{E,g}^n\phi_g^n\bar{I}_{g,m}^n=\varkappa_{B,g}^nB_g^n, \tag{7.3}$$

$$g=1,\ldots,N_g,\quad m=1,\ldots,N_\Omega,\quad n=1,\ldots$$

A reformulation of Eq. 7.3 that takes on a pseudo steady-state form can now be written as

$$\Omega_{x,m}\frac{\partial\phi_g^n\bar{I}_{g,m}^n}{\partial x}+\Omega_{y,m}\frac{\partial\phi_g^n\bar{I}_{g,m}^n}{\partial y}+\tilde{\varkappa}_{E,g}^n\phi_g^n\bar{I}_{g,m}^n=\bar{Q}_{g,m}^n, \tag{7.4}$$

with a modified opacity $\tilde{\varkappa}_{E,g}^n=\varkappa_{E,g}^n+\frac{1}{c\Delta t^n}$ and source $\bar{Q}_{g,m}^n=\varkappa_{B,g}^nB_g^n+\frac{\phi_g^{n-1}\bar{I}_{g,m}^{n-1}}{c\Delta t^n}$.

To derive a SCB (ref. Sec. 2.3.1) analogue for the NBTE, all cell- and subcell- averages must be conserved. In the following derivation g, m and n subscripts and superscripts are ignored for brevity. The SCB grid functions of normalized intensities are defined by the corresponding SCB grid functions of radiation intensities and their zeroth angular

moments to obtain the following unknowns in each cell:

$$\bar{I}_{i,j} = \frac{I_{i,j}}{\phi_{i,j}}, \quad \bar{I}_{i+\frac{1}{2},j} = \frac{I_{i+\frac{1}{2},j}}{\phi_{i+\frac{1}{2},j}}, \quad \bar{I}_{i,j+\frac{1}{2}} = \frac{I_{i,j+\frac{1}{2}}}{\phi_{i,j+\frac{1}{2}}}. \tag{7.5}$$

If the subcell averages (Eqs. 2.33) are to be preserved, then we have the following:

$$\bar{I}_{ij,1-} = \frac{I_{ij,1-}}{\phi_{i-\frac{1}{2},j}}, \quad \bar{I}_{ij,4+} = \frac{I_{ij,4+}}{\phi_{i-\frac{1}{2},j}}, \tag{7.6a}$$

$$\bar{I}_{ij,1+} = \frac{I_{ij,1+}}{\phi_{i,j-\frac{1}{2}}}, \quad \bar{I}_{ij,2-} = \frac{I_{ij,2-}}{\phi_{i,j-\frac{1}{2}}}, \tag{7.6b}$$

$$\bar{I}_{ij,2+} = \frac{I_{ij,2+}}{\phi_{i+\frac{1}{2},j}}, \quad \bar{I}_{ij,3-} = \frac{I_{ij,3-}}{\phi_{i+\frac{1}{2},j}}, \tag{7.6c}$$

$$\bar{I}_{ij,3+} = \frac{I_{ij,3+}}{\phi_{i,j+\frac{1}{2}}}, \quad \bar{I}_{ij,4-} = \frac{I_{ij,4-}}{\phi_{i,j+\frac{1}{2}}}, \tag{7.6d}$$

$$\bar{I}_{ij,1} = \frac{I_{ij,1}}{\phi_{ij}}, \quad \bar{I}_{ij,2} = \frac{I_{ij,2}}{\phi_{ij}}, \quad \bar{I}_{ij,3} = \frac{I_{ij,3}}{\phi_{ij}}, \quad \bar{I}_{ij,4} = \frac{I_{ij,4}}{\phi_{ij}}. \tag{7.6e}$$

The normalized intensities on each 'inner' subcell interface are given by

$$\bar{I}_{ij,\frac{1}{2}} = \frac{I_{ij,\frac{1}{2}}}{\phi_{ij}}, \quad \bar{I}_{ij,\frac{3}{2}} = \frac{I_{ij,\frac{3}{2}}}{\phi_{ij}}, \quad \bar{I}_{ij,\frac{5}{2}} = \frac{I_{ij,\frac{5}{2}}}{\phi_{ij}}, \quad \bar{I}_{ij,\frac{7}{2}} = \frac{I_{ij,\frac{7}{2}}}{\phi_{ij}}. \tag{7.7}$$

Eqs. 2.30, which represent spatial integration of the BTE over each subcell, can now be written for the NBTE as

$$\frac{1}{2}\Omega_x \Delta y_j \big(\bar{I}_{ij,\frac{3}{2}}\phi_{i,j} - \bar{I}_{ij,1-}\phi_{i-\frac{1}{2},j}\big) + \frac{1}{2}\Omega_y \Delta x_i \big(\bar{I}_{ij,\frac{1}{2}}\phi_{i,j} - \bar{I}_{ij,1+}\phi_{i,j-\frac{1}{2}}\big) + \frac{1}{4}\tilde{\varkappa}_{E,ij} A_{ij} \bar{I}_{ij,1}\phi_{i,j} = \frac{1}{4} A_{ij} \bar{Q}_{ij,1}, \tag{7.8a}$$

$$\frac{1}{2}\Omega_x \Delta y_j \big(\bar{I}_{ij,2+}\phi_{i+\frac{1}{2},j} - \bar{I}_{ij,\frac{3}{2}}\phi_{i,j}\big) + \frac{1}{2}\Omega_y \Delta x_i \big(\bar{I}_{ij,\frac{5}{2}}\phi_{i,j} - \bar{I}_{ij,2-}\phi_{i,j-\frac{1}{2}}\big) + \frac{1}{4}\tilde{\varkappa}_{E,ij} A_{ij} \bar{I}_{ij,2}\phi_{i,j} = \frac{1}{4} A_{ij} \bar{Q}_{ij,2}, \tag{7.8b}$$

$$\frac{1}{2}\Omega_x \Delta y_j \big(\bar{I}_{ij,3-}\phi_{i+\frac{1}{2},j} - \bar{I}_{ij,\frac{7}{2}}\phi_{i,j}\big) + \frac{1}{2}\Omega_y \Delta x_i \big(\bar{I}_{ij,3+}\phi_{i,j+\frac{1}{2}} - \bar{I}_{ij,\frac{5}{2}}\phi_{i,j}\big) + \frac{1}{4}\tilde{\varkappa}_{E,ij} A_{ij} \bar{I}_{ij,3}\phi_{i,j} = \frac{1}{4} A_{ij} \bar{Q}_{ij,3}, \tag{7.8c}$$

$$\frac{1}{2}\Omega_x\Delta y_j\big(\bar{I}_{ij,\frac{7}{2}}\phi_{i,j}-\bar{I}_{ij,4+}\phi_{i-\frac{1}{2},j}\big)+\frac{1}{2}\Omega_y\Delta x_i\big(\bar{I}_{ij,4-}\phi_{i,j+\frac{1}{2}}-\bar{I}_{ij,\frac{1}{2}}\phi_{i,j}\big)$$
$$+\frac{1}{4}\tilde{\varkappa}_{E,ij}A_{ij}\bar{I}_{ij,4}\phi_{i,j}=\frac{1}{4}A_{ij}\bar{Q}_{ij,4}. \quad (7.8d)$$

Eqs. 7.8 are by nature scaled to the magnitude of I. To formulate a discretization whose equations (and their residuals) are scaled to the same magnitude as $\bar{I}$, $\phi_{i,j}^{-1}$ is applied to find the following subcell-integral relations

$$\frac{1}{2}\Omega_x\Delta y_j\left(\bar{I}_{ij,\frac{3}{2}}-\frac{\phi_{i-\frac{1}{2},j}}{\phi_{i,j}}\bar{I}_{ij,1-}\right)+\frac{1}{2}\Omega_y\Delta x_i\left(\bar{I}_{ij,\frac{1}{2}}-\frac{\phi_{i,j-\frac{1}{2}}}{\phi_{i,j}}\bar{I}_{ij,1+}\right)$$
$$+\frac{1}{4}\tilde{\varkappa}_{E,ij}A_{ij}\bar{I}_{ij,1}=\frac{1}{4}A_{ij}\hat{\bar{Q}}_{ij,1}, \quad (7.9a)$$

$$\frac{1}{2}\Omega_x\Delta y_j\left(\frac{\phi_{i+\frac{1}{2},j}}{\phi_{i,j}}\bar{I}_{ij,2+}-\bar{I}_{ij,\frac{3}{2}}\right)+\frac{1}{2}\Omega_y\Delta x_i\left(\bar{I}_{ij,\frac{5}{2}}-\frac{\phi_{i,j-\frac{1}{2}}}{\phi_{i,j}}\bar{I}_{ij,2-}\right)$$
$$+\frac{1}{4}\tilde{\varkappa}_{E,ij}A_{ij}\bar{I}_{ij,2}=\frac{1}{4}A_{ij}\hat{\bar{Q}}_{ij,2}, \quad (7.9b)$$

$$\frac{1}{2}\Omega_x\Delta y_j\left(\frac{\phi_{i+\frac{1}{2},j}}{\phi_{i,j}}\bar{I}_{ij,3-}-\bar{I}_{ij,\frac{7}{2}}\right)+\frac{1}{2}\Omega_y\Delta x_i\left(\frac{\phi_{i,j+\frac{1}{2}}}{\phi_{i,j}}\bar{I}_{ij,3+}-\bar{I}_{ij,\frac{5}{2}}\right)$$
$$+\frac{1}{4}\tilde{\varkappa}_{E,ij}A_{ij}\bar{I}_{ij,3}=\frac{1}{4}A_{ij}\hat{\bar{Q}}_{ij,3}, \quad (7.9c)$$

$$\frac{1}{2}\Omega_x\Delta y_j\left(\bar{I}_{ij,\frac{7}{2}}-\frac{\phi_{i-\frac{1}{2},j}}{\phi_{i,j}}\bar{I}_{ij,4+}\right)+\frac{1}{2}\Omega_y\Delta x_i\left(\frac{\phi_{i,j+\frac{1}{2}}}{\phi_{i,j}}\bar{I}_{ij,4-}-\bar{I}_{ij,\frac{1}{2}}\right)$$
$$+\frac{1}{4}\tilde{\varkappa}_{E,ij}A_{ij}\bar{I}_{ij,4}=\frac{1}{4}A_{ij}\hat{\bar{Q}}_{ij,4}, \quad (7.9d)$$

where $\hat{\bar{Q}}^n_{ij,k}=\varkappa_{B,ij}\bar{B}_{ij}+\frac{\phi^{n-1}_{ij}}{\phi^n_{ij}}\frac{\bar{I}^{n-1}_{ij,k}}{c\Delta t^n}$ and $\bar{B}$ is defined in Eq. 1.17. Finally, the upwinding conditions for I (Eqs. 2.32) take on the following form for $\bar{I}$

$$\bar{I}_{ij,2+}=\frac{\phi_{i,j}}{\phi_{i+\frac{1}{2},j}}\bar{I}_{ij,2},\ \bar{I}_{ij,3+}=\frac{\phi_{i,j}}{\phi_{i,j+\frac{1}{2}}}\bar{I}_{ij,3},$$
$$\bar{I}_{ij,3-}=\frac{\phi_{i,j}}{\phi_{i+\frac{1}{2},j}}\bar{I}_{ij,3},\ \bar{I}_{ij,4-}=\frac{\phi_{i,j}}{\phi_{i,j+\frac{1}{2}}}\bar{I}_{ij,4},\quad \Omega_x>0,\Omega_y>0 \quad (7.10a)$$

$$\bar{I}_{ij,3+} = \frac{\phi_{i,j}}{\phi_{i,j+\frac{1}{2}}}\bar{I}_{ij,3},\ \bar{I}_{ij,4+} = \frac{\phi_{i,j}}{\phi_{i-\frac{1}{2},j}}\bar{I}_{ij,4},$$

$$\bar{I}_{ij,4-} = \frac{\phi_{i,j}}{\phi_{i,j+\frac{1}{2}}}\bar{I}_{ij,4},\ \bar{I}_{ij,1-} = \frac{\phi_{i,j}}{\phi_{i-\frac{1}{2},j}}\bar{I}_{ij,1},\quad \Omega_x < 0, \Omega_y > 0 \quad (7.10b)$$

$$\bar{I}_{ij,4+} = \frac{\phi_{i,j}}{\phi_{i-\frac{1}{2},j}}\bar{I}_{ij,4},\ \bar{I}_{ij,1+} = \frac{\phi_{i,j}}{\phi_{i,j-\frac{1}{2}}}\bar{I}_{ij,1},$$

$$\bar{I}_{ij,1-} = \frac{\phi_{i,j}}{\phi_{i-\frac{1}{2},j}}\bar{I}_{ij,1},\ \bar{I}_{ij,2-} = \frac{\phi_{i,j}}{\phi_{i,j-\frac{1}{2}}}\bar{I}_{ij,2},\quad \Omega_x < 0, \Omega_y < 0 \quad (7.10c)$$

$$\bar{I}_{ij,1+} = \frac{\phi_{i,j}}{\phi_{i,j-\frac{1}{2}}}\bar{I}_{ij,1},\ \bar{I}_{ij,2+} = \frac{\phi_{i,j}}{\phi_{i+\frac{1}{2},j}}\bar{I}_{ij,2},$$

$$\bar{I}_{ij,2-} = \frac{\phi_{i,j}}{\phi_{i,j-\frac{1}{2}}}\bar{I}_{ij,2},\ \bar{I}_{ij,3-} = \frac{\phi_{i,j}}{\phi_{i+\frac{1}{2},j}}\bar{I}_{ij,3},\quad \Omega_x > 0, \Omega_y < 0 \quad (7.10d)$$

7.2 Projection of the Normalized Boltzmann Transport Equation

A POD-Petrov-Galerkin projection is derived here for the NBTE. A Petrov-Galerkin scheme is selected to minimize the effects of numerical noise, which were observed with the POD-Galerkin projection of the BTE in Ch. 6. The Petrov-Galerkin technique will also enforce an optimality condition on the resulting form of the NBTE (see Sec. 3.3.2). This will ensure the derived ROM's accuracy will be maximal in a certain norm. The continuous case is addressed first before the discrete case. Let the NBTE (Eq. 1.16) be written in operator notation as follows

$$\frac{1}{c}\partial_t \bar{\boldsymbol{I}} + \mathcal{L}\bar{\boldsymbol{I}} + \hat{\mathcal{K}}(T, \boldsymbol{\phi})\bar{\boldsymbol{I}} = \bar{\mathcal{Q}}(T, \boldsymbol{\phi}), \quad (7.11)$$

where $\bar{\boldsymbol{I}} = (\bar{I}_1, \ldots, \bar{I}_{N_g})^\top$, $\boldsymbol{\phi} = (\phi_1, \ldots, \phi_{N_g})^\top$,

$$\mathcal{L} \equiv \boldsymbol{\Omega} \cdot \boldsymbol{\nabla}, \quad \hat{\mathcal{K}} \equiv \mathrm{diag}(\hat{\varkappa}_{E,1}, \ldots, \hat{\varkappa}_{E,N_g}), \quad \bar{\mathcal{Q}} \equiv (\varkappa_{B,1}\bar{B}_1, \ldots, \varkappa_{B,N_g}\bar{B}_{N_g})^\top \quad (7.12)$$

where $\hat{\varkappa}_{E,g}$ is defined by Eq. 1.18.

The normalized radiation intensities are expanded in a set of basis functions $\{\boldsymbol{u}_\ell\}_{\ell=1}^k$

that span all phase space

$$\bar{\boldsymbol{I}}_k(\boldsymbol{r},\boldsymbol{\Omega},t)=\sum_{\ell=1}^{k}\lambda_\ell(t)\boldsymbol{u}_\ell(\boldsymbol{r},\boldsymbol{\Omega}), \tag{7.13}$$

with $\boldsymbol{u}_\ell=(u_{\ell,1}\ldots,u_{\ell,N_g})^\top$. This expansion is then substituted in Eq. 7.11 to find

$$\sum_{\ell=1}^{k}\left[\frac{1}{c}\boldsymbol{u}_\ell\partial_t\lambda_\ell+\lambda_\ell\boldsymbol{\mathcal{L}}\boldsymbol{u}_\ell+\lambda_\ell\hat{\mathcal{K}}(T,\boldsymbol{\phi})\boldsymbol{u}_\ell\right]=\bar{\mathcal{Q}}(T,\boldsymbol{\phi}). \tag{7.14}$$

A Petrov-Galerkin projection of this equation onto some test basis $\{\boldsymbol{\psi}_\ell\}_{\ell=1}^k$ with $\boldsymbol{\psi}_\ell=(\psi_{\ell,1}\ldots,\psi_{\ell,N_g})^\top$ is sought. From Thm. 3.3.1 these basis functions are defined as $\boldsymbol{\psi}_\ell=\frac{d\mathcal{R}(\lambda_\ell\boldsymbol{u}_\ell)}{d\lambda_\ell}$, noting that the optimality of this basis is strictly in the discrete case and does not necessarily hold true in continuous space [140]. The residual operator $\mathcal{R}$ for the NBTE is defined from Eq. 7.11 as

$$\mathcal{R}\bar{\boldsymbol{I}}=\mathcal{J}\bar{\boldsymbol{I}}-\bar{\mathcal{Q}}, \tag{7.15}$$

where

$$\mathcal{J}=\partial_t+\boldsymbol{\mathcal{L}}+\hat{\mathcal{K}}. \tag{7.16}$$

Eq. 7.14 is projected onto this test basis with the inner product $\langle\boldsymbol{\psi}_{\ell'},\cdot\rangle$ for all $\ell'=1,\ldots,k$ to find the following ODE for $\lambda_\ell(t)$:

$$\sum_{\ell=1}^{k}\left[\frac{1}{c}\langle\boldsymbol{\psi}_{\ell'},\boldsymbol{u}_\ell\rangle\partial_t\lambda_\ell+\lambda_\ell\langle\boldsymbol{\psi}_{\ell'},\boldsymbol{\mathcal{L}}\boldsymbol{u}_\ell\rangle+\lambda_\ell\langle\boldsymbol{\psi}_{\ell'},\hat{\mathcal{K}}(T,\boldsymbol{\phi})\boldsymbol{u}_\ell\rangle\right]=\langle\boldsymbol{\psi}_{\ell'},\bar{\mathcal{Q}}(T,\boldsymbol{\phi})\rangle, \tag{7.17a}$$

$$\sum_{\ell=1}^{k}\langle\boldsymbol{\psi}_{\ell'},\boldsymbol{u}_\ell\rangle\lambda_\ell|_{t=0}=\langle\boldsymbol{\psi}_{\ell'},\boldsymbol{I}|_{t=0}\rangle \tag{7.17b}$$

$$\ell'=1,\ldots,k.$$

This inner product is defined in Eq. 6.6.

7.3 Projection in Discrete Space

The fully discrete NBTE can be written in operator notation in the same form as in Eq. 7.11. However, using the scheme outlined in Sec. 7.1.1, it is more straightforward to write

the discrete NBTE in the form

$$\mathcal{T}_h(\boldsymbol{\phi}^n, \boldsymbol{\phi}^{n-1})\bar{\boldsymbol{I}}^n + \mathcal{L}_h(\boldsymbol{\phi}^n)\bar{\boldsymbol{I}}^n + \mathcal{K}_h^n(T)\bar{\boldsymbol{I}}^n = \bar{\mathcal{Q}}_h^n(T, \boldsymbol{\phi}^n) + \bar{\mathcal{B}}_h(\boldsymbol{\phi}^n), \tag{7.18}$$

where $\bar{\boldsymbol{I}}^n \in \mathbb{R}^{\mathfrak{N}_I}$ holds the grid functions of the normalized radiation intensity across all phase space at the n^{th} instance of time, $\boldsymbol{\phi}^n \in \mathbb{R}^{\mathfrak{N}_\phi}$ holds the grid functions of the zeroth intensity moment over space and frequency at the n^{th} instance of time, $\mathcal{T}_h$ represents the discrete form of the time derivative in Eq. 7.2, and $\bar{\mathcal{B}}_h$ subsumes the boundary conditions on $\bar{I}$. The elements of $\bar{\boldsymbol{I}}^n$ are $\bar{I}^n_{g,m,i,j,l}$ with $g = 1, \ldots, N_g$, $m = 1, \ldots, N_\Omega$, $i = 1, \ldots, N_x$, $j = 1, \ldots, N_y$ being indexes of the frequency group, direction of motion, and $x-y$ position on the spatial grid, respectively. $l = 1, 2, 3, 4$ denotes the corner index of a spatial cell and thus $\mathfrak{N}_I = 4N_gN_\Omega N_yN_x$. The elements of $\boldsymbol{\phi}^n$ are similarly $\phi^n_{g,i,j}$ so that $\mathfrak{N}_\phi = N_gN_yN_x$.

Each of the discrete operators is defined as follows. The (backward Euler) temporal integration operator $\mathcal{T}_h : \mathbb{R}^{\mathfrak{N}_I} \to \mathbb{R}^{\mathfrak{N}_I}$ is defined as

$$(\mathcal{T}_h(\boldsymbol{\phi}^n, \boldsymbol{\phi}^{n-1})\bar{\boldsymbol{I}}^n)_{g,m,i,j,l} = \frac{1}{c\Delta t^n}\left(\bar{I}^n_{g,m,i,j,l} - \frac{\phi^{n-1}_{g,i,j}}{\phi^n_{g,i,j}}\bar{I}^{n-1}_{g,m,i,j,l}\right). \tag{7.19}$$

The operator $\mathcal{K}_h^n : \mathbb{R}^{\mathfrak{N}_I} \to \mathbb{R}^{\mathfrak{N}_I}$ is

$$(\mathcal{K}_h^n(T)\bar{\boldsymbol{I}}^n)_{g,m,i,j,l} = \varkappa^n_{E,g,i,j}(T)\bar{I}^n_{g,m,i,j,l}. \tag{7.20}$$

The source vector $\bar{\mathcal{Q}}_h^n \in \mathbb{R}^{\mathfrak{N}_I}$ has elements

$$(\bar{\mathcal{Q}}_h^n(T, \boldsymbol{\phi}^n))_{g,m,i,j,l} = \varkappa^n_{B,g,i,j}(T)\bar{B}^n_{g,i,j}(T, \boldsymbol{\phi}^n). \tag{7.21}$$

The spatial (streaming) operator $\mathcal{L}_h : \mathbb{R}^{\mathfrak{N}_I} \to \mathbb{R}^{\mathfrak{N}_I}$ can be split into $\mathcal{L}_h = \mathcal{L}_{1,h} + \mathcal{L}_{2,h}$, where $\mathcal{L}_{1,h}$ is defined as

$$\begin{bmatrix} (\mathcal{L}_{1,h}\bar{\boldsymbol{I}}^n)_{g,m,i,j,1} \\ (\mathcal{L}_{1,h}\bar{\boldsymbol{I}}^n)_{g,m,i,j,2} \\ (\mathcal{L}_{1,h}\bar{\boldsymbol{I}}^n)_{g,m,i,j,3} \\ (\mathcal{L}_{1,h}\bar{\boldsymbol{I}}^n)_{g,m,i,j,4} \end{bmatrix} = \begin{bmatrix} \gamma_{m,i,j} & \frac{\Omega_{x,m}}{\Delta x_i} & 0 & \frac{\Omega_{y,m}}{\Delta y_j} \\ -\frac{\Omega_{x,m}}{\Delta x_i} & \gamma_{m,i,j} & \frac{\Omega_{y,m}}{\Delta y_j} & 0 \\ 0 & -\frac{\Omega_{y,m}}{\Delta y_j} & \gamma_{m,i,j} & -\frac{\Omega_{x,m}}{\Delta x_i} \\ -\frac{\Omega_{y,m}}{\Delta y_j} & 0 & \frac{\Omega_{x,m}}{\Delta x_i} & \gamma_{m,i,j} \end{bmatrix} \begin{bmatrix} \bar{I}^n_{g,m,i,j,1} \\ \bar{I}^n_{g,m,i,j,2} \\ \bar{I}^n_{g,m,i,j,3} \\ \bar{I}^n_{g,m,i,j,4} \end{bmatrix}, \tag{7.22}$$

where

$$\gamma_{m,i,j} = \frac{|\Omega_{x,m}|}{\Delta x_i} + \frac{|\Omega_{y,m}|}{\Delta y_j}. \tag{7.23}$$

Using $\alpha_{i,j} = 1 - \delta_{i,j}$, the operator $\mathcal{L}_{2,h}$ is defined such that

$$(\mathcal{L}_{2,h}\bar{\boldsymbol{I}})_{g,m,ij,1} = \begin{cases} \alpha_{1,i}\frac{2\Omega_{x,m}}{\Delta x_i}\frac{\phi^n_{g,i-1,j}}{\phi^n_{g,i,j}}\bar{I}^n_{g,m,i-1j,2} & \\ \qquad + \alpha_{1,j}\frac{2\Omega_{y,m}}{\Delta y_j}\frac{\phi^n_{g,i,j-1}}{\phi^n_{g,i,j}}\bar{I}^n_{g,m,ij-1,4}, & \Omega_x > 0,\ \Omega_y > 0 \\ \alpha_{1,j}\frac{2\Omega_{y,m}}{\Delta y_j}\frac{\phi^n_{g,i,j-1}}{\phi^n_{g,i,j}}\bar{I}^n_{g,m,ij-1,4}, & \Omega_x < 0,\ \Omega_y > 0 \\ 0, & \Omega_x < 0,\ \Omega_y < 0 \\ \alpha_{1,i}\frac{2\Omega_{x,m}}{\Delta x_i}\frac{\phi^n_{g,i-1,j}}{\phi^n_{g,i,j}}\bar{I}^n_{g,m,i-1j,2}, & \Omega_x > 0,\ \Omega_y < 0 \end{cases} \tag{7.24a}$$

$$(\mathcal{L}_{2,h}\bar{\boldsymbol{I}})_{g,m,ij,2} = \begin{cases} \alpha_{1,j}\frac{2\Omega_{y,m}}{\Delta y_j}\frac{\phi^n_{g,i,j-1}}{\phi^n_{g,i,j}}\bar{I}^n_{g,m,ij-1,3}, & \Omega_x > 0,\ \Omega_y > 0 \\ -\alpha_{N_x,i}\frac{2\Omega_{x,m}}{\Delta x_i}\frac{\phi^n_{g,i+1,j}}{\phi^n_{g,i,j}}\bar{I}^n_{g,m,i+1j,1} & \\ \qquad + \alpha_{1,j}\frac{2\Omega_{y,m}}{\Delta y_j}\frac{\phi^n_{g,i,j-1}}{\phi^n_{g,i,j}}\bar{I}^n_{g,m,ij-1,3}, & \Omega_x < 0,\ \Omega_y > 0 \\ -\alpha_{N_x,i}\frac{2\Omega_{x,m}}{\Delta x_i}\frac{\phi^n_{g,i+1,j}}{\phi^n_{g,i,j}}\bar{I}^n_{g,m,i+1j,1}, & \Omega_x < 0,\ \Omega_y < 0 \\ 0, & \Omega_x > 0,\ \Omega_y < 0 \end{cases} \tag{7.24b}$$

$$(\mathcal{L}_{2,h}\bar{\boldsymbol{I}})_{g,m,ij,3} = \begin{cases} 0, & \Omega_x > 0,\ \Omega_y > 0 \\ -\alpha_{N_x,i}\frac{2\Omega_{x,m}}{\Delta x_i}\frac{\phi^n_{g,i+1,j}}{\phi^n_{g,i,j}}\bar{I}^n_{g,m,i+1j,4}, & \Omega_x < 0,\ \Omega_y > 0 \\ -\alpha_{N_x,i}\frac{2\Omega_{x,m}}{\Delta x_i}\frac{\phi^n_{g,i+1,j}}{\phi^n_{g,i,j}}\bar{I}^n_{g,m,i+1j,4} & \\ \qquad - \alpha_{N_y,j}\frac{2\Omega_{y,m}}{\Delta y_j}\frac{\phi^n_{g,i,j+1}}{\phi^n_{g,i,j}}\bar{I}^n_{g,m,ij+1,2}, & \Omega_x < 0,\ \Omega_y < 0 \\ -\alpha_{N_y,j}\frac{2\Omega_{y,m}}{\Delta y_j}\frac{\phi^n_{g,i,j+1}}{\phi^n_{g,i,j}}\bar{I}^n_{g,m,ij+1,2}, & \Omega_x > 0,\ \Omega_y < 0 \end{cases} \tag{7.24c}$$

$$(\mathcal{L}_{2,h}\bar{\boldsymbol{I}})_{g,m,ij,4} = \begin{cases} \alpha_{1,i}\frac{2\Omega_{x,m}}{\Delta x_i}\frac{\phi^n_{g,i-1,j}}{\phi^n_{g,i,j}}\bar{I}^n_{g,m,i-1j,3}, & \Omega_x > 0,\ \Omega_y > 0 \\ 0, & \Omega_x < 0,\ \Omega_y > 0 \\ -\alpha_{N_y,j}\frac{2\Omega_{y,m}}{\Delta y_j}\frac{\phi^n_{g,i,j+1}}{\phi^n_{g,i,j}}\bar{I}^n_{g,m,ij+1,1}, & \Omega_x < 0,\ \Omega_y < 0 \\ \alpha_{1,i}\frac{2\Omega_{x,m}}{\Delta x_i}\frac{\phi^n_{g,i-1,j}}{\phi^n_{g,i,j}}\bar{I}^n_{g,m,i-1j,3} & \\ \qquad - \alpha_{N_y,j}\frac{2\Omega_{y,m}}{\Delta y_j}\frac{\phi^n_{g,i,j+1}}{\phi^n_{g,i,j}}\bar{I}^n_{g,m,ij+1,1}, & \Omega_x > 0,\ \Omega_y < 0 \end{cases} \tag{7.24d}$$

The boundary vector $\bar{\mathcal{B}}_h \in \mathbb{R}^{\mathfrak{N}_I}$ which contains the boundary sources of the problem

assumes the following boundary conditions for the normalized radiation intensities

$$\bar{I}_g|_{x=0} = \bar{I}^{\text{in}}_{L,g} = \frac{I^{\text{in}}_{L,g}}{\phi_{L,g}}, \quad \Omega_{x,m} > 0, \tag{7.25a}$$

$$\bar{I}_g|_{y=0} = \bar{I}^{\text{in}}_{B,g} = \frac{I^{\text{in}}_{B,g}}{\phi_{B,g}}, \quad \Omega_{y,m} > 0, \tag{7.25b}$$

$$\bar{I}_g|_{x=L_x} = \bar{I}^{\text{in}}_{R,g} = \frac{I^{\text{in}}_{R,g}}{\phi_{R,g}}, \quad \Omega_{x,m} < 0, \tag{7.25c}$$

$$\bar{I}_g|_{y=L_y} = \bar{I}^{\text{in}}_{T,g} = \frac{I^{\text{in}}_{T,g}}{\phi_{T,g}}, \quad \Omega_{y,m} < 0 \tag{7.25d}$$

where L_x and L_y are the domain lengths in the x and y directions, respectively, and

$$\phi_{L,g} = \phi_g|_{x=0}, \quad \phi_{B,g} = \phi_g|_{y=0}, \quad \phi_{R,g} = \phi_g|_{x=L_x}, \quad \phi_{T,g} = \phi_g|_{y=L_y}. \tag{7.26}$$

Using these boundary conditions, $\bar{\mathcal{B}}_h$ takes the form

$$(\bar{\mathcal{B}}_h)_{g,m,ij,1} = \begin{cases} \delta_{1,i}\frac{2\Omega_{x,m}}{\Delta x_i}\frac{\phi^n_{L,g,j}}{\phi^n_{g,1,j}}\bar{I}^{\text{in}}_{L,g,m,j} + \delta_{1,j}\frac{2\Omega_{y,m}}{\Delta y_j}\frac{\phi^n_{B,g,i}}{\phi^n_{g,i,1}}\bar{I}^{\text{in}}_{B,g,m,i}, & \Omega_x > 0,\ \Omega_y > 0 \\ \delta_{1,j}\frac{2\Omega_{y,m}}{\Delta y_j}\frac{\phi^n_{B,g,i}}{\phi^n_{g,i,1}}\bar{I}^{\text{in}}_{B,g,m,i}, & \Omega_x < 0,\ \Omega_y > 0 \\ 0, & \Omega_x < 0,\ \Omega_y < 0 \\ \delta_{1,i}\frac{2\Omega_{x,m}}{\Delta x_i}\frac{\phi^n_{L,g,j}}{\phi^n_{g,1,j}}\bar{I}^{\text{in}}_{L,g,m,j}, & \Omega_x > 0,\ \Omega_y < 0 \end{cases} \tag{7.27a}$$

$$(\bar{\mathcal{B}}_h)_{g,m,ij,2} = \begin{cases} \delta_{1,j}\frac{2\Omega_{y,m}}{\Delta y_j}\frac{\phi^n_{B,g,i}}{\phi^n_{g,i,1}}\bar{I}^{\text{in}}_{B,g,m,i}, & \Omega_x > 0,\ \Omega_y > 0 \\ -\delta_{N_x,i}\frac{2\Omega_{x,m}}{\Delta x_i}\frac{\phi^n_{R,g,j}}{\phi^n_{g,N_x,j}}\bar{I}^{\text{in}}_{R,g,m,j} + \delta_{1,j}\frac{2\Omega_{y,m}}{\Delta y_j}\frac{\phi^n_{B,g,i}}{\phi^n_{g,i,1}}\bar{I}^{\text{in}}_{B,g,m,i}, & \Omega_x < 0,\ \Omega_y > 0 \\ -\delta_{N_x,i}\frac{2\Omega_{x,m}}{\Delta x_i}\frac{\phi^n_{R,g,j}}{\phi^n_{g,N_x,j}}\bar{I}^{\text{in}}_{R,g,m,j}, & \Omega_x < 0,\ \Omega_y < 0 \\ 0, & \Omega_x > 0,\ \Omega_y < 0 \end{cases} \tag{7.27b}$$

$$(\bar{\mathcal{B}}_h)_{g,m,ij,3} = \begin{cases} 0, & \Omega_x > 0,\ \Omega_y > 0 \\ -\delta_{N_x,i}\frac{2\Omega_{x,m}}{\Delta x_i}\frac{\phi^n_{R,g,j}}{\phi^n_{g,N_x,j}}\bar{I}^{\text{in}}_{R,g,m,j}, & \Omega_x < 0,\ \Omega_y > 0 \\ -\delta_{N_x,i}\frac{2\Omega_{x,m}}{\Delta x_i}\frac{\phi^n_{R,g,j}}{\phi^n_{g,N_x,j}}\bar{I}^{\text{in}}_{R,g,m,j} - \delta_{N_y,j}\frac{2\Omega_{y,m}}{\Delta y_j}\frac{\phi^n_{T,g,i}}{\phi^n_{g,i,N_y}}\bar{I}^{\text{in}}_{T,g,m,i}, & \Omega_x < 0,\ \Omega_y < 0 \\ -\delta_{N_y,j}\frac{2\Omega_{y,m}}{\Delta y_j}\frac{\phi^n_{T,g,i}}{\phi^n_{g,i,N_y}}\bar{I}^{\text{in}}_{T,g,m,i}, & \Omega_x > 0,\ \Omega_y < 0 \end{cases} \tag{7.27c}$$

$$(\bar{\mathcal{B}}_h)_{g,m,ij,4} = \begin{cases} \delta_{1,i}\frac{2\Omega_{x,m}}{\Delta x_i}\frac{\phi^n_{L,g,j}}{\phi^n_{g,1,j}}\bar{I}^{\text{in}}_{L,g,m,j}, & \Omega_x > 0,\ \Omega_y > 0 \\ 0, & \Omega_x < 0,\ \Omega_y > 0 \\ -\delta_{N_y,j}\frac{2\Omega_{y,m}}{\Delta y_j}\frac{\phi^n_{T,g,i}}{\phi^n_{g,i,N_y}}\bar{I}^{\text{in}}_{T,g,m,i}, & \Omega_x < 0,\ \Omega_y < 0 \\ \delta_{1,i}\frac{2\Omega_{x,m}}{\Delta x_i}\frac{\phi^n_{L,g,j}}{\phi^n_{g,1,j}}\bar{I}^{\text{in}}_{L,g,m,j} - \delta_{N_y,j}\frac{2\Omega_{y,m}}{\Delta y_j}\frac{\phi^n_{T,g,i}}{\phi^n_{g,i,N_y}}\bar{I}^{\text{in}}_{T,g,m,i}, & \Omega_x > 0,\ \Omega_y < 0 \end{cases} \tag{7.27d}$$

7.3.1 Scaling Equations with Opacity

When calculating inner products of Eq. 7.18 over all phase space, one possible source of numerical precision loss lies in the opacity function. In the multiphysical class of problems considered, $\varkappa$ can span many orders of magnitude across phase space, most especially across variations in photon frequency (see for instance, Fig. D.1). A method to reduce the numerical effects that this introduces is to scale the discrete NBTE equations in each cell and frequency group by $\varkappa$ in the same portion of phase space. This is achieved through the operator $(\tilde{\mathcal{K}}^n)^{-1} : \mathbb{R}^{\mathfrak{N}_I} \to \mathbb{R}^{\mathfrak{N}_I}$, defined as

$$\left((\tilde{\mathcal{K}}^n)^{-1}\boldsymbol{u}\right)_{g,m,i,j,l} = \begin{cases} \frac{1}{\varkappa^n_{E,g,i,j}}u_{g,m,i,j,l}, & g \in \hat{\mathbb{G}} \\ u_{g,m,i,j,l}, & g \notin \hat{\mathbb{G}} \end{cases} \tag{7.28}$$

where $\hat{\mathbb{G}} \subset \{1, \ldots, N_g\}$. When $(\tilde{\mathcal{K}}^n)^{-1}$ is applied to the discrete NBTE, each equation for the $(i,j)^{\text{th}}$ spatial cell for the m^{th} direction of motion in the g^{th} frequency group will be scaled by $\varkappa^n_{E,g,i,j}$, if $g \in \hat{\mathbb{G}}$. One reasonable set of frequency groups to comprise $\hat{\mathbb{G}}$ are those whose opacities are expected to be very large. Application of this operator to the left of Eq. 7.18 yields

$$\begin{aligned}(\tilde{\mathcal{K}}^n)^{-1}\Big(\mathcal{T}_h(\boldsymbol{\phi}^n, \boldsymbol{\phi}^{n-1})\bar{\boldsymbol{I}}^n + \mathcal{L}_h(\boldsymbol{\phi}^n)\bar{\boldsymbol{I}}^n + \mathcal{K}^n_h(T)\bar{\boldsymbol{I}}^n\Big) \\ = (\tilde{\mathcal{K}}^n)^{-1}\Big(\bar{\mathcal{Q}}^n_h(T, \boldsymbol{\phi}^n) + \bar{\mathcal{B}}_h(\boldsymbol{\phi}^n)\Big),\end{aligned} \tag{7.29}$$

or more concisely,

$$\check{\mathcal{T}}_h(\boldsymbol{\phi}^n, \boldsymbol{\phi}^{n-1})\bar{\boldsymbol{I}}^n + \check{\mathcal{L}}_h(\boldsymbol{\phi}^n)\bar{\boldsymbol{I}}^n + \check{\mathcal{K}}^n_h(T)\bar{\boldsymbol{I}}^n = \check{\bar{\mathcal{Q}}}^n_h(T, \boldsymbol{\phi}^n) + \check{\bar{\mathcal{B}}}_h(\boldsymbol{\phi}^n). \tag{7.30}$$

7.3.2 Formulation of POD Basis & Petrov-Galerkin Projection

In the framework of the MLQD equations, there exist two distinct pathways to collect an identical set of FOM snapshots for $\bar{I}$, which are assembled into a snapshot matrix and used to calculate the POD basis. The first way is to solve the target TRT problem with the MLQD system equipped with the NBTE. The second is to solve the TRT problem with the MLQD system equipped with the BTE and alternate boundary conditions given in Eqs. 2.10 & 2.18, and calculate snapshots of $\bar{I}$ from the obtained snapshots of I. This second procedure is the one elected to derive the following ROMs. From the solution to the BTE discretized with the SCB scheme over N_t time steps, the cell-corner intensity vectors are collected in the set $\{\boldsymbol{I}^n\}_{n=1}^{N_t}$. The set of normalized cell-corner intensity values $\{\bar{\boldsymbol{I}}^n\}_{n=1}^{N_t}$ can then be calculated by

$$\bar{I}^n_{g,m,i,j,l} = \frac{I^n_{g,m,i,j,l}}{\frac{1}{4}\sum_{m=1}^{N_\Omega} w_m (I^n_{g,m,i,j,1} + I^n_{g,m,i,j,2} + I^n_{g,m,i,j,3} + I^n_{g,m,i,j,4})}, \tag{7.31}$$

where $l = 1, 2, 3, 4$ and $\{w_m\}_{m=1}^{N_\Omega}$ are the angular quadrature weights associated with the discrete-ordinates scheme. The obtained snapshot vectors are collected in chronological order to construct following data matrix

$$\mathbf{A}^{\bar{I}} = [\bar{\boldsymbol{I}}^1 \ \bar{\boldsymbol{I}}^2 \ \dots \ \bar{\boldsymbol{I}}^{N_t}] \in \mathbb{R}^{\mathfrak{N}_I \times N_t}. \tag{7.32}$$

The POD basis that optimally represents the snapshots in $\mathbf{A}^{\bar{I}}$ in the W norm (ref. Eq. 3.30) is found via the weighted snapshot matrix

$$\hat{\mathbf{A}}^{\bar{I}} = \mathbf{W}^{1/2}\mathbf{A}^{\bar{I}}\mathbf{H}^{1/2}, \tag{7.33}$$

where $\mathbf{W}$ is the matrix of discrete phase-space integral weights that defines the inner product $\langle \cdot, \cdot \rangle_W$ corresponding to the continuous inner product (Eq. 6.6) which represents an integration over phase space. $\mathbf{H}$ is the matrix of discrete temporal integral weights defined by the used time integration scheme. The POD basis functions are the first k columns of the matrix $\mathbf{U} = [\boldsymbol{u}_1 \ \dots \ \boldsymbol{u}_r] \in \mathbb{R}^{\mathfrak{N}_I \times r}$, defined by

$$\mathbf{U} = \mathbf{W}^{-1/2}\hat{\mathbf{U}}, \tag{7.34}$$

where $r = \text{rank}(\hat{\mathbf{A}}^{\bar{I}})$ and $\hat{\mathbf{U}}$ is the matrix whose columns hold the left singular vectors of $\hat{\mathbf{A}}^{\bar{I}}$ (see Sec. 3.3.1). Since the backward-Euler scheme is used to discretize the time

variable, $\mathbf{H} = \text{diag}(\Delta t^1, \ \ldots, \ \Delta t^{N_t})$. In 2D Cartesian geometry the matrix $\mathbf{W}$ for the SCB scheme has a similar form to the one found in 1D slab geometry (ref. Eq. 6.16), and is defined by

$$\mathbf{W} = \bigoplus_{g=1}^{N_g} \bigoplus_{m=1}^{N_\Omega} \bigoplus_{j=1}^{N_y} \bigoplus_{i=1}^{N_x} \frac{w_m A_{i,j}}{4} \mathbb{I}_4, \quad \mathbb{I}_4 = \text{diag}(1,1,1,1). \tag{7.35}$$

This matrix can be derived in a similar manner to that shown in Sec. 6.2.1.

Let the normalized radiation intensities be expanded in the POD basis found in Eq. 7.34 by

$$\bar{\boldsymbol{I}}_k^n = \sum_{\ell=1}^{k} \lambda_\ell^n \boldsymbol{u}_\ell, \quad k \leq r. \tag{7.36}$$

Substituting this expansion into Eq. 7.18 gives

$$\sum_{\ell=1}^{k} \left[\frac{\lambda_\ell^n}{c\Delta t^n} (\tilde{\mathcal{K}}^n)^{-1} \boldsymbol{u}_\ell + \lambda_\ell^n \check{\mathcal{L}}_h(\boldsymbol{\phi}^n) \boldsymbol{u}_\ell + \lambda_\ell^n \check{\mathcal{K}}_h^n(T) \boldsymbol{u}_\ell \right]$$
$$= \check{\tilde{\mathcal{Q}}}_h^n(T, \boldsymbol{\phi}^n) + \check{\tilde{\mathcal{B}}}_h(\boldsymbol{\phi}^n) + \sum_{\ell=1}^{k} \frac{\lambda_\ell^{n-1}}{c\Delta t^n} (\tilde{\mathcal{K}}^n)^{-1} \boldsymbol{\varphi}^n \odot \boldsymbol{u}_\ell, \tag{7.37}$$

where the definition of $\mathcal{T}_h$ has been used, $\odot$ denotes the Hadamard product and the vector $\boldsymbol{\varphi}^n \in \mathbb{R}^{\mathfrak{N}_I}$ has elements $\varphi_{g,m,i,j,l}^n = \frac{\phi_{g,i,j}^{n-1}}{\phi_{g,i,j}^n}$. Now the Petrov-Galerkin test basis is introduced in discrete form, which will enforce optimal projection of the NBTE in the W norm by Thm. 3.3.1. The scaled discrete residual operator for the NBTE $\check{\mathcal{R}}_h^n : \mathbb{R}^{\mathfrak{N}_I} \to \mathbb{R}^{\mathfrak{N}_I}$ is defined as

$$\check{\mathcal{R}}_h^n \bar{\boldsymbol{I}}^n = \check{\mathcal{J}}_h^n \bar{\boldsymbol{I}}^n - \left(\check{\tilde{\mathcal{Q}}}_h^n + \check{\tilde{\mathcal{B}}}_h + (\tilde{\mathcal{K}}^n)^{-1} \boldsymbol{\varphi}^n \odot \frac{\bar{\boldsymbol{I}}^{n-1}}{c\Delta t^n} \right) \tag{7.38}$$

with

$$\check{\mathcal{J}}_h^n \bar{\boldsymbol{I}}^n = \frac{1}{c\Delta t^n} (\tilde{\mathcal{K}}^n)^{-1} \bar{\boldsymbol{I}}^n + \check{\mathcal{L}}_h \bar{\boldsymbol{I}}^n + \check{\mathcal{K}}_h^n \bar{\boldsymbol{I}}^n. \tag{7.39}$$

It is therefore straightforward to show that the test basis functions must be

$$\boldsymbol{\psi}_\ell = \frac{d\check{\mathcal{R}}_h^n(\lambda_\ell^n \boldsymbol{u}_\ell)}{d\lambda_\ell^n} = \check{\mathcal{J}}_h^n \boldsymbol{u}_\ell. \tag{7.40}$$

Eq. 7.37 is projected onto this basis by applying the inner product $\langle \boldsymbol{\psi}_{\ell'}, \cdot \rangle_W$ for all

$\ell' = 1, \ldots, k$ to obtain the following equations for $\{\lambda_\ell^n\}_{\ell=1}^k$:

$$\sum_{\ell=1}^{k} \lambda_\ell^n \left[\frac{1}{c\Delta t^n} \langle \check{\mathcal{J}}_h^n \boldsymbol{u}_{\ell'}, (\tilde{\mathcal{K}}^n)^{-1} \boldsymbol{u}_\ell \rangle_W + \langle \check{\mathcal{J}}_h^n \boldsymbol{u}_{\ell'}, \check{\mathcal{L}}_h(\boldsymbol{\phi}^n) \boldsymbol{u}_\ell \rangle_W + \langle \check{\mathcal{J}}_h^n \boldsymbol{u}_{\ell'}, \check{\mathcal{K}}_h^n(T) \boldsymbol{u}_\ell \rangle_W \right]$$
$$= \langle \check{\mathcal{J}}_h^n \boldsymbol{u}_{\ell'}, \check{\tilde{\mathcal{Q}}}_h^n(T, \boldsymbol{\phi}^n) \rangle_W + \langle \check{\mathcal{J}}_h^n \boldsymbol{u}_{\ell'}, \check{\tilde{\mathcal{B}}}_h(\boldsymbol{\phi}^n) \rangle_W + \sum_{\ell=1}^{k} \frac{\lambda_\ell^{n-1}}{c\Delta t^n} \langle \check{\mathcal{J}}_h^n \boldsymbol{u}_{\ell'}, (\tilde{\mathcal{K}}^n)^{-1} \boldsymbol{\varphi}^n \odot \boldsymbol{u}_\ell \rangle_W, \tag{7.41a}$$

$$\sum_{\ell=1}^{k} \lambda_\ell^{n-1} \langle \check{\mathcal{J}}_h^n \boldsymbol{u}_{\ell'}, (\tilde{\mathcal{K}}^n)^{-1} \boldsymbol{\varphi}^n \odot \boldsymbol{u}_\ell \rangle_W = \langle \check{\mathcal{J}}_h^n \boldsymbol{u}_{\ell'}, (\tilde{\mathcal{K}}^n)^{-1} \boldsymbol{\varphi}^n \odot \boldsymbol{I}^{n-1} \rangle_W, \quad n = 1 \tag{7.41b}$$

$$\ell' = 1, \ldots, k.$$

7.3.3 Calculation of Zeroth Moment Data

Several of the operators involved in the NBTE depend nonlinearly on the zeroth moment ϕ. By definition, the test basis functions $\{\boldsymbol{\psi}_\ell\}$ also have nonlinear dependence on ϕ (and T). By this fact every inner product in Eq. 7.41a requires information on the zeroth intensity moment function. In the case where the LOQD equations are consistently discretized with the NBTE, ϕ can simply be defined from the low-order solution. When an independent discretization scheme is used however, this cannot be the case.

Let $\phi^{lo} = cE$ be the zeroth moment defined from the low-order solution. With an independent discretization scheme (outside the limit of fine grids) $\phi \neq \phi^{lo}$. When ϕ^{lo} is used in the NBTE in place of ϕ then implicitly the solution is $\bar{I}^{lo} = \frac{I}{\phi^{lo}} \neq \bar{I}$. This solution even does not reside in the same space as the Eddington tensor, shown by a simple calculation

$$\mathfrak{f} = \mathcal{P}_{\Omega,2} \bar{I} = \frac{\mathcal{P}_{\Omega,2} I}{\mathcal{P}_{\Omega,0} I} = \frac{\mathcal{P}_{\Omega,2} \bar{I}^{lo}}{\phi / \phi^{lo}}, \tag{7.42}$$

where the projection operators $\mathcal{P}_{\Omega,i}$ are defined in Eq. 2.1.

In the case of independent discretization, ϕ must be stored from the FOM solution of the considered TRT problem. For the discretizations considered here there exist three distinct grid functions of the zeroth moment: ϕ_c, ϕ_v and ϕ_h that lie on the cell centers, vertically aligned cell faces, and horizontally aligned cell faces, respectively. The vectors for each of these grid functions over phase space at each instance of time are collected

into separate snapshot matrices as the columns

$$\mathbf{A}^{\phi_\gamma} = [\boldsymbol{\phi}_\gamma^1 \ \boldsymbol{\phi}_\gamma^2 \ \dots \boldsymbol{\phi}_\gamma^{N_t}] \in \mathbb{R}^{N_g \mathfrak{N}_\gamma \times N_t}, \quad \gamma = v, h, c \tag{7.43}$$

where $\mathfrak{N}_\gamma$ is the DoF in space for a given grid function (ref. Eq. 4.2).

Compression of this data via the POD or DMD is prone to numerical issues since the zeroth moment spans many orders of magnitude across phase space and time. Numerical calculation of the POD or DMD will naturally limit how small the reconstructed values can be compared to the largest magnitudes in the dataset, even at full rank. Although this does not ordinarily pose a problem, the POD projected NBTE (Eq. 7.41a) depends solely on *ratios* of the zeroth moments. As such in areas where the zeroth moment values have been truncated to a certain precision, which can also produce negative values, these ratios can be entirely different (and sometimes nonphysical) than what is seen in the FOM solution. For the remainder of this work it is assumed that $\mathbf{A}^{\phi_\gamma}$ for $\gamma = v, h, c$ is known and available from the FOM to any considered TRT problem.

The matrices $\mathbf{A}^{\phi_\gamma}$ are stored instead of snapshot matrices for the ratios between grid functions of ϕ because it is the more memory efficient option. The ratios of ϕ required to define the discrete NBTE can be represented as five distinct grid functions representing $\frac{\phi_{i,j}^n}{\phi_{i+1,j}^n}$, $\frac{\phi_{i,j}^n}{\phi_{i+\frac{1}{2},j}^n}$, $\frac{\phi_{i,j}^n}{\phi_{i,j+1}^n}$, $\frac{\phi_{i,j}^n}{\phi_{i,j+\frac{1}{2}}^n}$ and $\frac{\phi_{i,j}^{n-1}}{\phi_{i,j}^n}$. The grid functions of the zeroth moment at the cell centers must also be stored to define $\mathcal{Q}_h$. Storing this information as a series of snapshots would require roughly double the amount of memory space as just storing the grid functions of ϕ.

7.4 Formulation of the Reduced Order Model

The class of ROMs derived in this chapter model TRT physics with the POD-Petrov-Galerkin (POD-PG) projected NBTE combined with the multilevel system of LOQD equations coupled with the MEB equation. This model is henceforth referred to as the POD-PG NBTE-QD ROMs, is formulated by

1. The POD-Petrov-Galerkin projected high-order NBTE (Eq. 7.41a)
2. The multigroup LOQD system (Eqs. 2.3) with BCs in Eq. 2.10
3. The effective grey LOQD system (Eqs. 2.13) with BCs in Eq. 2.18
4. TheMEB equation (Eq. 2.20)

Calculation of the POD basis functions and zeroth intensity moments used in these ROMs can be done before solving any TRT problems and comprises the method's offline stage. The online stage of the ROMs when used to solve TRT problems is outlined in Alg. 6. Since the test basis depends nonlinearly on T, all inner products must be continuously updated during the iteration process. A maximum number of high-order iterations s is defined as $s_{\max}$ which can be used to further reduce the ROM's computational cost while incurring some penalty to the accuracy.

At the beginning of each time step T, $\mathfrak{f}_g$ and G_g are initialized with the previous time step solution (or initial condition). Each grid function of ϕ is reconstructed for the current time instant by $\boldsymbol{\phi}_\gamma^n = \mathcal{H}(t^n)\mathbf{A}^{\phi_\gamma}$, where $\mathcal{H}(t^n)$ returns the column of $\mathbf{A}^{\phi_\gamma}$ that corresponds to time t^n, or if no column exists for the given time the columns nearest in time to t^n are interpolated to t^n. The low-order system is iterated to convergence with the initialized quantities at the zeroth s iteration. At each following s iteration, the POD projected NBTE is solved to update $\mathfrak{f}_g$ and G_g before the low-order system is solved again.

Algorithm 6: Obtaining the solution to TRT problems with the POD-PG NBTE-QD ROM

Input: k, $\{\boldsymbol{u}_\ell\}_{\ell=1}^k$, $\mathbf{A}^{\phi_\gamma}$ $\gamma = v, h, c$

$n = 0$

while $t^n \leq t^{end}$ **do**

  $n = n + 1$

  $T^{(0)} = T^{n-1}$

  $\mathfrak{f}_g^{(0)} = \mathfrak{f}_g^{n-1}$, $G_g^{(0)} = G_g^{n-1}$

  Compute $\boldsymbol{\phi}_\gamma^n = \mathcal{H}(t^n)\mathbf{A}^{\phi_\gamma}$

  $s = -1$

  while $s < s_{max}$,
  $\|T^{(s)} - T^{(s-1)}\| > \epsilon_1\|T^{(s)}\| + \epsilon_2$,
  $\|E^{(s)} - E^{(s-1)}\| > \epsilon_1\|E^{(s)}\| + \epsilon_2$ **do**

    $s = s + 1$

    if $s \geq 1$ **then**

      Update $\{\boldsymbol{\psi}_\ell\}_{\ell=1}^k$ with $T^{(s-1)}$, $\boldsymbol{\phi}_\gamma^n$

      Update all inner products in Eq. 7.41a with $\{\boldsymbol{\psi}_\ell\}_{\ell=1}^k$, $T^{(s-1)}$, $\boldsymbol{\phi}_\gamma^n$

      Solve the projected NBTE (Eq. 7.41a) for $\{\lambda_\ell\}_{\ell=1}^k$

      Compute $\bar{\boldsymbol{I}}_k^n = \sum_{i=\ell}^k \lambda_\ell^n \boldsymbol{u}_\ell$

      Compute $\mathfrak{f}_g^{(s)} = \mathcal{P}_{\Omega,2}\bar{I}_{k,g}^n$, $G_g^{(s)} = \langle|\boldsymbol{n}_\Gamma \cdot \boldsymbol{\Omega}|, \bar{I}_{k,g}^n\rangle_\Omega$

    end

    $q = 0$

    while $\|T^{(s,q)} - T^{(s,q-1)}\| > \epsilon_1\|T^{(s,q)}\| + \epsilon_2$,
    $\|E^{(s,q)} - E^{(s,q-1)}\| > \epsilon_1\|E^{(s,q)}\| + \epsilon_2$ **do**

      $q = q + 1$

      Update $\varkappa_{E,g}, \varkappa_{B,g}, \tilde{\varkappa}_{R,g}, B_g$ with $T^{(s-1,q)}$

      Solve multigroup LOQD equations (Eqs. 2.3) with $\mathfrak{f}_g^{(s)}$, $G_g^{(s)}$ for $E_g^{(s,q)}$, $\boldsymbol{F}_g^{(s,q)}$

      Compute spectrum-averaged closures for the effective grey problem with $E_g^{(s,q)}$, $\boldsymbol{F}_g^{(s,q)}$

      Solve effective grey problem (Eqs. 2.13 and 2.20) for $T^{(s,q)}$, $E^{(s,q)}$, $\boldsymbol{F}^{(s,q)}$

    end

    $T^{(s)} \leftarrow T^{(s,q)}$

  end

  $T^n \leftarrow T^{(s)}$

  $\mathfrak{f}_g^n \leftarrow \mathfrak{f}_g^{(s)}$, $G_g^n \leftarrow G_g^{(s)}$

end

7.5 Numerical Results

In this section the POD-PG NBTE-QD ROM's performance and abilities are demonstrated through the use of numerical testing. There is a necessity for this process borne out of the current lack of complete theoretical results. What can be proved in theory includes (i) the POD basis formed in Sec. 7.3.2 will optimally represent the NBTE solution in the W norm for any given rank, (ii) the test basis formed in Sec. 7.3.2 enforces that the solution to Eq. 7.41a will have minimal error in the W norm. Results needed to relate the relationship between Eq. 7.41a and the (multiphysical) low-order system do not yet exist. No parameterization or hyper-reduction is considered in the following analysis, as the viability of those pieces depends on having a robust ROM to be built upon, and this is the subject of current investigations.

The POD-PG NBTE ROM is tested for how accurately it can reproduce the FOM solution to a single TRT problem, using the same full-order solution to create its databases. The ROM is also tested for how *predictably* it behaves with variations in the parameter ξ that determines the rank of expansion. If the ROM's accuracy and cost can be reliably predicted based on ξ then its use in parametric applications is much more practical. In this way the model can be dynamically tuned for needed accuracy and available computational resources.

When generating full-order solutions in the method's offline stage to create the POD bases, the MLQD method with the BTE and BCs defined in Eqs. 2.10 & 2.18 is used. The zeroth intensity moment is calculated from the full-order radiation intensities, which are then normalized to find $\bar{I}$. Since the NBTE discretization scheme derived in Sec. 7.1.1 is consistent with the SCB scheme for the BTE, this solution for $\bar{I}$ is equivalent to that of the MLQD method with the NBTE. Both $s_{\max} = \infty$ and $s_{\max} = 1$ are considered for the FOM (ref. Alg. 1), so that two solution databases can be considered: one that has been fully converged in its iterations, and another using only a single transport sweep per time step. This latter option can be used where a cheaper offline stage is desired.

The **F-C Test A** is used to evaluate the POD-PG NBTE-QD ROM (see Sec. 4.4.1), using a smaller interval of time and coarser mesh in space. $T^0 = 1$ eV and $T^{\text{in}} = 1$ KeV are used. A time interval of $t \in [0, 3\text{ns}]$ is considered, discretized into $N_t = 150$ uniform time steps $\Delta t = 2 \times 10^{-2}$ ns. A uniform grid of 10×10 cells (i.e. $N_x = N_y = 10$) with side lengths of $\Delta x = \Delta y = 0.6$ cm is used to discretize the slab. The number of DoF describing $\bar{\boldsymbol{I}}^n$ at each instance of time t^n is $\mathfrak{N}_I = 9.792 \times 10^5$. The number of DoF in phase space and time is equal to $\mathfrak{N}_I N_t = 1.4688 \times 10^8$.

F-C Tests A and **B** (see Secs. 4.4.1 & 6.4) use a temporal interval of $t \in [0, 6\text{ns}]$. The region of $t \in [3, 6\text{ns}]$ is in the near steady-state regime and adds little complexity to the problem. If this ROM can be proven robust for the complicated and rapid transient regimes of this problem, the latter temporal region will not pose a challenge. Without the use of hyper-reduction techniques, adding these times to the ROM database (doubling the database in size) can result in an excessive increase in the posed computational load. The same is true for refinements in the spatial grid.

When generating solutions to the F-C problem, the following convergence criteria are used (ref. Algs. 1 & 6): $\epsilon_1 = 10^{-14}$ and $\epsilon_2 = 10^{-15}$. Also when applying the opacity normalization operator $(\tilde{\mathcal{K}}^n)^{-1}$ (see Sec. 7.3.1) we define $\hat{\mathbb{G}} = \{1, \ldots, N_g\}$. The F-C opacity function spans many orders of magnitude across frequency and temperature (see Fig. D.1), but $\varkappa_{E,1} \gg \varkappa_{E,g}$ for groups $g = 2, \ldots, N_g$ within the used group structure. It is this first (diffusive) energy group that tends to limit the precision at which the projection inner products can be calculated. Furthermore the high-frequency groups have small opacities, and it is these groups that dominate the problem's dynamics. Inverting all groups ensures that the most important frequency ranges have their effects preserved above all others.

7.5.1 Analysis of POD Databases & Singular Values

The singular value distributions of the weighted snapshot matrices (ref. Eq. 7.33) holding $\bar{I}$ from the FOM solution are shown in Fig. 7.1. The solutions found with both $s_{\max} = \infty$ and $s_{\max} = 1$ are shown. Notably, both plots are nearly identical. This is reasonable given that a single transport sweep in the context of the MLQD methodology should well approximate the converged solution. In both plots there are three discernible regions of sharp decrease in singular value magnitudes, each followed by a region where the rate of decrease slows dramatically. The third and last region of stagnation is where the limits of numerical precision become dominant and no further reduction is possible. Tab. 7.1 displays the ranks of expansion k that correspond to several different values of ξ, calculated via Eq. 3.12. The values shown are calculated for the FOM solution using $s_{\max} = \infty$. The ranks for the solution using $s_{\max} = 1$ are identical and thus not shown.

Fig. 7.2 plots the s iteration counts for the POD-PG NBTE-QD ROM using $s_{\max} = \infty$ for different values of ξ at each time step. These iteration counts can be compared to those shown in Fig. D.5, which plots the s iteration counts for the MLQD method using the BCs defined in Eqs. 2.10 & 2.18. Most time steps are solved in 3 or 4 s iterations using the POD-PG NBTE-QD ROM, with only a single time step requiring 5 iterations

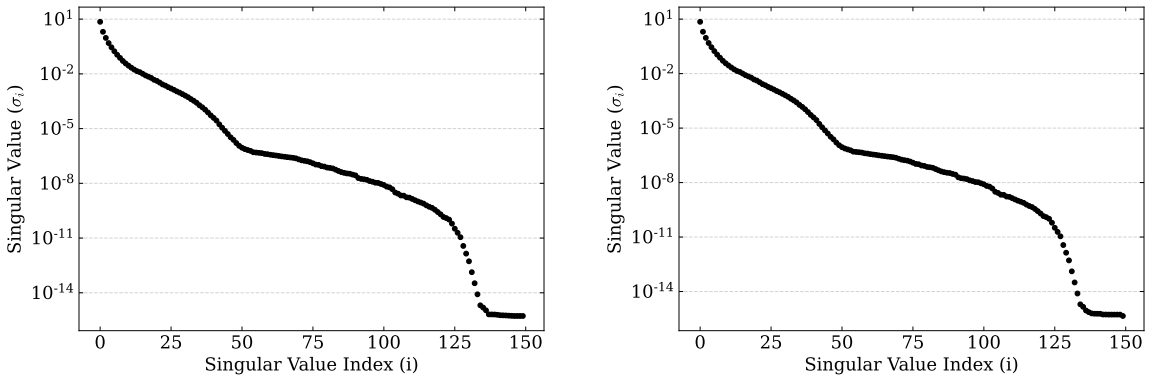

(a) $s_{\max} = \infty$ (b) $s_{\max} = 1$

Figure 7.1: Singular value spectra of the weighted snapshot matrices holding $\bar{I}$ solutions of the FOM using $s_{\max} = \infty$ and $s_{\max} = 1$

ξ	k
10^{-2}	9
10^{-4}	32
10^{-6}	45
10^{-8}	88
10^{-10}	117
10^{-12}	128
10^{-14}	132
10^{-16}	149

Table 7.1: Ranks k for the POD expansion of $\bar{I}$ corresponding to different values of ξ

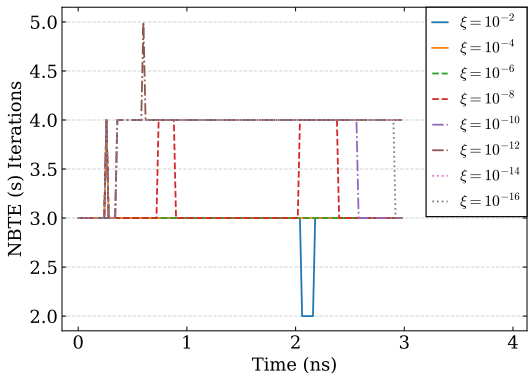

Figure 7.2: High-order (NBTE or s) iteration count per time step using the POD-PG NBTE-QD ROM (ref. Alg. 6) with $s_{\max} = \infty$ and various ξ values.

for several ξ. The iteration count actually increases as ξ is decreased; for $\xi \geq 10^{-8}$ most time steps are solved with 3 projected NBTE solves, wheras for $\xi \leq 10^{-10}$ most time steps require 4 solves.

7.5.2 Error Analysis & Convergence of ROMs

The accuracy of the POD-PG NBTE-QD ROM w.r.t. the FOM solution in discrete space is now analyzed, along with the convergence behavior of its errors with ξ. Two cases are investigated: (i) $s_{\max} = \infty$ and (ii) $s_{\max} = 1$ for both the offline and online stages of the ROM. Let the POD-PG NBTE-QD ROM using $s_{\max} = s_1$ for the offline full-order iterations and $s_{\max} = s_2$ for the online ROM iterations be written concisely as model($s_1|s_2$). Therefore case (i) is model($\infty|\infty$) and case (ii) is model(1|1). In each case the online stage of the ROM is consistent with the data generated in the offline stage, and therefore both models are expected to see convergence in their errors with ξ to the FOM solution used in generating their POD bases.

Figs. 7.3 & 7.4 plot the relative errors of the material temperature (T) and total radiation energy density (E) in the 2-norm over space at every instance of time for model($\infty|\infty$) and model(1|1), respectively. The errors are calculated w.r.t. the FOM solution used to generate their respective databases (i.e. using $s_{\max} = \infty$ and $s_{\max} = 1$, respectively). Each curve on the plots corresponds to a different value of ξ used to define the ROM. As ξ is decreased, the ROM errors decrease uniformly in time and stagnate after $\xi < 10^{-10}$ at a level less than 10^{-12} which can be considered converged to the FOM solution within the bounds of finite precision. For all considered ξ except for $\xi = 10^{-2}$, the relative errors for both T and E increase rapidly in the beginning stage of the problem before leveling off to a stable level that only slightly increases with time. This behavior is attributed to the fact that the POD projected NBTE retains a source term from the previous time step due to its temporal discretization scheme, which will lead to an accumulating error effect at each instance of time until saturation occurs.

Figs. 7.5 & 7.6 plot the same relative errors for model($\infty|\infty$) and model(1|1), respectively, vs ξ instead of vs time. Each curve in these plots corresponds to a select instance of time. In this view the behavior of the ROM errors with ξ is much more clearly represented. Here let the ROM errors be written as the function $\epsilon(x) = \frac{\|x_{\text{FOM}} - x_{\text{ROM}}\|_2}{\|x_{\text{FOM}}\|_2}$. Then for both models, the primary behavior is that $\epsilon(E) \approx \epsilon(T) \approx \xi \cdot 10^{-2}$, until stagnation occurs on the level of $\epsilon(E) \approx \epsilon(T) \approx 10^{-12}$

The results shown so far demonstrate that the POD-PG NBTE-QD ROM can reproduce

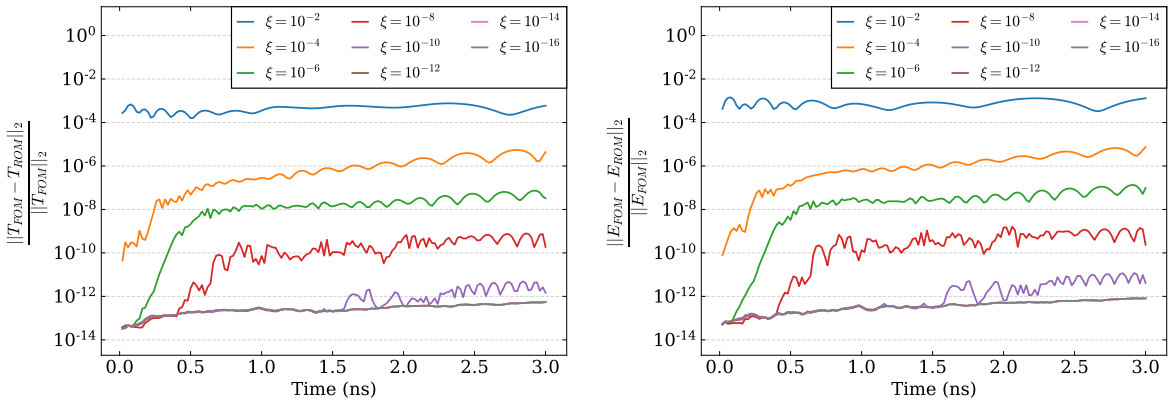

(a) Material Temperature

(b) Radiation Energy Density

Figure 7.3: Relative errors w.r.t. the FOM using $s_{\max} = \infty$ (ref. Alg. 1) in the 2-norm of the POD-PG NBTE ROM using $s_{\max} = \infty$ in its offline and online stages (ref. Alg. 6) for several ξ, plotted vs time

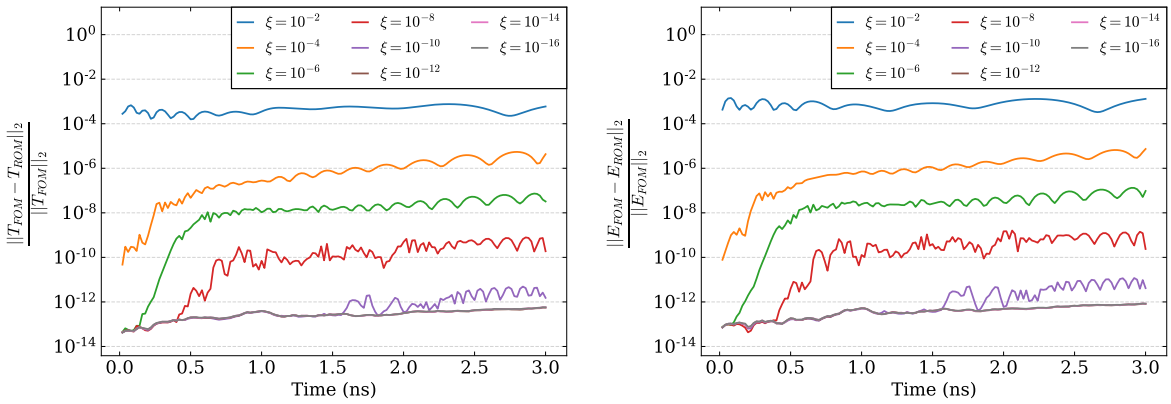

(a) Material Temperature

(b) Radiation Energy Density

Figure 7.4: Relative errors w.r.t. the FOM using $s_{\max} = 1$ (ref. Alg. 1) in the 2-norm of the POD-PG NBTE ROM using $s_{\max} = 1$ in its offline and online stages (ref. Alg. 6) for several ξ, plotted vs time

the FOM solution with high levels of accuracy in the 2-norm sense across space at every instance of time. Furthermore, as ξ is decreased the ROM solution also predictably converges to the FOM solution that was used to generate the applied POD basis functions. The next step in this analysis is to demonstrate whether the 2-norm accuracy of this ROM is indicative of the local error levels in space. To this end plots will be shown of the relative errors w.r.t. the FOM solution over the entire spatial domain for select instances

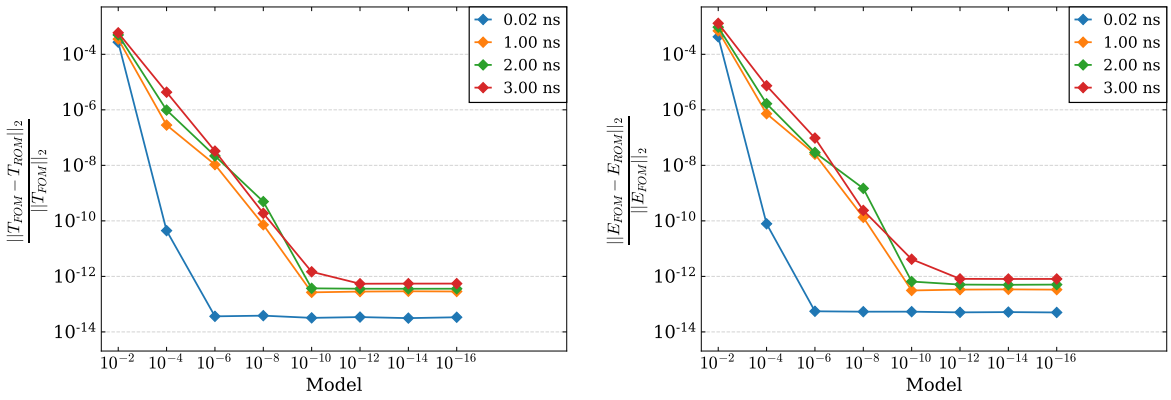

(a) Material Temperature

(b) Radiation Energy Density

Figure 7.5: Relative errors w.r.t. the FOM using $s_{\max} = \infty$ (ref. Alg. 1) in the 2-norm of the POD-PG NBTE ROM using $s_{\max} = \infty$ in its offline and online stages (ref. Alg. 6) at several times, plotted vs ξ

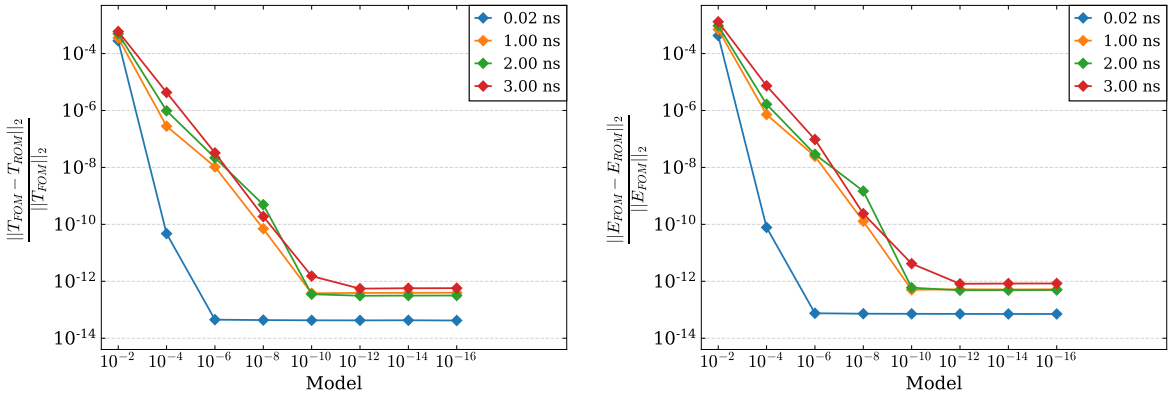

(a) Material Temperature

(b) Radiation Energy Density

Figure 7.6: Relative errors w.r.t. the FOM using $s_{\max} = 1$ (ref. Alg. 1) in the 2-norm of the POD-PG NBTE ROM using $s_{\max} = 1$ in its offline and online stages (ref. Alg. 6) at several times, plotted vs ξ

of time. Only model($\infty|\infty$) is considered here, and restricted to $\xi = 10^{-2}, 10^{-4}$. Local error analysis for model(1|1) yields essentially the same results compared to model($\infty|\infty$). The two largest considered values for ξ represent the lowest-rank expansions of $\bar{I}$ and are not only the most practical ξ for application but will incur the largest errors. These shown errors will converge with decreasing ξ, following the behavior shown in the 2-norm already. Fig. 7.7 plots the spatially local relative errors in T and E for model($\infty|\infty$) with $\xi = 10^{-2}, 10^{-4}$ at times of $t = 1, 2, 3$ ns. This figure takes the form of two tables that

display the relative cell-wise error in the ROM across F-C test domain. The first (top) table shows errors in the material temperature (T) and the second (bottom) shows errors in the total radiation energy density (E). Each row corresponds to a different value of ξ and each column to the specific instance of time. Although only three instances of time are shown, the color scale shown to the right of each row depicts the entire range of values for all time instances. In accordance with Fig. 7.3, the highest levels of spatial errors are found at the final time step with $\xi = 10^{-4}$ and are relatively uniform across space and time for $\xi = 10^{-2}$. Note that the highest errors for $\xi = 10^{-2}$ are found in the range $t \in [0.06, 0.26 \text{ ns}]$ and exist on the right half of the domain. There exist no sharp spikes in the local error levels and the ROM is able to reproduce the FOM solution at all spatial points to a level close to the 2-norm errors shown in Fig. 7.3.

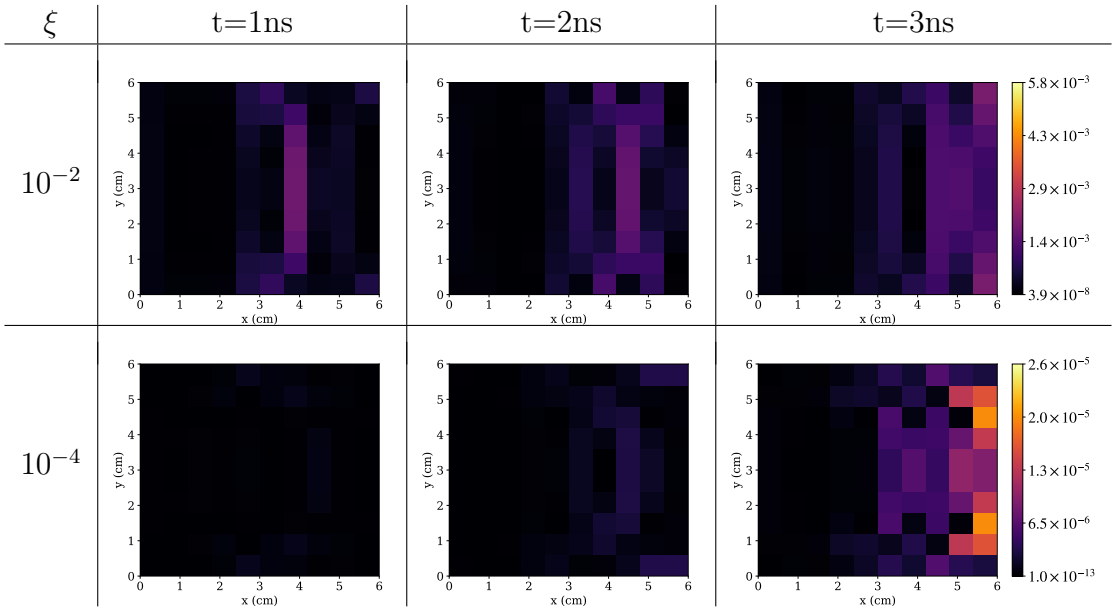

(a) Material Temperature

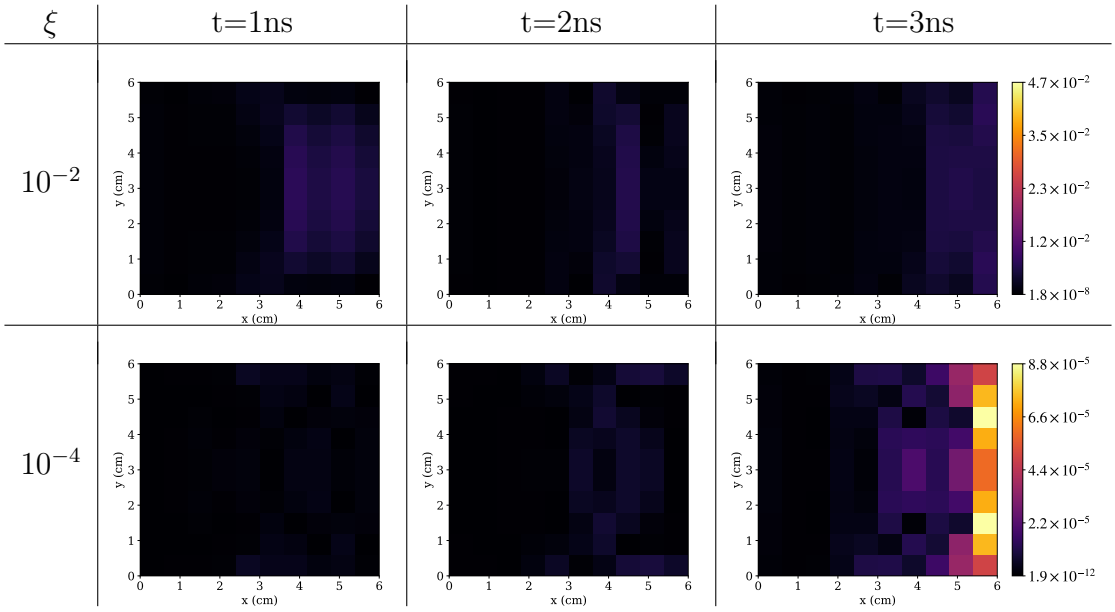

(b) Radiation Energy Density

Figure 7.7: Cell-wise relative error in material temperature (T) and total radiation energy density (E) over the spatial domain at times t=1, 2, 3 ns for the POD-PG NBTE ROM using $s_{\max} = \infty$ for $\xi = 10^{-2}, 10^{-4}$.

7.5.3 Performance of the ROM using a Single NBTE Iteration

In this section, the ROM using $s_{\max} = 1$ in its online stage will be evaluated w.r.t. the full-order solution found using $s_{\max} = \infty$ to determine how well this cheaper ROM can reproduce the fully-converged F-C test solution (and in the limit of fine grids, the continuous TRT solution). Cases when the POD basis functions are generated using $s_{\max} = \infty$ and $s_{\max} = 1$ are considered, i.e. model($\infty|1$) and model($1|1$). This is done to quantify effects on the ROM accuracy stemming from the quality of used POD basis functions.

Fig. 7.8 plots the relative errors of T and E in the 2-norm over space at every instance of time for model($\infty|1$) w.r.t. the FOM solution generated with $s_{\max} = \infty$. Fig. 7.9 plots the same errors calculated for the model($1|1$) solution. The error levels in both T and E for all ξ are nearly identical between the two models. Only $\xi \geq 10^{-8}$ is shown in both plots, as the error levels saturate by $\xi = 10^{-8}$ and no longer decrease with further increases in rank. This saturation level in accuracy for both models is actually the same relative difference between the FOM solutions using $s_{\max} = \infty$ and $s_{\max} = 1$. Note that $\xi = 10^{-2}$ is the only value that provides a solution whose errors are above the saturation point for all time instances. When $\xi = 10^{-4}$, the saturation point is met for times between 0 and 1.5 ns, where the largest errors are present. This is because as the problem evolves in time, the transients evolve more slowly and can be better captured by a single-iteration scheme.

These results establish that when the POD-PG NBTE-QD ROM uses $s_{\max} = 1$ in its online stage, there is little to no accuracy lost when $s_{\max} = 1$ is also used in the offline stage to generate the ROM data, compared to using $s_{\max} = \infty$ in the offline stage. This model is also able to converge in error w.r.t. the fully converged FOM solution up to the level that is seen with the FOM solution generated using $s_{\max} = 1$, regardless of $s_{\max}$ used in the offline stage. In other words, the POD-PG NBTE-QD ROM (with high enough rank) finds the same solution as the FOM using $s_{\max} = 1$ when only a single s iteration is performed in its online stage.

For the remainder of this chapter only model($\infty|\infty$) and model($1|1$) are considered, since the solutions generated for model($\infty|1$) do not provide anything new when compared to model($1|1$). Fig. 7.10 plots the local spatial errors of the model($1|1$) solution using $\xi = 10^{-2}, 10^{-4}$ relative to the FOM with $s_{\max} = \infty$ in the same format as Fig. 7.7, using different select instances of time to display. Since model($1|1$) tends to have the lowest accuracy in the rapidly evolving initial regime, times $t = 0.02,\ 0.2,\ 0.5$ ns are sampled. The shown color bars still encapsulate the entire range of errors for the whole temporal

interval. Once again there are no sharp peaks in the error levels across the spatial domain, and the values at all instances of time (encapsulated in the color scales to the right) are contained in a neighborhood of the 2-norm errors shown in Fig. 7.9.

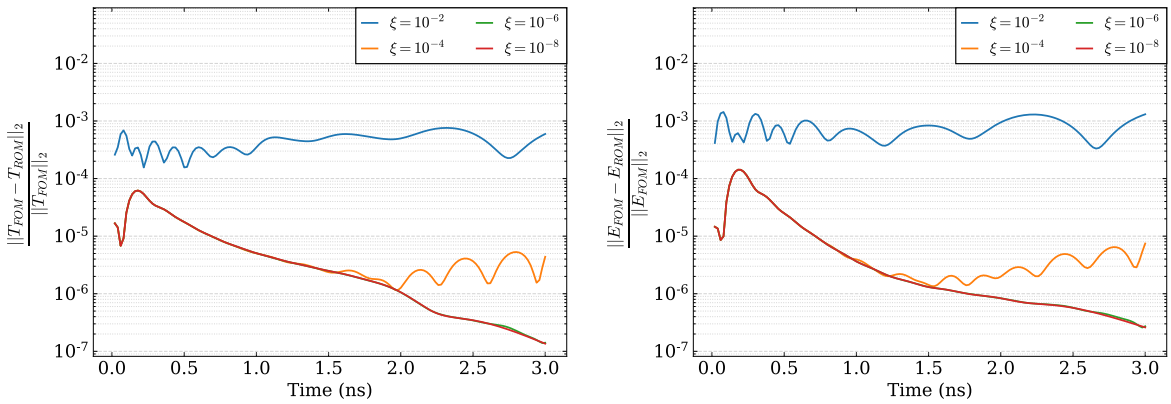

(a) Material Temperature (b) Radiation Energy Density

Figure 7.8: Relative errors w.r.t. the FOM using $s_{\max} = \infty$ (ref. Alg. 1) in the 2-norm of the POD-PG NBTE-QD ROM using $s_{\max} = 1$ in its online stage (ref. Alg. 6) and $s_{\max} = \infty$ in its offline stage for several ξ, plotted vs time

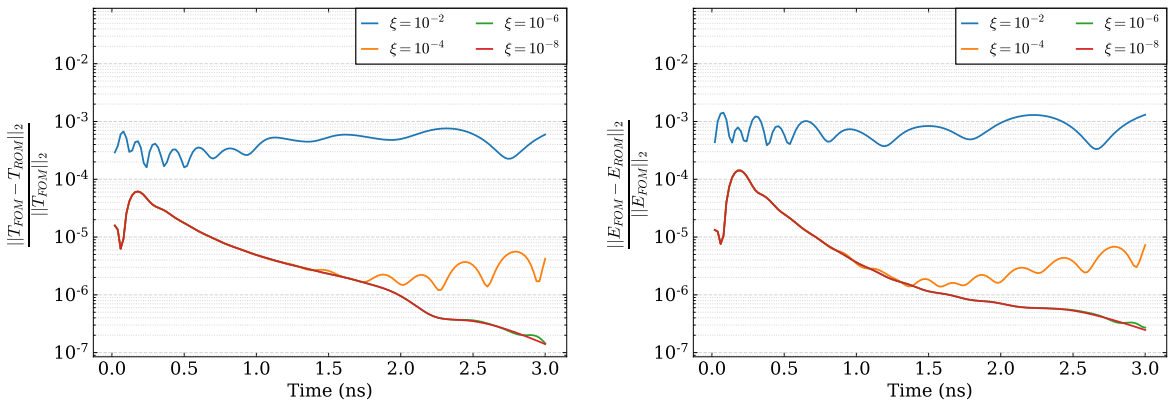

(a) Material Temperature (b) Radiation Energy Density

Figure 7.9: Relative errors w.r.t. the FOM using $s_{\max} = \infty$ (ref. Alg. 1) in the 2-norm of the POD-PG NBTE-QD ROM using $s_{\max} = 1$ in both its online (ref. Alg. 6) and offline stages for several ξ, plotted vs time

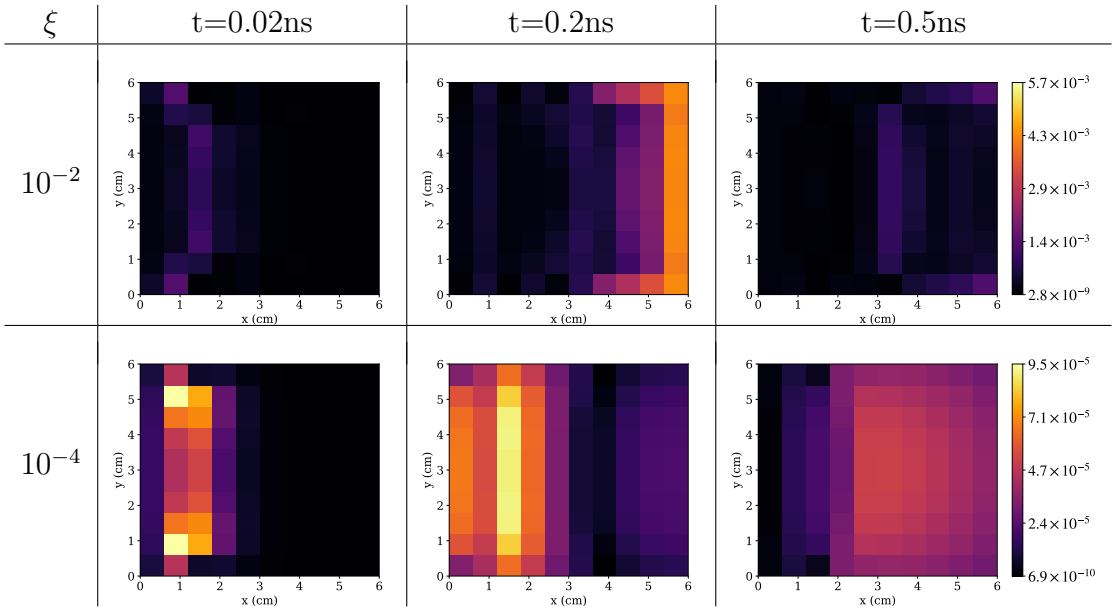

(a) Material Temperature

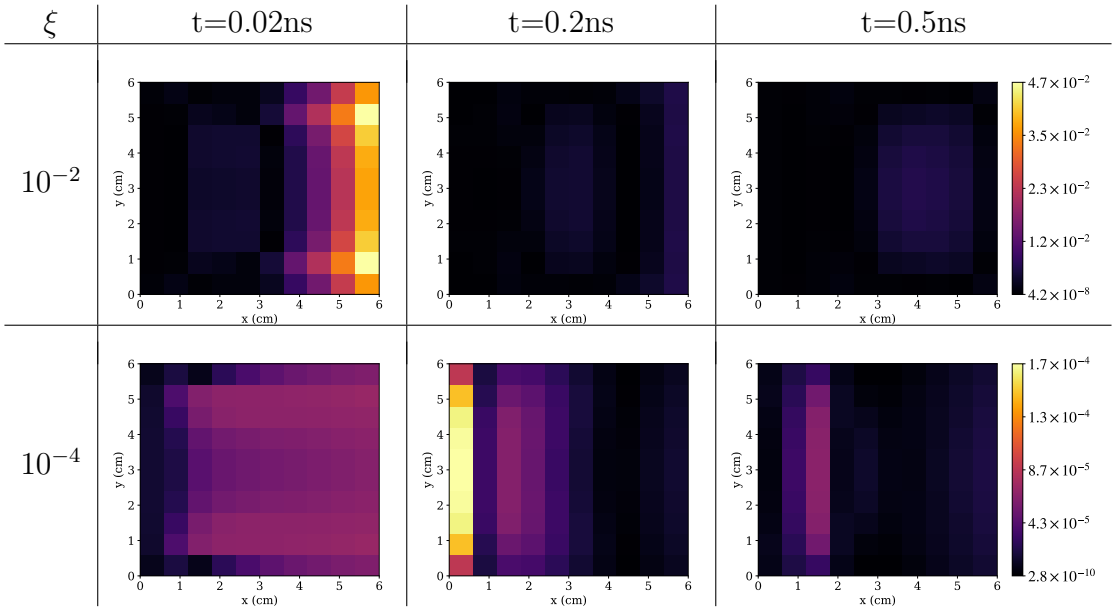

(b) Radiation Energy Density

Figure 7.10: Cell-wise relative error in material temperature (T) and total radiation energy density (E) over the spatial domain at times t=0.02, 0.2, 0.5 ns for the POD-PG NBTE-QD ROM using $s_{\max} = 1$ in its online and offline stages for $\xi = 10^{-2}, 10^{-4}$. Errors are calculated w.r.t. the FOM using $s_{\max} = \infty$ (ref. Alg. 1)

7.6 Reproduction of Physical Quantities

In this section the POD-PG NBTE-QD ROM is evaluated against the FOM in how well it can recreate important TRT physics. The first subject of study is the breakout time of radiation (see Sec. 4.5 for a description). Accurate simulation of this integral physical quantity depends on a model's ability to recreate the correct nonlinear wavefront of radiation as it propagates across the problem domain. Afterwards the frequency spectrum of radiation produced by the POD-PG NBTE-QD ROM is surveyed. This is a higher-fidelity measure of a ROM's success, and is a physical quantity of critical importance in applications involving radiation spectroscopy. It is assumed when referring to the FOM that $s_{\max} = \infty$ for the remainder of this analysis.

7.6.1 Modeling of Radiation Wave Breakout

Let $\bar{F}_R$, $\bar{E}_R$ and $\bar{T}_R$ be the total radiation flux and energy densities and the material temperature integrated along the right boundary of the F-C test as defined in Eqs. 4.11. The FOM solution for these quantities is shown in Fig. 4.13. Each of $\bar{F}_R$, $\bar{E}_R$ and $\bar{T}_R$ represent a different measure of the amount of radiation that has reached the drive-opposite side of the test domain over time, which is what might be measured by a detector during an experiment.

Fig. 7.11 plots the relative error for each quantity produced by model$(\infty|\infty)$ at each instance of time w.r.t. the FOM solution. All considered values of ξ are included here, and similar behavior to Fig. 7.3 is seen. Each quantity is observed to converge to the FOM solution as ξ decreases, and errors propagate in time with a slight rate of increase for $\xi \leq 10^{-4}$. The errors in $\bar{F}_R$, $\bar{E}_R$ and $\bar{T}_R$ are generally higher than the 2-norm error of T and E for any given ξ before the limits of numerical precision become dominant. This difference in error levels is between one and two orders of magnitude. This is not to say however, that the breakout quantities are of low accuracy. The observed errors are all approximately bounded by ξ.

Fig. 7.12 plots the relative error for each quantity produced by model$(1|1)$ at each instance of time w.r.t. the FOM solution, only including $\xi \geq 10^{-8}$. As before further decreases in ξ do not decrease the observed error. For $\xi = 10^{-2}$, the errors are largely the same for both model$(1|1)$ and model$(\infty|\infty)$. The same is true for the latter half of the temporal interval with $\xi = 10^{-4}$. Otherwise for $\xi \leq 10^{-4}$ across the entire time window model$(1|1)$ can successfully reproduce each breakout quantity to below an order of 10^{-4}.

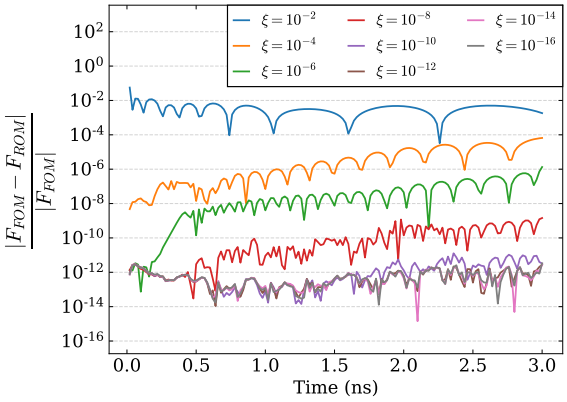

(a) $\bar{F}_R$

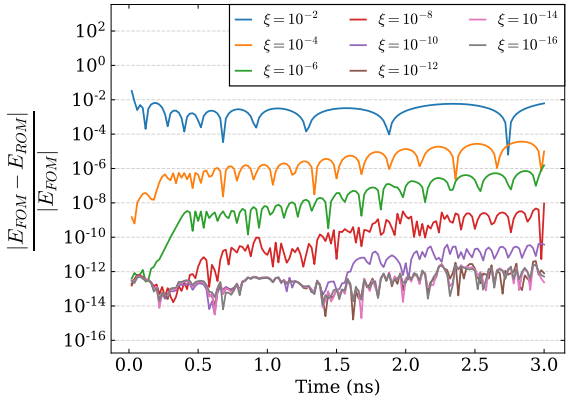

(b) $\bar{E}_R$

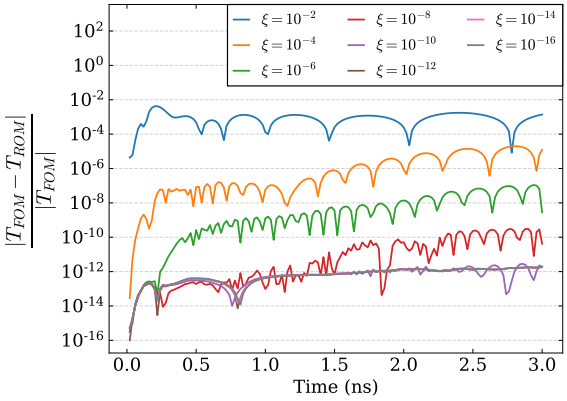

(c) $\bar{T}_R$

Figure 7.11: Relative error for the POD-PG NBTE-QD ROMs using $s_{\max} = \infty$ in the offline and online stages with various ξ values for data located at and integrated over the right boundary of the domain.

7.6.2 Radiation Spectrum

The frequency spectrum of radiation is now analyzed by calculating errors in the reduced-order groupwise radiation energy densities. These energy densities are averaged over the frequency interval they represent to produce $\bar{E}_g = \frac{E_g}{\nu_g - \nu_{g-1}}$. Three points on the spatial domain are chosen for comparisons with the FOM: (i) the midpoint of the domain, (ii) the midpoint of the right boundary, (iii) the bottom corner of the right boundary. These points represent well a spectrum of different levels of anisotropy in the radiation intensity distribution. The FOM solution for $\bar{E}_g$ is given in Fig. 4.17, and is described in Sec. 4.5.2. Only zoomed-in plots of the frequency spectrum are shown here, disregarding the final

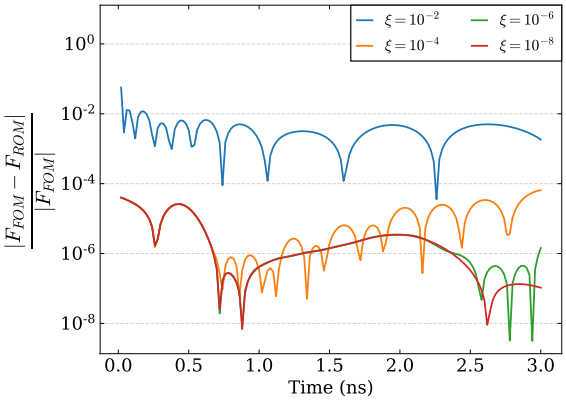

(a) $\bar{F}_R$

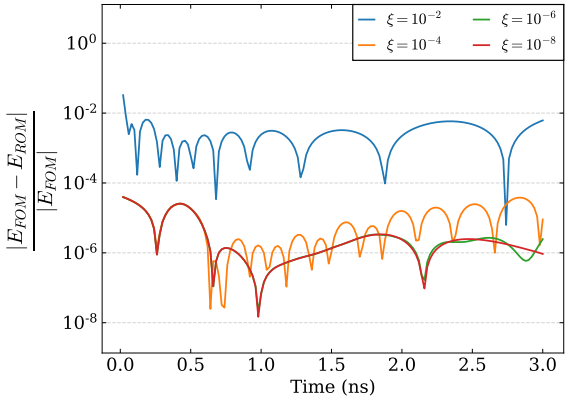

(b) $\bar{E}_R$

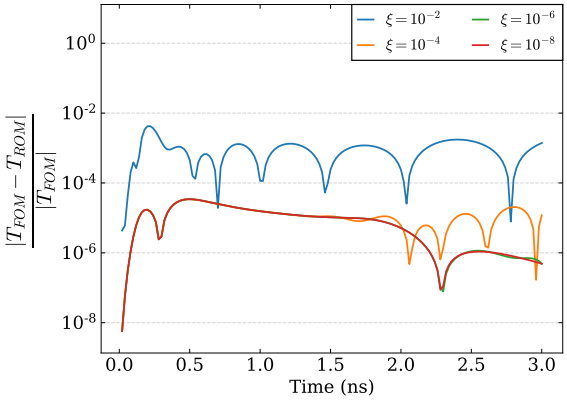

(c) $\bar{T}_R$

Figure 7.12: Relative error for the POD-PG NBTE-QD ROMs using $s_{\max} = 1$ in the offline and online stages with various ξ values for data located at and integrated over the right boundary of the domain.

point in the spectrum whose errors do not deviate significantly from the other points.

Figs. 7.13 and 7.14 plot the relative errors of the average multigroup radiation energy densities produced by model$(\infty|\infty)$ with $\xi = 10^{-2}, 10^{-4}$ at several instances of time. These points in time are chosen to sample important regions in the time interval of the F-C test (see for example Fig. 4.13). When $\xi = 10^{-2}$ the earliest time steps have the largest levels of error, whereas with $\xi = 10^{-4}$ it is the later times that display the largest errors. As ξ is decreased further this behavior of frequency errors increasing with time continues, and is an artifact of the results shown in Fig. 7.3 which demonstrates that the overall ROM solution loses accuracy as time moves on. The ROM's accuracy increases with frequency for most time steps, with the largest errors present in low frequency groups.

This is especially prevalent at the corner point of the right boundary, where the most anisotropy is present. This effect demonstrates that the POD-PG NBTE ROM is well equipped to reproduce the transport effects and streaming regimes of TRT problems even with very low rank expansions.

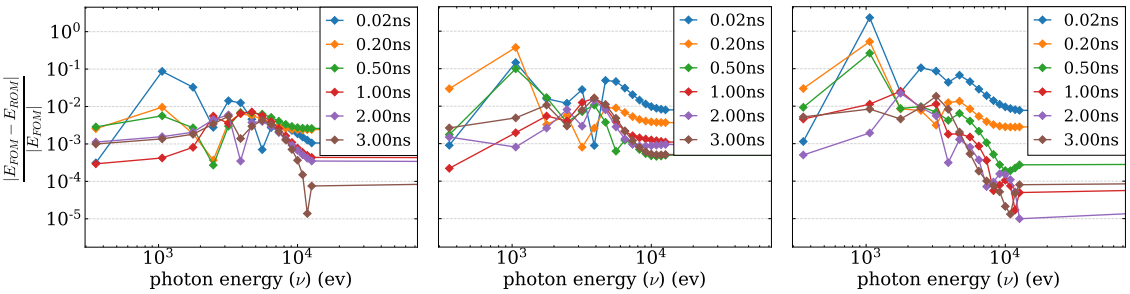

(a) $y = 3$cm, $x = 3$cm (b) $y = 3$cm, $x = 6$cm (c) $y = 0$cm, $x = 6$cm

Figure 7.13: Relative errors of the radiation spectrum produced by the POD-PG NBTE-QD ROM using $s_{\max} = \infty$ and $\xi = 10^{-2}$ located at (i) the domain midpoint, (ii) the midpoint of the right boundary, (iii) the corner of the right boundary, taken at several time instances.

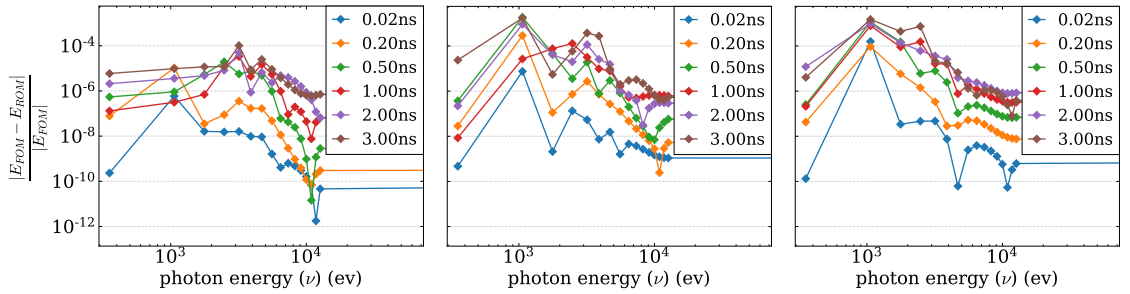

(a) $y = 3$cm, $x = 3$cm (b) $y = 3$cm, $x = 6$cm (c) $y = 0$cm, $x = 6$cm

Figure 7.14: Relative errors of the radiation spectrum produced by the POD-PG NBTE-QD ROM using $s_{\max} = \infty$ and $\xi = 10^{-4}$ located at (i) the domain midpoint, (ii) the midpoint of the right boundary, (iii) the corner of the right boundary, taken at several time instances.

Figs. 7.15 and 7.16 plot the same frequency errors for the solution of model(1|1) with $\xi = 10^{-2}, 10^{-4}$. In this case the earliest time steps show the largest levels of error for all ξ, as should be expected from the previous results in Fig. 7.9. When $\xi = 10^{-2}$ the accuracy is fairly level across the frequency range, except for the boundary corner point where accuracy increases with frequency. For $\xi = 10^{-4}$, accuracy increases with frequency at all considered spatial points. This is the same behavior as seen for all lower values of ξ. As with model($\infty|\infty$), model(1|1) can well approximate the streaming regime and anisotropy present in the F-C test with low rank.

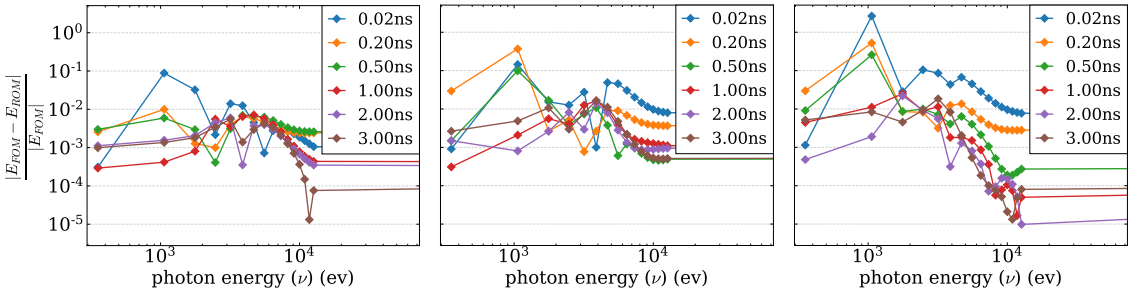

(a) $y = 3$cm, $x = 3$cm (b) $y = 3$cm, $x = 6$cm (c) $y = 0$cm, $x = 6$cm

Figure 7.15: Relative errors of the radiation spectrum produced by the POD-PG NBTE-QD ROM using $s_{\max} = 1$ and $\xi = 10^{-2}$ located at (i) the domain midpoint, (ii) the midpoint of the right boundary, (iii) the corner of the right boundary, taken at several time instances.

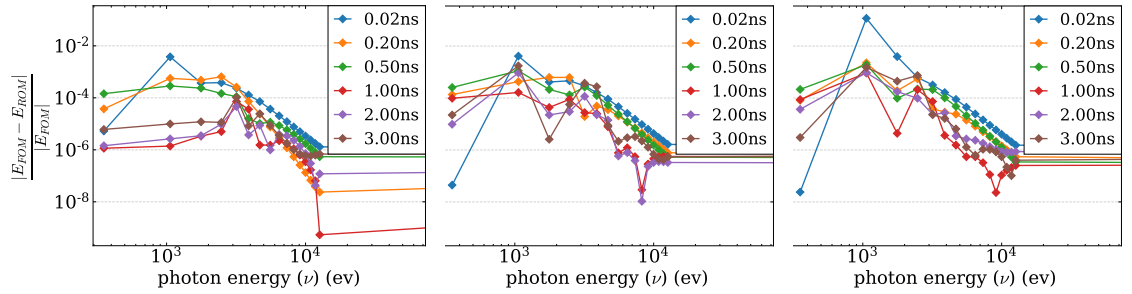

(a) $y = 3$cm, $x = 3$cm (b) $y = 3$cm, $x = 6$cm (c) $y = 0$cm, $x = 6$cm

Figure 7.16: Relative errors of the radiation spectrum produced by the POD-PG NBTE-QD ROM using $s_{\max} = 1$ and $\xi = 10^{-4}$ located at (i) the domain midpoint, (ii) the midpoint of the right boundary, (iii) the corner of the right boundary, taken at several time instances.

Temporal integrals are now presented of the so far investigated spectral errors. Instead of analyzing error plots for specific instances of time, the 2-norm and ∞-norm of this data calculated the interval $t \in [0, 3\text{ns}]$ will be shown. Having already explored how these errors evolve with the problem's transients, this view is provided to give a clear sense of the average behavior. Figs. 7.17, 7.18 and 7.19 plot the 2-norm and ∞-norm (in time) of the relative errors in the model($\infty|\infty$) solution. Each figure represents one of the three chosen points on the spatial domain. All considered values of ξ are shown here to give a complete picture of how the frequency errors converge in a temporal-integral sense. For all $\xi \leq 10^{-4}$ and before numerical precision becomes limiting, the high frequency groups are again reproduced with significantly higher accuracy than low frequency groups. This effect becomes more pronounced as the solution becomes more anisotropic. Furthermore each energy group decreases in error when ξ is decreased.

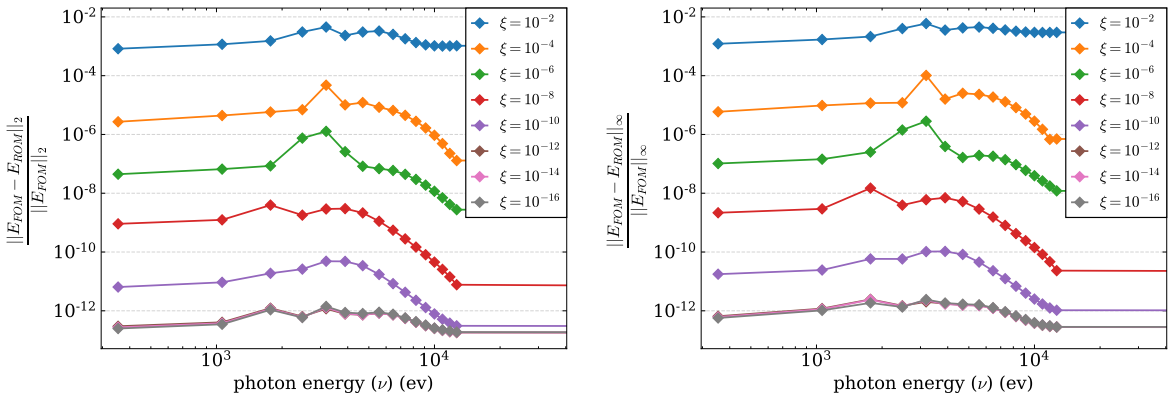

(a) 2 norm

(b) infinity norm

Figure 7.17: Relative errors of the radiation spectrum produced by the POD-PG NBTE-QD ROM using $s_{\max} = \infty$ located at the domain midpoint in the 2-norm and ∞-norm along the temporal interval $t \in [0, 3\text{ns}]$

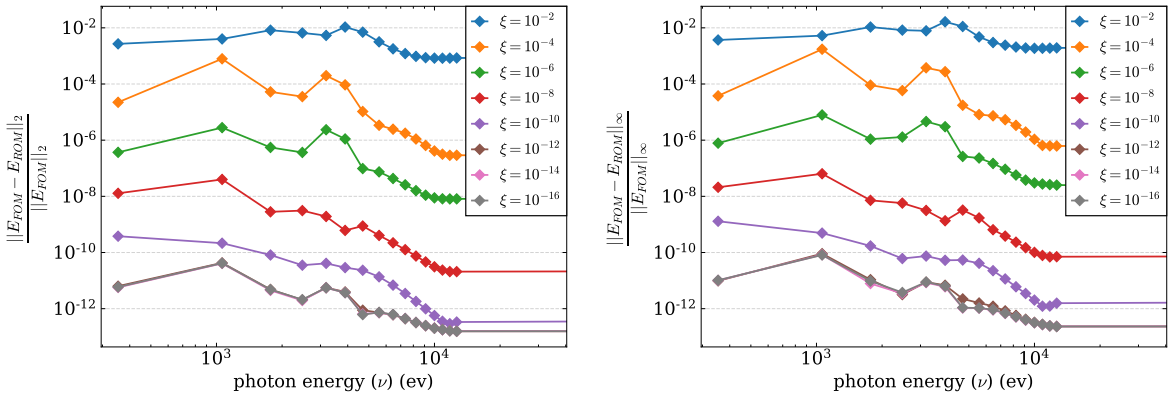

(a) 2 norm

(b) infinity norm

Figure 7.18: Relative errors of the radiation spectrum produced by the POD-PG NBTE-QD ROM using $s_{\max} = \infty$ located at the midpoint of the right boundary in the 2-norm and ∞-norm along the temporal interval $t \in [0, 3\text{ns}]$

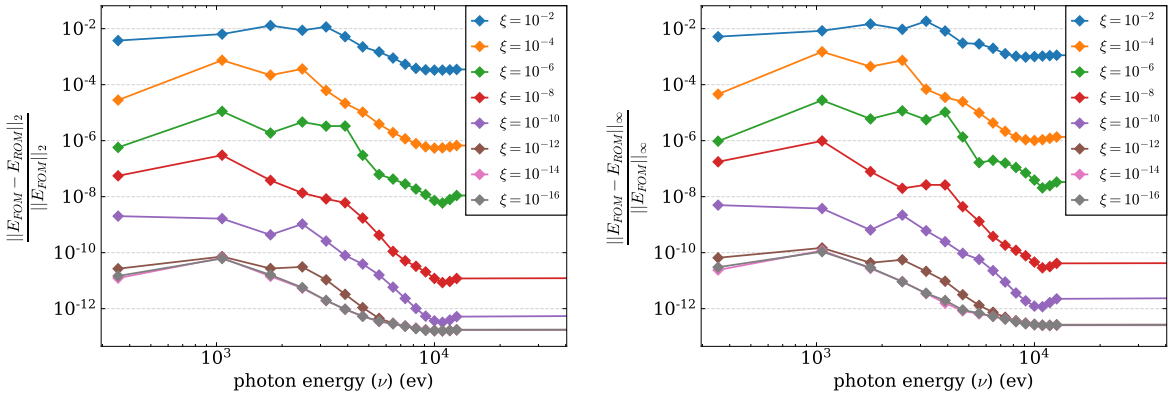

(a) 2 norm

(b) infinity norm

Figure 7.19: Relative errors of the radiation spectrum produced by the POD-PG NBTE-QD ROM using $s_{\max} = \infty$ located at the corner of the right boundary in the 2-norm and ∞-norm along the temporal interval $t \in [0, 3\text{ns}]$

Figs. 7.20, 7.21 and 7.22 plot the 2-norm and ∞-norm (in time) of the relative errors in the model(1|1) solution. Each figure represents one of the three chosen points on the spatial domain. Only $\xi \geq 10^{-8}$ is shown, as the error saturates at $\xi = 10^{-8}$. When $\xi = 10^{-2}$, these error plots are essentially the same as for model($\infty|\infty$). At $\xi = 10^{-4}$ the high-frequency groups are recreated to almost the saturation point of error, while the low frequency ranges have elevated levels of error at points on the right domain boundary. At the domain midpoint most groups are found at the near saturation point of error for $\xi = 10^{-4}$. Errors converge uniformly along the frequency axis with decreases in ξ to the saturation point, although decreases in ξ past a value of 10^{-4} essentially only reduce the error of low-frequency diffusive groups of radiation. At the saturation point all groups are found with errors below 10^{-4}, most lying below 10^{-5}.

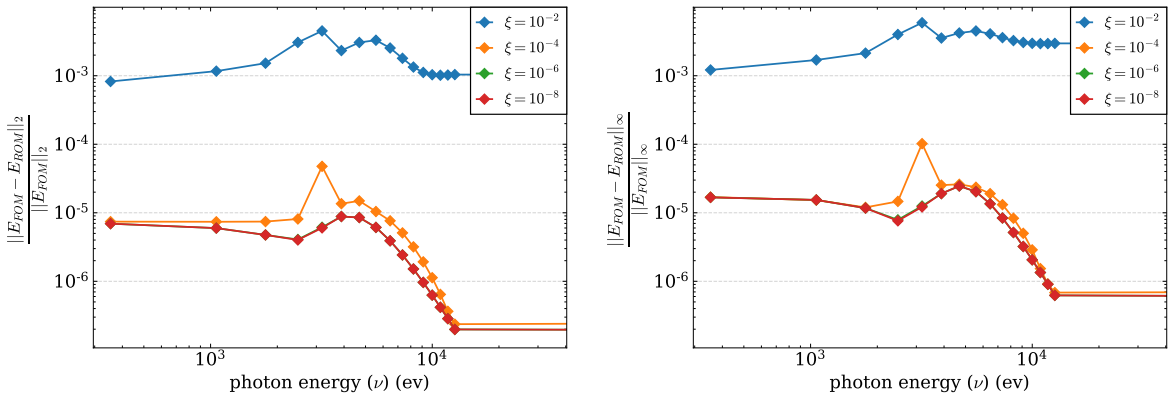

(a) 2 norm

(b) infinity norm

Figure 7.20: Relative errors of the radiation spectrum produced by the POD-PG NBTE-QD ROM using $s_{\max} = 1$ located at the domain midpoint in the 2-norm and ∞-norm along the temporal interval $t \in [0, 3\text{ns}]$

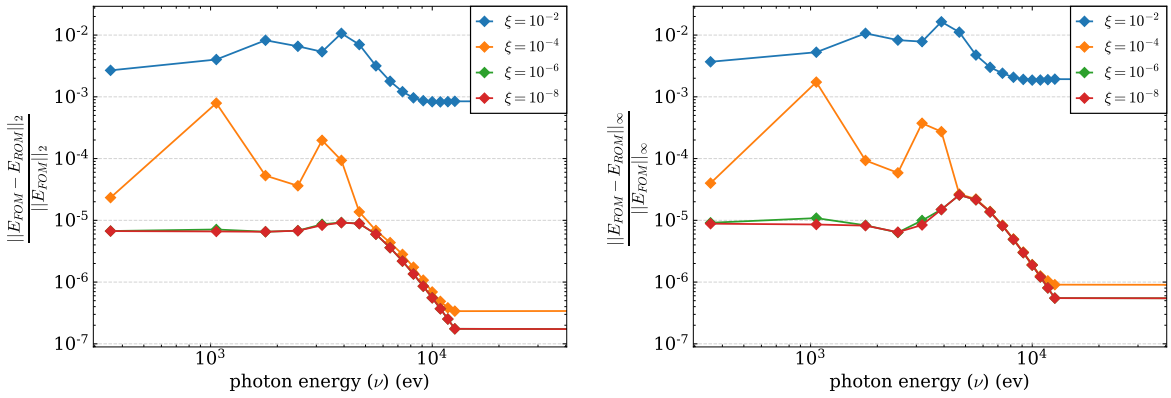

(a) 2 norm

(b) infinity norm

Figure 7.21: Relative errors of the radiation spectrum produced by the POD-PG NBTE-QD ROM using $s_{\max} = 1$ located at the midpoint of the right boundary in the 2-norm and ∞-norm along the temporal interval $t \in [0, 3\text{ns}]$

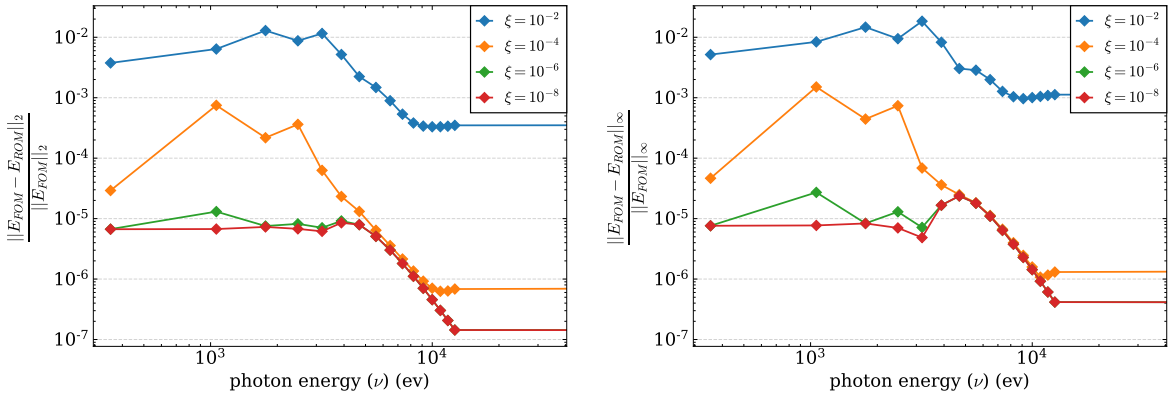

(a) 2 norm

(b) infinity norm

Figure 7.22: Relative errors of the radiation spectrum produced by the POD-PG NBTE-QD ROM using $s_{\max} = 1$ located at the corner of the right boundary in the 2-norm and ∞-norm along the temporal interval $t \in [0, 3\text{ns}]$

7.7 Discussion

In this chapter a ROM is presented for TRT problems constructed using a POD-Petrov-Galerkin projection of the normalized Boltzmann equation, whose solution constructs closures for the LOQD moment equations. The model is tested on the 2-dimensional F-C test problem. One POD basis describing the normalized intensities is used that can describe all encountered physical regimes. The ROM is demonstrated to reproduce the FOM solution to the F-C test with high accuracy while using very low-rank expansions of the high-order intensities. Errors in the ROM solution are shown to decrease linearly with the parameter ξ that determines rank. Both the breakout time of radiation in the F-C test and the spectrum of radiation are found with high accuracy at low rank. Similar performance of the ROM is observed when using only a single high-order iteration at each time step.

By projecting the BTE that solves for a normalized radiation intensity distribution, and scaling the discrete equations with the opacity function, numerical noise in the POD basis and projection procedure were minimized and the resulting ROM was shown to have no significant sensitivities or numerical issues. This is also in part due to the choice of a Petrov-Galerkin projection scheme as opposed to a Galerkin projection scheme. Projection of the NBTE with a POD-Galerkin scheme has been investigated and found to be somewhat less accurate than the used Petrov-Galerkin projection. It is worth noting that although the Petrov-Galerkin projection scheme has higher computational complexity compared to the Galerkin projection scheme due to the nonlinear dependence of the introduced test basis functions with the solution, with the application of hyper-reduction techniques [153, 154, 140] the computational cost of both schemes will be essentially the same.

The robustness and accuracy of the developed ROM make extensions of the model attractive for parametric applications, and for classes of radiative transfer problems with other involved multiphysics.

CHAPTER

8

IMPLICIT METHODS WITH REDUCED MEMORY FOR THERMAL RADIATIVE TRANSFER

This chapter presents an approximate implicit method with reduced memory for the BTE in TRT problems in the context of the MLQD methodology. The memory requirements in TRT problems is largely determined by the dimensionality of grid functions of the radiation intensity. The backward Euler time integration scheme is considered, where grid functions of the intensity must be stored from the previous time step at each time. In this numerical method the high-dimensional intensity from the previous time level is approximated by means of the low-rank POD. A variant of this method is also presented, where the POD is found for the remainder term of the P_2 expansion of the intensity function. This method enables a reduction in the storage requirements for time dependent problems of TRT. The results presented in this chapter have been published in [87] and presented at the 2021 International Conference on Mathematics and Computational Methods Applied to Nuclear Science and Engineering.

8.1 Fundamental Approach

Temporal discretization schemes for the BTE involve the discrete solution at the previous time level. Consider the multigroup BTE (Eq. 1.6) discretized with the backward-Euler (BE) time integration scheme

$$\frac{1}{c\Delta t^n}(I_g^n - I_g^{n-1}) + \mathbf{\Omega}\cdot\boldsymbol{\nabla} I_g^n + \varkappa_{E,g}^n(T) I_g^n = \varkappa_{B,g}^n(T) B_g^n(T). \tag{8.1}$$

In 3D geometry this requires storing in memory a 6-dimensional grid function that approximates the transport solution on a given mesh in phase space. There are different approaches for developing approximate methods for time-dependent transport problems that reduce memory requirements [155, 156, 57, 157, 158]. For instance, the α-approximation of the intensity in time reduces the BTE to a transport equation of steady-state form with a modified opacity [155]. This approximation assumes that the intensity varies exponentially over each time interval. The approximate rate of change in time can be obtained by means of the solution of low-order moment equations. As such, the α-approximation rids one of the need to store the high-dimensional solution from the previous time level [155]. This approximation method for the time-dependent BTE demonstrated good accuracy in TRT problems [99, 109]. Analysis showed that there are some limitations for the BTE in the α-approximation [157].

Recently, approximate implicit methods with reduced memory for the time-dependent BTE have been proposed [158]. They use the modified backward Euler (MBE) time integration scheme that applies the POD of the transport solution from the previous time step to compress the data and reduce memory requirements [30, 33, 138]. The accuracy of the method depends on the order of the low-rank POD of the discrete transport solution. The error decreases as rank increases. The MBE scheme is applied here within the framework of the MLQD method for solving TRT problems [99, 101, 103].

In the approximate implicit scheme, the multigroup BTE is discretized by the MBE time integration scheme given by [158]

$$\frac{1}{c\Delta t^n}(I_g^n - \hat{I}_g^{n-1}) + \mathbf{\Omega}\cdot\boldsymbol{\nabla} I_g^n + \varkappa_{E,g}^n(T) I_g^n = \varkappa_{B,g}^n(T) B_g^n(T), \tag{8.2}$$

where the grid functions of group intensity $\hat{I}_g^{n-1}$ are approximated by the low-rank POD of the solution I_g^{n-1} computed at the time step $n-1$.

1D slab geometry is considered here, and the BTE is discretized in space with the

step-characteristics (SC) scheme. The SC scheme for the Eq. 8.2 is formulated for the cell-edge $\left(I^n_{g,m,i+1/2}\right)$ and cell-average $\left(I^n_{g,m,i}\right)$ angular fluxes by means of the detailed particle balance equation and weighted auxiliary relation

$$\frac{\Delta x_i}{c\Delta t^n}\left(I^n_{g,m,i} - \hat{I}^{n-1}_{g,m,i}\right) + \mu_m\left(I^n_{g,m,i+1/2} - I^n_{g,m,i-1/2}\right) + \varkappa^n_{E,g,i} I^n_{g,m,i}\Delta x_i = 2\pi\varkappa^n_{B,g,i} B^n_{g,i}\Delta x_i\,, \quad (8.3a)$$

$$I^n_{g,m,i} = \gamma^n_{g,m,i} I^n_{g,m,i-1/2} + (1-\gamma^n_{g,m,i}) I^n_{g,m,i+1/2}\,, \quad (8.3b)$$

$$\gamma^n_{g,m,i} = \frac{1}{\tau^n_{g,m,i}} - \frac{1}{e^{\tau^n_{g,m,i}} - 1}\,, \quad \tau^n_{g,m,i} = \frac{1}{\mu_m}\left(\varkappa^n_{E,g,i} + (c\Delta t^n)^{-1}\right)\Delta x_i\,, \quad (8.3c)$$

where μ_m is the discrete directional cosine.

8.2 Approximation of the Specific Intensity

8.2.1 POD of the Intensity

The MBE scheme needs to store the vector of intensities in phase space $\boldsymbol{I}^n \in \mathbb{R}^{\mathfrak{N}_I}$ where $\mathfrak{N}_I = N_g N_\Omega \mathfrak{N}^\Gamma_I$ and $\mathfrak{N}^\Gamma_I$ is the intensity DoF in space (on the domain Γ). Let $\boldsymbol{I}^n_{g,m} \in \mathbb{R}^{\mathfrak{N}^\Gamma_I}$ be the vector of intensities for the discrete angle $m = 1, \ldots, N_\Omega$ in group $g = 1, \ldots, N_g$. At the n^{th} time step. The intensity grid function can be used to construct the following data matrix:

$$\mathbf{A}^{I_g}_\Omega = [\boldsymbol{I}^n_{g,1} \ldots \boldsymbol{I}^n_{g,N_\Omega}] \in \mathbb{R}^{\mathfrak{N}^\Gamma_I \times N_\Omega}, \quad (8.4)$$

which takes the form of a matrix of snapshots in angle, as opposed to the traditional temporal snapshots [30]. The grid function of group intensities in space and angle can now be approximated by the low-rank POD [33, 138] by calculating the SVD of $\mathbf{A}^{I_g}_\Omega$ as

$$\mathbf{A}^{I_g}_\Omega = \mathbf{U}\mathbf{S}\mathbf{V}^\top, \quad (8.5)$$

where $\mathbf{S} = \operatorname{diag}(\sigma_1, \ldots, \sigma_r) \in \mathbb{R}^{r\times r}$ is the matrix of singular values, $\mathbf{U} = [\boldsymbol{u}_1 \ \ldots \ \boldsymbol{u}_r] \in \mathbb{R}^{\mathfrak{N}^\Gamma_I \times r}$ and $\mathbf{V} = [\boldsymbol{v}_1 \ \ldots \ \boldsymbol{v}_r] \in \mathbb{R}^{N_\Omega \times r}$ are the matrices of left and right singular vectors respectively, and $r = \operatorname{rank}(\mathbf{A}^{I_g}_\Omega)$ (see Sec. 3.1). The approximate group intensity $\hat{\boldsymbol{I}}^n \approx \boldsymbol{I}^n$

is defined by the rank-k POD of $\mathbf{A}_\Omega^{I_g}$ given by Eq. 3.9, or equivalently:

$$\mathbf{A}_{\Omega,k}^{I_g} = \sum_{\ell=1}^{k} \sigma_\ell \boldsymbol{u}_\ell \otimes (\boldsymbol{v}_\ell)^\top , \quad k \leq r , \quad \text{where} \quad \mathbf{A}_{\Omega,k}^{I_g} = [\hat{\boldsymbol{I}}_{g,1}^n \dots \hat{\boldsymbol{I}}_{g,N_\Omega}^n] . \tag{8.6}$$

In this manner the vectors of group intensities for each discrete direction are each represented by the expansion in Eq. 3.7 with no centering ($\bar{\boldsymbol{a}} = 0$). Here the case when all groups use the same rank k is considered. The low-rank approximation (Eq. 8.6) requires storage of the first k singular values and associated left and right singular vectors. Thus, this approximation leads to memory allocation of a data set with the number of elements $kN_g(\mathfrak{N}_I^\Gamma + N_\Omega + 1)$. The ranks k can be chosen according to various criteria.

8.2.2 POD of the Remainder Term

Let us now cast the group intensity at each direction as its P_2 approximation and define the resulting remainder term as

$$\Delta I_{m,i} = I_{m,i} - \frac{1}{2}\Big(\tilde{\phi}_i + 3\mu_m \tilde{F}_i + \frac{5}{4}\big(3\mu_m^2 - 1\big)\big(3\mathfrak{f}_i - 1\big)\tilde{\phi}_i\Big) , \tag{8.7}$$

where the subscripts g and n have been neglected for brevity, $i = 1, \dots, \mathfrak{N}_I^\Gamma$ is the index of spatial DoF and the P_2 expansion coefficients are calculated by the solution of the high-order BTE, namely,

$$\tilde{\phi}_i = \sum_{m=1}^{N_\Omega} I_{m,i} w_m , \quad \tilde{F}_i = \sum_{m=1}^{N_\Omega} \mu_m I_{m,i} w_m , \quad \mathfrak{f}_i = \frac{\sum_{m=1}^{N_\Omega} \mu_m^2 I_{m,i} w_m}{\sum_{m=1}^{N_\Omega} I_{m,i} w_m} . \tag{8.8}$$

Let $\Delta \boldsymbol{I}_{m,g} \in \mathbb{R}^{\mathfrak{N}_I^\Gamma}$ be the vector of the discrete grid function $\Delta I_{g,m,i}^n$ for the angle m in group g. This grid function is described by the data matrices constructed of its angular snapshots in each group

$$\mathbf{A}_\Omega^{\Delta I_g} = [\Delta \boldsymbol{I}_{g,1}^n \dots \Delta \boldsymbol{I}_{g,N_\Omega}^n] \in \mathbb{R}^{\mathfrak{N}_I^\Gamma \times N_\Omega}, \tag{8.9}$$

The SVD of these matrices is

$$\mathbf{A}_\Omega^{\Delta I_g} = \mathbf{U}' \mathbf{S}' (\mathbf{V}')^\top, \tag{8.10}$$

where $\mathbf{S}' = \mathrm{diag}(\sigma_1', \dots, \sigma_{r'}') \in \mathbb{R}^{r' \times r'}$, $\mathbf{U}' = [\boldsymbol{u}_1' \ \dots \ \boldsymbol{u}_{r'}'] \in \mathbb{R}^{\mathfrak{N}_I^\Gamma \times r'}$, $\mathbf{V}' = [\boldsymbol{v}_1' \ \dots \ \boldsymbol{v}_{r'}'] \in \mathbb{R}^{N_\Omega \times r'}$, and $r' = \mathrm{rank}(\mathbf{A}_\Omega^{\Delta I_g})$ (see Sec. 3.1). An approximation of the group remainder

term $\Delta\hat{\boldsymbol{I}}^n \approx \Delta\boldsymbol{I}^n$ is defined by the rank-k POD of $\mathbf{A}_{\Omega}^{\Delta I_g}$ given by

$$\mathbf{A}_{\Omega,k}^{\Delta I_g} = \sum_{\ell=1}^{k} \sigma'_\ell \boldsymbol{u}'_\ell \otimes (\boldsymbol{v}'_\ell)^\top \,, \quad k \leq r' \,, \quad \text{where} \quad \mathbf{A}_{\Omega,k}^{\Delta I_g} = [\Delta\hat{\boldsymbol{I}}_{g,1}^n \ldots \Delta\hat{\boldsymbol{I}}_{g,N_\Omega}^n] \,. \tag{8.11}$$

This approximation can be interpreted as expanding the P_2 remainder of the group intensities at each discrete angle with Eq. 3.7 where $\bar{\boldsymbol{a}} = 0$. Approximate intensities are calculated as the sum of the P_2 approximation and rank-k estimated remainder term

$$\hat{I}_{m,i} = \frac{1}{2}\Big(\tilde{\phi}_i + 3\mu_m \tilde{F}_i + \frac{5}{4}\big(3\mu_m^2 - 1\big)\big(3\mathfrak{f}_i - 1\big)\tilde{\phi}_i\Big) + \Delta\hat{I}_{m,i} \,. \tag{8.12}$$

This approximation needs to store in memory $N_g[k(\mathfrak{N}_I^\Gamma + N_\Omega + 1) + 2\mathfrak{N}_I^\Gamma]$ elements (assuming all groups use k POD expansion terms) that includes in each group (i) $k(\mathfrak{N}_I^\Gamma + N_\Omega + 1)$ elements for the remainder term POD representation and (ii) $2\mathfrak{N}_I^\Gamma$ elements for vectors of two angular moments $\tilde{\phi}$, $\tilde{F}$.

8.3 Numerical Results

Let the developed scheme be denoted as the MBE-SC scheme, whose algorithm for TRT problems is outlined in Alg. 7. Analysis of the presented numerical method using the MBE-SC scheme to reduce memory requirements is done using the F-C test in 1D slab geometry (ref. Appendix D). The **F-C Test B** is used here (see Sec. 6.4.1). The SC scheme is used to discretize the BTE in space with $\mathfrak{N}_I^\Gamma = N_x = 100$ cells.

The discrete solution of the MLQD method with the MBE-SC scheme, namely, the total radiation energy density E_h^k and temperature T_h^k of the approximate implicit method with the rank k POD is compared to the discrete solution T_h and E_h of the MLQD method with the BE-SC scheme on the corresponding grid in the phase space and time. Numerical results of the MBE-SC scheme that uses a rank-k approximation of the previous time level radiation intensities in all groups are presented in Fig. 8.1. The plots show the relative error in reproducing the discrete solution in ∞-norm, namely, $\frac{||T_h - T_h^k||_\infty}{||T_h||_\infty}$ and $\frac{||E_h - E_h^k||_\infty}{||E_h||_\infty}$ for the complete range of $k = 1, \ldots, r$. The results obtained with the MBE-SC scheme using the rank-k POD of the remainder term of the previous time step intensities in each group are shown in Fig. 8.2. Note that in this test, the full rank is $r = r' = N_\Omega = 8$. Results with the full-rank POD ($k = 8$) of both methods illustrate that they accurately reproduce the discrete solution of the MLQD method with the BE-SC scheme on the

Algorithm 7: MLQD algorithm for TRT problems with the MBE scheme

$n = 0$
while $t^n \leq t^{end}$
  $n = n + 1$
  $T^{(0)} = T^{n-1}$
  $\mathfrak{f}_g^{(0)} = \mathfrak{f}_g^{n-1}$
  $s = -1$
  while $\|T^{(s)} - T^{(s-1)}\| > \epsilon_1 \|T^{(s)}\| + \epsilon_2$,
    $\|E^{(s)} - E^{(s-1)}\| > \epsilon_1 \|E^{(s)}\| + \epsilon_2$ **do**
    $s = s + 1$
    if $s \geq 1$ **then**
      Update $\varkappa_{E,g}, \varkappa_{B,g}, B_g$ with $T^{(s-1)}$
      if *using* P_2 *remainder* **then**
        Let $\hat{I}_g^{n-1}$ be represented by $\tilde{\phi}_g$, $\tilde{F}_g$, $\mathfrak{f}_g^{n-1}$ and rank-k POD of of ΔI_g^{n-1}
      end
      else
        Let $\hat{I}_g^{n-1}$ be represented by the rank-k POD of I_g^{n-1}
      end
      Solve the BTE with the MBE scheme (Eq. 8.2) for $I_g^{(s)}$ using $\hat{I}_g^{n-1}$
      Compute $\mathfrak{f}_g^{(s)}$ from $I_g^{(s)}$ (Eq. 2.4)
    end
    $\ell = 0$
    while $\|T^{(s,\ell)} - T^{(s,\ell-1)}\| > \epsilon_1 \|T^{(s,\ell)}\| + \epsilon_2$,
      $\|E^{(s,\ell)} - E^{(s,\ell-1)}\| > \epsilon_1 \|E^{(s,\ell)}\| + \epsilon_2$ **do**
      $\ell = \ell + 1$
      Update $\varkappa_{E,g}, \varkappa_{B,g}, \tilde{\varkappa}_{R,g}, B_g$ with $T^{(s-1,\ell)}$
      Solve multigroup LOQD equations (Eqs. 2.3) with $\mathfrak{f}_g^{(s)}$ for $E_g^{(s,\ell)}$, $\boldsymbol{F}_g^{(s,\ell)}$
      Compute spectrum-averaged closures for the effective grey problem with $E_g^{(s,\ell)}$, $\boldsymbol{F}_g^{(s,\ell)}$
      Solve effective grey problem (Eqs. 2.13 and 2.20) for $T^{(s,\ell)}$, $E^{(s,\ell)}$, $\boldsymbol{F}^{(s,\ell)}$
    end
    $T^{(s)} \leftarrow T^{(s,\ell)}$
  end

```
    T^n ← T^(s)
    f_g^n ← f_g^(s)
    if using P_2 remainder then
        Calculate φ̃_g, F̃_g from I_g^(s) (Eq. 8.8)
        Calculate ΔI_g^n with P_2 terms and I_g^n = I_g^(s)
        Obtain rank-k POD representation of ΔI_g^n
    end
    else
        Calculate rank-k POD representation of I_g^n = I_g^(s)
    end
end
```

given grid as expected. In case $k = 5, 6, 7$ the solution of the method with the POD of the remainder term has very small error. This is due to explicit accounting for the first three Legendre moments of the intensity (Eq. 8.12). The singular eigenvalues σ'_ℓ for $\ell = 5, 6, 7$ in groups are very small. In this test problem, the method with POD of the remainder term is predominantly more accurate than to the method with POD of the intensity for

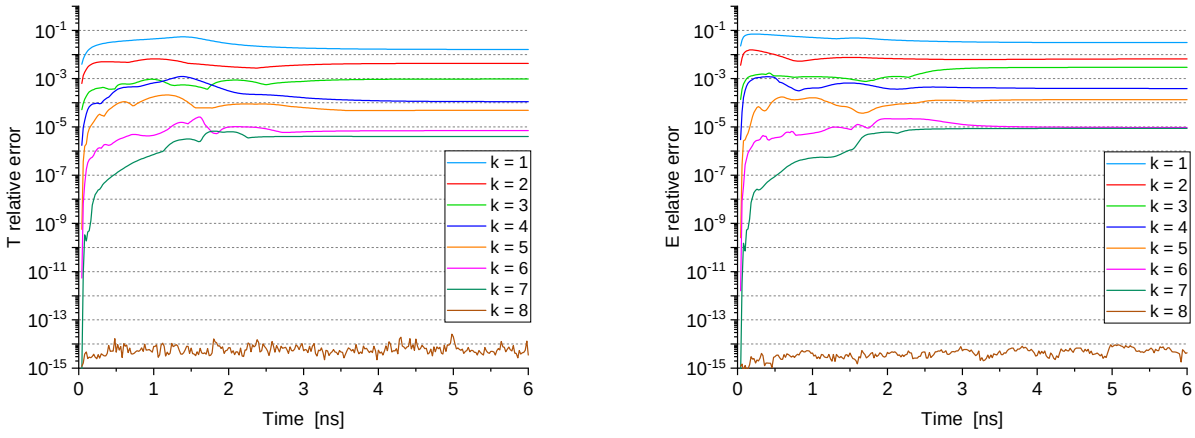

(a) $\frac{||T_h - T_h^k||_\infty}{||T_h||_\infty}$. (b) $\frac{||E_h - E_h^k||_\infty}{||E_h||_\infty}$.

Figure 8.1: Relative error in ∞-norm of the solution of the MLQD method with the MBE-SC scheme and POD of the intensity compared to the discrete solution on the corresponding grid in phase space and time.

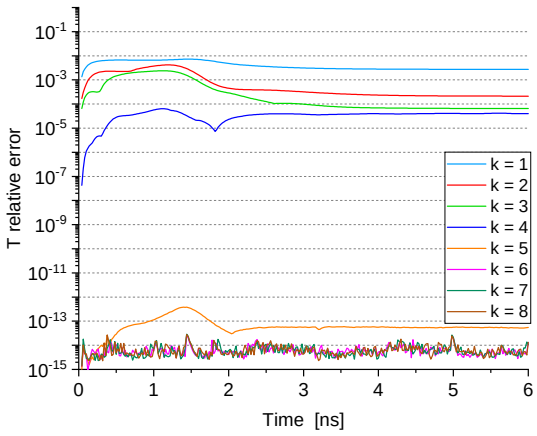

(a) $\frac{||T_h - T_h^k||_\infty}{||T_h||_\infty}$.

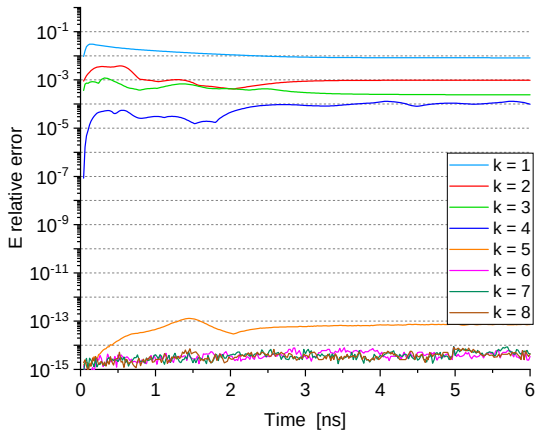

(b) $\frac{||E_h - E_h^k||_\infty}{||E_h||_\infty}$.

Figure 8.2: Relative error in ∞-norm of the solution of the MLQD method with the MBE-SC scheme and POD of the remainder term compared to the discrete solution on the corresponding grid in phase space and time.

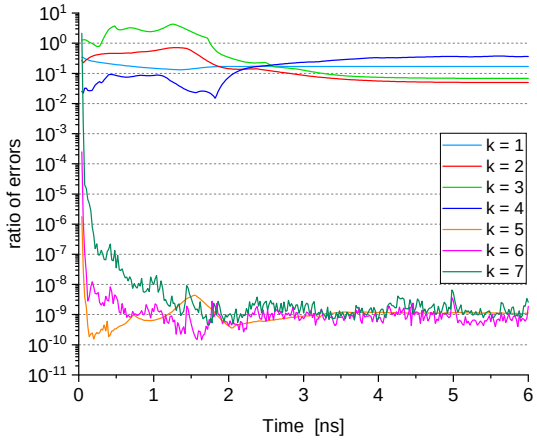

(a) $\frac{||T_h - T_h^k||_\infty^{\text{POD-RT}}}{||T_h - T_h^k||_\infty^{\text{POD-I}}}$.

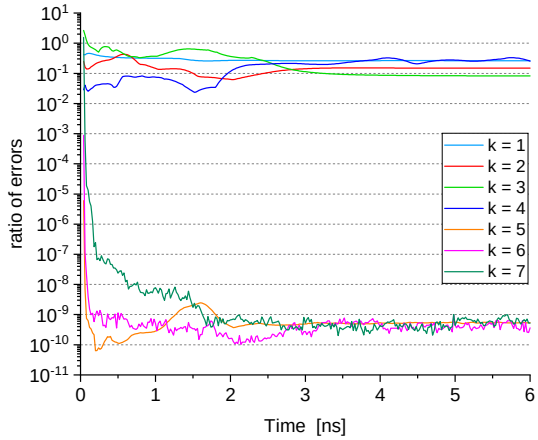

(b) $\frac{||E_h - E_h^k||_\infty^{\text{POD-RT}}}{||E_h - E_h^k||_\infty^{\text{POD-I}}}$.

Figure 8.3: The error of the method with POD of the remainder term (POD-RT) over the error of the method with POD of intensity (POD-I).

the given rank k. However, it uses more data for the same rank k. Fig. 8.3 shows the ratio between errors of the method with the POD of the remainder term (POD-RT) and the one with the POD of the intensity (POD-I).

The gains in memory allocation depend on both the number of spatial cells N_x and angular directions N_Ω and hence are problem specific. For the phase-space grid used in the test, the size of the data set stored by this MLQD method with the BTE discretized the BE-SC scheme at the end of each time step is $N_g(N_x \times N_\Omega + 2 \times N_x + 1) + 2 \times N_x + 1 = 17218$. This includes the data for (i) the multigroup BTE, (ii) the multigroup and grey LOQD equations, and (iii) the MEB equation. Tab. 8.1 shows the percentage reduction of required data storage sizes of the MLQD method with each of the two versions of the MBE-SC scheme compared to that of the MLQD method with the BE-SC scheme. Negative values indicate an increase in storage compared to the BE-SC scheme. In this test, the method with POD of intensities shows gains in memory for all ranks less than full rank, i.e. $k = 1, \ldots, 7$. The method with POD of the remainder term reduces memory allocation for $k = 1, \ldots, 5$.

Rank (k)	1	2	3	4	5	6	7
POD-I	68.2	57.5	46.7	35.9	25.2	14.4	3.7
POD-RT	48.5	37.7	27.0	16.2	5.4	-5.3	-16.1

Table 8.1: Reduction [%] in memory storage of previous step data of the MBE ROM compared to the FOM (N_x=100, N_Ω=8).

Figs. 8.4 and 8.5 present the results of spatial mesh refinement for the fixed time step size $\Delta t = 2 \times 10^{-2}$ ns. They show the relative error of E in ∞-norm for uniform meshes with $\Delta x = 0.24$, 0.12, 0.06, 0.03 cm. The number of DoF of the discrete intensity increases with refinement of spatial mesh. The results show that the change in the relative error decreases with refinement. The factor of change on fine meshes approaches one. This indicates that the error due to low-rank POD of data representing intensities tends to a limit as $\Delta x \to 0$ for the fixed time step Δt. Figs. 8.6 and 8.7 present the relative error of E in ∞-norm for the numerical solution computed with refined time steps ($\Delta t = 4 \times 10^{-2}$, 2×10^{-2}, 10^{-2}, 5×10^{-3} ns) on the spatial mesh with $\Delta x = 6 \times 10^{-2}$ cm. These results show increase in the relative error in reproducing the discrete solution on the given grids. More analysis is needed to study properties of the methods.

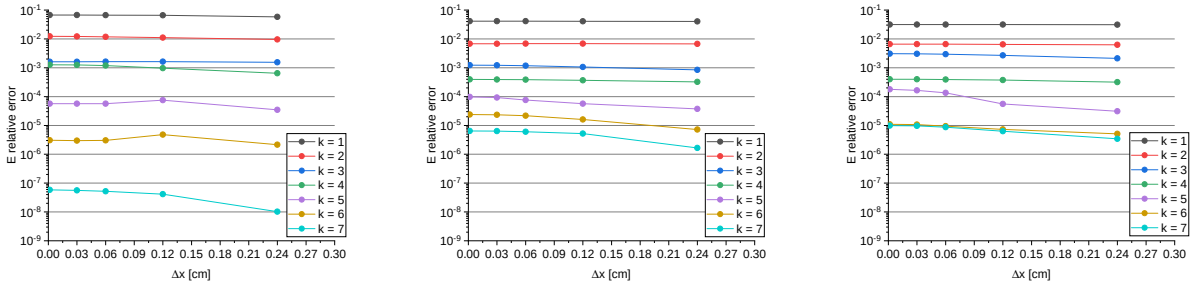

(a) $\frac{||E_h - E_h^k||_\infty}{||E_h||_\infty}$ at $t = 0.4$ ns (b) $\frac{||E_h - E_h^k||_\infty}{||E_h||_\infty}$ at $t = 1$ ns (c) $\frac{||E_h - E_h^k||_\infty}{||E_h||_\infty}$ at $t = 6$ ns

Figure 8.4: Results of refinement of spatial mesh for the MLQD method with the MBE-SC scheme and POD of the intensity for $\Delta t = 2 \times 10^{-2}$.

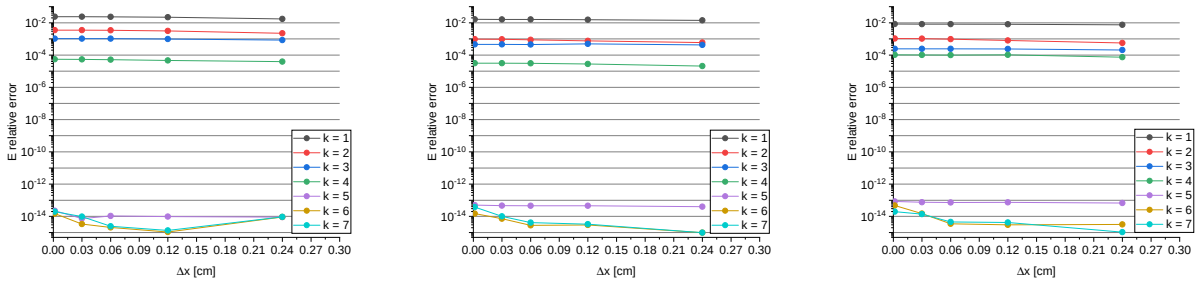

(a) $\frac{||E_h - E_h^k||_\infty}{||E_h||_\infty}$ at $t = 0.4$ ns (b) $\frac{||E_h - E_h^k||_\infty}{||E_h||_\infty}$ at $t = 1$ ns (c) $\frac{||E_h - E_h^k||_\infty}{||E_h||_\infty}$ at $t = 6$ ns

Figure 8.5: Results of spatial mesh refinement for the MLQD method with the MBE-SC scheme and POD of the remainder term for $\Delta t = 2 \times 10^{-2}$ ns.

8.4 Discussion

In this chapter implicit methods with an approximate time evolution operator in the BTE and reduced memory for TRT problems are presented. The obtained results showed that the proposed methods reproduce the numerical solution of the underlying discretization method on the given phase-space grid with various degrees of accuracy while reducing storage of data between time steps. The accuracy depends on the rank of the POD of the data representing intensity from the previous time level. It is possible to achieve accuracy that is good for practical routine simulations and significantly reduce memory usage. There are extra computational costs due to calculations of the POD of intensities. The proposed approximate implicit methods are intended for computer architectures on which one can take advantage of extra computations for reduction of memory storage. The proposed approach can be applied to various time integration methods and different kinds of transport problems.

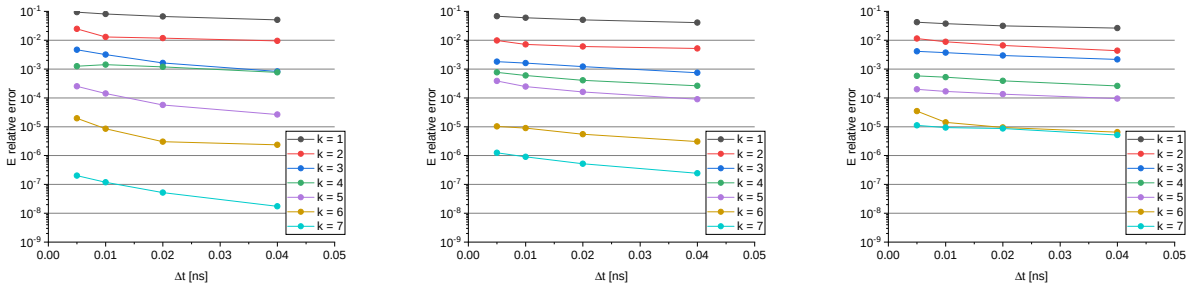

(a) $\frac{||E_h - E_h^k||_\infty}{||E_h||_\infty}$ at $t = 0.4$ ns (b) $\frac{||E_h - E_h^k||_\infty}{||E_h||_\infty}$ at $t = 1$ ns (c) $\frac{||E_h - E_h^k||_\infty}{||E_h||_\infty}$ at $t = 6$ ns

Figure 8.6: Results of time step refinement the MLQD method with the MBE-SC scheme and POD of the intensity $\Delta x = 6 \times 10^{-2}$ cm.

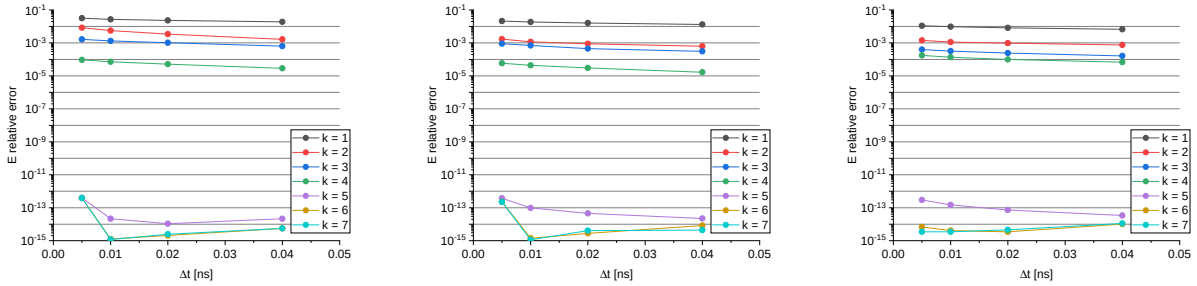

(a) $\frac{||E_h - E_h^k||_\infty}{||E_h||_\infty}$ at $t = 0.4$ ns (b) $\frac{||E_h - E_h^k||_\infty}{||E_h||_\infty}$ at $t = 1$ ns (c) $\frac{||E_h - E_h^k||_\infty}{||E_h||_\infty}$ at $t = 6$ ns

Figure 8.7: Results of time step refinement the MLQD method with the MBE-SC scheme and POD of the remainder term for $\Delta x = 6 \times 10^{-2}$ cm.

CHAPTER

9

CONCLUSIONS

In this work four distinct reduced order models and one numerical method with memory reduction for thermal radiative transfer are developed. Each model is founded on the nonlinear projective approach, or the method of moments, and makes use of the multilevel set of LOQD moment equations coupled to the MEB equation. The LOQD equations are closed with the Eddington tensor that is computed with the shape function of normalized radiation intensities. The ROMs developed in this work use various data-based methodologies to construct advanced and accurate estimations for these closures. The numerical method with reduced memory uses a data-based methodology to approximate grid functions of high-order solutions at previous time levels.

9.1 Overarching Conclusions

Each of the four developed ROMs is shown to effectively reduce the dimensionality of the TRT problem. The models have been demonstrated to be robust for this nonlinear multiphysical class of problems, where a focus has been placed on supersonic radiation shock type problems. All of the models can solve the TRT problem with a spectrum of

accuracy levels depending on the corresponding rank of approximation used. With low rank, each model still finds good accuracy in the solution. The developed method for memory reduction in TRT simulations was shown to effectively reduce storage requirements, while maintaining acceptable levels of accuracy.

9.2 Summary of Results

The DET class of ROMs (presented in Ch. 4) approximates the Eddington tensor with projection-based data-driven methods, specifically considering the POD, DMD and DMD-E. Numerical results showed that with each of the three methods, the DET ROMs could reproduce the FOM TRT solution to high accuracy with very low rank representations of the Eddington tensor. With the POD and DMD the ROM accuracy was found to have a linear relationship with the parameter that determines rank, thus allowing for a-priori predictions of ROM performance. Errors in the ROM solutions were shown to be relatively uniform across all space, frequency and time. The parameterized DET ROM with the POD was developed based on parameterization with respect to the inverse cube of a characteristic temperature. This produced relatively uniform accuracy across the entire considered parameter space.

The TCA class of ROMs (presented in Ch. 5) approximates the Eddington tensor over all phase space and time at once by constructing a linear radiative transfer problem whose opacities and emission source are evaluated using a diffusion solution over the phase space and time. Numerical results showed that this ROM improves upon the accuracy of various diffusion models for TRT by 1-2 orders of magnitude in space and time. The low-frequency range of radiation is improved upon by the same amount. In the high-frequency range where there are significant transport effects present, the TCA ROM improves upon the diffusion model accuracy by up to 4-5 orders of magnitude.

The POD-G BTE-QD class of ROMs (presented in Ch. 6) uses a low-dimensional POD projection of the BTE to estimate the Eddington tensor. The solution to this projected BTE poses low computational burden to calculate and represents the high-order intensities as a low dimensional expansion of global basis functions in phase space. Numerical results demonstrated that this ROM can solve TRT problems with a range of accuracies depending on the used rank of approximation. Low levels of error are produced even with very low rank representations of the high order intensities. Errors are shown to converge linearly with the parameter that determines rank.

The POD-PG NBTE-QD class of ROMs (presented in Ch. 7) uses a low-dimensional POD projection of the NBTE to estimate the Eddington tensor. A discretization scheme for the NBTE is also presented that is consistent with a scheme for the BTE. The projected NBTE provides a low-dimensional representation of the normalized radiation intensities that determine the Eddington tensor by a linear superposition. Numerical results showed that this ROM can solve TRT problems with a large spectrum of accuracies that depends on the rank of expansion for the normalized intensities. With very low dimensional representations of the NBTE (and normalized intensities) this model finds accurate solutions to the TRT problem. The solution errors converge linearly with the parameter that determines rank. This model was also found to produce accurate solutions to the TRT problem while only using a single iteration of the POD projected NBTE at each instant of time. Error levels along the frequency spectrum of radiation decrease in the high frequency ranges.

The MBE-SC scheme for the BTE (presented in Ch. 8) approximates the radiation intensities at the previous time level with a low-rank POD expansion. Numerical results demonstrate that the method effectively reduces the memory requirements of TRT simulations while maintaining several different levels of accuracy compared to the BE-SC scheme based on the rank of POD expansion. The reduction in memory invokes extra computational cost at each time step, making this method attractive for computing architectures that can take advantage of using extra computation to reduce needed memory storage.

9.3 Future Work

All developed ROMs are constructed in such a way that allows for natural extension to a wide class of multiphysical high-energy density problems, such as radiation hydrodynamics problems. The effective grey low-order moment system can be coupled to any set of involved multiphysics equations. The necessary changes to each model include the incorporation of any additional terms to account for the coupled multiphysics effects. For instance, a conduction term could be added to the MEB equation with no additional changes to the system of moment equations. This also holds true for the MBE-SC numerical method. For the DET, TCA and POD-PG NBTE-QD models, an extension into 3D geometry is another natural next step. The same can be said for the MBE-SC scheme and POD-G BTE-QD ROM into multi-D geometry.

Parameterization can be considered as a future research item for all ROMs, which have each been shown robust and accurate to the target class of problems. This is a promising direction for further development given the performance and quality of each model. For this purpose, one can consider reduced basis techniques [42, 69] or interpolation procedures, including manifold interpolation [159, 160]. The parameterization developed for the DET ROMs in Ch. 4 would likely perform well for each of the other developed ROMs. The basic approach of implicit time approximation with reduced memory can also be applied to different spatial discretizations or time integrators.

REFERENCES

[1] J. J. Duderstadt and W. R. Martin. *Transport Theory*. John Wiley & Sons, 1979.

[2] S Chandrasekhar. *Radiative Transfer*. Dover Publications Inc., 1960.

[3] D. H. Sampson. *Radiative Contribution to Energy and Momentum Transport in a Gas*. Interscience Publisher, 1965.

[4] K. H. A. Winkler and M. L. Norman. *Astrophysical Radiation Hydrodynamics*, volume 188 of *Nato ASI Series C: Mathematical and Physical Sciences*. Springer Netherlands, 1986.

[5] F. H. Shu. *The Physics of Astrophysics*. University Science Books, 1991.

[6] J. Lenoble. *Atmospheric Radiative Transfer*. Studies in Geophysical Optics and Remote Sensing. A. DEEPAK Publishing, 1993.

[7] G. E. Thomas and K. Stamnes. *Radiative Transfer in the Atmosphere and Ocean*. Cambridge, 1999.

[8] M. Faghri and B. Sundén. *Transport Phenomena in Fires*, volume 20 of *Developments in Heat Transfer*. WIT, 2008.

[9] R. P. Drake. *High-Energy-Density-Physics: Foundation of Interial Fusion and Experimental Astrophysics*. Springer, 2018.

[10] Ya. B. Zel'dovich and Yu. P. Raizer. *Physics of Shock Waves and High-Temperature Hydrodynamic Phenomena*. Academic Press, 1967.

[11] G. C. Pomraning. *The Equations of Radiation Hydrodynamics*. Elsevier Science & Technology, 1973.

[12] D. Mihalas and B. Weibel-Mihalas. *Foundation of Radiation Hydrodynamics*. Oxford University Press, 1984.

[13] J. I. Castor. *Radiation Hydrodynamics*. Cambridge University Press, 2004.

[14] G. L. Olson, L. H. Auer and M. L. Hall. Diffusion, P_1, and other approximate forms of radiation transport. *Journal of Quantitative Spectroscopy & Radiative Transfer*, 64:619–634, 2000.

[15] J. E. Morel. Diffusion-limit asymptotics of the transport equation, the $P_{1/3}$ equations, and two flux-limited diffusion theories. *Journal of Quantitative Spectroscopy & Radiative Transfer*, 65:769–778, 2000.

[16] K. H. Simmons and D. Mihalas. A linearized analysis of the modified P_1 equations. *Journal of Quantitative Spectroscopy & Radiative Transfer*, 66:263–269, 2000.

[17] C. D. Levermore. Moment closure hierarchies for kinetic theories. *Journal of Statistical Physics*, 83:1021–1065, 1996.

[18] C. D. Hauck. High-order entropy-based closures for linear transport in slab geometry. *Communications in Mathematical Sciences*, 9:187–205, 2011.

[19] G. W. Alldredge, C. D. Hauck, and A. L. Tits. High-order entropy-based closures for linear transport in slab geometry II: A computational study of the optimization problem. *SIAM Journal on Scientific Computing*, 34:B361–B391, 2012.

[20] J. M. LeBlanc and J. R. Wilson. Analytic closures for m1 neutrino transport. *The Astrophysical Journal*, 161:541–551, 1970.

[21] D. S. Kershaw. Flux limiting nature‘s own way – a new method for numerical solution of the transport equation. Technical report, Lawrence Livermore National Laboratory, Livermore, CA, 1976.

[22] C. D. Levermore. Relating Eddington factors to flux limiters. *Journal of Quantitative Spectroscopy & Radiative Transfer*, 31:149–160, 1984.

[23] E. M. Murchikova, E. Abdikamalov, and T. Urbatsch. Analytic closures for M1 neutrino transport. *Monthly Notices of the Royal Astronomical Society*, 469:1725–1737, 2017.

[24] D. J. Lucia, P. S. Beran and W. A. Silva. Reduced-order modeling: New approaches for computational physics. *Progress in Aerospace Sciences*, 40:51–117, 2004.

[25] T. Hastie, R. Tibshirani and J. Friedman. *The elements of statistical learning.* Springer, 2009.

[26] P. Benner, S. Gugercin and K. Willcox. A survey of projection-based model reduction methods for parametric dynamical systems. *SIAM Review*, 57:483–531, 2015.

[27] S. L. Brunton and J. N. Kutz. *Data-Driven Science and Engineering*. Cambridge, 2019.

[28] P. Benner, S. Givet-Talocia, A. Quarteroni, G. Rozza, W. Schilders, and L. M. Silveria. *Model Order Reduction: Volume 2: Snapshot-Based Methods and Algorithms*. De Gruyter, 2020.

[29] J. L. Lumley. The structure of inhomogeneous turbulent flows. In A. M. Yaglmo and V. I. Takarski, editors, *Atmospheric Turbulence and Radio Wave Propagation*, pages 166–178. 1967.

[30] L. Sirovich. Turbulence and the dynamics of coherent structures, parts i-iii. *Quarterly of Applied Mathematics*, XLV:561–590, 1987.

[31] L. Sirovich. Chaotic dynamics of coherent structures. *Physica D*, 37:126–145, 1989.

[32] N. Aubry. The hidden beauty of the proper orthogonal decomposition. *Theoretical and Computational Fluid Dynamics*, 2:339–352, 1991.

[33] G. Berkooz, P. Holmes and J. L. Lumley. The proper orthogonal decomposition in the analysis of turbulent flows. *Annual Review of Fluid Mechanics*, 25:539–575, 1993.

[34] P. Holmes, J. L. Lumley, and G. Berkooz. *Coherent Structures, Dynamical Systems and Symmetry*. Cambridge University Press,, Cambridge, 1996.

[35] C. W. Rowley, I. Mezić, S. Bagheri, P. Schlatter, and D. S. Henningson. Spectral analysis of nonlinear flows. *J. Fluid Mech*, 641:115–127, 2009.

[36] P. J. Schmid. Dynamic mode decomposition of numerical and experimental data. *Journal of Fluid Mechanics*, 656:5–28, 2010.

[37] J. H. Tu, C. W. Rowley, D. M. Luchtenburg, S. L. Brunton and J. N. Kutz. On dynamic mode decomposition: Theory and applications. *Journal of Computational Dynamics*, 1:391–421, 2014.

[38] M. O. Williams, I. G. Kevrekidis and C. W. Rowley. A data-driven approximation of the Koopman operator: Extending dynamic mode decomposition. *Journal of Nonlinear Science*, 25:1307–1346, 2015.

[39] I. Goodfellow, Y. Bengio and A. Courville. *Deep Learning*. MIT Press, 2016.

[40] F. Chinesta, A. Ammar, A. Laygue and R. Keunings. An overview of the proper generalized decomposition with applications in computational rheology. *Journal of Non-Newtonian Fluid Mechanics*, 166:578–592, 2011.

[41] B. C. Moore. Principal component analysis in linear systems: controllability, observability, and model reduction. *IEEE transactions on automatic control*, 26:17–32, 1981.

[42] A. Quarteroni, A. Manzoni and F. Negri. *Reduced Basis Methods for Partial Differential Equations: An Introduction*. Springer, 2015.

[43] K. Kunisch and S. Volkwein. Galerkin proper orthogonal decomposition methods for a general equation in fluid dynamics. *SIAM J. Numer. Anal.*, 40:492–515, 2002.

[44] C. W. Rowley and S. T.M. Dawson. Model reduction for flow analysis and control. *Annu. Rev. Fluid Mech.*, 49:187–417, 2017.

[45] C. W. Rowley. Model reduction for fluids, using balanced proper orthogonal decomposition. *International Journal of Bifurcation and Chaos*, 15:997–1013, 2004.

[46] C. W. Rowley, T. Colonius and R. M. Murray. Model reduction for compressible flows using POD and Galerkin projection. *Physica D*, 189:115–129, 2004.

[47] T. R. Smith, J. Moehlis and P. Holmes. Low-dimensional modelling of turbulence using the proper orthogonal decomposition: A tutorial. *Nonlinear Dynamics*, 41:275–307, 2005.

[48] T. Bui-Thanh, M. Damodaran, and K. Willcox. Proper orthogonal decomposition extensions for parametric applications in compressible aerodynamics. In *Proc. of 21st Applied Aerodynamics Conference*, page 11, 23-28 June 2003, Orlando, FL, 2003.

[49] K. Taira, S. L. Brunton, S. T.M. Dawson, C. W. Rowley, T. Colonius, B. J. McKeon, O. T. Schmidt, S. Gordeyev, V. Theofilis and L. S. Ukeiley. Modal analysis of fluid flows: and overview. *AIAA Journal*, 55(12):4013–4041, 2017.

[50] Y. Choi, P. Brown, W. Arrighi, R. Anderson and K. Huynh. Space-time reduced order model for large-scale linear dynamical systems with application to Boltzmann transport problems. *Journal of Computational Physics*, 424, 2021.

[51] P. A. Behne, J. C. Ragusa and J. E. Morel. Model order reduction for S_N radiation transport. In *Proc. of Int. Conf. on Mathematics and Computational Methods Applied to Nuclear Science and Engineering (M&C 2019)*, page 10 pp, 2019.

[52] P. Behne, J. C. Ragusa, and M. Tano. Projection-based parametric model order reduction for transport simulation based on affine decomposition of the operators. In *Proc. of Int. Conf. on Mathematics and Computational Methods Applied to Nuclear Science and Engineering (M&C 2021)*, page 10 pp, 2021.

[53] A. K. Hardy, J. E. Morel and C. Ahrens. Dynamic mode decomposition for subcritical metal systems. In *Proc. of Int. Conf. on Mathematics and Computational Methods Applied to Nuclear Science and Engineering (M&C 2019)*, page 10 pp, 2019.

[54] Z. M. Prince and J. C. Ragusa. Proper generalized decomposition of multigroup neutron diffusion with seperated space-energy representation. In *Proc. of Int. Conf. on Mathematics and Computational Methods Applied to Nuclear Science and Engineering (M&C 2019)*, page 10 pp, 2019.

[55] K. A. Dominesey and W. Ji. Reduced-order modeling of neutron transport seperated in space and angle via proper generalized decomposition. In *Proc. of Int. Conf. on Mathematics and Computational Methods Applied to Nuclear Science and Engineering (M&C 2019)*, page 10 pp, 2019.

[56] Z. M. Prince and J. C. Ragusa. Seperated representation of spatial dimensions in S_N neutron transport using the proper generalized decomposition. In *Proc. of Int. Conf. on Mathematics and Computational Methods Applied to Nuclear Science and Engineering (M&C 2019)*, page 10 pp, 2019.

[57] Z. Peng, R. G. McClarren and M. Frank. A low-rank method for time-dependent transport calculations. In *Proc. of Int. Conf. on Mathematics and Computational Methods Applied to Nuclear Science and Engineering (M&C 2019)*, page 10 pp, 2019.

[58] Z. Peng and R. McClarren. A high-order / low-order (HOLO) algorithm with low-rank evolution for time-dependent transport calculations. *Transactions of the American Nuclear Society*, 121:805–807, 2019.

[59] Z. Peng, R. G. McClarren and M. Frank. A low-rank method for two-dimensional time-dependent radiation transport calculations. *Journal of Computational Physics*, 421:109735, 2020.

[60] Z. Peng and R. G. McClarren. A low-rank method for the discrete ordinate transport equation compatible with transport sweeps. In *Proc. of Int. Conf. on Mathematics and Computational Methods Applied to Nuclear Science and Engineering (M&C 2021)*, page 10 pp, 2021.

[61] Z. Huang, Y. Chen, A. Christlieb, and L. Roberts. Machine learning moment closure models for the radiative transfer equation I: directly learning a gradient based closure. *Journal of Computational Physics*, 453:110941, 2022.

[62] Z. Huang, Y. Chen, A. Christlieb, L. Roberts, and W.-A. Yong. Machine learning moment closure models for the radiative transfer equation II: enforcing global hyperbolicity in gradient based closures. preprint on arXiv:2105.14410v1, math.NA, 2021.

[63] M. M. Pozulp. 1D transport using neural nets, S_N, and MC. In *Proc. of Int. Conf. on Mathematics and Computational Methods Applied to Nuclear Science and Engineering (M&C 2019)*, page 10 pp, 2019.

[64] M. M. Pozulp, P. S. Brantley, T. S. Palmer, and J. L. Vujic. Heterogeneity, hyperparameters, and GPUs: Towards useful transport calculations using neural networks. In *Proc. of Int. Conf. on Mathematics and Computational Methods Applied to Nuclear Science and Engineering (M&C 2021)*, page 10 pp, 2021.

[65] M. H. Elhareef, Z. Wu, and Y. Ma. Physics-informed deep learning neural network solution to the neutron diffusion model. In *Proc. of Int. Conf. on Mathematics and Computational Methods Applied to Nuclear Science and Engineering (M&C 2021)*, page 10 pp, 2021.

[66] A. G. Buchan, A. A. Calloo, M. G. Goffin, S. Dargaville, F. Fang, C. C. Pain, and I. M. Navon. A POD reduced order model for resolving angular direction in neutron/photon transport problems. *Journal of Computational Physics*, 296:138–157, 2015.

[67] J. Tencer, K. Carlberg, M. Larsen, and R. Hogan. Accelerated solution of discrete Ordinates approximation to the Boltzmann transport equation for a gray absorbing-emitting medium via model reduction. *Journal of Heat Transfer*, 139:122701, 2017.

[68] L. Soucasse, A. G. Buchan, S. Dargaville and C. C. Pain. An angular reduced order model for radiative transfer in non grey media. *Journal of Quantitative Spectroscopy & Radiative Transfer*, 229:23–32, 2019.

[69] Z. Peng, Y. Chen, Y. Cheng, and F. Li. A reduced basis method for radiative transfer equation. *Journal of Scientific Computing*, 91(5), 2022.

[70] A. C. Hughes and A. G. Buchan. An adaptive reduced order model for the angular discretisation of the Boltzmann transport equation using independent basis sets over a partitioning of the space-angle domain. *International Journal for Numerical Methods in Engineering*, pages 1–19, 2022.

[71] R. Elzohery and J. Roberts. Modeling neutronic transients with galerkin projection onto a greedy-sampled, POD subspace. *Annals of Nuclear Energy*, 162:108–487, 2021.

[72] R. Elzohery and J. Roberts. Exploring transient, neutronic, reduced-order models using DMD/POD-Galerkin and data-driven DMD. *EPJ Web Conf.*, 247:15019, 2021.

[73] R. Elzohery and J. Roberts. A multiphysics reduced-order model for neutronic transient using POD-Galerkin projection and DEIM. *Transactions of the American Nuclear Society*, 125:440–443, 2021.

[74] A. L. Alberti and T. S. Palmer. Reduced order modeling of the twigl problem using proper generalized decomposition. In *Proc. of Int. Conf. on Mathematics and Computational Methods Applied to Nuclear Science and Engineering (M&C 2019)*, page 14 pp, 2019.

[75] A. L. Alberti and T. S. Palmer. Reduced-order modeling of nuclear reactor kinetics using proper generalized decomposition. *Nuclear Science and Engineering*, 194:837–858, 2020.

[76] K. A. Dominesey and W. Ji. Reduced-order modeling of neutron transport seperated in energy by proper generalized decomposition with applications to nuclear reactor physics. *Journal of Computational Physics*, 449:110744, 2022.

[77] P. German, J. C. Ragusa, C. Fiorina, and M. T. Retamales. Reduced-order modeling of parameterized multi-physics computations for the molten salt fast reactor. In *Proc. of Int. Conf. on Mathematics and Computational Methods Applied to Nuclear Science and Engineering (M&C 2019)*, page 10 pp, 2019.

[78] P. German, J. C. Ragusa, and C. Fiorina. Application of multiphysics model order reduction to Doppler/neutronic feedback. *Nuclear Sci. Technol.*, 5:17, 2019.

[79] P. German, M. E. Tano, and J. C. Ragusa. Reduced-order modeling of coupled neutronics and fluid dynamics in the zero-power molten salt fast reactor. In *Proc. of Int. Conf. on Mathematics and Computational Methods Applied to Nuclear Science and Engineering (M&C 2021)*, page 10 pp, 2021.

[80] A. Cherezov, R. Sanchez and H. G. Joo. A reduced-basis element method for pin-by-pin reactor core calculations in diffusion and SP_3 approximations. *Annals of Nuclear Energy*, 116:195–209, 2018.

[81] T. R. F. Phillips, C. E. Heaney, B. S. Tollit, P. N. Smith, and C. C. Pain. Reduced-order modelling with domain decomposition applied to multi-group neutron transport. *Energies*, 14:1369, 2021.

[82] J. M. Coale and D. Y. Anistratov. A reduced-order model for thermal radiative transfer problems based on multilevel quasidiffusion method. In *Proc. of Int. Conf. on Mathematics and Computational Methods Applied to Nuclear Science and Engineering (M&C 2019)*, page 10 pp, Portland, OR, 2019.

[83] J. M. Coale and D. Y. Anistratov. Reduced-order models for nonlinear radiative transfer based on moment equations and POD/DMD of Eddington tensor. preprint on arXiv:2107.09174v1, math.NA, 2021.

[84] J. M. Coale and D. Y. Anistratov. Data-driven grey reduced-order model for thermal radiative transfer problems based on low-order quasidiffusion equations and proper orthogonal decomposition. *Transactions of the American Nuclear Society*, 121:836–839, 2019.

[85] L. Fagiano and R. Gati. On the order reduction of the radiative heat transfer model for the simulation of plasma arcs in switchgear devices. *Journal of Quantitative Spectroscopy & Radiative Transfer*, 169:58–78, 2016.

[86] J. M. Coale and D. Y. Anistratov. Reduced-order models for thermal radiative transfer based on POD-Galerkin method and low-order quasidiffusion equations. In *Proc. of Int. Conf. on Mathematics and Computational Methods Applied to Nuclear Science and Engineering (M&C 2021)*, page 10 pp, Raleigh, NC, 2021.

[87] D. Y. Anistratov and J. M. Coale. Implicit methods with reduced memory for thermal radiative transfer. In *Proc. of Int. Conf. on Mathematics and Computational Methods Applied to Nuclear Science and Engineering (M&C 2021)*, page 10 pp, Raleigh, NC, 2021.

[88] A. L. Alberti and T. S. Palmer. Reduced order modeling of non-linear radiation diffusion via proper generalized decomposition. *Transactions of the American Nuclear Society*, 119:691–694, 2018.

[89] M. Girault, Y. Liu, Y. Billaud, D. Saury, and D. Lemonnier. Reduced order models for conduction and radiation inside sem-transparent media via the model identification method. *International Journal of Heat and Mass Transfer*, 168:120598, 2021.

[90] J. Qian, Y. Wang, H. Song, and K. Pant. Projection-based reduced-order modeling for spacecraft thermal analysis. *Journal of Spacecraft and Rockets*, 52(3):978–989, 2015.

[91] L. Soucasse, B. Podvin, P. Rivière, and A. Soufiani. Reduced-order modelling of radiative transfer effects on Rayleigh-Bénard convection in a cubic cell. *J. Fluid Mech.*, 898:A2, 2020.

[92] L. Soucasse, B. Podvin, P. Rivière, and A. Soufiani. Low-order models for predicting radiative transfer effects on Rayleigh-Bénard convection in a cubic cell at different rayleigh numbers. *J. Fluid Mech.*, 917:A5, 2021.

[93] R. Pinnau and A. Schulze. Model reduction techniques for frequency averaging in radiative heat transfer. *Journal of Computational Physics*, 226:712–731, 2007.

[94] R. E. Alcouffe, B. A. Clark, and E. W. Larsen. The diffusion-synthetic acceleration of transport iterations, with application to a radiation hydrodynamics problem. In J. U. Brackbill and B. I. Cohen, editors, *Multiple Time Scales*, volume 3 of *Computational Techniques*, chapter 4, pages 74–112. Academic Press, 1985.

[95] R. Turpault, M. Frank, B. Dubroca, and A. Klar. Multigroup half space moment approximations to the radiative heat transfer equations. *Journal of Computational Physics*, 198:363–371, 2004.

[96] S. R. Johnson and E. W. Larsen. An anisotropic diffusion approximation to thermal radiative transfer. In *Proc. of Int. Conf. on Mathematics and Computational Methods Applied to Nuclear Science and Engineering (M&C 2011)*, page 10 pp, Rio de Janerio, RJ, Brazil, 2011.

[97] E. E. Lewis and W. F. Miller. *Computational Methods of Neutron Transport*. American Nuclear Society, 1993.

[98] V. Ya. Gol'din, D. A. Gol'dina, A. V. Kolpakov, and A. V. Shilkov. Mathematical modeling of hydrodynamics processes with high-energy density radiation. *Problems of Atomic Sci. & Eng.: Methods and Codes for Numerical Solution of Math. Physics Problems*, 2:59–88, 1986. in Russian.

[99] D. Y. Anistratov, E. N. Aristova, and V. Ya. Gol'din. A nonlinear method for solving problems of radiation transfer in a physical system. *Mathematical Modeling*, 8:3–28, 1996. in Russian.

[100] E. N. Aristova, V. Ya. Gol'din, and A. V. Kolpakov. Multidimensional calculations of radiation transport by nonlinear quasi-diffusion method. In *Proc. of Int. Conf. on Math. and Comp., M&C 1999*, pages 667–676, Madrid, Spain, 1999.

[101] V. Ya. Gol'din. A quasi-diffusion method of solving the kinetic equation. *USSR Comp. Math. and Math. Phys.*, 4:136–149, 1964.

[102] L. H. Auer and D. Mihalas. On the use of variable Eddington factors in non-LTE stellar atmospheres computations. *Monthly Notices of the Royal Astronomical Society*, 149:65–74, 1970.

[103] V. Ya. Gol'din and B. N. Chetverushkin. Methods of solving one-dimensional problems of radiation gas dynamics. *USSR Comp. Math. and Math. Phys.*, 12:177–189, 1972.

[104] V. Ya. Gol'din. On mathematical modeling of problems of non-equilibrium transfer in physical systems. In *Modern Problems of Mathematical Physics and Computational Mathematics*, pages 113–127. Nauka, Moscow, 1982. in Russian.

[105] K. A. Winkler, M. L. Norman, and D. Mihalas. Implicit adaptive-grid radiation hydrodynamics. In J. U. Brackbill and B. I. Cohen, editors, *Multiple Time Scales*, volume 3 of *Computational Techniques*, chapter 6, pages 146–185. Academic Press, 1985.

[106] D.Y. Anistratov and V. Ya. Gol'din. Multilevel quasidiffusion methods for solving multigroup transport k-eigenvalue problems in one-dimensional slab geometry. *Nuclear Science and Engineering*, 169:111–132, 2011.

[107] A. Tamang and D.Y. Anistratov. A multilevel quasidiffusion method for solving space-time multigroup neutron kinetics equations coupled with the heat transfer equation. *Nuclear Science and Engineering*, 177:1–19, 2014.

[108] L. R. Cornejo and D. Y. Anistratov. The multilevel quasidiffusion method with multigrid in energy for eigenvalue transport problems. *Progress in Nuclear Energy*, 101:401–408, 2017.

[109] D. Y. Anistratov. Stability analysis of a multilevel quasidiffusion method for thermal radiative transfer problems. *Journal of Computational Physics*, 376:186–209, 2019.

[110] M. L. Adams and E. W. Larsen. Fast iterative methods for discrete-ordinance particle transport calculations. *Prog. Nucl. Energy*, 40:3–159, 2002.

[111] G. C. Pomraning. An extension of the Eddington approximation. *J. Quant. Spectrosc. Radiat. Transfer*, 9:407–422, 1969.

[112] N. Y. Gnedin and T. Abel. Multi-dimensional comsological radiative transfer with a variable eddington tensor formalism. *New Astronomy*, 6:437–455, 2001.

[113] C. D. Levermore and G. C. Pomraning. A flux-limited diffusion theory. *The Astrophysical Journal*, 248:321–334, 1981.

[114] T. L. Becker, A. B. Wollaber, and E. W. Larsen. A hybrid Monte Carlo-deterministic method for global particle transport calculations. *Nuclear Science and Engineering*, 155(2):155–167, 2007.

[115] M. M. Miften and E. W. Larsen. The quasi-diffusion method for solving transport problems in palanar and spherical geometries. *Transport Theory and Statistical Physics*, 22:2:165–186, 1993.

[116] M. M. Miften and E. W. Larsen. A symmetrized quasidiffusion method for solving transport problems in multidimensional geometries. In *Mathematical Methods and Supercomuting in Nuclear Applications*, Karlsruhe, Germany, 1993.

[117] V. Ya. Gol'din and N. N. Kalitkin. Finding the solutions of constant sign of ordinary differential equations. *USSR Comp. Math. and Math. Phys.*, 6(1):228–230, 1966.

[118] M. L. Adams. Subcell balance methods for radiative transfer on arbitrary grids. *Transport Theory & Statistical Physics*, 26:385–431, 1997.

[119] V. Ya. Gol'din. Characteristic difference scheme for non-stationary kinetic equation. *Soviet Mathematics Doklady*, 1:902–906, 1960.

[120] K. Takeuchi. A numerical method for solving the neutron transport equation in finite cylindrical geometry. *Journal of Nuclear Science and Technology*, 6:446–473, 1969.

[121] J. R. Askew. A characteristic formulation of the neutron transport equation in complicated geometries. Technical Report M1108, Atomic Energy Establishment, 1972.

[122] H. D. Brough and C. T. Chudley. Characteristic ray solutions of the transport equation. In J. Lewis and M. Becker, editors, *Advances in Nuclear Science and Technology*, volume 12, pages 1–30. Plenum Press, 1980.

[123] J. R. Askew and M. J. Roth. WIMS-E: A scheme for neutronics calculations. Technical Report AEEW-R-1315, United Kingdom Atomic Energy Authority, 1982.

[124] M. Edenius, K. Ekberg, B. H. Forssén, and D. Knott. *CASM0-4, A fuel assembly burnup program, User's manual.* Studsvik/SOA-93/1, Studsvik of America, 1993.

[125] M. Zika and M. Adams. Acceleration for long-characteristics assembly-level transport problems. *Nuclear Science and Engineering*, 134:135–158, 2000.

[126] E. N. Aristova and A.V. Kolpakov. A combined finite difference scheme for an elliptic operator in an oblique-angled cell. *Math. Model. Comput. Exp.*, 1:187–196, 1993.

[127] P. Ghassemi and D. Y. Anistratov. Multilevel quasidiffusion method with mixed-order time discretization for multigroup thermal radiative transfer problems. *Journal of Computational Physics*, 409:109315, 2020.

[128] M. Loève. *Probability Theory*. Van Nostrand, 1955.

[129] J. L. Lumley. *Stochastic Tools in Turbulence*. Academic Press, 1972.

[130] J. L. Lumley. Coherent structures in turbulence. In R. E. Meyer, editor, *Transition and Turbulence*, pages 215–242. Academic Press, 1981.

[131] S. Volkwein. Model reduction using proper orthogonal decomposition, 2013. Lecture Notes, University of Konstanz.

[132] I. C. F. Ipsen. *Numerical Matrix Analysis*. Society for Industrial and Applied Mathematics, 2009.

[133] K. K. Chen, J. H. Tu, and C. W. Rowley. Variants of dynamic mode decomposition: Boundary condition, Koopman, and Fourier analyses. *Journal of Nonlinear Science*, 22:887–915, 2012.

[134] B. O. Koopman. Hamiltonian systems and transformation in Hilbert space. In *Proc. Natl. Acad. Sci. U.S.A.*, volume 17, pages 315–318, 1931.

[135] B. O. Koopman and J. V. Neumann. Dynamical systems of continuous spectra. In *Proc. Natl. Acad. Sci. U.S.A.*, volume 18, pages 255–263, 1932.

[136] M. Budišić, R. Mohr, and I. Mezić. Applied Koopmanism. *CHAOS*, 22:047510, 2012.

[137] A. Alla and J. N. Kutz. Nonlinear model order reduction via dynamic mode decomposition. *SIAM J. Sci. Comput.*, 439:B778–B796, 2017.

[138] K. Kunisch and S. Volkwein. Galerkin proper orthogonal decomposition methods for a general equation in fluid dynamics. *SIAM J. Numer. Anal*, 40:492–515, 2002.

[139] O. Ghattas T. Bui-Thanh, K. Willcox. model reduction for large-scale systems with high-dimensional parametric input space. *SIAM J. Sci. Comput.*, 30(6):3270–3288, 2008.

[140] H. Antil K. Carlberg, M. Barone. Galerkin v. least-squares Petrov-Galerkin projection in nonlinear model reduction. *Journal of Computational Physics*, 330:693–734, 2017.

[141] K. Carlberg Y. Choi. Space-time least-squares Petrov-Galerkin projection for nonlinear model reduction. *SIAM J. Sci. Comput.*, 41(1):A26–A58, 2019.

[142] J. A. Fleck and J. D. Cummings. An implicit Monte Carlo scheme for calculating time and frequency dependent nonlinear radiation transport. *J. of Comp. Phys.*, 8:313–342, 1971.

[143] L. K. Abu-Shumays. Angular quadratures for improved transport computations. *Transport Theory & Statistical Physics*, 30:169–204, 2001.

[144] A. S. Moore, T. M. Guymer, J. Morton, B. Williams, J. L. Kline, N. Bazin, C. Bently, S. Allan, K. Brent, A. J. Comley, K. Flippo, J. Cowan, J. M. Taccetti, K. Missack-Tamashiro, D. W. Schmidt, C. E. Hamilton, K. Obrey, N. E. Lanier, J. B. Workman, R. M. Stevenson. Characterization of supersonic radiation waves. *Journal of Quantitative Spectroscopy & Radiative Transfer*, 159:19–28, 2015.

[145] T. M. Guymer, A. S. Moore, J. Morton, J. L. Kline, S. Allan, N. Bazin, J. Benstead, C. Bentley, A. J. Comley, J. Cowan, K. Flippo, W. Garbett, C. Hamilton, N. E. Lanier, K. Mussack, K. Obrey, L. Reed, D. W. Schmidt, R. M. Stevenson, J. M. Taccetti, J. Workman. Quantifying equation-of-state and opacity errors using integrated supersonic diffusive radiation flow experiments on the National Ignition Facility. *Physics of Plasmas*, 22:043303, 2015.

[146] C. L. Fryer, E. Dodd, W. Even, C. J. Fontes, C. Greeff, A. Hungerford, J. Kline, K. Mussack, I. Tregillis, J. B. Workman, J. Bernstead, T. M. Guymer, A. S. Moore and J. Morton. Uncertainties in radiation flow experiments. *High Energy Density Physics*, 18:45–54, 2016.

[147] C. L. Fryer, A. Diaw, C. J. Fontes, A. L. Hungerford, J. Kline, H. Johns, N. E. Lanier, S. Wood, T. Urbatsch. Designing radiation transport tests: Simulation-driven uncertainty-quantification of the COAX temperature diagnostic. *High Energy Density Physics*, 35:100738, 2020.

[148] C. W. Rowley and J. E. Mardsen. Reconstruction equations and the Karhunen-Loève expansion for systems with symmetry. *Physica D*, 142:1–19, 2000.

[149] J. Reiss, P. Schulze, J. Sesterhenn and V. Mehrmann. The shifted proper orthogonal decomposition: A mode decomposition for multiple transport phenomena. *SIAM Journal of Scientific Computing*, 40:A1322–A1344, 2018.

[150] D. Anistratov and N. Stehle. Computational transport methodology based on decomposition of a problem domain into transport and diffusive subdomains. *Journal of Computational Physics*, 231:8009–8028, 2012.

[151] N. Stehle, D. Anistratov, and M. Adams. A hybrid transport-diffusion method for 2D transport problems with diffusive subdomains. *Journal of Computational Physics*, 270:325–344, 2014.

[152] O. San and J. Borggaard. Principal interval decomposition framework for POD reduced-order modeling of convective boussinesq flows. *Int. J. Numer. Meth. Fluids*, 78:37–62, 2015.

[153] S. Chaturantabut and D. C. Sorensen. Nonlinear model reduction via discrete empirical interpolation. *SIAM J. Sci. Comput.*, 32:2737–2764, 2010.

[154] K. Carlberg, C. Farhat, J. Cortial, and D. Amsallem. The GNAT method for nonlinear model reduction: Effective implementation and application to computational fluid dynamics and turbulent flows. *Journal of Computational Physics*, 242:623–647, 2013.

[155] V. Ya. Gol'din, G. V. Danilova, and B. N. Chetverushkin. Approximate method for solving time-dependent kinetic equation. In *Computational Methods in Transport Theory*, pages 50–57. Atomizdat, Moscow, 1969. (in Russian).

[156] A. Matsekh , L. Chacon, H. Park, and G. Chen. Machine learning for memory reduction in the implicit monte carlo simulations of thermal radiative transfer. Technical Report LA-UR-18-25444, Los Alamos National Laboratory, 2018.

[157] P. Ghassemi and D. Y. Anistratov. An approximation method for time-dependent problems in high energy density thermal radiative transfer. *Journal of Computational and Theoretical Transport*, 41:31–50, 2020.

[158] D. Y. Anistratov. Implicit methods with reduced memory for time-dependent boltzmann transport equation. *Transactions of American Nuclear Society*, 122:367–370, 2020.

[159] D. Amsallem and C. Farhat. Interpolation method for adapting reduced-order models and application to aerolasticity. *AIAA Journal*, 46(7):1803–1813, 2008.

[160] M. Oulghelou and C. Allery. Non intrusive method for parametric model order reduction using a bi-calibrated interpolation on the Grassman manifold. *Journal of Computational Physics*, 426:109924, 2021.

APPENDICES

APPENDIX

A

ACRONYMS

A summary of all acronyms & abbreviations is documented in Table A.1.

Table A.1: A summary of acronyms & abbreviations used in alphabetical order.

Acronym	Abbreviation
Algorithm	Alg.
Boltzmann Transport Equation	BTE
Data-driven Eddington Tensor	DET
Dynamic Mode Decomposition	DMD
Deep Neural Network	DNN
Degrees of Freedom	DoF
Eddington Tensor	ET
Equation	Eq.
Equilibrium-subtracted Dynamic Mode Decomposition	DMD-E
Figure	Fig.
Flux-Limited Diffusion	FLD
Full-Order Model	FOM
Low-Order Quasidiffusion	LOQD

Multilevel Quasidiffusion	MLQD
Normalized Boltzmann Transport Equation	NBTE
Proper Orthogonal Decomposition	POD
POD-Galerkin	POD-G
POD-Petrov-Galerkin	POD-PG
Quasidiffusion	QD
Reduced-Order Model	ROM
Section	Sec.
Table	Tab.
Transport Corrected Approximation	TCA
Thermal Radiative Transfer	TRT
Variable Eddington Factor	VEF
With Respect To	w.r.t.

APPENDIX

B

VARIABLES & CONSTANTS

A summary of all variables & constants is documented in Table B.1.

Table B.1: A summary of common variables & constants and their abbreviations in alphabetical order.

Variable	Abbreviation
Boltzmann constant	k
Directional cosine	μ
Eddington tensor	$\mathbf{f}$
Kronecker delta	$\delta_{i,j}$
Material energy density	ε
Material heat capacity	c_v
Material opacity	$\varkappa$
Material temperature	T
Normalized radiation intensity	$\bar{I}$
Outward normal to Γ	$\boldsymbol{n}_\Gamma$
Particle direction of motion vector	$\boldsymbol{\Omega}$
Photon frequency	ν

Planck's constant	h
Planckian distribution function	B
Radiation constant	a_R
Spatial domain	Γ
Spatial domain boundary	$\partial\Gamma$
Spatial domain length (x direction)	L_x
Spatial domain length (y direction)	L_y
Spatial position	$\boldsymbol{r}$
Stefan-Boltzmann constant	σ_R
Radiation energy density	E
Radiation flux	$\boldsymbol{F}$
Radiation intensity	I
Relative POD error in Frobenius norm	ξ
Spatial position	$\boldsymbol{r}$
Speed of light	c
Time	t
Unit sphere	$\mathcal{S}$
Zeroth intensity moment	ϕ

APPENDIX

C

RAY TRACING ON 2D ORTHOGONAL SPATIAL GRIDS

We have an orthogonal grid whose vertices are located at the coordinates (c_i^x, c_j^y) for $i = 0, \ldots, N_x$ and $j = 0, \ldots, N_y$. If $\{\Delta x_i\}_{i=1}^{N_x}$ and $\{\Delta y_j\}_{j=1}^{N_y}$ are the cell widths in the $\boldsymbol{e}_x$ and $\boldsymbol{e}_y$ directions, these coordinates are defined as

$$c_i^x = c_{i-1}^x + \Delta x_i, \quad i = 1, \ldots N_x, \tag{C.1}$$

$$c_j^y = c_{j-1}^y + \Delta y_j, \quad j = 1, \ldots N_y, \tag{C.2}$$

$$c_0^x = c_0^y = 0.$$

The area of each cell is $A_{ij} = \Delta x_i \Delta y_j$. The set of particle directions is $\{\Omega_m\}_{m=1}^{N_\Omega}$. Let $\bar{\boldsymbol{\Omega}}_m$ be the projection of $\boldsymbol{\Omega}_m$ onto the x-y plane. The angle between $\bar{\boldsymbol{\Omega}}_m$ and the positive x axis is

$$\theta_m = \begin{cases} \arctan(\frac{\Omega_{m,y}}{\Omega_{m,x}}) & \Omega_{m,y} > 0,\ \Omega_{m,x} > 0 \\ \pi - \arctan(-\frac{\Omega_{m,y}}{\Omega_{m,x}}) & \Omega_{m,y} > 0,\ \Omega_{m,x} < 0 \end{cases} \tag{C.3}$$

The goal of this formulation is to trace characteristics along an underlying spatial grid

in such a way that no one characteristic crosses multiple cells at once (i.e. characteristics may not travel through mesh vertices). To accomplish this, an initial distribution of characteristics will be calculated such that each cell vertex defines a boundary between characteristics width-wise. In other words, each boundary between characteristics intercepts a single cell vertex. An example initial distribution of characteristics is depicted in Fig. C.1.

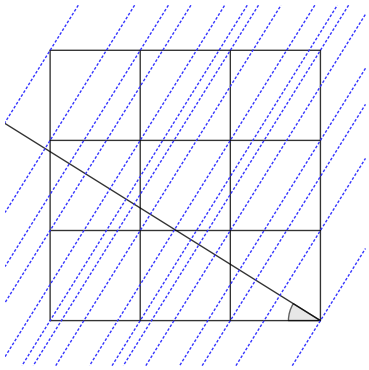

Figure C.1: Characteristic mesh for some direction traced over a 3x3 uniform grid

This yields $(N_x+1)(N_y+1)$ boundary lines which can be described with the equations

$$g_{m,i,j}(x) = y = b_{m,i,j} + s_m x, \quad b_{m,i,j} = c_j^y - s_m c_i^x, \qquad \text{(C.4)}$$
$$i = 0, \ldots N_x, \quad j = 0, \ldots N_y,$$

with slopes

$$s_m = \begin{cases} \tan(\theta_m) & \theta_m \in [0, \frac{\pi}{4}] \\ 1/\tan(\frac{\pi}{2} - \theta_m) & \theta_m \in [\frac{\pi}{4}, \frac{\pi}{2}] \\ -1/\tan(\theta_m - \frac{\pi}{2}) & \theta_m \in [\frac{\pi}{2}, \frac{3\pi}{4}] \\ -\tan(\pi - \theta_m) & \theta_m \in [\frac{3\pi}{4}, \pi] \end{cases} \qquad \text{(C.5)}$$

The midlines along each characteristic are then described by

$$t_{m,k}(x) = y = \frac{\hat{b}_{m,k} + \hat{b}_{m,k+1}}{2} + s_m x, \quad k = 1, \ldots (N_x+1)(N_y+1) - 1,$$

where the set $\{\hat{b}_{m,k}\}_{k=1}^{(N_x+1)(N_y+1)}$ contains the values of $b_{m,i,j}$ in ascending order

$$\{\hat{b}_{m,k}\}_{k=1}^{(N_x+1)(N_y+1)} = \{b_{m,k} \in \{b_{m,i,j}\}_{i,j=1}^{N_x,N_y} \mid b_{m,k} < b_{m,k+1},\ k = 1, \ldots, (N_x+1)(N_y+1)-1\}. \tag{C.6}$$

Each characteristic is finally segmented at each cell interface encountered in the underlying spatial mesh, yielding a series of connected segments that each lie over a single spatial cell. An example set of characteristic segments for a 2×2 spatial grid is shown in Fig. C.2.

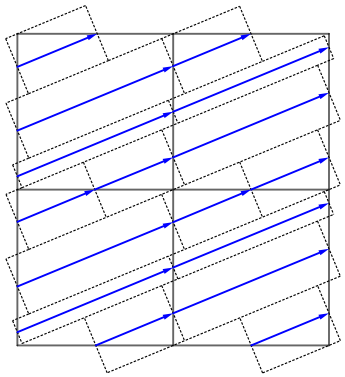

Figure C.2: Characteristics traced over a sample 2x2 grid for $\theta = \frac{\pi}{8}$

The mesh of characteristics is refined by introducing a maximum width $w_{\max}$. Any characteristics calculated from the initial ray tracing procedure that have a width $w_k > w_{\max}$ are split into 2 characteristics of width $\frac{w_k}{2}$. Characteristics are continuously split into even halves by width until none are wider than $w_{\max}$.

APPENDIX

D

THE FLECK-CUMMINGS NUMERICAL TEST PROBLEM

Numerical testing for each of the ROMs presented in this work is carried out on the well-known Fleck-Cummings (F-C) problem [142]. Both 1D slab and 2D Cartesian geometries are considered. In 1D geometry this F-C test takes the form of a homogeneous slab 6 cm in length. In 2D geometry the F-C test is fashioned as a square homogeneous domain in the $x-y$ plane, 6 cm in length on both sides. The domain is initially at a temperature of T^0, the left boundary of the domain is subject to incoming radiation with blackbody spectrum at a temperature of T^{in}, and there is no incoming radiation at the other boundaries. The material is characterized by an opacity of

$$\varkappa(\nu, T) = \frac{\varkappa^*}{\nu^3}\left(1 - e^{-\frac{\nu}{T}}\right), \quad \varkappa^* = 27 \times 10^9 \left[\frac{\text{eV}^3}{\text{cm}}\right] \tag{D.1}$$

where ν and T are measured in eV, and a material energy density that is linear in temperature

$$\varepsilon(T) = c_v T, \tag{D.2}$$

with volumetric material heat capacity $c_v = 0.5917 a_R (T^{\text{in}})^3$ with units cm^{-3}. Fig. D.1 plots the opacity from Eq. D.1 against photon energy for several material temperatures. The considered ranges for ν and T are typical for the F-C test.

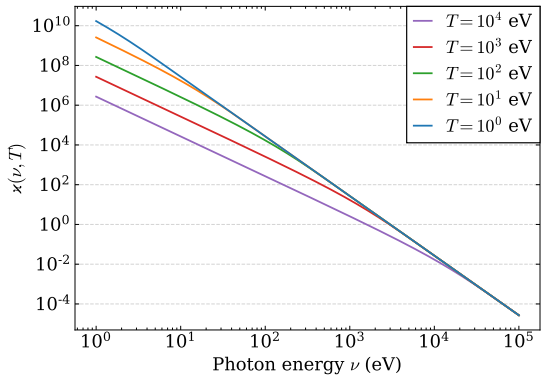

Figure D.1: The F-C test spectral opacity $\varkappa(\nu, T)$ plotted vs photon frequency for several material temperatures.

The nominal parameters for this test are $T^0 = 1$ eV and $T^{\text{in}} = 1$ KeV. This creates an initial condition with a large discontinuity at the left boundary. Both T and E take the form of a nonlinear wave that first rapidly forms on the left boundary before propagating to the right. After this the domain is continuously heated. Eventually the solution reaches a regime close to steady state. Some discrete solutions to this F-C test (obtained via the MLQD method, see Sec. 2.1) for the material temperature and total radiation energy density for $T^0 = 1$ eV and $T^{\text{in}} = 1$ KeV are depicted in Figs. D.2 and D.3. Fig. D.2 shows the solution in 2D Cartesian geometry at times $t = 1, 2, 3$ ns over the entire spatial domain. Figure D.3 shows the solution in 1D slab geometry for several instants of time. Note that this 1D solution is a close approximation to the midline ($y = 3$ cm) of the 2D solution. In both cases the BTE was discretized in space with the SCB scheme (ref. Secs. 2.2 & 2.3.1). In the 2D case, a uniform grid of 20×20 cells was used to discretize the domain and The Abu-Shumays angular quadrature set q461214 with 36 discrete directions per quadrant [143] is used to discretize in angle. In the 1D case, the spatial domain was discretized into 60 uniformly distributed cells and the double S_4 Gauss quadrature set is used to discretize the angular direction. All numerical tests use the 17 frequency group structure defined in Tab. D.1. This group structure is created to capture well the Planck

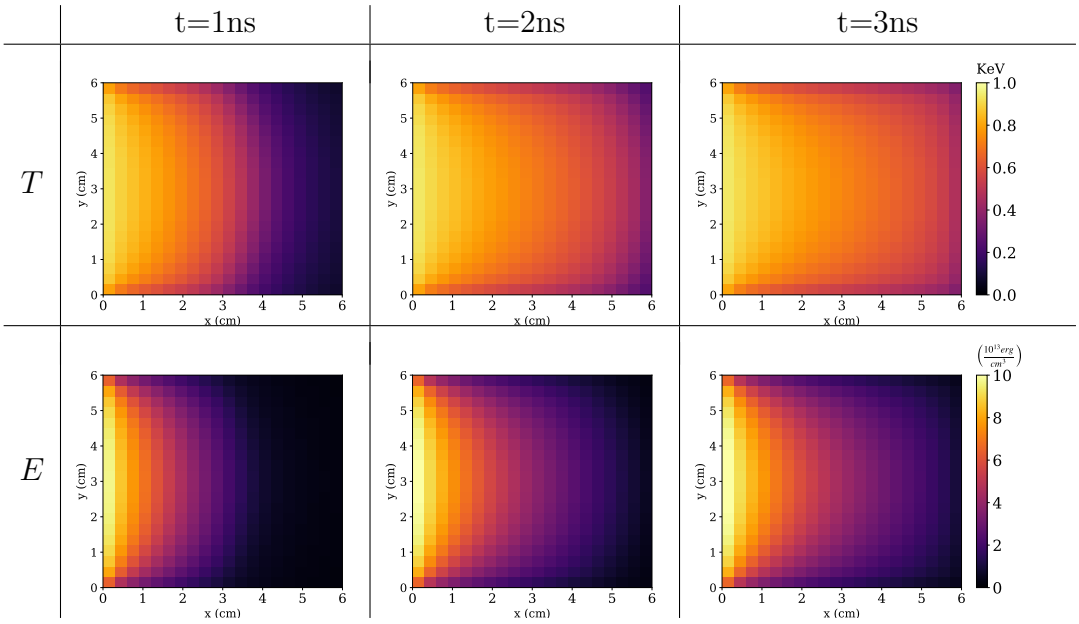

Figure D.2: Solution for the material temperature (T) and total radiation energy density (E) of the F-C test problem in 2D Cartesian geometry with $T^0 = 1$ eV and $T^{\text{in}} = 1$ KeV over the spatial domain at times t=$1, 2, 3$ ns. The BTE is discretized with the SCB scheme and low-order equations are discretized with a finite volumes scheme.

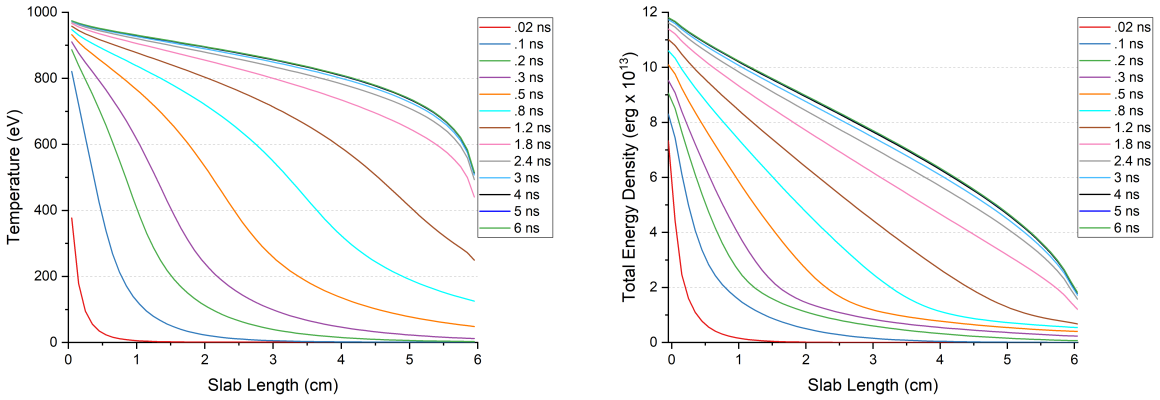

(a) Material Temperature

(b) Radiation Energy Density

Figure D.3: Solution for the material temperature (T) and total radiation energy density (E) of the F-C test problem in 1D slab geometry with $T^0 = 1$ eV and $T^{\text{in}} = 1$ KeV. Several instants of time are pictured. The BTE is discretized with the SCB scheme and low-order equations are discretized with a finite volumes scheme.

spectrum at the boundary temperature $B(\nu, T^{\text{in}})$ at the nominal value. All presented methods also use the same implicit time integration scheme (backward-Euler) and solve for the time interval $t \in [0, t^{\text{end}}]$ with uniform time steps $\Delta t = 2 \times 10^{-2}$ ns. Note that in 2D geometry with the considered grids, when the BTE is discretized in space with the conservative method of characteristics (ref. Sec. 2.3.2), the F-C solution for E and T differs from that shown Fig. D.2 at an order of $10^{-2} - 10^{-3}$ and no distinct qualitative differences can be easily noticed.

g	1	2	3	4	5	6	7	8	9
ν_g [KeV]	0.7075	1.415	2.123	2.830	3.538	4.245	5.129	6.014	6.898
g	10	11	12	13	14	15	16	17	
ν_g [KeV]	7.783	8.667	9.551	10.44	11.32	12.20	13.09	1×10^7	

Table D.1: Upper boundaries for each frequency group

The F-C test was chosen as the platform for investigating the numerical performance of all ROMs developed in this work for several reasons. At the nominal values for T^0 and T^{in}, the initial condition for this test manifests as a large discontinuity on the left boundary. Resolving this discontinuity, and the ensuing rapid evolution of the radiation wavefront on the left boundary is a challenge. The wavefront then propagates across the test domain until it reaches the right boundary. Several physical regimes are encountered during the evolution of the F-C test in different energy ranges, since the opacity function varies across a wide range magnitudes in both ν and T. Radiation in low-frequency ranges resides primarily in the diffusive regime, while higher frequency radiation exists mostly in the streaming regime. Each portion of the domain once heated also experiences effects of both local and non-local radiation emitted from the nearby material and boundary source, respectively.

The high-order iteration counts (s iterations in Alg. 1) for the 2D F-C test as described above solved with the MLQD method are shown in Figs. D.4 and D.5. The only difference between the two plots is in the low-order boundary conditions. The method in Fig. D.4 is the default MLQD formulation as described in Sec. 2.1. Fig. D.5 shows iteration counts for the MLQD method that uses the alternative BCs defined in Eqs. 2.10 & 2.18.

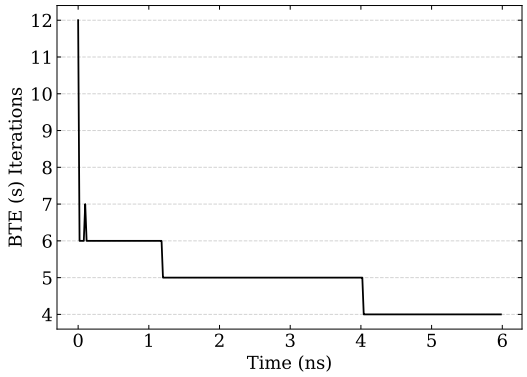

Figure D.4: High-order (BTE or s) iteration count per time step using the MLQD method (see Sec. 2.1 & Alg. 1) for the 2D F-C test problem with $T^0 = 1$ eV and $T^{\text{in}} = 1$ KeV.

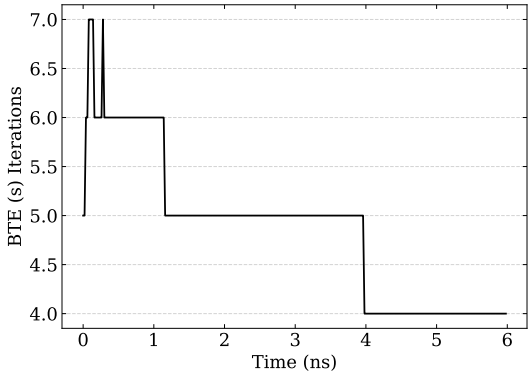

Figure D.5: High-order (BTE or s) iteration count per time step using the MLQD method (see Sec. 2.1 & Alg. 1) equipped with alternative BCs defined in Eqs. 2.10 & 2.18 for the 2D F-C test problem with $T^0 = 1$ eV and $T^{\text{in}} = 1$ KeV.

APPENDIX

E

DIMENSIONLESS EQUATIONS FOR GREY TRT PROBLEMS WITH FLECK-CUMMINGS OPACITY

In this appendix, a dimensionless analysis is performed on the LOQD and MEB equations describing the grey TRT problem. Characteristic parameters of the TRT problem are identified that will influence the TRT solution via scaling relationships. The F-C test problem described in Appendix D is given consideration to establish specific relationships between the F-C test parameters and the TRT solution.

The primary goal of this analysis is to identify the essential manner in which moments of the radiation intensities can be described using characteristic quantities of the TRT problem. Energy exchange between radiation and matter occurs on the grey scale (see Eq. 1.3) and the fundamental behavior of the TRT problem is driven by the grey radiation

energy density and flux

$$E(\boldsymbol{r},t)=\frac{1}{c}\int_0^\infty\int_{4\pi} I(\boldsymbol{r},\boldsymbol{\Omega},\nu,t)\;d\Omega d\nu, \tag{E.1}$$

$$\boldsymbol{F}(\boldsymbol{r},t)=\int_0^\infty\int_{4\pi} \boldsymbol{\Omega} I(\boldsymbol{r},\boldsymbol{\Omega},\nu,t)\;d\Omega d\nu, \tag{E.2}$$

which are governed by the grey LOQD equations

$$\frac{\partial E}{\partial t}+\boldsymbol{\nabla}\cdot\boldsymbol{F}+c\varkappa(T)E=4\pi\varkappa(T)B(T), \tag{E.3a}$$

$$\frac{1}{c}\frac{\partial \boldsymbol{F}}{\partial t}+c\boldsymbol{\nabla}\cdot(\mathfrak{f}E)+\varkappa(T)\boldsymbol{F}=0, \tag{E.3b}$$

closed with the grey Eddington (QD) tensor

$$\mathfrak{f}(\boldsymbol{r},t)=\frac{\int_0^\infty\int_{4\pi}(\boldsymbol{\Omega}\otimes\boldsymbol{\Omega})I(\boldsymbol{r},\boldsymbol{\Omega},\nu,t)\;d\Omega d\nu}{\int_0^\infty\int_{4\pi} I(\boldsymbol{r},\boldsymbol{\Omega},\nu,t)\;d\Omega d\nu}. \tag{E.4}$$

The grey LOQD equations are coupled with the MEB equation cast in terms of the grey unknowns as

$$\frac{\partial\varepsilon(T)}{\partial t}=c\varkappa(T)E-4\pi\varkappa(T)B(T). \tag{E.5}$$

$\varkappa(T)$ is the grey opacity and the Planckian function $B(T)=\int_0^\infty B(\nu,T)\;d\nu$ is

$$B(T)=\frac{\sigma_R}{\pi}T^4, \tag{E.6}$$

where $B(\nu,T)$ is defined in Eq. 1.5.

Dimensionless forms of the grey LOQD and MEB equations are now derived to investigate how the fundamental quantities that govern the TRT problem are related to certain characteristic variables. Specifically, these equations are scaled with respect to the characteristic width of the spatial domain (L) and temperature that represents energy deposition in the domain ($\hat{T}$). Here consideration is for the case with a linear material energy density

$$\varepsilon(T)=c_vT, \tag{E.7}$$

where the volumetric heat capacity c_v has units cm^{-3}, and opacity function of the following

form:

$$\varkappa(T) = \frac{\varkappa_0}{T^p}, \quad p \geq 0, \tag{E.8}$$

where $\varkappa_0$ is some constant. Dimensionless variables for space and time are defined as

$$\boldsymbol{\rho} = \frac{\boldsymbol{r}}{L}, \quad \tau = \frac{c}{L}t. \tag{E.9}$$

Dimensionless dependent variables are thus defined as

$$\mathfrak{E}(\boldsymbol{\rho}, \tau) = c\frac{E(\boldsymbol{r}, t)}{\hat{B}}, \quad \mathfrak{F}(\boldsymbol{\rho}, \tau) = \frac{\boldsymbol{F}(\boldsymbol{r}, t)}{\hat{B}}, \quad \theta(\boldsymbol{\rho}, \tau) = \frac{T(\boldsymbol{r}, t)}{\hat{T}}, \tag{E.10}$$

where $\hat{B} = B(\hat{T})$. Lastly dimensionless forms of various parameters and functions are introduced

$$\sigma = \frac{L\varkappa_0}{\hat{T}^p}, \quad \eta = \frac{\pi c_v c}{\sigma_R \hat{T}^3}, \quad \beta = \frac{B}{\hat{B}} = \theta^4. \tag{E.11}$$

It is important to recognize that the Eddington tensor $\mathfrak{f}$ is a dimensionless quantity by definition (ref. Eq. E.4). In fact, applying a similar scaling as above to the radiation intensities to derive a dimensionless form of the BTE will not have any effect on $\mathfrak{f}$. Only the necessary scaling relationships for the low-order system that governs our quantities of interest ($E,\ \boldsymbol{F},\ T$) are considered. A change of variables is performed on the radiation energy balance equation (Eq. E.3a) by introducing the relations in Eq. E.10 to get

$$\frac{\hat{B}c}{cL}\frac{\partial \mathfrak{E}}{\partial \tau} + \frac{\hat{B}}{L}\boldsymbol{\nabla}_\rho \cdot \mathfrak{F} + \frac{\varkappa_0}{\hat{T}^p\theta^p}\hat{B}\mathfrak{E} = 4\pi\frac{\varkappa_0}{\hat{T}^p\theta^p}B, \tag{E.12}$$

which when recombined becomes the dimensionless radiation energy balance equation

$$\frac{\partial \mathfrak{E}}{\partial \tau} + \boldsymbol{\nabla}_\rho \cdot \mathfrak{F} + \frac{\sigma}{\theta^p}\mathfrak{E} = 4\pi\frac{\sigma}{\theta^p}\beta(\theta). \tag{E.13}$$

The variables in Eq. E.10 are similarly substituted into the radiation momentum balance equation (Eq. E.3b) to find

$$\frac{\hat{B}c}{cL}\frac{\partial \mathfrak{F}}{\partial \tau} + \frac{\hat{B}}{L}\boldsymbol{\nabla}_\rho \cdot (\mathfrak{f}\mathfrak{E}) + \frac{\varkappa_0}{\hat{T}^p\theta^p}\hat{B}\mathfrak{F} = 0, \tag{E.14}$$

which when recombined becomes the dimensionless radiation momentum balance equation

$$\frac{\partial \mathfrak{F}}{\partial \tau} + \boldsymbol{\nabla}_{\rho} \cdot (\mathfrak{f}\mathfrak{E}) + \frac{\sigma}{\theta^{p}}\mathfrak{F} = 0. \tag{E.15}$$

The scalings in Eq. E.10 applied to the MEB equation (Eq. E.5) with a material energy density of the form in Eq. E.7 yields

$$\frac{c_v c\hat{T}}{L}\frac{\partial \theta}{\partial \tau} = \frac{\varkappa_0}{\hat{T}^{p}\theta^{p}}(\hat{B}\mathfrak{E} - 4\pi B). \tag{E.16}$$

This equation can be recombined to form

$$\frac{c_v c\hat{T}}{\hat{B}}\frac{\partial \theta}{\partial \tau} = \frac{\sigma}{\theta^{p}}(\mathfrak{E} - 4\pi\beta(\theta)), \tag{E.17}$$

which is equivalent to the following equation, which is the dimensionless MEB equation

$$\eta\frac{\partial \theta}{\partial \tau} = \frac{\sigma}{\theta^{p}}(\mathfrak{E} - 4\pi\beta(\theta)). \tag{E.18}$$

Equations E.13, E.15 and E.18 comprise a dimensionless description of the grey TRT problem. Each of these equations is seen to scale with the quantity σ defined in Eq. E.11. The function $\frac{\sigma}{\theta^{p}}$ can actually be interpreted as the dimensionless opacity of the TRT problem and will impact the solution behavior in the same way as $\varkappa(T)$. The solution will then effectively vary with the TRT problem's characteristics as a function of $\hat{T}^{-p}$.

Consider for example the F-C test defined in Appendix D. Using the spectral opacity $\varkappa(\nu, T)$ defined for this test problem (Eq. D.1), the characteristic grey opacity can be calculated as

$$\varkappa(T) = \frac{\int_0^{\infty} \varkappa(\nu, T)B(\nu, T)\ d\nu}{\int_0^{\infty} B(\nu, T)\ d\nu}, \tag{E.19}$$

which when evaluated takes the form

$$\varkappa(T) = \frac{\tilde{\varkappa}}{T^3}\,, \tag{E.20}$$

where

$$\tilde{\varkappa} = \frac{\varkappa^*}{\int_0^{\infty} \frac{x^3}{e^x - 1}dx} = \frac{15\varkappa^*}{\pi^4}\ \left[\frac{\mathrm{eV}^3}{\mathrm{cm}}\right]. \tag{E.21}$$

The grey solution of the F-C test will then in principle scale with $\hat{T}^{-3}$, where $\hat{T}$ might be defined as the temperature of incoming radiation (radiation drive temperature) T^{in}.